Impact of formate, citrate and gluconate on the retention behavior of Pu(III/IV), Cm(III) and Eu(III) by cement phases

Zur Erlangung des akademischen Grades eines

DOKTORS DER NATURWISSENSCHAFTEN

(Dr. rer. nat.)

von der KIT-Fakultät für Chemie und Biowissenschaften

des Karlsruher Instituts für Technologie (KIT)

genehmigte

DISSERTATION

von

Dipl. Chem. Rosa Ester Guidone

KIT-Dekan: Prof. Dr. Hans-Achim Wagenknecht
Referent: Prof. Dr. Horst Geckeis
Korreferentin: Prof. Dr. Barbara Lothenbach

Tag der mündlichen Prüfung: 26.04.2023

Erklärung

Hiermit versichere ich, dass ich die vorliegende Arbeit selbstständig verfasst und keine anderen als die angegebenen Quellen und Hilfsmittel verwendet habe. Darüber hinaus versichere ich, dass alle Stellen der Arbeit, die wörtlich oder inhaltlich aus anderen Werken übernommen wurden, als solche kenntlich gemacht sind und die elektronische Version der Arbeit mit der schriftlichen übereinstimmt, und dass die vorliegende Arbeit in gleicher oder ähnlicher Form bislang nicht an einer Hochschule des In- oder Auslands als Bestandteil eines Promotionsverfahrens vorgelegt wurde. Zudem versichere ich, dass ich keinen vorausgegangenen Promotionsversuch unternommen habe, und dass kein Promotionsverfahren an einer anderen Fakultät läuft oder erfolglos beendet wurde. Die Satzung des Karlsruher Instituts für Technologie (KIT) zur Sicherung guter wissenschaftlicher Praxis wurde in der jeweils gültigen Fassung beachtet. Weiterhin versichere ich, dass die Abgabe und Archivierung der Primärdaten gemäß Abs. A (6) der Regeln zur Sicherung guter wissenschaftlicher Praxis des KIT beim Institut gesichert ist.

_____

Ort,   Datum

_____

Unterschrift

Acknowledgments

Abstract

Radioactive waste is generated by different anthropogenic activities, e.g. nuclear power plants, military applications, medicine, research, industry, among others. Underground repositories are one of the most favored options for disposal of radioactive waste. The safety and the long-term performance of such repositories rely on a multi-barrier concept, which includes technical and geological barriers. Cementitious materials are widely used for construction and conditioning purposes, in particular in the context of low and intermediate level wastes (L/ILW). The possible infiltration of groundwater can initiate a series of dissolution and precipitation processes that can affect the composition of cement (cement degradation). Cementitious materials impose alkaline and hyperalkaline conditions ($10 \leq \mathrm{pH} \leq 13$) over a very long period of time, whereas strongly reducing conditions are expected due to the anaerobic corrosion process of the steel-based materials present in the repository. The main solid phases in hydrated cements: calcium silicates hydrates (C-S-H), ettringite, monosulfate, monocarbonate, and hemicarbonate (AFm phases), can retain radionuclides present in the waste, thus preventing or slowing down their release from the disposal site.

Organic ligands can be present in the waste as decontamination agents (e.g. EDTA, citrate), generated *in situ* through the decomposition of complex organic materials (e.g. cellulose, spent filter, ion exchange resins, etc.), but also as cement additives widely used in modern cementitious material to improve the workability and the final performance of the material (e.g. formate, citrate, gluconate). These ligands can form stable and soluble complexes with radionuclides (L) (e.g. An(III/IV)-OH-L, Ca-An(III/IV)-OH-L), eventually enhancing their mobility. Although expected to be weak, the interaction of organic ligands with cement hydrates can also alter the surface properties of those hydrates, affecting their retention properties with respect to radionuclides.

This study aims at a quantitative description and mechanistic understanding of sorption processes. This includes the uptake of formate, citrate and gluconate uptake on AFm phases, ettringite and C-S-H phases, as well as the impact of these organic ligands on the uptake of Eu(III), Cm(III) and Pu(III/IV) by the cement phases. These radionuclides have been chosen as representative of the actinides in the oxidation states +III and +IV, as expected in the reducing conditions predicted to develop after the repository closure. This study is divided into two main blocks:

1. The first part of this study investigates the cement-ligand (cement-L) interactions (binary system). Sorption experiment and thermodynamic calculations (by using the thermodynamic software GEMS) were carried out to identify the main effect of the organic ligands on the structure and composition of AFm phases (Ms, Mc, Hc), ettringite (AFt) and C-S-H phases (with a variable Ca/Si ratio, C/S = 0.8 -1.4) under hyperalkaline conditions (pH = 13.3).

2. The second block focuses on the impact of formate, citrate and gluconate on the retention of Pu (under hyperalkaline and reducing conditions), Eu(III) and, Cm(III) by AFm phases (Ms, Mc, Hc), ettringite (AFt) and C-S-H phases (ternary system) based on sorption experiments. In ad-

dition, the Pu-L systems (in absence of Ca) were investigated by systematic solubility experiments. To gain insight on the aqueous speciation and retention mechanism, the uptake of Cm(III) on C-S-H phases in presence and in absence of gluconate was further investigated by TRLFS spectroscopic studies.

The investigation of the binary system was carried out at the Cement & Asphalt Laboratory at Empa (Dübendorf, Switzerland), while the study of the ternary system was performed at the Institute for Nuclear Waste Disposal (INE) at KIT (Karlsruhe, Germany).

Binary system investigation: uptake of formate, citrate and gluconate on cement phases under hyperalkaline conditions:

Formate

Kinetic experiments conducted for contacting times t_{eq} = 1-14 days ([FOR]$_{tot}$ = 221 mM), indicate that steady state sorption conditions were obtained within 7 days. No additional phases were formed after 7 days of contacting time for most of the investigated systems.

Formate has a small effect on solid structure of C-S-H phases, AFm phases and ettringite. For all phases, an increase of the total calcium concentration in solution with the increase of formate concentration as well as a strong decrease of pH (by 2 pH units for Mc and of 4 pH units for ettringite at high formate concentration) has been observed. The pH decrease is due to the presence of high formate concentrations in solution while the sodium concentration was kept constant and equal to 0.2 M in all cases. A higher uptake of formate was observed on Ms and Hc and thus a more moderate pH decrease of less than 0.5 pH units. Formate sorbs weakly on all C-S-H phases with R_d values in the range of 3 to 7 dm^3/kg. A pH decrease of less than 1 pH unit was observed for C-S-H phases with high C/S (C/S = 1.4 and 1.2). This is explained by the initial presence of portlandite in this system, which was dissolved at high formate concentrations and thus compensated the decrease in pH observed for AFm and AFt phases. For C-S-H phase with a C/S ratio of 0.8, where no portlandite buffered the pH, a decrease of 3 pH units was observed. Sorption experiments on AFm phases and ettringite indicated that formate sorbed exclusively on the outer surface sites of Ms and ettringite, whereas both outer and inner surface sites of Hc are occupied. Formate weakly sorbs on Mc. The uptake of formate on hydrated cement paste, HCP occurs with an average R_d of 8.6 ± 0.3 dm^3/kg. This is in line with the sorption quantified for the individual cement phases.

Citrate

Kinetic experiments conducted for contacting times t_{eq} = 1-14 days ([CIT]$_{tot}$ = 34 mM) indicate that steady state sorption conditions were obtained within 4 days. No additional phases were formed after 7 days of contacting time, with the exception of the precipitation of Ca$_3$(C$_6$O$_5$H$_7$)$_2$·4H$_2$O detected for C-S-H phase with a C/S=1.4 at t_{eq} = 14 days. The dissolution of portlandite at the highest citrate concentration was also observed by XRD. Citrate has a negligible effect on the structure of C-S-H phases, ettringite and Mc while a clear increase of the interplanar distance was observed for Hc and a

slight increase for Ms. For sorption experiments on C-S-H phases, the presence of citrate resulted in an increase of the calcium concentration in solution, while the pH remained relatively constant. The calcium concentration is enhanced for high citrate concentrate and clearly indicates the formation of aqueous Ca-citrate complexes, such as CaCit⁻, which dominate the aqueous speciation. Citrate sorbs linearly with the increase of citrate concentration and with the concentration of Ca ions at the surface of C-S-H particles, i.e. with C/S ratio. Citrate sorbs strongly on Hc and Ms, and only moderately on ettringite and Mc. The high citrate uptake, $R_d = (154 \pm 16)$ dm^3·kg^{-1} observed on HCP is due to the sorption on high C/S C-S-H phases as well as on AFm phases and ettringite.

Gluconate

Kinetic experiments conducted for contacting times t_{eq} = 1-14 days ($[GLU]_{tot}$ = 21 mM), indicate that steady state sorption conditions were obtained within 7 days. No additional phases were formed after 7 days of contacting time for all phases. The presence of gluconate has a negligible impact on the structure of C-S-H phases, AFm phases and ettringite. The increase of Ca concentration observed for C-S-H, AFm phases and ettringite with the increase of gluconate concentration, supports the formation of Ca-gluconate complexes in solution. Gluconate does not significantly affect the pH values (ΔpH < 0.2 pH units) of the AFm phases and ettringite. In the case of C-S-H phases, gluconate decreases the pH by about 0.5 pH units for C-S-H 0.8, and less than 0.3 pH units for C/S > 1.0. This difference is explained by the dissolution of portlandite present at high C/S ratio, which buffers the pH values in the presence of gluconate. The uptake of gluconate on C-S-H phases increases with the increase of Ca ions at the surface of C-S-H phases. Gluconate sorbs weakly on Mc, whereas a strong uptake has been observed for Hc, followed by Ms and AFt. The uptake on HCP increases linearly with the gluconate concentration with an average distribution coefficient of R_d coefficient of (11.2 ± 1.0) dm^3·kg^{-1}, which is very close to the distribution coefficient obtained for C-S-H phase with a C/S of 1.4.

Ternary system investigation: impact of formate, citrate and gluconate on the uptake of Pu and Eu under hyperalkaline conditions:

Solubility of Pu in the presence of formate, citrate and gluconate

The solubility of PuO$_2$(ncr, hyd) in the presence of formate resulted in similar low concentrations as those determined in formate-free systems, indicating that the interaction between formate and Pu are weak for both HQ and Sn(II) redox buffered systems. A similar outcome was observed for the solubility of Pu in the presence of citrate, indicating a weak complexing behavior of citrate under very alkaline conditions. A strong increase of plutonium concentration with increasing gluconate concentration points towards the formation of stable aqueous Pu-GLU complexes. At very low gluconate concentrations ($[GLU]_{tot}$ < $[Sn(II)]_{tot}$), differences in solubility are rationalized by proposing the formation of Sn(II)-OH-GLU complexes, which decrease $_{free}$ available for the complexation with Pu. At higher gluconate concentrations, where the ligand is present in excess to Sn(II), the Pu concentrations determined in HQ

and Sn(II) systems overlap with each other within the corresponding experimental uncertainties. A linear trend with a slope of ≈ 1 can be tentatively proposed for the solubility diagram showing $[Pu]_{eq}$ vs $[GLU]_{tot}$, which suggests the formation of a Pu-OH-GLU complex with a stoichiometry Pu : GLU = 1 : 1. The formation of the complex $Pu(OH)_3(GLU_{-2H})^{2-}$ was proposed considering also the analogy with ISA. The fit of the solubility data considering this chemical model resulted in an equilibrium constant $\log \beta°_{(1,3,1,-2)} = -(17.4 \pm 1.3)$ for the chemical reaction $Pu^{4+} + 3H_2O(l) + GLU^- \leftrightarrow Pu(OH)_3(GLU_{-2H})^{2-} + 5H^+$. This value must be considered tentative, until solubility experiments under varying pH_m are conducted to validate the proposed stoichiometry of the complex in terms of (Pu : OH) ratio.

Sorption of Pu(III/IV) on cement hydrates in the presence of formate, citrate and gluconate

Sorption experiments with Pu on C-S-H, AFm and AFt in the absence of organic ligands show a strong retention of plutonium with $\log R_{d,0} = (6.1 \pm 1.2)$ $dm^3 \cdot kg^{-1}$. Although the uptake of Pu has been previously investigated in the literature, this is one of the first experimental evidences available in the literature supporting the strong uptake of plutonium by AFm and AFt phases.

Formate and citrate do not show a significant effect on the retention of plutonium by C-S-H phases with C/S = 0.8 and 1.4. This is in agreement with the solubility experiments, and further supports that formate and citrate cannot compete with hydrolysis nor with Pu sorption on the C-S-H phases in the hyperalkaline conditions investigated in this work. In contrast to formate and citrate, gluconate decreases Pu uptake in C-S-H phases for both low and high C/S ratios. No differences were observed for the two redox buffers used, except at $\log[GLU/M]_{tot} = -1.5$, which may be due to the different redox state of Pu in the presence of Sn(II) and of HQ. No clear differences were observed in those solubility experiments, hinting towards the possible formation of stable surface complexes of the type > Pu(III)-OH-GLU.

Formate has no effect on the uptake of Pu on AFm phases and ettringite, similarly to the observation on C-S-H phases. In contrast, citrate induces a decrease of Pu retention at $\log[CIT] > -2$. Considering the negligible effect of citrate on the Pu solubility, the decrease on Pu retention can be possibly explained by the modification AFm phases and ettringite surfaces by citrate. Gluconate decreases the uptake of Pu for gluconate concentrations higher than 10^{-4} M on AFm phases and ettringite for both redox buffers. These observations reflect the impact of gluconate on the aqueous speciation of Pu as well as on the surface properties of AFm phases and ettringite.

Sorption of Eu(III) on cement hydrates in the presence of formate, citrate and gluconate

Eu(III) sorbs strongly on C-S-H phases in the ligand-free system ($R_{d,0} = 10^{-6.5}$ $dm^3 \cdot kg^{-1}$), consistently with previous studies available in the literature for Ln(III). The presence of formate has a negligible impact on Eu(III) retention on C-S-H phases as only weak Eu(III) complexes with formate form under hyperalkaline conditions. Citrate has also a negligible impact on Eu(III) uptake on C-S-H phases. A

slight decrease of Eu(III) retention was only observed for C-S-H(C/S=1.4)-Eu(III)-CIT systems with $[CIT]_{tot} > 10^{-2}$ M and contact times shorter than 60 days. This probably reflects the initial formation of complexes in the aqueous phase, which is afterwards outcompeted by the incorporation of Eu(III) in the C-S-H structure at longer equilibration times. Gluconate has a negligible effect on Eu(III) retention on C-S-H 0.8 at $[GLU]_{tot} < 10^{-2}$ M, whereas a moderate decrease in the retention is observed for gluconate concentrations $[GLU]_{tot} = 10^{-1.5}$ M and at longer equilibration times. For C-S-H 1.4, a strong decrease of Eu(III) retention was observed already for $[GLU]_{tot} > 10^{-3}$ M. These observations support that stable Eu(III)-GLU complexes are being formed in C-S-H 1.4 systems. Considering the higher Ca concentrations present in solution for C-S-H 1.4-Eu(III)-GLU system, the sorption results hints towards the formation of quaternary aqueous complexes involving Ca ions, i.e. Ca-Eu(III)-(OH)-GLU. This was further studied by TRLFS analyses with Cm(III).

TRLFS study on the uptake of Cm(III) by C-S-H phases in the absence and presence of gluconate

The Cm(III) TRLFS investigations carried out on the aqueous phase of the Cm(III)-GLU-C-S-H (C/S = 0.8) system indicated the formation of at least two aqueous complexes with a peak maxima at ≈ 616 nm and ≈ 610 nm. The second peak at lower wavelength number is visible only at high ligand concentration, i.e. $[GLU]_{tot} = 10^{-1.5}$ M. The characterization of the aqueous phase of the Cm(III)-GLU-C-S-H (C/S = 1.4) system show the same peaks, although the species at ≈ 610 nm forms at lower gluconate concentration, and becomes predominant at gluconate concentration $[GLU]_{tot} = 10^{-3}$ M. Considering that the only parameter changing in both aqueous solutions is the concentration of Ca ($[Ca]_{tot,eq} \approx 10^{-5}$–$10^{-4}$ M (C/S = 0.8) and $[Ca]_{tot,eq} \approx 10^{-3}$–$10^{-2}$ M (C/S = 1.4), these observations are interpreted as the formation of a quaternary complex Ca-Cm(III)-OH-GLU at ≈ 610 nm, which forms at lower gluconate concentrations for C-S-H 1.4 due to the higher Ca content of this system.

The TRLFS spectra of the Cm(III)-GLU-C-S-H (C/S = 0.8) suspension are characterized by one main peak at ≈ 620 nm, both in presence and in absence of gluconate. The analysis of the Cm(III) emission spectra together with the determination of lifetime indicates the formation of two main Cm(III) species incorporated into the structure of the C-S-H phases. This is in line with previous observations available in the literature. In the case of the Cm(III)-C-S-H (C/S = 1.4) suspension system in the absence of gluconate, a similar emission spectra is observed, with a main peak at ≈ 620 nm, indicating the formation of similar Cm(III) species. In agreement with previous studies, the lifetime determination supports the formation of three species, two species incorporated into the C-S-H structure (as for C-S-H 0.8) and a third species possibly sorbed on the C-S-H surface. In the presence of gluconate, the band at ≈ 620 nm strongly reduces in intensity for the Cm(III)-C-S-H (C/S = 1.4) system while a band at ≈ 610 nm appears for $[GLU]_{tot} \geq 10^{-3}$ M. The position at ≈ 610 nm agrees well with the emission spectra collected for the solutions system, indicating the formation of Ca-Cm(III)-OH-GLU aqueous species in the suspension system at high Ca concentrations. These results together with the Eu(III) sorption study indicate that the strong retention decrease observed for the C-S-H 1.4 can be interpreted in terms of Ca-An(III)/Ln(III)-

GLU complex formation. In line with previous solubility studies available in the literature with Nd(III), this work confirms the key role of Ca in the formation of aqueous complexes of Ln(III)/An(III) with gluconate, with the consequent impact on the retention of these radionuclides by cement.

The results obtained within this study provide quantitative insights on sorption phenomena and highlight the possible sorption mechanisms occurring for the Cement-L and Cement-RN-L systems. The present work clearly underlines the strong sorption of α-hydroxycarboxylic acids (e.g. citrate, gluconate) by cement phases and the impact they have on the uptake of tri- and tetravalent actinides as well as of trivalent lanthanides under hyperalkaline and reducing conditions. This study provides also strong evidences on the key role of Ca in the formation of ternary / quaternary complexes with tri- and tetravalent actinides and gluconate, and thus on the retention processes.

The results of the present study provide a sound basis for the quantitative description and the mechanistic understanding of the uptake of An(III)/Ln(III) and An(IV) by cement phases in the presence of key organic ligands expected in repositories for the disposal of L/ILW.

Table of Contents

List of abbreviations

ACW:	Artificial Cement pore Water
AFm (phases):	Alumina-Ferric oxide-mono-phase/substituted ($Al_2O_3 \cdot Fe_2O_3$ – mono)
AFt:	Alumina-Ferric oxide-mono-phase/substituted, $Al_2O_3 \cdot Fe_2O_3$ – tri (in this study it is used to indicate only ettringite, $Ca_6Al_2(SO_4)_3(OH)_{12} \cdot 26H_2O$)
am:	amorphous
An:	Actineds
BET:	Brunauer-Emmett-Teller analysis
C:	cement phase or hydrated cement (e.g. Ms, C-S-H, PC)
C/S:	Calcium to Silicon ratio (Ca/Si)
C-S-H:	Calcium Silicates Hydrates
CIT:	citrate, $(C_6H_5O_7)^{3-}$
CH:	portlindite ($Ca(OH)_2$)
cr:	crystalline
EW:	exempt waste
EXAFS:	Extended X-ray Absorption Fine Structure
FOR:	formate, $(CHO_2)^-$
FT-IR:	Fourier Transform Infrared spectroscopy
GLU:	gluconate, $(C_6H_{11}O_7)^-$
Hc:	hemicarbonate, $Ca_4Al_2(CO_3)_{0.5}(OH)_{13} \cdot 5.5H_2O$
HCP:	Hydrated Cement Paste
HLW:	High Level Waste
HQ:	Hydroqinone
HSAB	hard-and-soft acids-and bases theory
hyd:	hydrated
IAEA	International Atomic Energy Agency
IAP:	Ion activity product
(SF)-ICP-MS:	Sector Field-Inductively Coupled Plasma – Mass Spectrometry
ICP-OES:	Inductively Coupled Plasma – Optical Emission Spectroscopy
ISA:	iso-saccharinic acid
L:	(organic) ligand
L/ILW:	Low/Intermediate-level waste
Ln:	Lantanides
LSC:	Liquid scintillation counting
Mc:	monocarbonate, $Ca_4Al_2(CO_3)(OH)_{12} \cdot 5H_2O$
Ms:	monosulfate, $Ca_4Al_2(SO_4)(OH)_{12} \cdot 8H_2O$

ncr:	nanocrystallyne
NEA-TDB	Nuclear Energy Agency-Thermochemical Database
NPOC:	Non Purgeable Organic Carbon
PC:	(ordinary) Portland Cement
QXRD:	Quantitative X-ray Diffraction
R_d:	Distribution coefficient, $[dm^3/kg]$
RN:	radionuclide
s:	solid
S/L:	solid to liquid ratio $[g/dm^3]$
SRA	shrinkage-reducing admixtures
T:	temperature $[°C]$
TGA:	Thermogravimentic Analysis
TRLFS:	Time Resolved Laser induced Fluorescence Spectroscop
UV-Vis-NIR:	Ultraviolet-Visible Near Infrared spectroscopy
VLLW:	Very low-level waste
VSLW:	Very short-lived waste
XRPD:	X-ray Powder Diffraction
XPS:	X-ray Photoelectron Spectroscopy
XRF:	X-ray Fluorescence Spectroscopy

1.Introduction

1.1.   Motivation of the study

Deep geological repositories are one of the options considered for the disposal of low and intermediate level nuclear waste (L/ILW) [1, 2]. The long-term safety of such facilities relies on a multi-barrier concept for the minimization of the release of the radionuclides into the biosphere. Large amounts of cementitious materials are used in repositories for L/ILW, for both building and waste stabilization purposes. An important role of cement is to stabilize and reduce the mobility of radionuclide with the time. In the context of the performance assessment of deep geologic repositories for L/ILW, it is important to address the uptake of key radionuclides and understand the controlling sorption mechanisms on cement and cementitious materials.

A large inventory of organic materials is also expected in repositories for L/ILW, either in the form of cement additives (*e.g.,* gluconic acid, citric acid) widely used to improve the physicochemical and mechanical properties of cement, or otherwise as part of the waste, e.g. cellulose-based materials, spent ion-exchange resins, decontamination agents (*e.g.,* EDTA, NTA, citrate, etc.), among others. The presence of organics represents a challenge in the context of the performance assessment of this repository system: organic compounds may reduce radionuclide retention onto cement by forming stable and soluble complexes. The formation of such complexes may enhance radionuclide mobility and therefore have an impact on the long-term performance of a deep geological repository.

Actinides are one of the main radionuclides present in nuclear waste, primarily in high-level waste (HLW) but also in L/ILW. In the reducing conditions expected after repository closure due to the anoxic corrosion of iron, actinides will be predominantly found in the +III and +IV oxidation state. The uptake of tri- and tetravalent actinides on heterogeneous mineral system, as cement, depends (besides other factors) on the chemical composition and thermodynamic stability of cement phases (*e.g.,* due the presence of organic ligands) at the relevant pH and redox conditions of the repository system. Carboxylic acids are considered strong complexing agents compared to the other organic compounds (*e.g.,* alkanes, alkenes, alcohols). Recent sorption studies [3] with selected organic ligands and cement phases (C-S-H phases, AFm phases and ettringite) found out that the sorption of organic ligands increases with the increase of the acidity (pKa) of the organic compounds.

In general, for ordinary Portland cement (PC), C-S-H phases are considered the main sink for the sorption of actinides and therefore representative for the total uptake on hydrated cement. Several studies have previously assessed the impact of gluconate and α-ISA (as main degradation product of cellulose in alkaline conditions) on the uptake of lanthanides and actinides by cement and C-S-H in alkaline and reducing condition [1, 4-6]. However, limited information is available concerning the effect of other low molecular weight organics (*e.g.,* formate and citrate) on radionuclide uptake by cement. Likewise scarce

studies were carried out to quantify the uptake of An(III/IV) and Ln(III) by secondary cement phases (*e.g.*, AFt and AFm phases) that are expected to persist until the stage III of the cement degradation process [7].

The present study aims at a quantitative and mechanistic description of the binary and ternary systems cement phases / organics, cement phases / radionuclides and cement phases / radionuclides / organics in hyperalkaline conditions (pH = 13.3) representative of the degradation stage I of cement. The cement phases considered in this work are C-S-H, AFm phases, and sulfate-AFt. Formate, citrate and gluconate are investigated as low molecular weight organic ligands expected in the repository as cement additives and / or waste components. Plutonium has been chosen as a very relevant actinide in the context of nuclear waste disposal, although with a relatively small inventory in L/ILW. Eu(III) is often considered as a redox-stable analogue of trivalent actinides like Am(III) or Pu(III), based on the similar ionic radii (*i.e.*, $r_{Eu^{3+}}$ = 1.07 Å, $r_{Pu^{3+}}$ = 1.10 Å, $r_{Am^{3+}}$ = 1.12 Å, all for coordination numbers CN = 8) and same charge. Wet-chemistry sorption studies conducted with ^{242}Pu(III/IV) and ^{152}Eu(III) are complemented with TRLFS studies taking advantage of the very favorable spectroscopic properties of Cm(III), which provides speciation information both in the aqueous and in the solid phases at trace metal concentrations.

1.2. Repository systems for low and intermediate level radioactive waste (L/ILW)

Radioactive waste is generated by different kinds of activities (medicine, research, industry, military applications, etc.) and with wide variety of physical and chemical forms and concentrations.

The International Atomic Energy Agency defined the radioactive waste as ''*Any material that contains or is contaminated by radionuclides at concentrations or radioactivity levels greater than the exempted quantities established by the competent authorities, and for which no use is foreseen*'' [8]. The following classification is defined by IAEA, providing general boundaries between the waste classes [9]:

1. Exempt waste (EW): waste with low activity level or below clearance levels. After subsequent regulatory control, it is not considered radioactive waste.

2. Very short-lived waste (VSLW): waste that can be stored for limited period of time. After subsequent regulatory control step, it will be assessed for further use or discharge. This waste class includes often very short-lived radionuclides used for research and medical purposes.

3. Very low-level waste (VLLW): this class of waste includes soil and debris with low levels of activity (for β- and γ-emitting radionuclides in 0.1 m^3 < 400 kBq or ~ 4 Bq/g and < 40 kBq per item). The waste is disposed in near surface type facilities with limited regulatory control.

4. Low-level waste (LLW): waste with limited amounts of long-lived radionuclides. This class covers a broad range of wastes (short-lived radionuclides with higher activity and long-lived radionuclides with low levels of activity), which require a robust isolation and containment for a period up to a few hundreds of years (*e.g.*, deep geological repository).

5. Intermediate-level waste (ILW): waste containing mainly long-lived radionuclides, which requires higher degree of isolation and containment. Given that the long-lived radionuclides

present in the ILW are alpha emitting radionuclides that will decay to a level of activity not acceptable for the near surface disposal, this waste class has to be disposed at greater depth (from the order of tens of meters to a few hundred meters).

6. High-level waste (HLW): waste with levels of activity high enough to generate heat by radioactive decay processes, and waste with large amounts of long-lived radionuclides. The disposal in deep (several hundred meters) and stable geological site is a suitable option for the HLW.

Among the possible alternatives, the "geological disposal" remains the most favored option for waste disposal in terms of safety, handling and cost-effectiveness. In particular, the deep geological repository is generally preferred for the disposal of HLW and in some countries such as Germany or Switzerland also for L/ILW. The safety concept of deep geological repositories relies in the multi-barrier system, where the host rock is chosen according to specific physical and chemical requirements capable to ensure a stability and performance for a long period of time. In the framework of the Swiss disposal concept for L/ILW [2], cement is used for the stabilization of the waste and the construction of engineering barriers (backfill, containers) in order to reduce the radionuclide release from the cementitious near field into the host rock. The waste is first solidified into the cement matrix in steel drums, which are placed in large concrete containers (Figure 1). The large containers are then stacked into disposal caverns, where a special mortar is used as backfill. The overlying host rock (argillaceous rocks in the Swiss concept, *e.g.*, Opalinus clay) provides the last geological barrier. Material inventories of L/ILW and ILW estimates that cement (hardened cement paste, HCP) accounts for 20 wt.% in the near cementitious field [1]. In this context, radionuclide mobility is strongly dependent on the uptake by cement and radionuclide solubility behavior in the hyperalkaline conditions defined by cementitious systems.
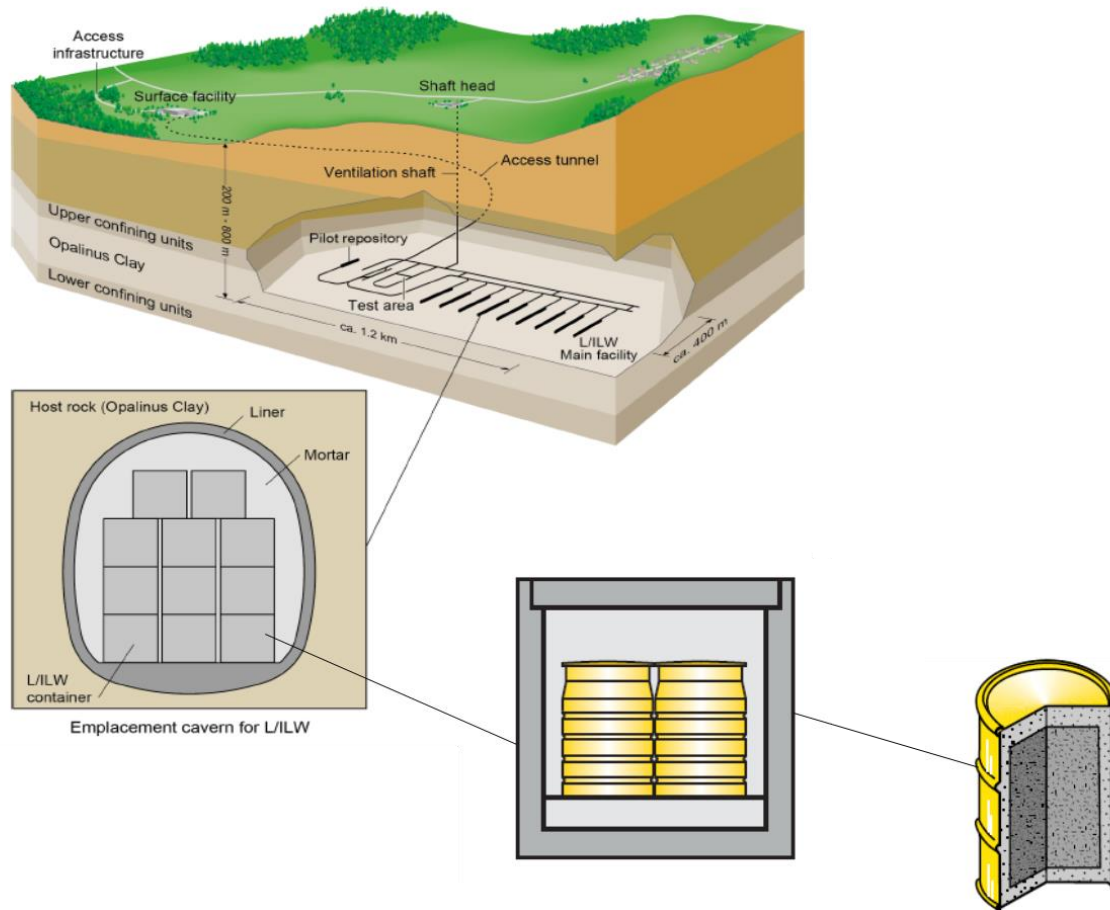
Figure 1. General set-up foreseen for the L/ILW geological repository according to the Swiss concept. Picture taken from [2].

1.3. Hydrated cement composition

Cement is a mixture of several anhydrous minerals, which form by heating limestone and clay to about 1450 ºC in a rotary kiln. The resulting material (i.e. clinker) is then ground with gypsum (to slow down the setting time) in order to make ordinary Portland cement (PC). Portland cement is generally defined by the amount of four main components, which are: tricalcium silicate, C_3S (or Ca_3SiO_5, alite), dicalcium silicate C_2S (or Ca_2SiO_4, belite), aluminate ($C_3A = Ca_3Al_2O_6$) and ferrite ($C_4(A,F) = Ca_4(Al_xFe_{1-x})_4O_{10}$). Several additional phases such as calcium sulphate, calcium carbonate, calcium and magnesium oxides, sodium and potassium sulphates can be present in minor quantities. After the hydration of PC, the main cement phases are: portlandite ($CH = Ca(OH)_2$), calcium silicate hydrates (C-S-H) phases, calcium aluminate phases (AFt and AFm phases), hydrotalcite ($[Mg_6Al_2(OH)_{16}] \cdot CO_3 \cdot 4H_2O$) and siliceous hydrogarnet ($Ca_3(Al,Fe)_2(SiO_4)_y(OH)_{12-4y}$). Thermodynamic modelling [10] allows to estimate the composition of hydrated Portland cement as function of time. For example, for PC (CEM I 42.5 N, w/c = 0.4) after 28 days of hydration time the phase assemblage after hydration process is made of: ~ 40 wt.% C-S-H, ~ 18 wt.% CH, ~ 14 wt.% AFt, ~ 13 wt.% AFm phases, ~ 3 wt.% hydrotalcite and ~ 11 wt.% of unhydrated clinker. Differences in the mineral composition may arise from the chemical composition of the clinker and the amount of water (expressed through the water to cement ratio, w/c) used for the hydration process. Radionuclide uptake by cement is a process strongly dependent on the

mineral phases present, and thus an appropriate knowledge of the chemical composition of hydrated cement is also very relevant in the context of nuclear waste disposal. Radionuclide uptake may also depend on the crystallinity and morphology of the solid: for example a high sorption for both anions and (mostly) cations is expected from low crystallinity phases as for C-S-H than for crystalline C-S-H phases [11]. The uptake is also influenced by the size, atom radii and valence of the sorbent species. In addition to sorption, the uptake on cement phases may occur also through solid solution formation as found for Eu(III) on calcite [12] or for iodide on Ms or Hc phases [13].

1.3.1.   C-S-H phases

The hydration of both C_3S and C_2S in PC (CEM I 42.5 N), leads to the formation of ~ 40 wt. % C-S-H phases [10]. The chemical composition of the C-S-H phases is usually described in terms of calcium to silica ratio (C/S), which range between ~ 0.7 and ~ 1.5 [14]. In hydrated cements, C-S-H with C/S of 1.7 is often observed [15]. C-S-H composition varies also with the cement degradation stage (see section 1.5), and in the context of waste disposal it may be also affected by the interaction with some of the waste materials (e.g. decomposition of organic material in alkaline conditions, metal corrosion, etc.). Despite their low crystallinity, the structure of C-S-H phases is often described as a defect tobermorite, a naturally occurring mineral. The structure of tobermorite consists of Ca-O sheets connected to the silica tetrahedra (≡Si(OH)$_2$ silanediol group) atoms in the *dreierketten* conformation [14-16]. This conformation consists of repetitive ternary unit of bridging and non-bridging silica tetrahedra. The non-bridging silica tetrahedra are connected on both sides of Ca-O sheets. The bridging silica tetrahedra has two unshared oxygen atoms neutralized by H^+ thus forming the silanediol group. The silicate end-group (silanol group) connected to another silicate group carries only one unshared oxygen. The length of the silica chain depends on the C/S: with the increase of C/S (which correspond to an increase of the pH pore solution), Ca^{2+} ions progressively substitute the interlayer protons that neutralize the negative charge of bringing silica, while the bridging tetrahedra from the silica chains. The substituting role of Ca^{2+} ions indicate the potential sorption of other cations, for example of actinides and lanthanides [17]. The C-S-H surface charge, often investigated via zeta potential measurements, is controlled by Ca^{2+} content [18] and the pH [19] in the cement pore water. In general, the zeta potential is dependent on the composition of C-S-H phases: for high C/S, the uptake of anionic species is favorable [20], while for low C/S the C-S-H surface exhibits a net negative surface charge and cationic species tend to sorb strongly on C-S-H phases [19]. Due to the high surface area ($\approx$ 150 m^2/g, determined by BET) [21], the uptake of metal species is found to be high [22, 23]. Adsorption can be considered as the first uptake mechanism on C-S-H phases as suggested by several modern experimental studies, carried out with synchrotron-based spectroscopic techniques (e.g., XAFS) and advanced laser-based methods (e.g., TRLFS. The studies of Tits et al., Stumpf et al., Mandaliev et al., Gaona et al. [24-29] suggested that the surface sorption is the first uptake step, followed by the incorporation of the metal cation in the solid

phase structure. The latest step is responsible for the long-term incorporation of radionuclides in C-S-H and therefore in hydrated cement.

1.3.2. AFm phases

AFm phases (or aluminoferrite-monophase) belong to a subgroup of the layered double hydroxide family [30-32]. The general formula can be expressed as $[Ca_4(Al,Fe)_2(OH)_{12}] \cdot X \cdot nH_2O$, where X refers to two single charged anions or one double charged anion. The main layer (see Figure 2.), structurally similar to brucite or portlandite, consists of a sheet of $M(OH)_6$ octahedral anions, where one third of the divalent cations, M^{2+} (i.e. Ca^{2+}) is replaced by a trivalent cation, M^{3+} (i.e. Al^{3+} and/or Fe^{3+}) at a stoichiometric ratio for $M^{2+}:M^{3+}$ of 2:1. The substitution of Ca^{2+} results in a permanent positive net charge of the main layers with chemical formula of $[Ca_4(Al,Fe)_2(OH)_{12}]^{2+}$, which is compensated by the interlayer anions. In the interlayer space, additional water molecules are also present. The layer thickness (distance between two main layers) depends on the type of anion, X, and the number of water molecules, n, accommodated in this region. In Portland cement, the most common interlayer anions are OH^-, CO_3^{2-}, SO_4^{2-}, which result in hemi- ($OH^- + \frac{1}{2} CO_3^{2-}$) (Hc), monocarbonate (Mc) (CO_3^{2-}) and monosulfate (Ms) (SO_4^{2-}) AFm phases, respectively. The anion content depends on the cement composition and the environment. For instance, the use of cement in marine applications can increase the substitution of the pre-existing anion with chloride Cl^-, thus leading to the formation of other phases such as Friedel's salts ($[Ca_4Al_2(OH)_{12}][2Cl \cdot 4H_2O]$) and Kuzel's salt ($[Ca_4Al_2(OH)_{12}][Cl(SO_4)_{0.5} \cdot 5H_2O]$) [33, 34]. The partial interlayer substitution may result in the presence of two or more interlayer anions (e.g. Hc with OH^- and CO_3^{2-}) and in the formation of solid solutions. The interlayer anions (e.g. OH^-) can be also replaced by organic ions, alcohols, carboxylic acid anions and sulfonates [35]. The interlayer water content may also vary as a function of temperature and relative humidity [36, 37]. A clear example is the case of monosulfate, which exists (and co-exists in specific cases) in different hydration states (Ms9, Ms10.5, Ms12, Ms14, Ms16). Given their structure, AFm phases show a strong uptake towards anions, in particular for oxyanions such as selenite, chromate, molybdate and borate [38]. In the case of the sorption of SeO_3^{2-} and MoO_4^- on AFm phases (Ms and AFm-Cl_2), a three-step sorption mechanism was proposed by [39, 40] involving surface adsorption, formation of new AFm-phases and formation of Ca-precipitates. Similar sorption mechanism (i.e, solid solution formation, anion exchange reaction) was also formulated for the iodide uptake on AFm phases [41] or as surface adsorption, solid solution formation, and formation of new AFm-phases [13].
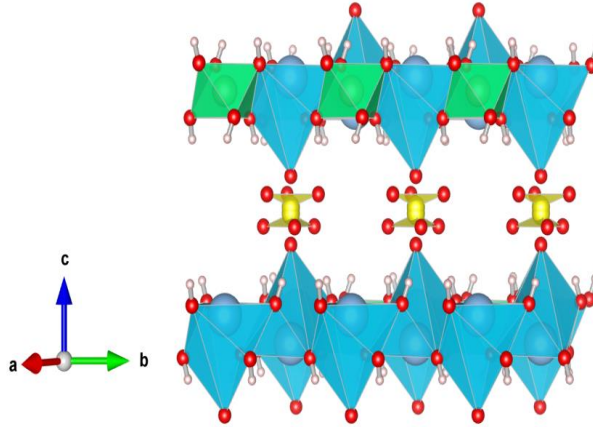
Figure 2. Monosulfate structure as an example of AFm phases structure [30]: the interlayer anion X position is occupied by SO_4^{2-}. Ca-octahedra are represented in light blue, Al-octahedra in green, the sulfate anion in yellow, oxygen in red, hydroxyl groups in pink. Interlayer water molecules are omitted for clarity. The outer surfaces and the interlayer region of an AFm phase provide possible sorption sites for radionuclides. The structure is visualized with VESTA [42].

1.3.3. Ettringite (AFt)

AFt (or aluminoferite-triphases) general chemical formula is $[Ca_6(Al,Fe)_2(OH)_{12}] \cdot X_3 \cdot nH_2O$, where X denotes a doubly charged anion. In the case of ettringite, X corresponds to SO_4^{2-}. Ettringite forms hexagonal prismatic crystals: columns of $Al(OH)_3$ octahedra alternating with edge sharing CaO_8 polyhedral. The positively charged columns are balanced by X anions (or sulfate ions in the case of ettringite) located in the resulting interchannels together with several water molecules. Ettringite, due to its structure, is known for the potential incorporation of oxyanions such as AsO_4^{3-}, CrO_4^-, SeO_4^{2-} or SeO_3^{2-}, which are of particular interest in the context of waste management (not necessarily linked to the nuclear applications). The retention of these anions can be described in terms of solid solution formation [43-45], involving the substitution of the pre-existent anion (e.g. SO_4^{2-}). Since ettringite exhibits a net negative surface charge [23], the anion adsorption has less relevance compared to the bulk incorporation and substitution of the pre-existent anionic species. No evidences were found for a strong uptake of monovalent anions on AFt. The uptake of mono-charged anion is generally negligible, probably because of the narrow interchannels, which prevent the replacement of one bivalent anion by two monovalent anions due to space restrictions in the columnar structure. The cation substitution of Al^{3+} by Fe^{3+} in the ettringite structure has been observed by Möschner et al. [46].

1.4. Cement degradation by groundwater ingress

The composition of hydrated cement plays also a relevant role in the long-term performance of underground repositories for L/ILW. In the absence of any degradation process induced by the interaction with waste components, cement may be subject to chemical degradation caused by ground

water infiltration. Cement degradation is caused by the disequilibrium between the host rock groundwater and hydrated cement, and it is mainly characterized by three stages with a progressive decrease of pH in the cement pore water. In the first stage, the cement pore water is dominated by the dissolution of Na and K oxides / hydroxides, resulting in a high pH of about 13.2. The second stage is controlled by the portlandite solubility, which buffers the pore water composition at pH ~ 12.5 and [Ca] ~ 20 mM. The third degradation stage is dominated by the incongruent dissolution of C-S-H phases and other phases, while pH decreases to lower values (~ 10). The pH decreasing rate and the time scale of the different stages may depend on many factors such as the exchange rate of pore water in the near field and the environment physical conditions (e.g. temperature). During the geochemical evolution of the cementitious near-field, AFm phases and portlandite are expected to be present up to the second stage and C-S-H phases, ettringite, calcite and OH-hydrotalcite are expected until the degradation stage III [7]. In addition, zeolitic phases might form [47].

1.5. Organic ligands expected in the waste and their interaction with cement

The presence of organic compounds represents a high concern for the safety case of cement-based repository. The main concern depends on their chemical stability under hyperalkaline and reducing condition, complexing behavior with radionuclides in the cement matrix that may enhance their mobility in the host rock and the consequently in the geosphere. The speciation of organic substances depends amongst others on pH and redox conditions, as well as the presence of major elements like Ca, Mg or Fe and microbial activities at the site of interest.

The presence of organic compounds in the repository system may arise from several possible sources. The massive use of cement in repositories for L/ILW represents a very important source of organics as organic additives such as plasticizers are used to control the cement setting time and its workability. Organic compounds may also be present in the disposed waste generated by nuclear power plants, medicine and research facilities. Spent filters, ion exchange resins and decontamination agents contribute to the organic fraction expected in the deep geological repository for L-ILW. The decomposition of high molecular weight organics may take place by biotic and abiotic processes, including also radiolytic processes [48]. As one of the main components of the organic material fraction in the L/ILW repositories, cellulose degradation under the hyperalkaline conditions defined by cementitious systems results in the formation of two main degradation products: (1-3), 3-deoxy-2-C-hydroximethyl-D-erythro-pentonic acid (often labelled as α-isoccharinic acid, α-ISA) and 3-deoxy-2-C-hydroximethyl-D-threo-pentonic acid (referred as β-ISA). Short chain aliphatic acids (e.g. formic acid, acetic acid, lactic acid) appear as minor products [49]. The extent of cellulose degradation depends on two main reactions (peeling-off and alkaline hydrolysis) and according to [50] the complete cellulose degradation occurs within 1000-10'000 years. By comparing the complexing role of the two ISA

diastereomers, the long term performance of geological repository depend mainly on the complexing behavior of α-ISA, since it has shown a stronger affinity for heavy metals and radionuclides compared to β-ISA [51].

In the context of construction and cement-based materials, chemical admixtures are used as an integral part of everyday concrete production. It is possible to identify the following class of additives: water-reducing and set-retarding admixtures, high-range water-reducing admixtures, mid-range water-reducing admixtures, admixtures for suppressing alkali-silica reactions, viscosity-modifying and anti-washout admixtures, shrinkage-reducing admixtures (SRA), and cold weather accelerators [52]. Taking into account chemical and environmental safety, compounds based on low molecular weight, low basicity carboxylic acids have become very popular [53, 54]. Popovics [55] observed that water soluble organic materials belonging to the carboxylic acid group are some of the most effective chloride-free accelerators for cement hydration. The short chain structure is a key factor for the rapid dissolution of calcium ions from the cement clinkers. Indeed, accelerating properties have been reported for short-chained monocarboxylic acids (C1 to C4) and their salts (formic, acetic, propionic and butyric), while longer-chained carboxylic acid homologues (> C4) act as retarders (e.g., sucrose, glucose, α-hydroxycarboxylic acids [56-59].

The corrosion of activated/non-activated steel, may also contribute to the formation of ^{14}C-organic compounds [60]. The main source of ^{14}C in low- and intermediate-level radioactive waste in Switzerland are activated metallic nuclear fuel components and reactor core components (~ 85%) as well as spent filters and ion exchange resins used for the removal of radioactive contaminants in a number of liquid processes and waste streams. Carbon-14 can be released in a variety of organic compounds depending on the nature of the waste material and on the chemical conditions of the near field. Detailed speciation studies on the chemical form of carbon released during the corrosion of irradiated metals [61-65] reported the formation of (HCOOH) and acetic acids (CH_3COOH), formaldehyde (HCHO), methanol (CH_3OH) and ethanol (C_2H_5OH). Instead, Hardy & Gillham, Campbell et al., Deng et al, Burris et al., Agrawal et al. [66-69] reported the formation of volatile and reduced hydrocarbons, in particular alkanes and alkenes (e.g. methane, ethane, ethene, propane, propene and butane). Thermodynamic modelling conducted by Wieland & Hummel [60] in hyperalkaline and anoxic conditions, reported that the formation of organic compounds seem to be limited in conditions relevant for the deep geological repository. The most stable carbon species were methane and carbonate-based species and small organic molecules, with up to 5 carbon atoms (C5). The authors [60] underlined that possibly different scenario might be obtained assuming, for instance, a kinetic hindrance of alkene formation.

1.5.1. Low molecular weight organics (LMW)

The notation of low molecular weight organics refers to the class of organic compounds with short carbon chain, which can include several organic molecules classes, such as alcohols, alkane, alkene,

aldehyde and carboxylic acids, among others. In the following sections, the main chemical properties of the Na salts of formic, citric and gluconic acids are described. Based on the type of application of modern concrete and cement-based material, Na-formate, Na-citrate and Na-gluconate are added in determined concentration interval expressed in terms of weight fraction per dry weight of cement mixture. The concentration used are 2-4 wt. % for formate [54, 70-73], 0.03-8 wt.% for citrate [74] and 0.03-2 wt.% for gluconate [75-77]. It has been demonstrated that most of citrate and gluconate is sorbed on the initially formed cement hydrates [77, 78], while the sorption of formate is much weaker [79]. If the retarder is applied with some delay, the sorption of 0.05 wt.% Na-gluconate is reduced from 80% to 40% [77]. In the nuclear field, citrate is often used as decontaminating agent, and thus it is also found in specific waste streams in nuclear waste, mostly in L/ILW.

The main risk of organics in a deep geological repository arises from the complexing power of LMW organics with radionuclides: the formation of soluble and stable RN-L complexes may enhance the release of radionuclide into the geosphere. In this study, the impact of Na-formate, Na-citrate and Na-gluconate on selected radionuclides onto cement hydrates at redox and hyperalkaline conditions relevant for the deep geological system, is investigated. In order to better asses the role on radionuclides retention reduction by cement and the sorption mechanism, this study has been divided in two main parts: the first part focuses on the binary system L-cement interactions, the second part of this study focuses on the uptake behavior of radionuclides in presence and in absence of the above-mentioned organic ligands (ternary systems).

1.5.1.1.   Na-Formate (FOR)

Sodium formate, HCOONa (HCOO$^-$ in the anionic form, see Figure 3) is the sodium salt of formic acid. Based on the theory of hard-and-soft acids-and bases (HSAB) [80] [81] formate belongs to the class of hard bases. The negatively charged carboxylate group represents a strong binding site (Coulomb interactions) which can especially complex smaller divalent cations such as Mg^{2+}, Ca^{2+}, Zn^{2+} and Cd^{2+}(group IIA and IIB) [80]. In general, as hard acid, formate is less selective in the binding with cations with similar size. Divalent cations preferentially bridge both anionic oxygen atoms in the formate plane [82]. In the acidic form, the conformation *trans* (the relative position of the hydrogens C-H and O-H, are in opposite sides of the C-O plane) is favored over the conformation *cis* (the two hydrogens face each other) [83].
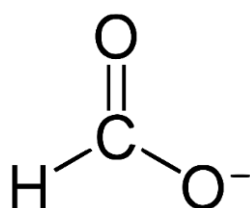

Figure 3. Chemical structure of formate.

In the admixture industry, formate is a known cement accelerator and is also used as antifreezing additive for concretes [72, 84]. The effect of $Ca(HCOO)_2$ depends on the cement composition. Gebler [70] observed that the compressive strength at one day of hydration in concretes containing calcium formate is higher at a C_3A/SO_3 ratio > 4. Hewlett [85] compared the calcium salts of chloride, nitrite and formate, and related their accelerating efficiencies to the mobility of the anions within the silicate particles. Therefore, the anion size is the major factor. Due to its large ion size (0.45 nm) $Ca(HCOO)_2$ is less suitable than anions with smaller size: 0.34 nm for nitrite and 0.27 nm for chloride [85]. Heikal [86] claimed that the accelerating effect of $Ca(HCOO)_2$ on calcium silicate hydrate formation is mainly attributed to the fact that the diffusion rate of $HCOO^-$ ions is much higher than for the Ca^{2+} ions, and that the $HCOO^-$ ions can penetrate into the hydrated layers covering C_3S and β-C_2S grains. As a consequence, the precipitation of $Ca(OH)_2$ is accelerated as well as the decomposition of calcium silicates [86]. The biggest problem in using $Ca(HCOO)_2$ as an accelerating admixture for concrete is its low solubility in water (approx. 16g/100g H_2O at room temperature). Therefore, appropriate calcium formate solutions are not commercially available, so that it must be added to concrete or cement mixture in solid form, which can create dispensing problems. Sodium formate (NaHCOO), which has also accelerating properties [70], is approximately 3 times more soluble in water. The potential problem in the use of sodium formate is that significant amounts of alkali are added to the mixture, which can increase the risk for deleterious alkali silica reaction [87].

1.5.1.2.   Na₃-Citrate (CIT)

Trisodium citrate dihydrate, $Na_3C_6H_5O_7 \cdot 2H_2O$, is one of the sodium salts of anhydrous citric acid (2-hydroxypropane-1,2,3-tricarboxylic acid). The structure of citrate (Figure 4) is characterized by three carboxylic groups, located at both ends and in the middle position (C3) of the main chain, and one hydroxyl group. All functional groups are potential coordination sites and can contribute to the chelate formation with metal ions (M^{x+}). Above pH 7, all carboxylic groups are deprotonated, while the hydroxyl group is a very weak acid and deprotonates at pH > 12 [88]. This pK_a can be however, significantly decreased, when a metal ion is complexed. In the presence of metal ions, citrate forms easily chelating complexes, which may be limited by steric constraints. Experimental observations with citrate complexes [89-91] evidenced a correlation between the charge density and size of the metal ion: only two carboxylates group and the hydroxyl group can complex the same metal ion. Potentiometric and solubility studies do not provide unequivocal results about the origin of the protons released in the complexation reaction. Hence, equilibrium reactions representing the formation of the complexes M(OH)(CIT) and M(CIT$_{-H}$) (with CIT$_{-H}$ representing a citrate ligand with a deprotonated alcohol group) involve the same number of protons, and thus cannot be differentiated by the methods mentioned above. Spectroscopic methods provide important information about the structure and conformation of metal ion-citrate complexes. An interesting example is the Al^{3+}-citrate (1:2) complex investigated by Matzapetakis et al [91] at pH ~ 8, where each citrate molecule is coordinated to the Al^{3+} ion through the

central hydroxyl group and two carboxylate groups located in the equatorial plane and in the axial position (terminal carboxylate). Similar tridentate coordination was reported for the nickel-citrate complex, $[Ni(CIT)(H_2O)_2]_2^{2-}$ investigated by Baker et al. [90] and also for the structure of hexahydrate, tetrahydrate and anhydrous calcium citrate reported by Kaduk [92].

The solubility of citrate-metal ion solids is usually pH dependent: in the alkaline region, the formation of metal-hydroxo-citrate complexes and the possible precipitation of hydroxides, oxides and hydroxocitrates must be considered. For acidic pH values, the protonation of citrate increases the solubility of metal ion-citrate salts. In the review on thermodynamic data of organic ligands published in the 9th volume of thermodynamic database of the Nuclear Energy Agency (NEA-TDB), Hummel and co-workers [88] critically selected thermodynamic data on the citrate system with metal ions of relevance in the context of nuclear waste disposal. Hummel and co-authors reported that the solubility of citrate and metal ions belonging to the group IA (e.g. Na^+ and K^+) is very high. For M^{2+} metals, the solubility of M^{2+}-citrate depends on the nature of metal cation and on the pH value. The solubility of these complex follows the trend Mg > Ca > Cd > Zn [93]. At pH ≈ 4.2 the solubility of Mg-citrate (for $[Mg]_{tot} = 0.12$ M) is 0.04 M, while the solubility of Ca-citrate, Zn-citrate at the same pH are 0.005 M and 0.0006 M, respectively [94-96]. In the context of cement-based repositories, the interaction of citrate with Ca plays an important role in the aqueous chemistry of this ligand. The high calcium concentration typical for hydrated cementitious systems may impose a solubility limit on the citrate concentration. In the example of the calculated solubility $Ca_3(CIT)_2 \cdot 4H_2O$ in $CaCl_2$ solution shown by Hummel et al. [88], two main effects can be differentiated if the Ca concentration in solution increases: i) higher Ca concentration decreases the citrate concentration in equilibrium with $Ca_3(CIT)_2 \cdot 4H_2O$ (i.e. common-ion effect); ii) due to side reactions related to the protonation of CIT^{3-} and formation of $HCIT^{2-}$, H_2CIT^- and $H_3CIT_{(aq)}$ and Ca-citrate aqueous complexes (i.e. $Ca(HCIT)_{(aq)}$ and $Ca(H_2CIT)^+$), pH values decrease resulting in increasing solubility.
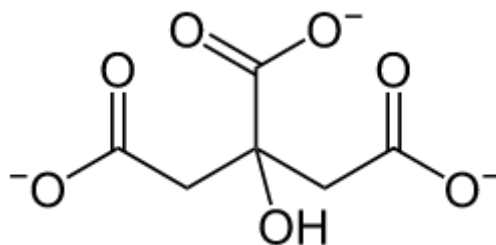
Figure 4. Chemical structure of citrate.

Sodium citrate is one of the most widely used additives and complexing agents in different industries. The addition of sodium citrate influences the hydration of cement-based materials. Citrate may accelerate the hydration of C_3A and C_4AF [97]. On the other hand, the citric acid is an excellent retarder

in ettringite-based binder as reported by Burris and Kurtis [98]. Rottstegge et al. [99] reported that the presence of sodium citrate (0.4 wt.%) retard the hydration of alite and prevent the precipitation of hydration products and dissolution of clinker. Therefore, depending on the dosage of sodium citrate, it is possible to obtain different results [74]. Singh et al. [100] confirmed that 0.1 wt% citric acid has accelerating effect on the hydration of PC, while for concentration > 0.1 wt.%, a retarding effect was observed. A decrease of the zeta potential in the presence of citrate clearly indicates the adsorption of citrate ions on the cement grains surface at the Stern layer [100]. Furthermore, sodium citrate and citric acid may have a different effect on the strength of cementitious materials [101-103]. Still under discussion is the nature of the interaction between citrate, cement grains and cement phases. As a hydroxycarboxylate, citrate forms complexes with Ca^{2+} ions leading to the formation of carboxylate complexes [104, 105]. The adsorption of citrate on the surface of cement particles was considered also the origin of retardation for the hydration of Portland cement [78]. Citrate sorbs on the surface of cement particles due to the electrostatic interaction between particle surface and carboxyl groups of sodium citrate/ citrate acid.

1.5.1.3.   Na-Gluconate (GLU)

Gluconate (GLU) is another example of a low molecular weight organic ligand expected in the hyperalkaline conditions defined by cement systems. As for citrate, sodium gluconate is used in the cement production as a cement-dispersing and retarding agent [33, 100, 106, 107]. The use of sodium gluconate as an additive enhances the dispersion of cement particle, reducing the amount of water, which in turn results in an increase of the strength and durability of the final hydrated material. The conjugated acid form of gluconate, D-gluconic acid, is a polyhydroxy carboxylic acid. In acidic solutions, gluconic acid is in equilibrium with the δ-GLU lactone and the γ-GLU lactone of the acid as shown in the Figure 5.
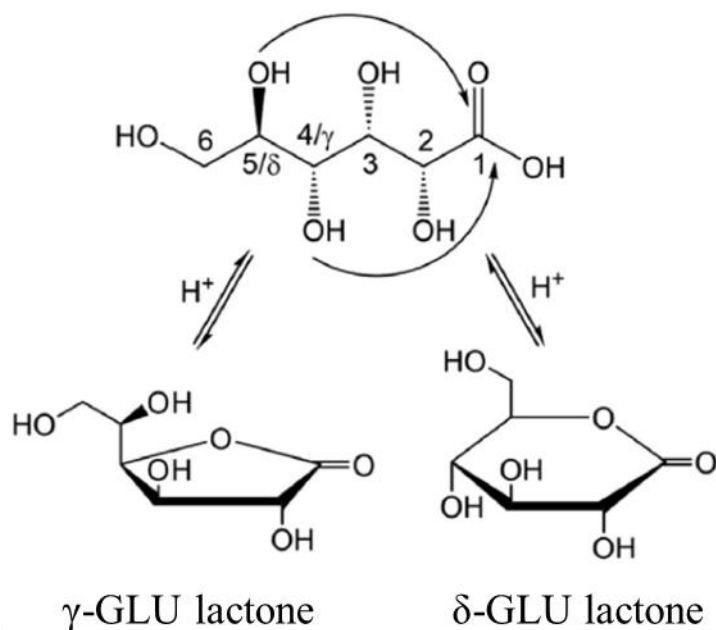
Figure 5. Chemical structure of D-gluconic acid and schematic representation of the nucleophilic attack of –OH group and the formation of γ- and δ-GLU lactones [108].

In the acidic form (at pH < 3), gluconic acid is a mild complexing ligand, while the anionic form $(HOCH_2(CHOH)_4COO^-)$ exhibits strong complexing capacities. The high complex stability is related to the presence of the alcohol group in alpha position (next to the carboxylic group) that may participate in the formation of chelates with 5-member rings [109-121]. Since gluconate shares many of chemical properties of α-ISA, it is possible to compare it with the extensive series of thermodynamic data selected for the complexation of α-ISA with alkali and alkaline metals and with radionuclides relevant for the nuclear waste disposal reported in the NEA-TDB project [88].

For pH range 2 < pH < 10 the complexing behavior of gluconate with alkaline earth metals is weak and COO^- is the only functional group involved in the formation of mononuclear complexes [119]. For acidic pH, both lactonization and protonation-deprotonation reaction take place. In general, the protonation reaction is much faster than the lactonization process, and it is characterized by a protonation constant equal to ≈ 3.8 (I = 0) [122]. The lactonization process leads to the formation of two cyclic structures (depending if the nucleophilic attach to the carbon atom C1 occurs from the alcoholic group linked to the carbon atom in position C4 or C5): the first case yields to 5-membered lactone (D-glucono-γ-lactone) and in the second case to the 6-memebered lactone (D-glucono-δ-lactone) (Figure 5). The recent work of Kutus et al. [123] reported that the lactonization constant of gluconic acid for the formation of γ-lactone and δ-lactone differ of ca. 0.2 log_{10} units (I = 0.8 M). Reversely, the L-gluconate shows a lower thermodynamic stability in the 6-memebered ring arrangement.

At pH > 12, bi- and trinuclear Ca^{2+}-complexes with gluconate and with equivalent sugar carboxylate ligands (e.g. heptagluconate, D-gulonate, D-isosaccharinate) [124, 125] have been described. Polynuclear complexes have much higher stability in alkaline pH and are predominantly present as

$Ca_2(GluH_{-4})_2^{2-}$ (or $Ca_2(GluH_{-3})_2^0$ and $Ca_3(GluH_{-4})_2^0$, where the term $GluH_{-x}$ corresponds to a gluconate ion in which x-alcohol groups are deprotonated. The higher thermodynamic stability depends also on the binding sites of OH^- groups: previous studies [125, 126] suggest that the deprotonation of C2-OH promotes the polynuclear complex formation. In general, for many complexes, COO^- and C2-OH participate as the main binding sites in the formation of aqueous complexes with divalent cations like Co^{2+}, Ni^{2+}, Cu^{2+}, Zn^{2+} [115, 127, 128]. The C3-OH group was identified as complexing group for gluconate solids compounds, such as $CaGlu_2(s)$ and complexes with Eu^{3+} and Nd^{3+} [129-131].

1.5.2.   Interaction of formate, citrate and gluconate with cement

As discussed in Section 1.5, organic compounds are expected in the radioactive waste disposal. Although several studies indicate that some organics may exhibit very strong complexing behavior in the relevant conditions of disposal system (alkaline pH and redox conditions), a more limited information is available for the uptake of LMW organics by cementitious materials and cement phases. An accurate knowledge of this interaction is particularly important (i) to quantify the concentration of free-ligand remaining in solution after sorption on cement hydrates, and (ii) to understand the alterations of the surface properties of cement, and the corresponding implications for the uptake of radionuclides.

Only a few studies have previously investigated the uptake of formate by HCP [3, 61]. Wieland et al. [3] investigated the sorption of several C-14 labelled small molecules organics (i.e. formic acid, acetic acid, acetaldehyde, formaldehyde, ethanol, methanol) on HCP (S/L = 333 g·dm^{-3}) and AFm phases, such as Ms (S/L ≈ 100 g·dm^{-3}), Hc, Mc (S/L ≈ 106 g·dm^{-3}) and ettringite (S/L ≈ 20 g·dm^{-3}). The authors observed that the strength of the uptake for the investigated organics followed the sequence alcohol < aldehyde < carboxylate and that the uptake of formate was higher compared to the other organic ligands investigated. The uptake increased with the contacting time. At a contact time of 90 days, formate sorbed on hydrated cement phases in the following order: CSH > Hc > Ms ~ AFt > Mc. Summarizing the results obtained, the partition coefficient of small organic molecule investigated on cement phase and HCP (S/L = ≈ 333 g·dm^{-3}) was found to range typically from 0.01 and 1 dm^3/kg. This is also in agreement with the recent investigation conducted by Nedyalkova and co-authors [132] on PC (S/L = 130 g·dm^{-3}, hydration time = 30 days), confirming the weak interaction of formate with hydrated cement.

There are no previous studies in the literature investigating the uptake of citrate by hydrated cement paste, although some studies have tackled the interaction of other chelating ligands (e.g. EDTA) with cement [133]. One aspect to be considered in studies involving citrate in cement systems is the possible precipitation of the Ca-salt, i.e. $Ca_3(CIT)_2\cdot4H_2O$, which can also result in a decrease of the free-ligand concentration available for the complexation of radionuclides.

The uptake of gluconate and α-ISA by cement and C-S-H phases was extensively investigated in the past 30 years. For instance, the study conducted by Glaus and co-authors [134] focused on the uptake of gluconate and ISA by cement. Sorption experiments were conducted on hydrated cement paste using

a S/L ratio ranging between 5 and 25 g/dm³ and with a supernatant solution composition typical for cement pore water (ACW, pH = 13.4, [Na] = 114 mM, [K] = 180 mM, [Ca] = 2 mM) [135] and for a contacting time ranging from 1 to 90 days. Sorption data were interpreted using a two-site Langmuir isotherm, which postulates the presence of two sorption sites (strong and weak) on the hydrated cement surface. The same approach was also adopted to model the uptake of ISA. In general, the uptake of gluconate [134] was stronger and distribution ratios of $R_d \approx 3\text{-}4 \cdot 10^3$ dm³/kg (for [GLU]$_{tot}$ = 10^{-7}-10^{-4} M) were observed. Another important aspect is that the uptake of gluconate was found to be irreversible due to the strong interaction with active sites of cement (and C-S-H phases). Androniuk and co-workers [136] investigated the sorption of gluconate on C-S-H phases by combining wet-chemistry sorption studies and molecular dynamics (MD) simulations. For a contact time of 3 days, the authors reported R_d values of 285, 40, 4.5 dm³/kg for the uptake by C-S-H with C/S of 0.8, 1.0 and 1.38, respectively. The fast sorption kinetics was interpreted in terms of surface sorption rather than incorporation of the sorbed ligans. These results evidenced the complexing role of Ca ions with gluconate molecules connected to the composition of C-S-H phases: the uptake increases with the increase of C/S ratio. Based on their MD calculations, Androniuk et al. proposed that the interaction between Ca and gluconate occurs mainly at the surface of C-S-H particle, where gluconate molecules are initially driven by electrostatic forces towards the surface of C-S-H particle, followed by the complexation and formation of Ca-gluconate surface complexes. In agreement with Androniuk et al., Nalet and Nonat [136, 137] reported that the uptake of gluconate is higher on C-S-H phases with C/S = 1.58 than for 0.85 (S/L= 50 g/ dm³). C-S-H phases with high C/S ratios (C/S > 1) have a positive apparent surface charge due to Ca^{2+} uptake, which overcompensates the negative surface charge of C-S-H caused by deprotonated silanol groups [19]. Therefore, Nalet and Nonat [137] interpreted the gluconate sorption to occur through interaction with Ca ions at the surface of the C-S-H particles. Speciation calculations [138] showed that the increase of C/S in C-S-H also contributes to the formation of aqueous Ca-gluconate complexes (i.e. $Ca_3GLU_2(OH)_4$), which is the most dominant aqueous species at [GLU]$_{tot}$ = 200 mM. Due to the formation of strong aqueous Ca-gluconate complexes, the free concentration of Ca decreases with the increase of the organic concentration. Depending on the experimental conditions, the formation of aqueous Ca-GLU complexes can lead to the desorption of calcium ion from the C-S-H suface until a point where the calcium mediated sorption on C-S-H is lowered or no longer possible. It also was reported that gluconate interacts not only with calcium ions and hydroxide but also with silicates [138]. Experimental observations in this work indicated the possible formation of Ca-Si-gluconate complexes, with the ternary complex $Ca_3Glu_2(H_3SiO_4)_2(OH)_2^0$ becoming relevant mainly for 0.9 < C/S < 1.2 and prevailing over other Si-complexes (H_4SiO_4, $H_4SiO_4^-$, $H_2SiO_4^{2-}$).

1.6. Introduction to Lanthanides (Ln) and Actinides (An)

Lanthanides and actinides belong to the f-block of the periodic table. Due to the chemical similarities, especially for trivalent oxidation states, lanthanides are often used as non-radioactive / redox-stable analogues for key An(III), i.e. Am and Pu.

Lanthanides are located in the groups 3-12 of the 6th period of the periodic table. Since the 4f shell is being filled progressively through the period (the atomic number increases from 57 (La) to 71 (Lu)), the general electronic configurator is [Xe] $4f^{1-14}5d^{0-1}6s^2$, where [Xe] is the correspondent electronic configuration of the nearest noble gas (in this case Xenon). The 4f electrons are sufficiently shielded from the environment by the 5s and 5p orbitals therefore their contribution to valence forces is negligible. In a few cases, the energy difference between the 4f and 5d electrons is sufficiently small that changes in the surrounding environment can lead to promotion of a 4f electron to the valence shell (5d orbital). This results in formation of the tetravalent ions as in the case of Ce(IV). Alternatively, the result may be the transfer of the 5d electron to a 4f orbital, leading to the formation of divalent ions (e.g., Sm^{2+}, Eu^{2+} and Yb^{2+}) [139].

Actinides are placed it the groups 3-12 of the periodic table. The electronic shells 4f and 5f are progressively filled across the actinides series and the atomic number increases from 89 (Ac) to 103 (Lr). In addition to elements like thorium, protactinium and uranium, occurring in significant amounts naturally on earth, eleven transuranic elements have been produced artificially by nuclear reactions. Actinides have the general electronic configuration: $[Rn]5f^{1-14}6d^{0-1}7s^2$, where radon is the nearest noble gas and [Rn] refers to its configurations. The early actinides are characterized by a rich redox chemistry, as shown in Figure 6 .

Figure 6. Main oxidation states of the lighter actinides. Oxidation states highlighted in blue are the most stable in aqueous systems. Modified from Altmaier et al. [140].

Actinides are classified as hard Lewis acids [141] and therefore, tend to form strong complexes or to bind strongly to oxygen-containing hard bases (e.g. the hydroxyl groups present on the surface of C-S-H phases). The strength of this interaction is expected to correlate with the effective charge of the

actinide ion, Z_{eff}. Whilst oxidation states +III and +IV are characterized by the stability of the cations An^{3+} and An^{4+}, at the oxidation states +V and +VI stable linear actinyl moieties, i.e. AnO_2^{n+}, (with n = 1, 2), form. These oxidation states are accordingly characterized by the increasing effective charges AnO_2^{+} (Z_{eff} = 2.3), An^{3+} (Z_{eff} = 3), AnO_2^{2+} (Z_{eff} = 3.2) and An^{4+} (Z_{eff} = 4) [139]. In aqueous systems, the oxidation state +III is stable for trans-americium elements (e.g. Cm), while Pu presents this state only in very reducing conditions. The lighter actinide elements exhibit a broad range of oxidation states. The 5f electrons are much more delocalized and are energetically closer to the valence of 6d and 7s electrons [142-144] compared to the 4f electrons. Therefore, due to the smaller promotion energies of the 5f → 6d transitions, the lighter actinide ions exhibit an intermediate character between the d-transition elements (magnetic properties are studied in terms of delocalized or exchanged s and d valence electrons) and the lanthanide elements (the localized 4f electrons are essentially unaffected by chemical bonding). With the progressive filling of the 5f orbitals and the increase in the nuclear charge, the energy difference between the 5f orbitals and the outer orbitals increases. Consequently, the 5f electrons become more localized and participate less in the bonding interactions. This localization explains the marked stabilization of the trivalent oxidation state for the heavier actinides. The divalent lanthanides are more stable than divalent actinides. In fact, Am^{2+} does not exist as a stable species in aqueous solution [145]. Tetravalent oxidation state can be obtained for a number of the actinide elements, although the +IV state is quite unstable for the heaviest members of the series [145, 146]. The chemistry of the An(IV) species shows a general resemblance to that of Ce(IV). The rate of reduction of the An(IV) species follows the order $Bk^{4+} < Am^{4+} < Cm^{4+} < Cf^{4+}$ which resembles the order of thermodynamic stability as predicted from the reduction potentials of the M^{4+}/M^{3+} couples [147].

As strong electron acceptors (hard Lewis acids), both lanthanides and actinides tend to interact with strong electron donors (hard Lewis basis) according to the hard and soft acids and bases (HSAB) [141]. The aquatic chemistry of actinides depends on physical parameters like pH, E_h, temperature, pressure or partial pressure of reactive gas phases (e.g. O_2, CO_2) and chemical parameters like the concentration of the actinide, and presence of complexing ligands or reactive surfaces. The Pourbaix diagram is often used to plot the relevant oxidation states of actinides as function of, for example, pH and E_h values. Since the present study focuses on uptake behavior of radionuclide under reducing conditions foreseen for L/ILW disposal, the oxidation states +III (for Ln and An) and +IV (An) have been taken into account [148].

1.6.1. Trivalent lanthanides and actinides: Ln(III)/An(III)

1.6.1.1. Uptake of trivalent actinides and lanthanides on cements

The uptake of Eu, Nd and Am by cementitious materials has been extensively studied by Wieland, Tits and co-workers [5, 12, 26, 27, 149-151]. Sorption experiments conducted by Wieland et al. with Eu(III) [149] on sulphate-resistant Portland cement at pH = 13.3 resulted in very high R_d values of 10^6 dm^3/kg and 10^5 dm^3/kg for solid to liquid ratios of 0.01 $g \cdot dm^{-3}$ and 0.1 $g \cdot dm^{-3}$, respectively. Similar values were

found by Tits et al. [151] for Eu(III) sorption on C-S-H phases with a C/S of 1.09 ($R_d \approx 10^6$ dm^3/kg), thus supporting that C-S-H phases are the main sink of An(III) and Ln(III) in cement systems. The [Eu]$_{eq}$ solution concentration was found to range between 10^{-12} M and 10^{-8} M. The uptake kinetics was found to be fast, and steady-state conditions were reached within 1 day. The overview dedicated to the sorption experiments conducted by [5] of europium on C-S-H phase with $0.75 \le$ C/S ≤ 1.5 in ACW (pH = 13.3) and a S/L of 0.5 g·dm^{-3}, confirmed the previous observations by obtaining a $R_d = 7\ 10^5$ dm^3/kg. No effect of the composition of the C-S-H phases on the Eu(III) uptake was found. The same authors studied the uptake of Eu(III) ([Eu]$_{tot}$ = 2·10^{-9} M) and Am(III) ([Am]$_{tot}$ = 3·10^{-10} M) on HCP, in hyperalkaline conditions (Stage I), obtaining a similar sorption behavior for americium and europium ($R_d \approx 10^5$ dm^3/kg). Very strong sorption ($R_d \approx 10^5$ dm^3/kg) was also observed for the uptake of europium by calcite [12]. A dependency of R_d with the solid to liquid ratio in the sorption study was observed by the authors, whereas the differences observed for calcites with different degree of crystallinity may support that surface complexation has an important role in the retention of Ln(III)/An(III) by calcite. Time-resolved laser fluorescence studies reported that the incorporation of Eu(III)/Cm(III) is one of the mechanisms responsible of the overall uptake on calcite. Tits et al. and Mandaliev et al. [24, 27, 150, 152] proposed a two-step process: i) in a first step the trivalent actinide or lanthanide rapidly forms an inner surface complex or a surface precipitate on the C–S–H phases. In the second process ii), which is slow compared to the first step, the trivalent actinide or lanthanide becomes incorporated in the C–S–H structure by substituting the Ca^{2+} in the C–S–H interlayer and in the Ca-octahedral layer.

Spectroscopic studies (TRLFS, EXAFS) investigating the interaction of metal cations with C-S-H phases provided relevant insights in the uptake mechanisms: the physical adsorption is usually followed by the incorporation of An(III)/Ln(III) in the C-S-H structure [26, 27]. The latter process is mainly responsible for the long-term immobilization of radionuclides into the cement matrix. The sorption mechanism of Nd(III) and Eu(III) by HCP and C-S-H phases was investigated using EXAFS spectroscopy by Mandaliev and co-authors [26, 27, 150, 152]. The authors proposed a two step sorption process: in the first step Nd(III) is bound to the bridging Si of silanediol groups ($\equiv$Si-(OH)$_2$); in the second step the substitution of the structural Ca ions present in the C-S-H structure may take place given the similar ionic radii of An^{3+} / Ln^{3+} ($r_{Eu^{3+}}$ = 1.07Å, $r_{Nd^{3+}}$ = 1.11Å, $r_{Am^{3+}}$ = 1.10Å, $r_{Cm^{3+}}$ = 1.09Å) and Ca^{2+} ($r_{Ca^{2+}}$ = 1.12Å) in the octahedral coordination mode [153] (CN=8)). These observations are also in agreement with TRLFS measurements conducted for the Cm(III) uptake by cement and C-S-H phases [24, 25]. Stumpf and co-authors observed that Cm(III) incorporated into the cement structure is characterized by long emission lifetimes. For longer equilibration times, Cm fluorescence band intensity increases and red-shifts, indicating that the fraction of incorporated Cm increases. Using the correlation defined by Kimura and Choppin [154], Tits et al.[24] determined the presence of two main Cm(III) species in the solid phase: one complex with 1.4 H$_2$O molecules in the first coordination sphere, and another complex with no water molecules bound in the first coordination sphere of Cm(III). The first complex would correspond to a sorbed species in the interlayer region of C-S-H, whereas the second

species with no H_2O would correspond to an incorporated species involving the substitution of Ca ions of the Ca-O main layer. The authors observed that the R_d distribution ratios were not dependent on pH values (or at least the reported values scatter within the experimental error) nor on the C/S of C-S-H. It is worth to notice that the incorporation of Cm(III) (and Eu) can be considered as the slow sorption process since dissolution and recrystallization of the C-S-H phases are involved at this stage ($t_{eq} > 60$ days) [152].

1.6.1.2.   Solubility and thermodynamic properties of trivalent actinides and lanthanides – An(III)/Ln(III)

As mentioned in the section 1.6.1, the aqueous speciation and thermodynamic properties of trivalent actinides and lanthanides are similar. This applies for both the coordination chemistry as well as for the complex formation in solution. Systematic trends in thermodynamic data are often correlated to the ionic radii or z^2/r (square of the formal charge (z) divided by ionic radii (r)). For example, Cm(III), and trivalent lanthanides such as Nd(III) and Eu(III), are often used as analogues of Pu(III) and Am(III). Americium(III) is redox stable in natural aquatic systems [155, 156] and as other transuranic elements, it has a strong tendency to hydrolyze. The americium solubility calculated by using the thermodynamic data reported in [157], indicated that for pH >11 the solubility is about $5 \cdot 10^{-10}$ M and limited by the solid phase $Am(OH)_3$(am). In the context of Ca-Si rich materials, as in the case of C-S-H phases and hydrated cement (HCP, PC), it is important to consider the eventual formation of Ca-Ln(III)/An(III)-OH and Ln(III)/An(III)-OH-Si complexes. The formation of the ternary complexes Ca-Ln(III)/An(III)-OH has been reported in the literature at intermediate to high concentrations of $CaCl_2$ (0.25–4.5 M) [158], but may also become predominant in less concentrated but hyperalkaline systems [159]. The only An(III)-silicate species selected in the NEA-TDB, $AmSiO(OH)_3^{2+}$, becomes only predominant in acidic conditions. Although the number of studies investigating the complexation of Ln(III)/An(III) with silicate in alkaline to hyperalkaline conditions is very limited, the formation of further species involving a hydrolyzed Ln(III)/An(III) moiety or the participation of the silicon species $SiO_2(OH)_2^{2-}$ (prevailing at pH > 12) can be anticipated to form in the hyperalkaline conditions defined by cementitious systems. Although significant efforts have been dedicated in the last decade to improve the thermodynamic description of solubility and complexation of Ln(III)/An(III) in alkaline to hyperalkaline conditions [158, 160], further thermodynamic studies targeting the effect of silicate in such conditions are clearly required.

1.6.2. Tetravalent actinides - An(IV)

As discussed above, An(IV) are classified as hard Lewis acids and therefore, tend to form strong complexes or to bind strongly to oxygen-containing hard bases (e.g. the hydroxyl groups present on the surface of C-S-H phases). U(IV), Np(IV) and Pu(IV) are the most relevant tetravalent actinides in the context of nuclear waste disposal [140]. Thorium(IV) is often considered as redox-stable analogue of

U(IV), Np(IV) and Pu(IV). It holds higher solubility limits, and thus provides a broader experimental window in sorption studies, which require the use of concentrations below the corresponding solubility-limit. However, as discussed in [5], Th(IV) shows a clearly weaker first hydrolysis constant compared to the rest of the tetravalent actinides (U, Pu, Np). Therefore, the use of Th(IV) as chemical analogue of tetravalent actinides in sorption experiments on cement may result in an underestimation of R_d distribution ratio. This aspect needs to be taken into account when assessing the retention of tetravalent actinides on the basis of experimental datasets obtained for Th(IV).

1.6.2.1.   Uptake of tetravalent actinides on cements

Gaona et al. studied the uptake of Np(IV) by C-S-H phases and HCP (hardened cement paste) under controlled reducing conditions by means of EXAFS measurements [28, 29]. The analyses conducted on Np(IV) loaded C-S-H indicated that the Np(IV) local structure and coordination changes with the C/S composition. In particular, for high C/S, the identification of large numbers for Ca and Si atoms in the Np coordination sphere, indicated that Np(IV) was taken up into the interlayer of C-S-H phase for long equilibration time experiments. Similar results were observed for Np(IV) taken up by HCP. This finding indicated that C-S-H phases are one of the main sinks of Np(IV) on HCP. Surface adsorption and incorporation into C-S-H structure may be considered as the main sorbing mechanisms. Similar conclusions were obtained from Np(IV) sorption experiment on Nirex reference vault backfill conducted by Baston et al. [161]. It is important to remark that C-S-H phases with C/S > 1.5 are expected to dominate the cement system composition up to the degradation stage II, while C-S-H phases with a C/S ~ 0.7 will dominate in the latter steps of the 3rd cement degradation stage. On the basis of the available experimental data and the chemical analogy between the tetravalent actinides (Np(IV), Pu(IV), U(IV)), Wieland and co-workers recommended a value for R_d of 10^5 dm^3/kg for the uptake of An(IV) within the cement degradation stages I-III [1, 162].

Höglund et al. [163] and Allard et al. [164] conducted sorption experiments with Pu on concrete and Portland cement (PC) at $12.5 < pH < 13.5$ and -380 mV$< E_h <$ +140 mV. At these experimental conditions, the predominant plutonium redox state was +IV and the correspondent R_d coefficient was found to range between 10^3 and 10^4 dm^3/kg. The obtained R_d values may be affected by the possible presence of colloids due to insufficient solid phase separation. Aggarwal et al. [165] studied the sorption of ^{238}Pu ($[^{238}Pu]_{in} = 2 \cdot 10^{-10}$ M) on different cement phases (C-S-H phases, hydrotalcite, C$_3$A, C$_3$S) and PC. In the pH range investigated ($\approx 12 < pH < \approx 13$), the R_d was found higher than 10^4 dm$^3 \cdot$kg^{-1}. The distribution values reported by Pointeau et al. [166] regarding the uptake of Pu(IV) on HCP (S/L = 0.5 g/L) and in the pH range of 10–12, were found to range between ~ 10^4 dm^3/kg and 10^6 dm^3/kg. As suggested by Wieland, the high scatter of the data might reflect limitations in the solid phase separation and possible presence of colloids [1]. The sorption study of Baston et al. [167] with Pu on hydrated cement was conducted at pH values ($12.2 < pH < 12.4$) representative for the cement degradation stage II. The authors reported a strong uptake, with $R_d > 10^6$ dm$^3 \cdot$kg^{-1} and propose that the surface uptake

mechanism is also applicable for the cement degradation stage III. The reference book by Ochs and co-workers recommended R_d values of $3 \cdot 10^4$ dm^3/kg for the uptake of Pu(IV) by cement in the degradation stages II and III [168]. This recommendation was based on the results reported by Allard et al. [164] and Höglund et al.[163]. Given the lack of available studies at the cement degradation stage I conditions, and valuing the uptake behavior of chemical analogues (e.g. U(IV)) a distribution ratio $R_d = 5 \cdot 10^3$ dm^3/kg was assigned by Ochs et al.[168]. Tasi and co-workers investigated the sorption of Pu by PC CEM I in the degradation stage II (pH $\approx$ 12.5) [4]. The authors used an initial Pu concentration $[Pu]_{in} = 10^{-8.3}$ M and buffered the redox conditions with Sn(II)Cl$_2$ (strongly reducing) or hydroquinone (mildly reducing). Tasi et al. reported an R_d value of $10^{6.3}$ dm^3/kg, obtained as average value of the measurement performed for systems with S/L=2–4 g/dm^3.

Regarding the sorption mechanisms, very few studies were carried out on the sorption mechanisms of Pu onto C-S-H phase and/or cementitious material. The uptake model proposed by Baston et al. [167] was derived in terms of surface complexation reactions, with -Si(OCa)$_2$OH$_2$PuO$_2$(OH)$_2$ defined as main surface complex of Pu. The decrease in sorption observed experimentally was attributed to the formation of the aqueous complex Pu(V)O$_2$ISA$_{-2H}^{2-}$. Experiments were performed under anoxic conditions, and thus the proposed model involving exclusively Pu(V) remains highly speculative. Ochs et al. [168] suggested that the surface sorption mechanism of U, Am, Np, Th may include i) surface complexation and, ii) incorporation into cement phases after sorption onto C-S-H phases [24].

1.6.2.2.   Solubility and thermodynamic properties of tetravalent actinides – An(IV)

Plutonium is a redox-sensitive element, which in the hyperalkaline conditions defined by cementitious systems is mainly (but not exclusively) expected in the oxidation state +IV (see Figure 7). Hence, the aqueous speciation of Pu(IV) in these conditions is dominated by the neutral hydrolysis species Pu(OH)$_4$(aq) in absence of carbonate and other complexing ligands. The solubility of Pu(IV) is controlled by the amorphous solid phase PuO$_2$(am, hyd), which defines a solubility limit of $\sim 10^{-10}$–10^{-11} M in hyperalkaline conditions. The recent solubility study of Tasi et al. [169] carried out using nanocrystalline PuO$_2$(ncr, hyd) in alkaline and reducing conditions (defined by either Sn(II) or hydroquinone) provides results in good agreement with thermodynamic calculations performed using data selected in the NEA-TDB [157, 170]. For mildly reducing condition determined by hydroquinone as redox buffer (pe + pH$_m$ = 9.5 $\pm$ 1.0) and $8 \leq pH_m \leq 13$ the solubility of Pu was very low and limited by PuO$_2$(ncr, hyd). The presence of a small fraction of Pu(III) in the solid phase was observed by XAFS measurements on the solubility samples buffered by the Sn(II) system (pe + pH$_m$ = 2 $\pm$ 1).
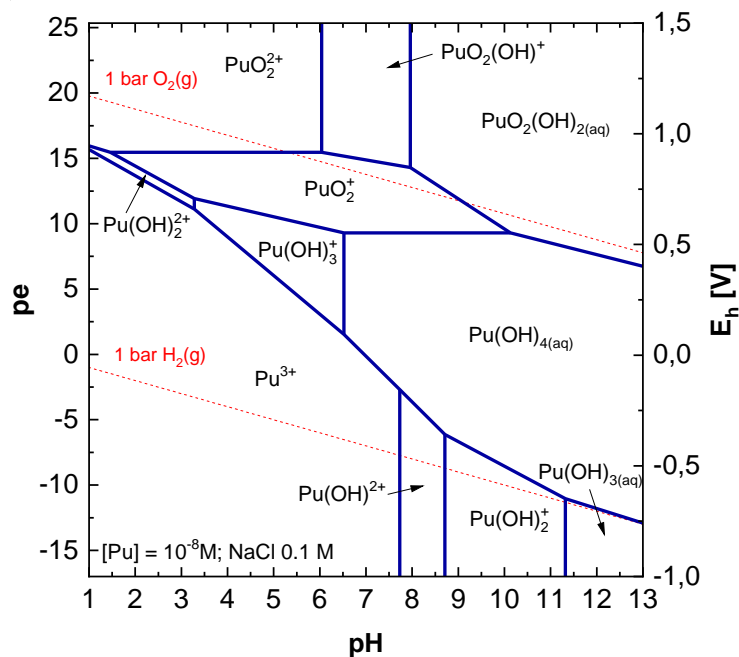
Figure 7. Pourbaix diagram of plutonium calculated for [Pu]$_{tot}$ =10^{-8} M and [NaCl] = 0.1 M, taken from [171]; only dissolved species are considered in this representation and solid phase precipitation is suppressed.

As discussed above, Th(IV) is often considered as chemical analogue of U(IV), Np(IV) and Pu(IV) in the solubility and thermodynamic studies, although due to its larger ionic diameter it is characterized by a weaker hydrolysis than the rest of the An(IV). Tits and co-workers [5] performed speciation calculations varying the solution composition of cement pore water (I = 0.3 M) and using thermodynamic data reported in the literature. Three different solution composition were investigated: i) a system with high calcium concentration (0.02 M) and low Si concentration (10^{-4} M), representative for the high C/S C-S-H phase; ii) a second system with both Si and Ca concentrations equal to 10^{-3} M; and iii) a third system with high Si concentration (8·10^{-3} M) and low Ca concentration (4·10^{-5} M), representative of C-S-H phase with a low C/S. The stability constants for the ternary Ca-Th(IV)-OH complex and the ternary Th(OH)$_3$(SiO(OH)$_3$)$_3^{2-}$ [172, 173] were applied, while the solubility was calculated taking into account the solubility product of the freshly precipitated amorphous ThO$_2$ phase [174]. For the low Si concentration, the main Th(IV) aqueous species is Th(OH)$_{4(aq)}$ and the solubility of ThO$_2$(am, fresh, hyd) is pH independent and equal to ca. 10^{-8} M. The complex Ca-Th(IV)-OH does not contribute significantly to the aqueous speciation. For the highest Si concentration, the complex Th(OH)$_3$(SiO(OH)$_3$)$_3^{2-}$ was found dominant for pH values 10 < pH < 13, and for pH higher than 13, the species Th(OH)$_4$(aq) was found again as dominant species. In the same pH range the Th(IV) solubility increases with the decrease of pH and reaches a value of approximately 10^{-6} M at pH = 10.0. Although analogous studies should be conducted for more relevant tetravalent actinides, e.g. U, Np or Pu, these prospective calculations show that An(IV)-silicate aqueous complexes may play a relevant role in cementitious environments, especially in the latter degradation stages characterized by high C/S ratios and thus higher Si concentrations in the aqueous phase.

1.7. Complexation of An(III)/Ln(III) and An(IV) with organic ligands

The presence of organic ligands in underground repositories for nuclear waste may have an impact on their long-term performance due to the possible formation of stable RN-L complexes that may increase the radionuclides mobilization into the geosphere. Considering the An(III/IV)/Ln(III)-L complex formation studies, it is possible to deduce that stability constants observed for short carbon-chain organics such as formate and acetate are very low compared to organic ligands with more than one functionality such as carboxylic acid group (e.g. EDTA [88, 175-179], citrate [88, 180], gluconate [117, 181], or ISA [88, 182-186]. Boggs et al [187] observed that the stability constants of organic ligands with actinides and lanthanides show a linear increase (higher stability) with the increase of carboxylic acid group number. Fröhlich et al. [188] investigated the stability constant of Cm(III)-FOR complexes by spectroscopic techniques (TRLFS) as function of the temperature, ligand concentration and at different ionic strength. The reported equilibrium constants correspond to complexes forming in acidic to near-neutral pH conditions, where Cm(III) is present as unhydrolyzed Cm^{3+}. Formate is not expected to outcompete the hydrolysis of Cm(III) in the hyperalkaline conditions defined by cementitious systems. Nevertheless, the An(III)-FOR (e.g. Pu(III), Am(III)) complexes were more stable than complexes with other carboxylic ligands such as acetate and propionate [189]. Complexation studies of Pu in presence of citrate carried out by Francis et al [190], indicate that citrate tends to form strong Pu-citrate complexes with a stoichiometric ratio of 1:2 only in acidic and neutral pH environment.

Concerning the solubility behavior of actinides and lanthanides in the presence of organic cement additives, it is worth highlighting the contribution by Adam et al. [191]. The authors investigated the impact of several organic ligands relevant in the context of cement-based repositories for L/ILW (i.e. adipic acid, methyl acrylate, citric acid, melamine, ethylene glycol, phthalic acid and gluconic acid) on the solubility of Nd(III), Th(IV) and U(VI). Different background electrolytes were considered (NaCl, $CaCl_2$, $MgCl_2$), and the pH_m (as -log [H^+] = pH_m) was varied from 9 to 13. The study reported that the solubility behavior of the selected radionuclides was affected by citrate and gluconate. The effect of these ligands on the radionuclide solubility was found stronger in NaCl media rather than in systems with $MgCl_2$ and $CaCl_2$. This can be possibly explained by the formation of binary complexes / compounds of the ligands with Mg and Ca, eventually resulting in a decrease of [L]$_{free}$ available for radionuclide complexation. At pH $\approx$ 9, citrate tends to increase the solubility of Nd(III), Th(IV) and U(VI), while no effect was found for higher pH values (pH $\approx$ 13). This observation is in agreement with the solubility results gained by Felmy et al. [180], who studied the effect of citrate (10^{-4} M -10^{-2} M) on the solubility of Th(IV) using $NaNO_3$ solutions (6.0 M–0.5 M) as ionic media. In contrast to this, gluconate increases the solubility of Th(IV) in NaCl (2.5 M and 5.0 M) solutions and for pH = 13. This observation was explained considering the formation of the aqueous complexes $Th(OH)_4GLU^-$, $Th(OH)_4(GLU)(GLU_{-H})^{2-}$ [180, 192]. In concentrated $CaCl_2$ solutions (1.0 M and 3.5 M), the solubility of Th(IV) in the presence of gluconate was virtually the same as for ligand-free systems. The increase

in solubility observed at $pH_m > 11$ is attributed to the predominance of the ternary complex $Ca_4[Th(OH)_8]^{4+}$, as reported by Altmaier et al. [172]. Two hypothesis are proposed by the authors to explain the deviation of the experimental solubility data from model calculations: i) the formation of possible quaternary solid phase Ca-Th-OH-GLU, or ii) the formation of ternary complex Ca-OH-GLU in solution [125]. Both options may decrease the free ligand concentration in the aqueous phase, and thus the capacity of gluconate to complex Th(IV).

1.8.   Impact of organic ligands on the uptake of An(III/IV)/Ln(III) by cement

Several aspects need to be taken into account when investigating the ternary system cement-radionuclide-organic. The concentration of the radionuclide should be below the solubility limit, but should remain high enough as to be accurately quantified by the considered (radio-)analytical technique. In this respect, the S/L ratio is a relevant parameter that requires optimization. An efficient solid phase separation (with either ultracentrifugation or ultrafiltration) is likewise required. In addition, the interaction of the organic ligand with the hydrated cement must be well characterized: the sorption of the organic ligand onto cement phases may decrease the free ligand concentration in solution able to complex the radionuclide. Also the stability of the cement phases or hydrated cement at high ligand concentration should be properly understood [1, 138]. In the case of strongly complexing ligands as ISA [193], gluconate [137] or citrate, the formation of stable complexes with Ca may enhance solid phases dissolution, in some cases eventually resulting in the full dissolution of the CaO fraction in the cement phase or hydrated cement. The dissolution of hydrated cement or cement phases (e.g. C-S-H, AFm phases) must be considered as side reaction that limits the maximum ligand concentration for RN-sorption studies at a given solid content.

Very few studies were conducted on the impact of formate and citrate on the uptake of An(III/IV) and Ln(III) by cement. The studies of Tanaka et al. [194] and Farr et al. [195] focused on the Pu(IV) uptake in presence and absence of citric acid on MnO_2 and $Mg(OH)_2$ respectively. For alkaline pH conditions, citrate did not have an impact of Pu retention on $Mg(OH)_2$. In analogy to the Th(IV)-GLU-calcite system [196], where the sorption reduction of Th(IV) by gluconate on calcite was explained in terms of formation of stable aqueous Th(IV)-OH-GLU complexes, it seems reasonable to assume that citrate forms less stable An(III/IV)-citrate complexes under hyper-lkaline conditions (see section 1.7).

Sorption studies conducted for Th(IV) and Eu(III) in the presence of gluconate with calcite [12, 196], hydrated cement and C-S-H phases [1, 197, 198] show a clear decrease of the uptake by solids with increasing ligand concentrations, which can be explained in terms of aqueous metal-ligand complex formation. The decrease of sorption of Eu(III) and Th(IV) on calcite in the presence of gluconic acid in ACW ($[Ca]_{tot} = 1.6\ 10^{-3}$ M, pH = 13.3) were attributed to the formation of Eu(III)-GLU (stoichiometric ratio 1:1) and Ca-Th(IV)-GLU (stoichiometric ratio 1:2:1) complexes. Complexation constants were determined considering $Eu(OH)_3(aq)$ and $Th(OH)_4(aq)$ as the predominant aqueous species for Eu(III) and Th(IV) under hyperalkaline conditions, respectively. Based on their experimental results, the

authors indicated that the maximum gluconate concentration expected to have negligible sorption reduction factor in cement-based repositories would be $[GLU]_{tot} = 10^{-7}$ M. Earlier sorption experiments of Tits et al. [199] suggested that the maximum concentration of GLU could be higher ($[163]_{aq}=10^{-4}$ M) than the one suggested for sorption experiments on calcite, due the possible co-sorption of ternary Ca-Th(IV)-GLU complexes. Sorption experiments with Np(IV) and ion exchange resins in the presence of gluconate (pH = 13.3) but in the absence of Ca, showed a clear decrease of the sorption at gluconate concentrations higher than $\approx 10^{-6}$ M [200]. Although, this concentration may be considered the upper limit for the absence or negligible impact of radionuclide uptake by cement, Wieland et al. [1] suggested to increase this threshold value due to the possible formation of ternary complexes (e.g. Ca-RN-(OH)-L).

1.9. Objectives of the thesis

The present Ph.D. thesis aims at a quantitative description and mechanistic understanding of the uptake of i) formate, citrate and gluconate and of ii) selected actinides (^{242}Pu(III/IV), ^{248}Cm(III)) and lanthanides (^{152}Eu(III)) by AFm phases (Ms, Mc, Hc), ettringite and C-S-H phases ($0.8 \leq C/S \leq 1.4$) in the absence and presence of formate, citrate and gluconate. The study targets boundary conditions (pH, pe, [Ca], etc.) representative of cement-containing underground repositories for L/ILW. The impact of formate, citrate and gluconate on the uptake of An(III)/Ln(III) and Pu(IV) by hydrated cement phases is investigated within a variety of experimental conditions (organic concentration, S/L, redox buffer), and following a stepwise approach that can be conceptualized in two main steps:

- the investigation of the binary system cement phases – organic ligands via sorption experiments,
- the investigation of the ternary system cement phases – radionuclides – organic ligands via sorption experiments, and complemented by means of advanced spectroscopic methods (TRLFS).

The studies conducted in the framework of this Ph.D. thesis can be divided in three main topics:

1. **Sorption of formate, citrate and gluconate on cement phases and hydrated PC under hyperalkaline conditions (Chapter 3.1):**

    This first part of the study focused on the uptake of formate, citrate and gluconate by selected cement phases (Ms, Mc, Hc AFt and C-S-H) and hydrated PC at the conditions relevant for the stage I of cement degradation (pH ~ 13.3). This investigation provides fundamental insights on the uptake of organic ligands (e.g. concentration of the ligand remaining in solution, aqueous complex speciation, sorption kinetics), which are also important inputs for the study of the ternary systems cement phases – radionuclides – organic ligands. In addition to the quantification of the sorbed ligand concentration on the specific cement hydrate, this first part of the Ph.D. thesis investigated the possible formation

of ligand-containing cement phases that could possibly act as sink for these organic ligands in cementitious systems. This latter investigation involved the synthesis of L-AFm and L-ettringite (with L = formate, citrate and gluconate) cement phases. Based on the characterization of both solid and liquid phases, thermodynamic modelling and thermodynamic calculations were considered to derive solubility constants of the new phases and to assess the aqueous speciation of formate, citrate and gluconate in the in the investigated systems.

2. **Solubility and sorption of Pu in presence of formate, citrate and gluconate on cement phases, under reducing and hyperalkaline conditions (Chapter 3.2):**

This study aimed at the characterization of the solubility, speciation and sorption of Pu under boundary conditions characteristic of cement systems. The solubility of Pu in the presence of FOR, CIT and GLU was investigated from undersaturation conditions using the well-defined solid phase $^{242}PuO_2$(ncr, hyd). Solubility experiments were carried out at constant pH (13.3) and varying the ligand concentration between 10^{-6} and 0.1 M. This study aimed at providing solubility upper limits to be considered in the definition of the sorption experiments, but also at gaining further insights on the aqueous speciation of plutonium in the presence of the investigated organic ligands. The study of the ternary system RN-L-C started with the investigation of Pu retention behavior in the absence and presence of organic ligands. Batch sorption experiments were carried out with ^{242}Pu varying S/L, ligand concentration, redox buffer (Sn(II)Cl$_2$, HQ) and order of addition of the individual components. The latter parameter was applied only for Pu-C-S-H-GLU system, in order to investigate the possible role of ternary / quaternary complexes Ca-Pu-OH-GLU in the kinetic hindering of the uptake by C-S-H phases, as previously described for the HCP-Pu-ISA system [4]. The final aim is to provide experimentally determined distribution coefficients (R_d) for Pu and to estimate the effect of formate, citrate and gluconate on the uptake, also considering the possible formation of stable complexes in the aqueous phase.

3. **Uptake of Eu(III)/Cm(III) by C-S-H phases in the presence of formate, citrate and gluconate under hyperalkaline conditions (Chapter 3.3):**

This study focuses on the uptake of Eu(III)/Cm(III) by C-S-H phases in presence and in absence of the investigated organic ligands. Eu(III) and Cm(III) are considered as analogues of Pu(III) and Am(III), on the basis of their same charge and similar ionic radii. Sorption batch experiments with ^{152}Eu(III) were carried out under alkaline condition relevant for cement degradation stage I. This system was investigated by varying S/L and ligand concentration. The main objective was the quantification of the distribution ratio of Eu and to study the influence of the ligand of interest on the retention of Eu by C-S-H. The evaluation of Eu-C-S-H-L benefited from the quantitative description carried out for the binary system (Chapter 3.1) and, only for gluconate, from the comprehensive

speciation description obtained for Cm(III)-C-S-H-GLU system based on spectroscopic (TRLFS) investigations.

TRLFS studies with the C-S-H-Cm(III) system were conducted in presence and absence of gluconate. The characterization of Cm(III) speciation both in the aqueous and solid phases provided information on the speciation of Cm(III) in the aqueous and solid phases, and thus on the mechanism driving the uptake of An(III)/Ln(III) in the absence and presence of organic ligands. The combination of wet-chemistry sorption experiments with advanced spectroscopic techniques providing information at molecular scale allows the quantitative description and mechanistic understanding for the retention of trivalent actinides under conditions representative of underground repositories for L/ILW.

The present study was performed in the framework of the EURAD-CORI (Cement-Organics-Radionuclides-Interactions) project.

2. Material and methods

The experiments carried out to investigate the binary system organic ligand-cement phase (C) (where cement phase stands for AFm, AFt, and C-S-H phases) were carried out at the Cement & Asphalt department at Empa (Dübendorf, Switzerland). Sample manipulation were performed under N_2 atmosphere and temperature (22 ± 2) °C.

The set of experiments focusing on RN-L-C ternary system were performed at the Institute for Nuclear Waste Disposal (INE) at KIT (Karlsruhe, Germany). Sample preparation and storage were performed under Ar atmosphere (with O_2 concentration below 2 ppm) at $T = (23 \pm 2)$ °C.

2.1. Chemicals

The ultra-pure water (Millipore, 18.2 MΩ, 22 ± 2 °C) used for solution preparation and synthesis of cement phases was boiled for at least three hours under continuous Ar purging. This step was applied to minimize the CO_2 content in the Milli-Q water. Al_2O_3 ($\geq 99.5\%$), $CaSO_4$ H_2O ($\geq 97.0\%$), Na-formate ($NaCHO_2$) ($\geq 98.0\%$), Na_3-citrate ($\geq 99.0\%$) ($Na_3C_6H_5O_7 \cdot 2H_2O$), Na-gluconate ($NaC_6H_{11}O_7$) and $SnCl_2$ ($\geq 98.0\%$) were purchased from Sigma-Aldrich. $Al_2(SO_4)_3 \cdot 18 H_2O$ ($\geq 60.0\%$), $CaCO_3$ ($\geq 99.0\%$), NaOH pellets ($\geq 99.0\%$), NaOH (Titrisol) were purchased from Merk (Supelko). SiO_2 – Areosil 200 was purchased from Evonik. The Pu stock solution used for sorption and solubility experiments has the following isotopic composition: 99.4 wt. % ^{242}Pu, 0.58 wt. % ^{239}Pu, 0.005 wt. % ^{238}Pu and 0.005 wt. % ^{241}Pu. In the solubility experiments, the use of the long-lived ^{242}Pu isotope ($t_{1/2} = 3.75 \cdot 10^5$ a) avoids potential redox processes induced by radiolysis effects in the case of shorter-lived isotopes. The ^{242}Pu stock solution was prepared starting from the acidic dissolution of $Na_2{}^{242}Pu_2O_7 \cdot xH_2O(am)$ solid phase, electrochemically synthesized. All details about the chemical preparation and characterization of the solid phase were reported in [201]. The resulting stock solution was qualitatively characterized by UV-Vis-NIR spectroscopy and the detailed composition was determined by combining liquid scintillation counting (LSC), standard induced coupled plasma mass spectroscopy (ICP-MS) and sector field induced coupled plasma mass spectroscopy (SF-ICP-MS) analyses. The Pu(VI) stock solution (in 0.1 M HCl) was further diluted in order to reach Pu concentrations of $\approx 10^{-8}$ M (sorption experiments with C-S-H) and $\approx 10^{-8.5}$ M (sorption experiments with AFm phases and ettringite). The choice of the +VI oxidation state with the in-situ reduction to Pu(IV) was motivated to minimize the possible formation of intrinsic colloids that may occur when spiking the plutonium in the +IV oxidation state to the alkaline conditions defined by cementitious systems.

Eu(III) sorption experiments were carried out by combining inactive ^{nat}Eu and ^{152}Eu stock solutions. The inactive Eu solution was prepared by adding 22.3 mg of $Eu(NO_3)_3 \cdot 6H_2O$ (Alfa Aesar, ≥ 99.9) in 5 cm^3 of 0.2 M of HCl. The inactive Eu sock solution was further diluted by a factor of 200, in order to obtain an initial total concentration of 10^{-7} M. The active europium stock solution ($[^{152}Eu(III)Cl_3] = 3.8 \ 10^{-6}$ M

in 0.5 HCl) was further diluted with Milli-Q water by a factor of 5. The total active europium concentration aimed for sorption experiments was $[^{152}Eu]_{tot} = 2 \cdot 10^{-9}$ M, i.e. $1.95 \cdot 10^5$ kBq/cm^3.

The isotopic composition of the Cm(III) stock solution consisted of 89.68% ^{248}Cm, 9.38 ^{246}Cm, 0.43 % ^{243}Cm, 0.30% ^{244}Cm, 0.14% ^{245}Cm and 0.07 ^{247}Cm. The initial total concentration of Cm applied for Time Resolved Laser Fluorescence Spectroscopy (TRLFS) was 10^{-7} M.

2.2. Synthesis of cement phases

For the experiments in the binary systems, Ms, Mc, Hc and AFt (i.e. sulfate-ettringite) were synthesized with an initial solid-to-liquid (S/L) ratio of 44.2, 46.3, 43.5 and 41.8 g/dm^3, respectively. C$_3$A (3CaO Al$_2$O$_3$) is used as a reactive precursor for the synthesis of AFm phases: CaCO$_3$ and Al$_2$O$_3$ were mixed at a 3:1 molar ratio and by heating the mixture to 800 ºC for 1 h, at 1000 ºC for another 4 h and at 1425 ºC for 24 h following the procedure reported in [202]. CaO was also used for AFm, AFt and C-S-H syntheses. CaO was obtained by heating CaCO$_3$ at 1000 ºC for 12 h, and cooling it down in a closed desiccator to minimize the CO$_2$ uptake.

Ms was synthesized by mixing CaSO$_4$ 2H$_2$O, C$_3$A with a stoichiometric ratio 1:1. Mc and Hc was prepared by mixing C$_3$A, CaCO$_3$ and CaO with 1:1 and 1:1/2:1/2 respectively. Sulphate based ettringite (3CaO·Al$_2$O$_3$·Ca$_3$(SO$_4$)$_3$·32H$_2$O) was synthesized by mixing CaO and Al$_2$SO$_4$·16.3 H$_2$O at a molar ratio of 6:1 in Milli-Q water. For the same experimental study, C-S-H phases with Ca/Si ratio of 0.8, 1.0, 1.2, and 1.4 were synthesized with an initial S/L of 55.3 g/dm^3. In order to assess the formation of new phases, due to the progressive incorporation of the organic ligand into cement phases, formate-AFm, citrate-AFm and gluconate-AFm were synthesized by mixing C$_3$A, CaO and the organic ligand in the stoichiometric ratio of 1:1:4 (S/L = 59.6 g/dm^3), 1:1:2/3 (S/L = 52.2 g/dm^3) and 1:1:2 (S/L=76.3 g/dm^3), respectively. Following the same approach, formate-AFt, citrate-AFt and gluconate-AFt were synthesized with a C$_3$A:CaO:L stoichiometric ratio 1:3:6 (S/L = 50.8 g/dm^3), 1:3:2 (S/L = 61.6 g/dm^3) and 1:3:6 (S/L = 104.8 g/dm^3), respectively. Hydrated Portland cement (PC, CEM 42.5 N) was prepared by mixing 1 kg of dry cement (c) with 400 g of Milli-Q water (w) (w/c = 0.4). The paste was equilibrated for 28 days at controlled temperature (20 ºC) in closed 0.5 dm^3 PE bottles and a part was ground by hand with an agate mortar to < 63 μm. 2.5 g of ground PC (d ≤ 63 μm) were used for sorption experiments in order to get a final S/L = 50 g/dm^3.

For the ternary system investigation (RN-L-C), AFm phases and AFt with an initial S/L of 5 g/dm^3 and C-S-H phases (C/S = 0.8, 1.4) with a S/L ratio of 1 g/dm^3 and 25 g/dm^3 were synthesized, using the procedures described above.

All cement phases were equilibrated for one month under continuous shaking (~ 100 rpm). Only for the binary system study, solid-liquid phase separation through filtration step was carried out. The separation of solid phase was performed through vacuum filtration over 0.45 μm nylon filter. AFm phases and ettringite were let dry under vacuum and in presence of oversaturated CaCl$_2$ solution (relative humidity

≈ 37%). C-S-H phases were dried in a in a freeze dryer for 7 days under liquid nitrogen in order to reduce CO_2 contact before further analysis.

2.3.   Methods

2.3.1.   Sorption experiments setup

In order to assess the impact of formate, citrate and gluconate on the retention of Pu(III/IV) and Eu(III) by cement phases at the cement degradation stage I conditions (pH ≈ 13.3), this study has been divided in two main blocks, i.e. (i) the uptake of formate, citrate and gluconate by cement hydrates, and (ii) the impact of formate, citrate and gluconate on the RN retention by cement phases.

In both steps, the uptake of organic ligand (for the binary system) and of the interest radionuclide (for the ternary system) was quantified through the distribution ratio R_d. The R_d coefficient was determined as follows:

$$R_d = \frac{C_{i,eq} - C_{i,0}}{C_{i,eq}} \cdot \frac{V}{m} [dm^3 \cdot kg^{-1}]$$

where $C_{i,eq}$ represent the equilibrium concentration [mol dm^{-3}] of the radionuclide / ligand of interest, $C_{i,0}$ the initial concentration [mol dm^{-3}], m is the mass [kg] of sorbent (cement hydrate) and V is the total volume [dm^3] of solution.

2.3.1.1.   Binary system (Cement-L)

Batch sorption experiments

The uptake of formate, citrate and gluconate was investigated via batch sorption experiments on the selected cement phases (AFm phases, AFt and C-S-H phases) and PC. All sorption experiments were conducted at the same pH conditions (pH ≈ 13.3), which represent the cement degradation stage I conditions. For each cement phase, the uptake of formate, citrate and gluconate were investigated in the organic concentration ranges of $2 \cdot 10^{-4}$ M ≤ [FOR]$_{tot, aimed}$ ≤ $2 \cdot 10^{-1}$, $2 \cdot 10^{-5}$ M ≤ [CIT]$_{tot, aimed}$ ≤ $3 \cdot 10^{-2}$ M, $2 \cdot 10^{-5}$ M ≤ [GLU]$_{tot, aimed}$ ≤ $2 \cdot 10^{-2}$ M, respectively, as shown in the Table 1. The aimed organic concentration of formate, citrate and gluconate was corrected by the experimental concentration determined by measuring blank solutions containing the aimed organic concentration. The results of this measurement are reported in the Table 1. Sorption experiments consisted in the addition of Na$_x$-organic ligand and 1 M NaOH solutions in order to obtain a total final Na concentration of [Na] = 0.2 M and a total volume of 50 cm^3 in all experiment. Samples were then sealed with Parafilm in order to reduce possible carbonation by CO_2 and were equilibrated for 7 days under continuous mixing (100 rpm).

31

Table 1. Aimed and measured concentration of formate, citrate and gluconate with a measurement error of ± 5%.

Formate aimed concentration, $[FOR]_{tot, aimed}$, [mM]	Formate measured concentration, $[FOR]_{tot, measured}$, [mM]	Citrate aimed concentration, $[CIT]_{tot, aimed}$, [mM]	Citrate measured concentration, $[CIT]_{tot, measured}$, [mM]	Gluconate aimed concentration, $[GLU]_{tot, aimed}$, [mM]	Gluconate measured concentration, $[GLU]_{tot, measured}$, [mM]
0.2	0.22	0.022	0.022	0.02	0.021
0.4	0.44	0.067	0.067	0.04	0.042
1	1.1	0.13	0.13	0.1	0.11
2	2.2	0.33	0.33	0.2	0.21
4	4.4	0.67	0.67	0.4	0.42
10	11	1.3	1.4	1	1.05
20	22	3.3	3.4	2	2.1
40	44	6.7	6.8	4	4.2
100	111	13	13	10	10.5
200	221	33	34	20	21

Kinetic sorption experiments

The same experimental approach as described above was applied for the kinetic experiments. For kinetic experiment a total initial organic concentration of formate $[FOR]_{tot} = 2\cdot10^{-1}$ M, citrate $[CIT]_{tot} = 3\cdot10^{-2}$ M and gluconate $[GLU]_{tot} = 2\cdot10^{-2}$ M and an equilibration time, $t_{eq} = 1, 2, 4, 7$ and 14 days were applied for all cement phases.

2.3.1.2. Ternary system (Cement-RN-L)

To study the effect of formate, citrate and gluconate on ^{242}Pu(III/IV) and ^{152}Eu(III) uptake, two series of sorption experiments were carried out, accounting for two different sequences in the addition of the individual components:

i) the first set-up consists in the addition of the selected RN (Pu or Eu) to the cement suspension, followed after 2 days of contact time before the addition of the corresponding organic ligand: (RN+C)+L;

ii) the second experimental set-up consists in the addition of the organic ligand and radionuclide together to the cement pore solution previously separated by centrifugation (8000 g, 10 min): (RN+L)+C (investigated only for RN = Pu).

The concentration of stable europium in the ^{152}Eu commercial stock solution was quantified as $[^{nat}Eu]_{tot} = 4.09\times10^{-7}$ M, which resulted in a concentration of $[^{nat}Eu]_{tot} = 3.1\times10^{-8}$ M in the individual samples after considering the corresponding dilution factors. The solid phase was added to the equilibrated

solution after 2 days of equilibration time. The first set-up is applied to investigate the direct impact of the different organic ligand and understanding the main mechanisms occurring between the L and the sorbed radionuclide on cement phases. The second experimental set-up was considered to understand the competitive behavior of the (Ca)-RN-L-OH ternary or quaternary complexes and the retained species on the hydrated cement phases. Note that previous studies with Cement-Pu-ISA and Cement-Nb-ISA following the second sequence of addition of the individual components resulted in significantly slower equilibration kinetics [4, 203].

(RN+C)+L

This order of addition (RN+C)+L was applied for all cement phases and radionuclides. In the case of Pu-C-S-H-L experiments, two S/L (1 g/dm^3 and 25 g/dm^3) ratios were investigated. HQ and Sn(II) were used as redox buffers with a total concentration of 2 mM. The predominance of Pu(IV) is expected for HQ buffered systems, whereas both Pu(III) and Pu(IV) eventually form in Sn(II)-buffered systems. All experiment were conducted at pH ≈ 13.3 (with [Na]$_{tot}$ = 0.2 M) with a total sample volume of V$_{tot}$ = 13 cm^3. Redox buffer solutions were prepared by dissolving 0.11 g of HQ and 0.19 g of Sn(II) in 10 cm^3 of 2 M NaOH solution. Only for Pu sorption experiments, to set the alkaline and redox conditions prior the addition of Pu stock solution, volumes of redox solutions and 2 M NaOH solutions were added to the samples, while for Eu sorption experiments only the 2 M NaOH solution was added before the introduction of Eu-active and -inactive stock solutions. Before spiking Eu and Pu stock solutions, pH$_c$ and E$_h$ (only for sorption experiments with Pu) were measured to confirm stable alkaline and redox conditions aimed for these experiments. Pu stock solution was spiked in the cement phases suspension in order to obtain an initial total concentration of 10^{-8} M for C-S-Hs and 10$^{-8.5}$ M for AFm phases and AFt. For the Eu sorption experiments, conducted only on C-S-H phases, a total initial concentration of [^{152}Eu] = 2·10^{-9} M was added in combination with 10^{-7} M of inactive Eu solution. After 2 days of equilibration time under continuous shaking, volumes of Na-formate, Na$_3$-citrate, Na-gluconate solutions were added to the suspensions. Additional volumes of ultra-pure water were added in order to obtain the same final total volume (13 cm^3) and therefore keep constant the S/L ratio for all systems. For each solid phase and radionuclide series, one sample was prepared containing only the RN (and redox buffer for Pu experiments), but without organic ligand. After the initialization of sorption experiments, pH$_c$ and E$_h$ were monitored at each sampling and [Pu]$_{aq}$ concentration were collected in the time-frame of 4 months. Further details on the sorption experiments settings are reported in the Table 2 (Pu) and Table 3 (Eu).

(RN+L)+C

The order of addition (RN+L)+C was applied only for Pu sorption experiments on C-S-H 0.8 and 1.4 in presence and absence of gluconate and using HQ as redox buffer. The pre-synthesized suspensions were centrifuged at 8000 g for 10 mins in order to separate the supernatant solution (pore cement solution)

from the solid phase. The solution was transferred in a new vial, and NaOH, HQ, [242]Pu, Na-GLU stock solution were added to the cement pore water. The solutions were let equilibrate for 2 days. The solids were added to the solutions and samples were thoroughly shaken in order to homogenize the system. Samples were equilibrated under continued shacking prior sampling steps. After the addition of the solid phase, pH_c and E_h values and $[Pu]_{aq}$ concentration were monitored at each sampling and collected in the time-frame of 4 months. Further details on the sorption experiments settings are reported in the Table 2.

Table 2. Experimental details of [242]Pu(III/IV) sorption experiments on C-S-Hs, AFm phases and AFt, with the order of addition (Pu+C)+L and (Pu+L)+C

Cement phase	S/L, $g \cdot dm^{-3}$	Nº Sample in absence of L	log[Formate/M]$_{tot}$	log[Citrate/M]$_{tot}$	log[Gluconate/M]$_{tot}$	Redox Buffer[a]	log[242Pu]$_{tot}$	Order of addition
C-S-H 0.8	1, 25	2 (per each S/L)	-4,-1.5	-4,-3,-2,-1.5	-4,-3,-2,-1.5	HQ, Sn(II)	-8	(Pu+C)+L
C-S-H 1.4	1,25	2 (per each S/L)	-4,-1.5	-4,-3,-2,-1.5	-4,-3,-2,-1.5	HQ, Sn(II)	-8	(Pu+C)+L
C-S-H 0.8	1, 25	2 (per each S/L)	-	-2,-1.5	-4,-3,-2,-1.5	HQ	-8	(Pu+L)+C
C-S-H 1.4	1, 25	2 (per each S/L)	-	-2,-1.5	-4,-3,-2,-1.5	HQ	-8	(Pu+L)+C
Ms	5	1	-4,-1.5	-4,-3,-2,-1.5	-4,-3,-2,-1.5	HQ, Sn(II)	-8.5	(Pu+C)+L
Mc	5	1	-4,-1.5	-4,-3,-2,-1.5	-4,-3,-2,-1.5	HQ, Sn(II)	-8.5	(Pu+C)+L
Hc	5	1	-4,-1.5	-4,-3,-2,-1.5	-4,-3,-2,-1.5	HQ, Sn(II)	-8.5	(Pu+C)+L
AFt	5	1	-4,-1.5	-4,-3,-2,-1.5	-4,-3,-2,-1.5	HQ, Sn(II)	-8.5	(Pu+C)+L

[a] The added redox buffer concentration was equal to 2 mM for all samples according to the procedure reported in [169].

Table 3. Experimental details of [152]Eu(III) sorption experiments on C-S-Hs with the order of addition (Eu+C)+L.

Cement phase	S/L, $g \cdot dm^{-3}$	Nº Sample in absence of L	log[Formate/M]$_{tot}$	log[Citrate/M]$_{tot}$	log[Gluconate/M]$_{tot}$	log[152Eu-active]$_{tot}$	log[Eu-inactive]$_{tot}$
C-S-H 0.8	1, 25	2[a] (per each S/L)	-1	-3,-2.5,-2,-1.5	-3,-2.5,-2,-1.5	-8.7	-7
C-S-H 1.4	1, 25	2[a] (per each S/L)	-1	-3,-2.5,-2,-1.5	-3,-2.5,-2,-1.5	-8.7	-7

[a] One additional sample in absence of organic ligand (S/L= 1 $g \cdot dm^{-3}$only) and initial concentration of active and inactive Eu log[152Eu-active]$_{tot}$= -8 and log[Eu-inactive]$_{tot}$ = -7, was carried out. No experimental data were reported to the low efficiency of the gamma-counter and high background threshold.

2.3.2.   Sample preparation: [248]Cm-TRLFS experiments

TRLFS measurements were carried out to gain insight on the sorption mechanism and the chemical speciation of the possible (aqueous and surface) complexes forming in the Ln(III)/An(III)-C-S-H-systems. For this analysis, Cm(III) is used because of it redox stability as well as the very favorable spectroscopic properties.

TRLFS spectra were collected for the Cm(III)-C-S-H-GLU system and two type of samples defined hereafter as *suspension* and *solution*. The suspension samples were prepared following the method described for the Eu and Pu sorption experiments and using the order of addition (Cm+C-S-H)+GLU.

Sample solutions were obtained from the pore water solution of the same sample used in the suspension like samples (i.e. C-S-H phases Ca/Si = 0.8, 1.4, S/L = 1 g/dm^3). The C-S-Hs pore solution was separated from the solid phase by centrifugation (4000 g for 20 minutes). Pre-synthesized C-S-H phases and pore solution were set at the total volume of 5 cm^3 and transferred in HDPE vials (Zinser analytics). A given volume of 2 M NaOH was spiked to both suspension and solution samples in order to set the same alkaline conditions applied in the sorption experiments, which resulted in a pH value of $\approx$ 13.3. A given volume of the ^{248}Cm stock solution was spiked to the samples to achieve a concentration of 10^{-7} M, and the sample was let equilibrate for 2 days before the addition of the organic ligand. Gluconate stock solution was introduced to the samples by covering the total concentration range 10^{-3} M $\leq$ [GLU]$_{tot}$ $\leq$ $10^{-1.5}$ M. Samples were equilibrated and characterized by TRLFS at t_{eq}= 7, 28 and 56 days, as described in the section 2.3.6.4.

2.3.3. Pu solubility experiments

The PuO$_2$(ncr, hyd) solid phase used for solubility experiments was prepared at KIT-INE in 2006 and was extensively characterized in a previous study [169, 204].

Pu solubility experiments were carried to gain additional insights on the complexation behavior of Pu with formate, citrate and gluconate at the same alkaline and redox conditions applied in the sorption batch experiments. For each organic ligand, both HQ (pe + pH$_m$ ~ 9) and Sn(II) (pe + pH$_m$ ~ 1) were used as redox buffer. Since formate and citrate were expected to form weak Pu-L complexes within the investigated experimental conditions, solution were prepared with a total ligand concentration of 10^{-2} M and $10^{-1.5}$ M. Solubility experiments with gluconate as organic ligand were performed within the concentration range 10^{-6} M $\leq$ [GLU]$_{tot}$ $\leq$ $10^{-1.5}$. All solubility experiments were conducted with the same ionic strength and alkaline conditions applied for sorption experiments: the sodium concentration arising from NaOH and Na-L solutions was kept constant and equal to 0.2 M. Solutions containing the redox buffer and organic ligands were contacted with approximatively 0.2 mg of PuO$_2$(am, hyd). Samples were then sealed with Parafilm, and equilibrated for 4 months under Ar-atmosphere, with a periodic gentle manual shaking in order to facilitate the attainment of equilibrium conditions. After the introduction of the Pu solid phase, pH$_m$, E$_h$, and [Pu]$_{tot}$ were measured periodically.

2.3.4. Phase separation

2.3.4.1. Binary system (C+L)

The phase separation was carried out in order to analyze the aqueous phase and determine the concentrations of formate, citrate and gluconate after sorption.

The suspensions were filtrated under vacuum through 0.45 μm nylon filter. The supernatant solution, was filtered through 0.45 μm nylon syringe filters before further analysis. An aliquot of the obtained

solution was used for the pH measurements. Two further aliquots were used for the ICP-OES and TOC measurements. AFm phases, ettringite and C-S-H phases were then dried as described in the section 2.2

2.3.4.2.   Ternary system (RN+L+C)

The determination of the total aqueous Pu and Eu concentrations in the sorption and solubility experiments was carried after phase separation. Sorption samples were firstly centrifuged at 8000 g for 5 minutes. For both solubility and sorption experiments, $320 - 420 \ \mu mm^3$ aliquots were withdrawn from the supernatant solution and transferred in the upper reservoir of 10 kDa Nanosep centrifugal device filter (pore size $\approx 2 - 3$ nm, Nanosep ®, Pall Life Sciences). The filters were centrifuged at 8000 g for 10 mins, in order to achieve a complete phase separation. The resulting solution was collected from the bottom reservoir of the Nanosep device and acidified in 2 wt. % HNO_3 solution, for Pu sorption and solubility experiments and for Eu sorption experiments. The acidified samples were analyzed for the determination of the total Pu concentration via SF–ICP–MS, and the total Eu concentration via gamma-counter analyses. In this study, the detection limit for Pu was $\sim 10^{-13}$ M (SF-ICP-MS, see Section 2.3.5.2) and $\sim 10^{-14}$ M for Eu (see Section 2.3.5.4).

2.3.5. Liquid phase characterization
2.3.5.1.   pH and E_h measurements

Binary system

An aliquot of the supernatant solution was used for the pH determination. The pH measurement was performed using a Knick pH-meter with a SE 100 pH/Pt 1000 electrode at room temperature. The instrument was calibrated with NaOH solution of known concentrations (0.1, 0.2, 0.5 and 1 M) to minimize the alkali error [205].

Ternary system

The determination of pH ($pH_m = -log [H^+/m]$) was achieved by combination pH-electrodes (Orion Ross, Thermo Scientific) freshly calibrated against standard pH buffers (pH = 10-13, Merk). The measured pH value in aqueous solutions at $I_m \geq 0.1$ mol kg^{-1}, pH_{exp}, is an operational apparent value related to the $[H^+]$ (in molal units) by the equation $pH_m = pH_{exp}+A_m$, where A_m is an empirical parameter including the activity coefficient of the proton, γ_{H^+}, and the liquid junction potential of the electrode for a given background electrolyte and ionic strength (temperature and pressure). The values of A_m for NaOH (NaCl-NaOH) solutions were taken from Altmaier et al. [140].

In alkaline systems with $m_{OH^-} > 0.03$ m, the H^+ concentration was calculated from the given m_{OH^-} and the conditional ion product of water (K'_w) at the ionic medium used in the experiments. The ion product of water K'_w was calculated from the standard state constant ($K°_w$) extrapolated using the Specific Ion interaction Theory (SIT) approach and the SIT coefficients reported in the NEA-TDB [157].

The redox potential was determined with combined Pt or Au and Ag/AgCl reference electrodes (Metrohm). The measured potentials were converted to E_h (versus standard hydrogen electrode: SHE) by correcting for the potential of the Ag/AgCl inner-reference electrode with 3 M KCl and T = 22 °C (+207 mV). E_h values were converted to pe = $-\log a_{e^-}$ according to equation (1).

$$E_h = -RT \ln(10) \, F^{-1} \log a_{e^-} \qquad (1)$$

where R is the ideal gas constant (8.31446 J mol^{-1} K^{-1}), F is the Faraday constant (96485.33 C mol^{-1}) and a_{e^-} is the activity of the electron. E_h values of the solutions were collected following the protocol described by (Altmaier 2011), which involved approximately 15-20 min of measurement time. In most of the E_h measurements for hydroquinone– (HQ) and Sn(II)– buffered samples, the absolute drift of the electrode was < 0.5 mV/min after the indicated time. The uncertainty of E_h values collected within 15 min of equilibration time ranged between ± 15 and ± 30 mV (calculated as 2σ of repeated E_h readings).

2.3.5.2. ICP-OES and SF-ICP-MS

The characterization of the aqueous phase in the binary system was performed by ICP-OES analysis. Total concentrations of Al, Ca, Na, Si and S were measured on an Agilent 5110 ICP-OES apparatus equipped with Agilent SPS 4 autosampler. Ar is used as inert carrier gas. The ICP-OES torch can reach temperatures near 10000 K, which allow the complete atomization and ionization of the sample. Molecular interferences are reduced due the presence of the cooled cone interface (CCI) located upside to the torch. The CCI removes the cool plasma tail from the axial optical path, minimizing the self-absorption and the recombination interferences. Furthermore, the Dichroic Spectral Combiner allows to capture and send to the detector both axial and radial view in one reading. All samples were diluted in 2 wt. % HNO$_3$ with dilution factors of 10, 100 and 1000.

The analysis of Pu in the aqueous phase of the binary and ternary systems was carried out by SF-ICP-MS. The quantification of the total Pu concentration in the sorption and solubility experiments was achieved by Thermo Scientific Element XR SF-ICP-MS instrument. This technique allows an optimal separation of the analyte ions from the spectral interferences due to the high mass resolution of the sector-field mass spectrometer (R = 10000). The combination of a dual-mode SEM with a Faraday detector increases the linear dynamic range and enables the analysis of any matrix element. For the determination of Pu in sorption and solubility experiments, samples were further diluted by a factor of 62.5 and 125 in 2 wt. % HNO$_3$.

2.3.5.3. Total organic carbon quantification (TOC)

The total organic concentration was measured using a Sievers 5310 C TOC analyser. The samples were diluted at least by a factor of 5 (for low organic concentrations) with 0.1 M HCl solution, and by a factor

of 10, 100 and 1000 with 0.01 M HCl at higher organic concentrations. After the sample is introduced into the Analyzer, 6 M phosphoric acid (H_3PO_4) (acid) is introduced into the sample at the programmed flow rate to reduce sample pH between 2 and 3. This step allows the accurate determination of TOC and IC. The acidified sample is treated with 15 wt. % ammonium persulfate ($(NH_4)_2S_2O_8$) (oxidizer) to promote oxidation of the organics. The sample is split for the measurement of total carbon, TC, and inorganic carbon, IC, contents respectively. The TC stream passes to an oxidation reactor where the sample is exposed to UV light. The UV lamp emits light at 185 nm and 254 nm resulting in the formation of powerful chemical oxidizing agents in the form of hydroxyl radicals (OH·) produced by the photolysis of water and persulfate. The hydroxyl radicals will completely oxidize organic compounds, converting the carbon atoms of the organic compound into CO_2. The TC moves from the oxidation reactor to the CO_2 Transfer Module, which consist in a gas-permeable membrane and separates the analyzer in two sides. One side consists in a closed loop of two conductivity cells (one for the TC stream and one for the IC stream) and the other side (DI side), consists of a distilled water pump, a distilled water reservoir, and ion exchange resin (resin bed). The CO_2 generated from the sample passes through the membrane into the distilled water supplied, while interfering compounds and oxidation by-products are blocked by the membrane and remain on the sample side. The CO_2 forms carbonic acid upon reaction with water, and the carbonic acid disassociates into hydrogen ions and bicarbonate ions. The distilled water is continuously pumped through the DI side of the analyzer, collecting the H^+ and HCO_3^- ions and H_2CO_3 and CO_2 molecules from the CO_2 transfer modules. The collected ions and molecules are delivered to the conductivity cell for measurement. Then the ion exchange resin removes the HCO_3^- and other ions. The water is then pumped back to the CO_2 transfer module to repeat the sequence. The CO_2 from the TC and IC sample streams are measured by the respective conductivity cells, and the conductivity readings are used to calculate the concentration of TC and IC. Once the values are measured, TOC is calculated as the difference of TC and IC.

2.3.5.4. Gamma counter

The determination of the total Eu concentration in solution was achieved with PerkinElmer 2480 Wizard[2] automatic gamma counter. In general, a gamma counter uses a scintillation crystal surrounding the sample to detect gamma rays: gamma rays interact with the crystal, and once absorbed, they produce light (photons). The produced light is measured by a light detector (e.g. photomultiplier tube).

The detector consists of thallium activated sodium iodide crystal (height = 80 mm, diameter = 75 mm). The detector is surrounded with 75 mm of lead shielding in order to reduce the background signal and the crosstalk from the conveyor. To best ensure the optimal counting efficiency, the detector is based on 4π geometry-like configuration. The generated γ radiation were sent to the NaI(Tl) crystal, causing the excitement of the crystal lattice centers, which relax under the emission of light. The emitted photons

are multiplied through a photomultiplier tube and converted into an electrical signal. The multichannel analyzer is calibrated in the range 15-2000 keV.

2.3.5.5. Zeta potential

Zeta potential measurements were carried out on selected binary C+L systems by using a Zeta Probe instrument (Colloidal Dynamics Inc., North Attleboro, MA) based on the electroacoustic method on stirred suspensions. An alternating high-frequency electric field was applied causing the oscillation of charged particle which generate sound waves. The instrument determines the dynamic mobility of charged particle present in a suspension, which is subsequently converted in zeta potential by the standard software. Prior to each measurement, pH meter (4.01, 7.01 and 10.01 standard solutions) and Zeta Probe instrument (KSiW, provided by Colloidal Dynamics Inc.) were calibrated. The zeta potential measurements were carried out at 23ºC in suspensions with a solid concentration of 4.8 wt. % in a total volume of 270 cm^3. The suspensions were titrated with citrate solution (0.09 M) from 3.3×10^{-4} M to 6.6×10^{-3} M with a titration increment step of 3.3×10^{-4} M. Milli-Q water was used as solvent for all suspensions measurement, therefore the pH of the system was not constant but varied at each citrate concentration. The zeta potential of the background solutions was measured at the same conductivity for each solution in a Teflon small volume static beaker. The zeta potential of each sample was recalculated accordingly by the software including the corresponding corrections as detailed in [206, 207].

2.3.6. Solid phase characterization

Solid phase characterization was carried out only on the cement-ligand binary system. Cement phases and PC after separation and drying steps were analyzed via XRPD, FT-IR and TGA analyses.

2.3.6.1. X-ray powder diffraction (XRPD)

XRPD characterization were carried out on the inactive binary system, after the drying method described in the section 2.3.4. XRPD analyses for L-AFm, L-AFt, ettringite, AFm phases and PC were performed on a Panalytical X'Pert Pro MPD diffractometer with θ-θ geometry, using CuKα radiation (λ = 1.54184 Å) equipped with a solid X-Celerator detector. XRPD patterns were recorded at room temperature in the interval 5º < 2θ < 70º with a step size of 0.017º (2θ) and a total counting time of ~ 2 s for each step. Due to the low crystallinity degree, the C-S-H XRPD scans were recorded with step size of 0.013º 2θ and with a fixed divergence slit size (0.25º 2θ) and an anti-scattering slit (0.5º 2θ) on the incident beam.

2.3.6.2. Fourier–transform infrared spectroscopy (FT-IR)

Infrared spectroscopy (FT-IR) analysis was carried out on Bruker Tensor 27 FT-IR spectrometer. Spectra were recorded in the wavelength range 4000 cm^{-1} - 400 cm^{-1} with a resolution of 4 cm^{-1}. This analysis was performed on powder samples in order to analyse the possible incorporation or interaction of formate, citrate and gluconate with the structure of the cement hydrates.

2.3.6.3. Thermogravimetric analysis (TGA)

TGA measurements were carried out on a Mettler Toledo TGA/SDTA 851 instrument (Mettler Toledo, Switzerland) on ~ 30 mg of sample using a heating rate of 20 °C/min and a temperature range between 30 °C and 980 °C under N_2 atmosphere. The water losses are reported as mass of H_2O/mass of initial (dried) sample. Portlandite (CH) was quantified based on the weight loss in temperature range 400-500 °C using the tangential method as detailed in Lothenbach et al. (Lothenbach, Durdzinski et al. 2016). The amount of CH was expressed relative to the mass of the samples at 600 °C.

2.3.6.4. Time resolved laser fluorescence spectroscopy (TRLFS)

The fluorescence optical behavior in solution of actinides (Pa(IV), UO_2^{2+}(VI), Am(III), Cm(III), Bk(III) and Cf(III))[208] is generated by the transition between the partially occupied electronic states in the *f* shell. In general, such behavior is characterized by a number of weak and sharp emission bands [209]. Electron configuration and oxidations state of the actinides are the main determining factor of the emission energy. Cm is used for spectroscopic investigation for its stable and reproducible fluorescence properties. According to the Cm fluorescence reported by Beitz et al. [210], when curium is irradiated with laser light of a wavelength of $\lambda = 396.6$ nm, it is excited from its electronic ground state Z (^{8}S'$_{7/2}$) to the F level. This absorption process is followed by a non-radiative decay to the A level (^{6}D'$_{7/2}$). Level A is the first excitation state and lies 16840 cm^{-1} above the ground state. Under the emission of fluorescence, a population of state Z from state A takes place. The stronger the ligand and the higher the number of coordinating ligands the stronger is the shift of the fluorescence light to higher wavelengths. This characteristic shift of the fluorescent wavelength allows to derive information on the chemical environment of the Cm(III) ion (mainly the first coordination sphere) and allows to derive Cm(III) speciation depending on different experimental parameters such as pH, nature and concentration of ligands, etc.

The measurement of the fluorescence lifetime of the excited state can provide additional insights on the coordination environment of Cm(III). Indeed, the decay of the fluorescence lifetime from the ^{6}D'$_{7/2}$ to ^{8}S'$_{7/2}$ state is characteristic for each species [211] and the decay of a single species can be explained with a mono exponential decay. Instead, the presence of different species in the sample, described by a bi- or multi exponential decay, has to be taken into account if the lifetime of the excited state is lower

than the exchange rate between ligands (as in the case of sorption systems) [212]. The fluorescence lifetime of Cm(III) depends on the quenching of its chemical surrounding which is mainly caused by O-H-vibrations. The substitution of water/OH ligands from the first hydration sphere of Cm(III) by other ligands reduces the quenching and increases the fluorescence lifetime [213]. This effect was empirically described for a H_2O/D_2O system by Kimura et al. [214]. A description of the hydration state of the Cm(III) ion is thus possible according to the following equation (2):

$$n_{H_2O} = 0.65 k_{obs} - 0.88 = \frac{0.65}{\tau} - 0.88 \tag{2}$$

Where n_{H2O} is the number of H_2O molecules in the first coordination sphere, and k_{obs} is the experimental delay time (ms^{-1}).

TRLFS measurements were performed with a Nd:YAG (Continuum Surelite II, $\lambda = 355$ nm, repetition rate: 10 s^{-1}) pumped dye laser system (Radiant dyes Narrow Scan, Dye: Exalite398, Energy: 1-2 mJ), operated at a constant excitation wavelength of $\lambda = 396.6$ nm (Figure 3.2). The resulting fluorescence was detected with an optical multichannel analyser with polychromator unit (Shamrock 303i, Andor, Grating: 1200 lines/mm, Range: $\lambda = 580$-620 nm) and an ICCD-camera (iStar, Andor; Modell DH720-18F-63) containing an integrated delay controller. Emission spectra were collected with a delay time of 1 μs after the laser pulse. To monitor the fluorescence lifetime, series of single spectra measurements with increasing delay time between the laser pulse and camera detection (steps: Δt = 10-400 μs) were taken. The fluorescence emission lifetime (τ) was obtained by fitting the integrated intensity (I) as a function of the delay time (t), according to (3):

$$I(\lambda) = I_0(\lambda) exp(-t/\tau) \tag{3}$$

Measurements of both suspension and solutions samples were conducted in quartz cuvettes. Suspensions samples were measured under continuous mixing determined by magnetic stirring.

2.3.7. Thermodynamic calculations

Thermodynamic calculations were carried out to obtain the solubility product of synthesized AFm-organic and AFt-organic phases based on the measured total concentrations. The thermodynamic modelling program GEM-Selektor (GEMS) [215] was used, which takes into account chemical interactions involving solids, solid solutions, metal ions, and aqueous electrolyte at once. General thermodynamic data were taken from the NAGRA/PSI database [88], data for cement hydrates from the

Cemdata18 database [216]. The CSHQ model [216, 217] was used to describe the alkali uptake and the composition of C-S-H.

The complexation of formate, citrate and gluconate with the different cations was considered using different complex formation constants as detailed in Table 4, Table 5 and Table 6.

Table 4. Thermodynamic data used for thermodynamic calculations on the formate system (HFor = formic acid).

Species	Reaction	log $\beta^0_{m,l}$	Reference
Aqueous complexes			
$HFor^0$	$H^+ + For^- \leftrightarrows HFor^0$	3.75	Calculated from $\Delta_f G°$ data by [79, 218]
$CaFor^+$	$Ca^{2+} + For^- \leftrightarrows Ca(For)^+$	1.43	Calculated from $\Delta_f G°$ data by [79, 218-220]
$Ca(For)_2^0$	$Ca^{2+} + 2For^- \leftrightarrows Ca(For)_2$	2.30	Calculated from $\Delta_f G°$ data by [79, 218-220]
$K(For)_2^-$	$K^+ + 2For^- \leftrightarrows K(For)^-_2$	-0.27	Calculated from $\Delta_f G°$ data by [79, 218-220]
$KFor^0$	$K^+ + For^- \leftrightarrows KFor^0$	0.03	Calculated from $\Delta_f G°$ data by [218-220]
$Na(For)_2^-$	$Na^+ + 2For^- \leftrightarrows Na(For)^-_2$	-0.23	Calculated from $\Delta_f G°$ data by [218-220]
$NaFor^0$	$Na^+ + For^- \leftrightarrows NaFor^0$	0.05	Calculated from $\Delta_f G°$ data by [218-220]
Solids			
$Ca(For)_2$ (formicaite)	$CaFor_2 \leftrightarrows Ca^{2+} + 2For^-$	not reported[1]	

[1] [221] reports a high solubility of $Ca(HCOO)_2$ of 166 g/dm^3 at 20°C.

Table 5. Thermodynamic data used for thermodynamic calculations on the citrate system (H_3Cit = citric acid).

Species	Reaction	log $\beta^0_{m,l}$	Reference
Aqueous complexes			
$HCit^{2-}$	$Cit^{3-} + H^+ \leftrightarrows HCit^{2-}$	6.36	[88]
H_2Cit^-	$HCit^{2-} + H^+ \leftrightarrows H_2Cit^-$	4.78	[88]
H_3Cit^0	$H_2Cit^- + H^+ \leftrightarrows H_3Cit^0$	3.13	[88]
$CaCit^-$	$Ca^{2+} + Cit^{3-} \leftrightarrows CaCit^-$	4.80	[88]
$CaHCit^0$	$Ca^{2+} + HCit^{2-} \leftrightarrows CaHCit^0$	2.92	[88]
CaH_2Cit^+	$Ca^{2+} + H_2Cit^- \leftrightarrows CaH_2Cit^+$	1.53	[88]
$KCit^{2-}$	$K^+ + Cit^{3-} \leftrightarrows KCit^{2-}$	1.42[b]	[222]
K_2Cit^-	$2K^+ + Cit^{3-} \leftrightarrows K_2Cit^-$	1.93[b]	[222]
$NaCit^{2-}$	$Na^+ + Cit^{3-} \leftrightarrows NaCit^{2-}$	1.54[b]	[222]
Na_2Cit^-	$2Na^+ + Cit^{3-} \leftrightarrows Na_2Cit^-$	2.38[b]	[222]
$AlHCit^+$	$Al^{3+} + Cit^{3-} + H^+ \leftrightarrows AlHCit^+$	12.90	[223, 224]
$AlCit^0$	$Al^{3+} + Cit^{3-} \leftrightarrows AlCit^0$	9.90	[223, 224]
$AlCitOH^-$	$Al^{3+} + Cit^{3-} + H_2O \leftrightarrows AlCitOH^- + H^+$	8.10	[223, 224]
$Al(Cit)_2^{3-}$	$Al^{3+} + 2Cit^{3-} \leftrightarrows AlCit_2^{3-}$	14.13	[223, 224]
$Al(Cit)_2(OH)^{4-}$	$Al^{3+} + 2Cit^{3-} + H_2O \leftrightarrows Al(Cit)_2(OH)^{4-} + H^+$	10.19	[223, 224]
$Al_3(Cit)_3(OH)_4^{4-}$	$3Al^{3+} + 3Cit^{3-} + 4H_2O \leftrightarrows Al_3(Cit)_3(OH)_4^{4-} + 4H^+$	20.6	[223, 224]
Solids			
$H_3Cit(H_2O)(cr)$	$H_3Cit(H_2O)(cr) \leftrightarrows H_3Cit^0 + H_2O$	1.33	[88]
$Ca_3Cit_2(H_2O)_4(cr)$	$Ca_3Cit_2(H_2O)_4(cr) \leftrightarrows 3Ca^{2+} + 4H_2O + 2Cit^{3-}$	-17.9	[88]

[a] Sari [225] suggested the formation of $CaH(Cit)_2^{3-}$, $Ca(Cit)_2^{4-}$ and $CaH_{-1}Cit^{2-}$ complexes, but did not give any details on the concentrations used, on the fitting procedure and did not report the experimental data, thus those data were not included in the present calculations following the recommendation in the NEA-TDB review on organics [88]. A recent study of Gácsi et al. [226] indicated that the formation of $CaH_{-1}Cit^{2-}$ is expected to be relevant only for very high pH values (pH > 15).

[b] The NEA-TDB review on organics [88] suggested the use of SIT interaction coefficients to describe the interaction between Na^+ or K^+ with citrate^{3-} at high ionic strength. As in the present work the extended Debye-Hückel was used and ionic strength was in all cases below 0.5 M, complexation constants were used. In all cases, less than 0.1% of total Na, K, or citrate in solution were present in those complexes and their consideration had a negligible effect on the calculated solubility products (less than 0.01 log units).

Table 6. Thermodynamic data used for thermodynamic calculations on the formate system (HGlu = gluconic acid).

Species	Reaction	log $\beta^0_{m,l}$	Reference
Aqueous complexes			
$HGlu^0$	$H^+ + Glu^- \leftrightarrows HGlu^0$	3.64	[126] [a]
$CaGlu^+$	$Ca^{2+} + Glu^- \leftrightarrows CaGlu^+$	1.56	[119] [a]
$Ca(Glu)_2^0$	$Ca^{2+} + 2Glu^- \leftrightarrows Ca(Glu)_2^0$	2.85	[227]
$CaGluOH^0$	$Ca^{2+} + Glu^- + OH^- \leftrightarrows CaGluOH^0$	3.95	[227]
$Ca_2Glu(OH)_3^0$	$2Ca^{2+} + 2Glu^- + 4OH^- \leftrightarrows Ca_2Glu_2(OH)_4^{2-}$	11.25	[227]
$Ca_3Glu_2(OH)_4^0$	$3Ca^{2+} + 2Glu^- + 4OH^- \leftrightarrows Ca_3Glu_2(OH)_4^0$	16.10	[227]
Solids			
$Ca(Glu)_2$	$Ca^{2+} + 2Glu^- \leftrightarrows Ca(Glu)_2$	-4.19	[12]

[a] Values expoated 0 M ionic strength using the WATEQ Debye-Hückel equation from those reported in the "Reference" column. Furthere details are reported in [227].

Activity coefficients of the aqueous species were calculated with the built-in extended Debye-Hückel equation and NaOH as a background electrolyte:

$$log\gamma_i = \frac{-A_y z_i^2}{1 + B_y a_i \sqrt{I}} + bI$$

z_i is the charge of species i, I is the effective molal ionic strength, $a_i = 3.31$, is a parameter dependent on the size of ion i, b corresponds to 0.98 in NaOH [228, 229], and A_y and B_y are P,T-dependent Debye-Hückel solvent parameters.

The solubility products and saturation indices were calculated from the activity of the species Ca^{2+}, $Al(OH)_4^-$, OH^-, SO_4^{2-}, CO_3^{2-}, CHO_2^-, $C_6H_7O_5^{3-}$ and $C_6H_{11}O_7^-$ and H_2O, obtained using GEMS based on the measured total concentrations.

3.1. Sorption of formate, citrate and gluconate on cement phases and PC under hyperalkaline conditions

In the present chapter, a discussion about the binary system organic ligand (L = formate, citrate, gluconate) and cement phases (C) is presented. In a first section the chemical stability (thermodynamic study) and structure (solid and liquid characterizations) of reference C-S-H, AFm and AFt phases without organic ligands are discussed. In a second step, the kinetics of formate, citrate, and gluconate sorption on pre-synthesized C-S-H, AFm, and AFt phases is studied, the possible sorption mechanism, complex speciation and, finally the sorption is quantified by distribution ratios, R_d values.

3.1.1. Reference phases without organics

3.1.1.1. Calcium silicate hydrates

In this section, the chemical features and structure of the reference C-S-H phases are described. These phases were used later in uptake experiments for formate, citrate and gluconate, which will be described in later sections including the effect of organics on C-S-H chemical structure and composition. Figure 8 shows the XRPD patterns of C-S-H phases with $0.8 \leq C/S \leq 1.4$ and with a total sodium concentration $[Na]_{tot} = 0.2$ M. C-S-H phases were the main phase present for all C/S ratio investigated. Due to the high hydroxide concentration, portlandite was detected for the two highest C/S ratios as also reported in [230]. With the increase of the C/S ratio, the interlayer distance (002) at ≈ 8 $2\theta°$ shifts towards higher $2\theta°$ values, and thus to smaller interlayer distances. The increase of the Ca concentration enhances the electrostatic forces between the positively charged interlayer region with the two negatively charged main layers [231, 232]. The reflection (101) at ≈ 17 $2\theta°$ is visible only for the C/S ratio of 0.8 and 1.0. This reflection is related to the bridging silica tetrahedra within the silica chain [230, 231], which are occupied at low C/S but empty at higher C/S in C-S-H. The TGA analysis (see Figure 1 in the Appendix 3.1) allowed determining a water loss of ≈ 0.20 g H_2O per g dry weight in agreement with the data reported by Lothenbach et al. and Yan et al. [230, 233].
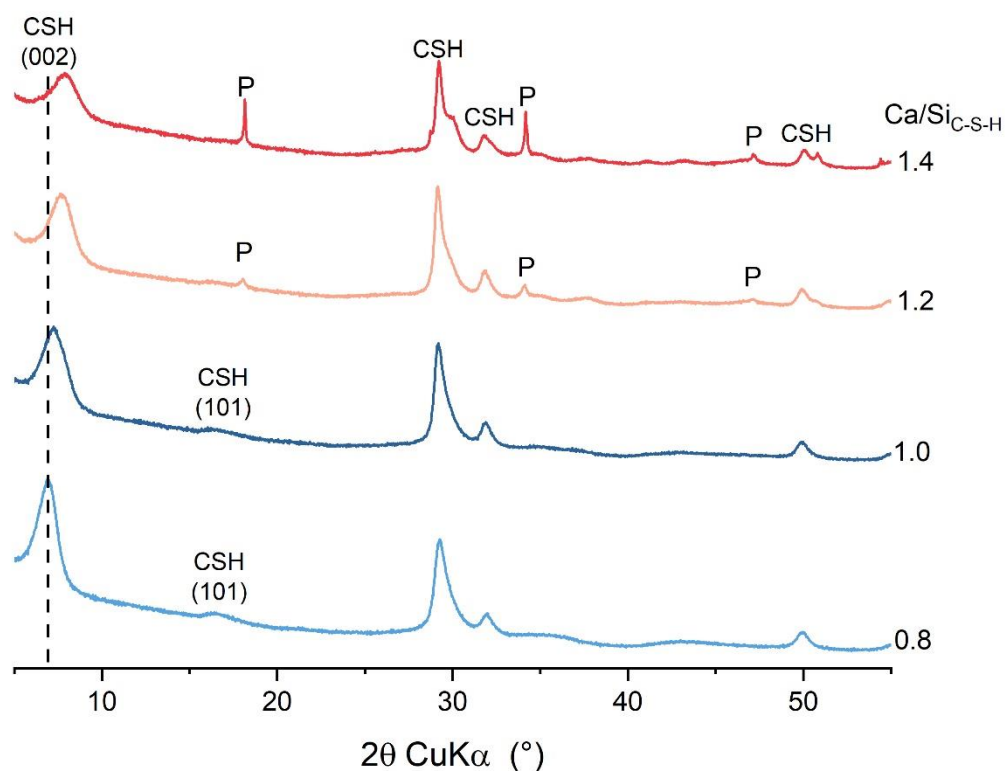
Figure 8. XRPD of C-S-H phases synthesized with a Ca/Si ratio of 0.8, 1.0, 1.2 and 1.4 and equilibrated for 2 months. CSH: C-S-H; P: portlandite.

The FT-IR analysis conducted on the reference C-S-H phases is reported in the Figure 9. The wavenumber range of 1400-800 cm^{-1} represents the stretching vibration bands of the Si-O bond, while the second range from 800 to 400 cm^{-1} is representative of the Si-O bending vibrations. The band at ~ 950 cm^{-1} is the result of the overlapping of several stretching Si-O bands. As observed by Yan et al. [230], the position of this band shifts toward lower wavenumber numbers if the silica chains are depolymerized. In the enlargement of the main peak region on the left side of Figure 9, no significant differences were detected for the band position of C-S-H phases with C/S of 1.2 and 1.4. The signals at 810 cm^{-1} and 500 cm^{-1} indicate stretching (i.e. [230, 234]) and bending vibration of the chains-end-sites of the silica tetrahedral, Q^1, respectively. The intensity of the signal at ~ 650 cm^{-1}, assigned to the Si-O-Si (O-Si-O) bending and water vibrations [235], increases with the increase of C/S ratio.

Figure 9. FT-IR spectra of C-S-H phases with a Ca/Si ratio of 0.8, 1.0, 1.2 and 1.4 in the wavenumber region (1400 – 400 cm^{-1}).

3.1.1.2. AFm phases

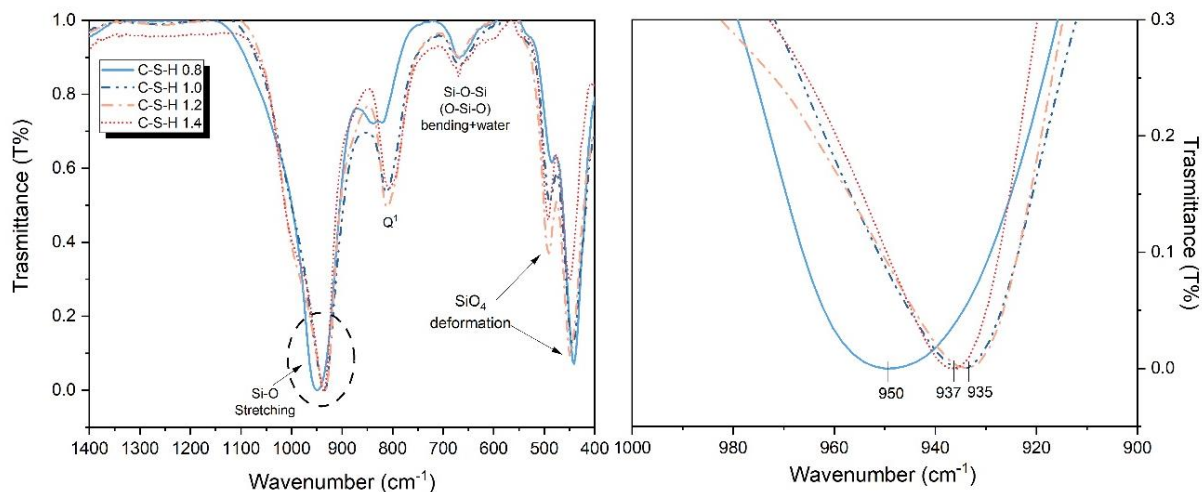As for C-S-H phases, different AFm phases (Ms, Mc, Hc), and ettringite were synthesised as references phases and used in later sections to study the formate, citrate and gluconate uptake on AFm phases and ettringite.

AFm have a layered structure consisting of positively charged main layers, $[Ca_4Al_2(OH)_{12}]^{2+}$, and anions and water present in the interlayer region, $[X_x \cdot nH_2O]^{2-}$. AFm phases form hexagonal or pseudo hexagonal crystals: Ms and Hc have a trigonal geometry [236, 237], while Mc has triclinic symmetry [31]. For well-crystalline phases, the XRPD analysis allows to determine the unit cell dimensions based on the position of the main basal reflections, which occur at low 2θ degrees as for AFm phases (Figure 10). Ms is characterised by a main basal reflection at ≈ 9.9º 2θ (8.9 Å), which corresponds to the interplanar distance (003), typical of crystalline monosulfate with 12 waters with a chemical formula $Ca_4Al_2(SO_4)(OH)_{12} \cdot 6H_2O$ (C_4AsH_{12}). The smaller reflection which appears at ≈ 9.4º 2θ (7.9 Å), indicates the formation of different hydrated forms of Ms, C_4AsH_{14}, predominant in suspension [36]. For the Hc phase, the characteristic (006) reflection at 10.9º 2θ (8.3 Å) indicates the formation of $Ca_4Al_2(CO_3)_{0.5}(OH)_{13} \cdot 5.5H_2O$. For this system, a secondary phase detected was tentatively assigned to carbonated hemicarbonate, $C_4Ac_{0.8}H_{10.2}$ [238] and labelled as cHc. Eventually, Mc defined with a triclinic structure, present a main basal spacing at 11.2 2θ angles which corresponds to interlayer distance of 7.9 Å [31, 32]. In addition, AFm phases have a characteristic reflection at ≈ 31º 2θ ($d_{(110), Ms}$ ≈ 2.8, Å, $d_{(110), Mc}$ = 2.9 Å; $d_{(110), Hc}$ = 2.9 Å) related to the main layer (110 or 220 plane).

48
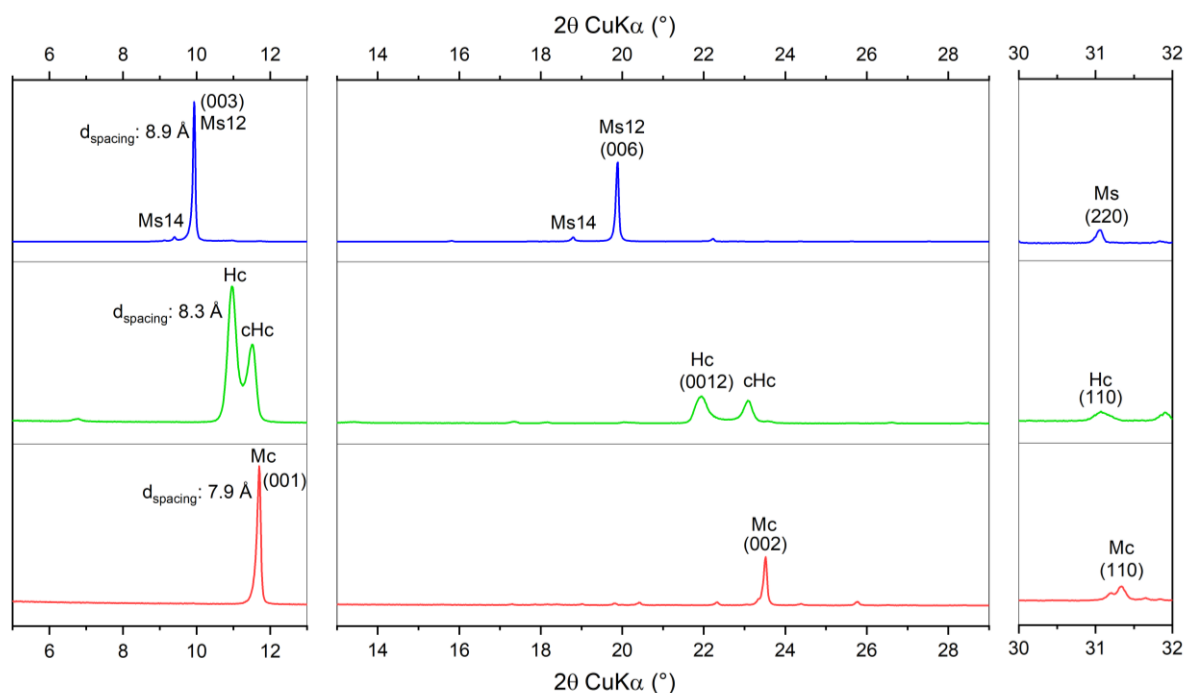
Figure 11. XRPD pattern diffraction of synthesized AFm phases, Ms, Hc, and Mc after 2 months of equilibration time. cHc: carbonated hemicarbonate; Hc: hemicarbonate; K: katoite ($Ca_3Al_2(OH)_{12}$); Mc: monocarbonate (C_4AcH_{11}); Ms12: monosulfate-12 (C_4AsH_{12}); Ms14: monosulfate-14 (C_4AsH_{14}): P: portlandite

The FT-IR spectra of Ms, Mc and Hc are shown in the Figure 12. The absorption bands from 3000 cm^{-1} to 3600 cm^{-1} are related to OH^- stretching vibrations resulting from the interlayer water within the AFm phases. The bands of Mc are narrower than those of Hc or Ms indicating more coordinated interlayer water in Mc. The main OH^- signal of Ms occurs at lower wavenumber than that of Hc indicating a stronger coordination of water in Ms than in Hc. The FT-IR spectrum of Ms is characterized by the vibration bands of the sulphate group SO_4^{2-}, with two vibration bands: v_3 at ≈ 1100 cm^{-1} and v'_3 at ≈ 1150 cm^{-1}. The latter band is visible as a shoulder of v_3 (Figure 12). The vibration bands v_2 and v_4 are observed at ≈ 460 cm^{-1} and at ≈ 980 cm^{-1} respectively. In general the sulphate group in water has a higher symmetry and only the vibration modes v_1 and v_3 are visible [239]. In addition, the splitting of the vibration mode v_3 has also been observed in [202]. For Mc, in the interlayer anion bond (CO_3^{2-}) to the main layer is defined by the stretching vibration vibration v_1 is observed at ≈ 1070 cm^{-1} [32]. Since in Hc the CO_3^{2-} is weakly bound to the main layer, the same stretching vibration occurs at ≈ 1090 cm^{-1} [34]. Additional bands visible for Hc are the bending vibration v_4 at ≈ 750 cm^{-1} and v_3 at ≈ 1400 cm^{-1} of the carbonate group.
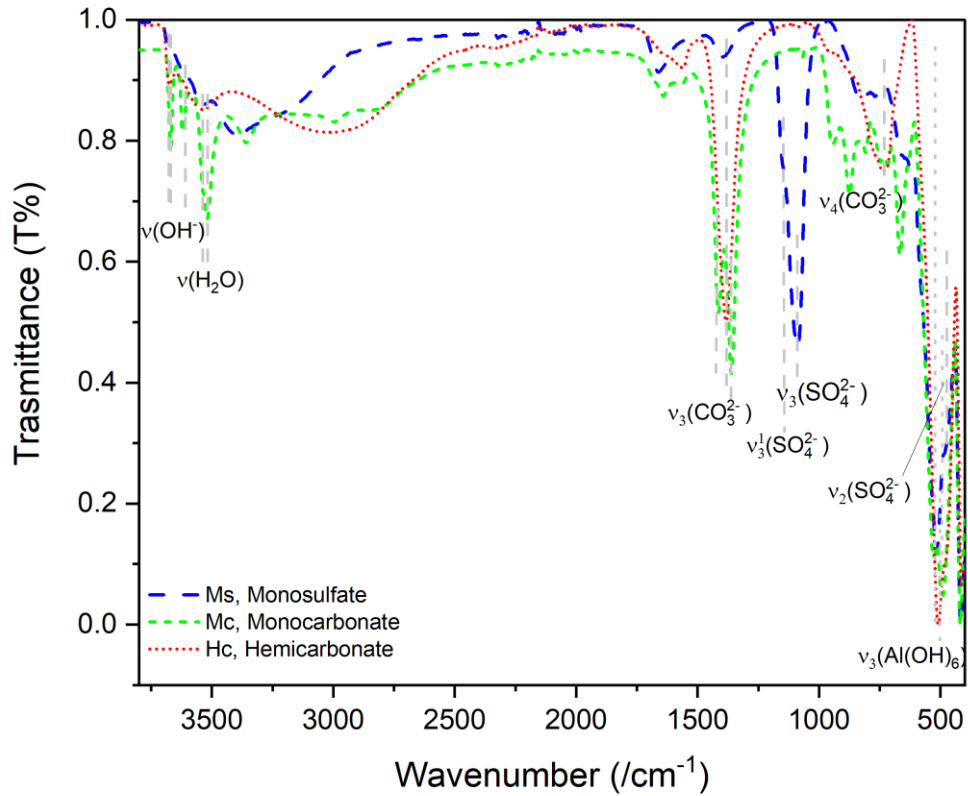
Figure 12. FT-IR spectra of the synthesized AFm phases in the frequencies ranges of 3800 – 400 cm^{-1}.

3.1.1.3. Ettringite

The hexagonal structure of ettringite structure consists of two elements: calcium aluminate hydrated columns $[Ca_6[Al(OH)_6]_2 \cdot 24H_2O]^{6+}$ and intra-channel sulfate ions and water molecules [240]. The XRPD patterns of the synthesized ettringite are shown in Figure 13. The XRPD spectra of ettringite is characterized by narrow well defined reflections including a main (100) signal at 9.7 Å in *a* direction (perpendicular to the columns) and a small (002) reflection (parallel to the column) at 10.7 Å.
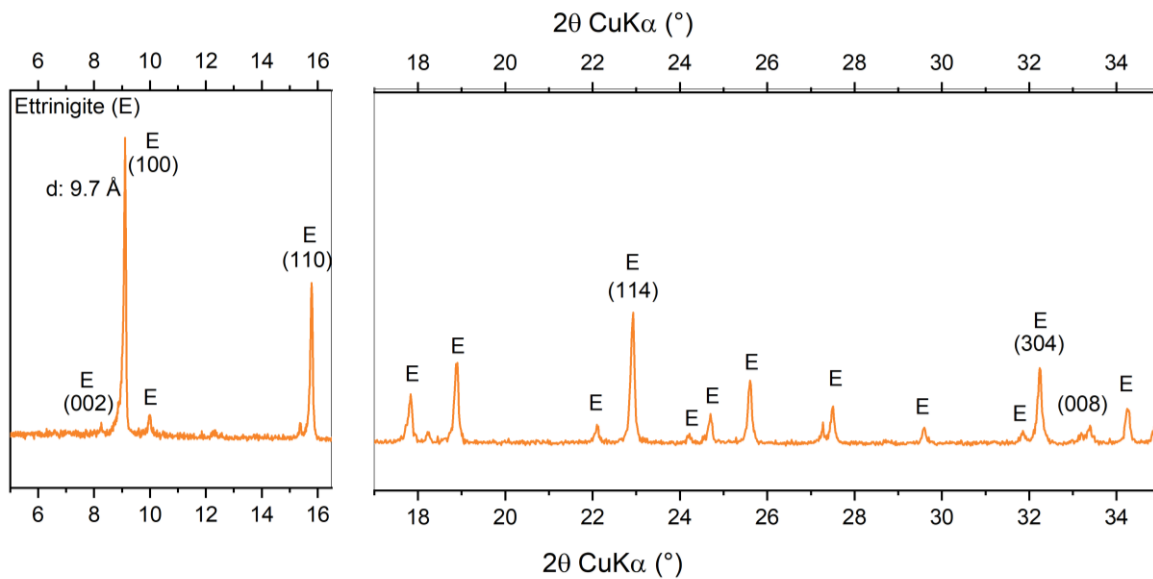
Figure 13. XRPD pattern diffraction of sulfate-AFt after 2 months of equilibration time. E: ettringite, P: portlandite.

For high wavenumbers, the FT-IR analysis (*Figure 14*) shows OH^- stretching vibrations of $Al(OH)_6^{3-}$ units at ≈ 3650 cm^{-1} [241]. The stretching vibration of H_2O with a maximum at ≈ 3390 cm^{-1} is well visible. The bending vibrations of hydroxyl groups related to Ca-OH and to the intra-channel water, are visible at 1660 cm^{-1} and 1633 cm^{-1} [241], and those of the Al-OH group at ≈ 880 cm^{-1} and 850 cm^{-1}. The sulfate group generates two symmetric stretching vibrations ν_1 and ν_3 at 1090 cm^{-1} and 989 cm^{-1} [241, 242]. The broad bands at ≈ 530 cm^{-1} and ≈ 610 cm^{-1} have been assigned by Myneni et al. [241] and Scholtzová et al. [242] to SO_4^{3-} symmetric and asymmetric bending vibrations (ν_2 and ν_4). Generally, these bands are difficult to distinguish due to the overlapping with Ca/Al-OH bending vibrations.

51
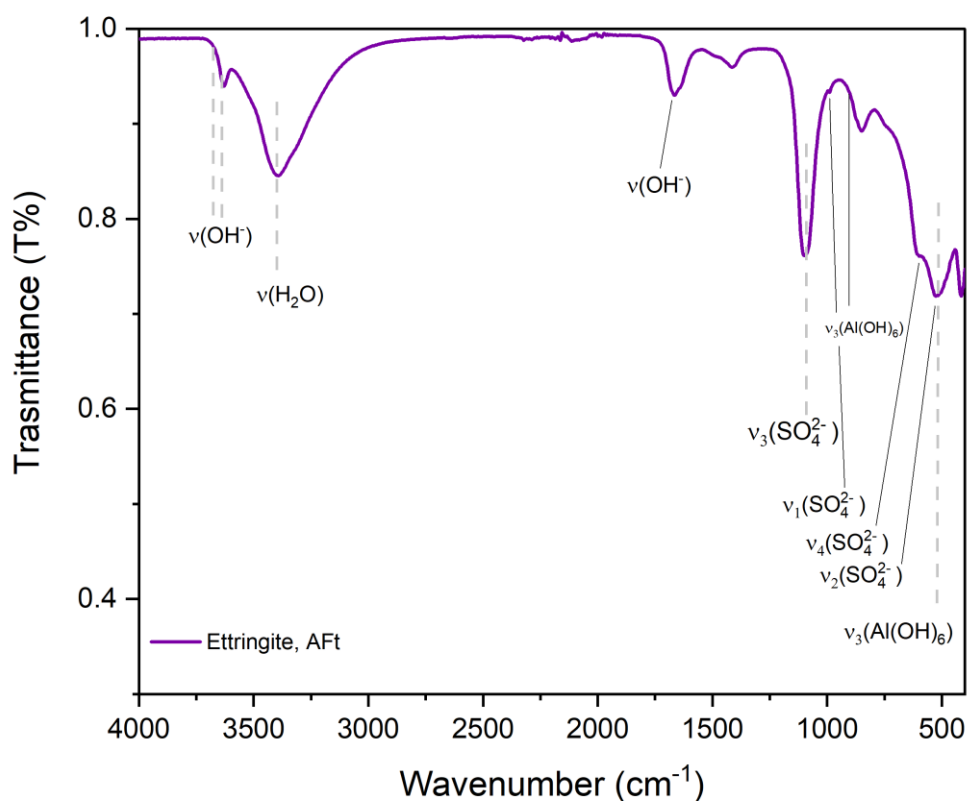
Figure 14. FT-IR spectra of the synthesized ettringite samples in the wavenumber region (3800 – 400 cm^{-1}).

3.1.1.4. L-AFm phases: FOR-AFm, CIT-AFm and GLU-AFm

In general, the structure of AFm phases (and C-S-H phases) depends on the electrical charge compensation between the positive charged main layers and the negatively charged intercalated anions. Consequently, the interlayer distance of the AFm phase is affected if organic molecules are intercalated. Furthermore, the distance between the AFm main layers depends on the size and spatial configuration of the intercalated anions and molecules and can be conventionally followed by measuring the basal distance by XRPD analysis.

The XRPD spectra of FOR-AFm, CIT-AFm and GLU-AFm are given in Figure 15. The XRPD of FOR-AFm (Figure 15a) indicates the formation of a well-crystalline layered structure with high intensity bands at 10.9º and at 21.8º 2θ corresponding to the interlayer distance (003) and (006) respectively. A d spacing of 8.1 Å was obtained in agreement with [35], who suggested the substitution of 2OH$^-$ with 2HCOO$^-$. Pöllman [35] equilibrated tetracalcium aluminate hydrate phases (C$_4$AH$_{19}$) with increasing formate concentration, and described for formate molar fraction higher than 0.6 mol.% a phase with the general formula $3CaO·Al_2O_3·Ca(HCOO)_2·11H_2O$. A main layer reflection (110) at 31.03º 2θ is characteristic for AFm-phases with trigonal geometry [30] as e.g. Ms or Hc, while for AFm with

monoclinic structure such as Mc, this reflection is shifted towards slightly higher 2θ values. In the case of formate-AFm, this reflection occurs for $\approx 31^\circ$ 2θ values, pointing towards a trigonal geometry. In addition, traces of portlandite were detected (reflection at $\approx 18^\circ$ 2θ).

The XRPD pattern of citrate-AFm, shown in the Figure 15b, also indicates the presence of a layered structure and thus towards an AFm-phase with a high intensity reflection at 7.2° 2θ ($d_{(003)} = 12.3$ Å), which is in agreement with the values reported by [35] for tetracalcium aluminate hydrate phases (C_4AH_{19}) equilibrated with increasing citrate concentrations ($0 \leq x_{mol,citrate} \leq 0.66$). The reflections at $\approx$ 14.5° 2θ (6.1 Å) related to the basal spacing (006) and the overlapped reflection at $\approx 23^\circ$ 2θ ($d_{spacing} = 4.0$ Å), which is likely correlated to the (009) reflection, are less intense. These broad reflection shapes indicate an only poorly ordered citrate-AFm structure as previously reported by [35]. In the case of citrate-AFm the characteristic (110) main layer reflection for AFm phases, is overlapped by the reflections of katoite ($Ca_3Al_2(OH)_{12}$). The presence of katoite indicates a rather low stability of citrate AFm and the detection of traces of tricalcium aluminate ($Ca_3Al_2O_6$) indicate the incomplete conversion of initial reagents used for the synthesis. In addition, some ill-ordered $Ca_3(Cit)_2(H_2O)_4$ (main reflections at 11° and 22° 2θ) was observed as also reported by [35].

The XRPD of gluconate-AFm, shown in the Figure 15c, again indicates the formation of layered phase structure with a main basal spacing at 8.6° 2θ, which correspond to an interlayer distance of 10.9 Å. The reflection (006) expected for $\approx 17^\circ$ 2θ ($d_{spacing} = 5.1$ Å), is again overlapped by the reflection of katoite. The typical (110) reflection is visible for $\approx 32^\circ$ angles. The presence of katoite indicates a low stability of gluconate AFm phase, while the detection of C_3A indicates that initial reagents used for the synthesis were not fully converted in the final product. In addition, traces of $Ca(C_6O_7H_{11})_2 \cdot H_2O$ were also observed.

In the case of formate-AFm phase, the interplanar distance of 8.1 Å is comparable to those observed for the reference AFm phases, Ms: 8.9 Å, Hc: 8.3 Å and Mc: 7.9 Å, such that no increase of the basal spacing is observed if formate is present in the interlayer due to the small dimension of the formate group, as also reported by [35]. However, an increase of the interlayer distance can be expected due to the larger size of citrate and gluconate, if compared to carbonate or sulphate ions, as previously observed for different organic containing AFm phases [243-246]. A comparable d-spacing (12.1 Å) and disordered structure in the stacking direction has been reported for citrate intercalated Ca-Al based LDH (AFm) phases [243] as well as for citrate containing Mg/Al layered double hydroxide (LDH) phases, which have similar to AFm phases a positively charged main layer and an interlayer containing anions and water, where basal spacing of d = 11.8 Å to 12.2 Å [243, 247, 248] were reported. In terms of spatial configuration, Zhang et al. [248] and [243] postulated a perpendicular orientation of citrate molecules in Mg-LDH resulting in "pillared" LDH. Although the linkage of two main layers by the terminal carboxylate groups in citrate is a possible coordination mode, also a 5-bond ring structure formed by coordination of a carboxylate and the deprotonated α-hydroxyl group with calcium could be possible as

observed by [249] for citrate sorbed on calcite. The potential role of the interaction of calcium-carboxylic groups of polycarboxylates with AFm phases has also been discussed by [250].
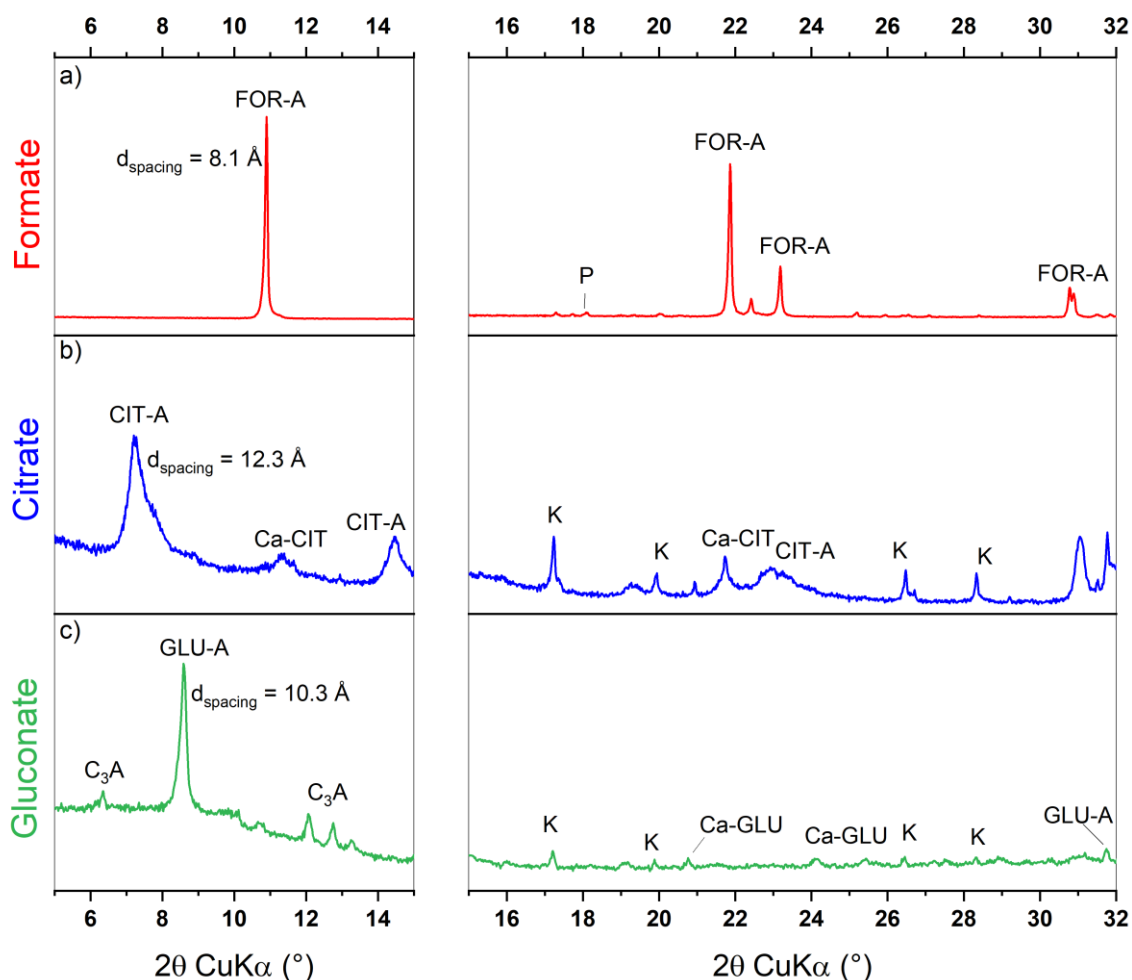
Figure 15. XRPD pattern diffraction of synthesized formate-AFm (a), citrate-AFm (b) and gluconate-AFm (c) after 2 months of equilibration time. C_3A: $Ca_3Al_2O_4$; Ca-CIT: calcium citrate ($Ca_3(C_6O_5H_7)_2 \cdot 4H_2O$); Ca-GLU: calcium gluconate hydrate ($Ca(C_6O_7H_{11})_2 \cdot H_2O$); CIT-A: citrate-AFm; FOR-A: formate-AFm; GLU-A: gluconate-AFm; K: katoite ($Ca_3Al_2(OH)_{12}$); P: portlandite ($Ca(OH)_2$).

The total concentrations measured for the different elements in the aqueous solution (seeTable 7) were used to calculate the ion activity products (IAP) for AFm phase (monosulfate (Ms), monocarbonate (Mc), hemicarbonate (Hc)) as well as for formate-, citrate-, and gluconate-AFm. The calculated ion activity products (IAP) of Ms, Mc and Hc are comparable to those reported in [251, 252] as indicated in Table 7. The solubility product, *log K^o_s*, of formate- and citrate-AFm is comparable to Ms and Hc, but higher than that of monocarbonate. In the case of gluconate-AFm, the solubility product is higher than those of AFm phases. Although the value of the solubility product is comparable due to the different number of anions in the dissolution equations, the solubility of citrate-AFm and gluconate-AFm is

higher than that of monosulfate and hemicarbonate, as also evidenced by the higher ion concentrations and the formation of katoite for both ligand-AFm phases.

Table 7. Measured pH (measurement error ± 0.1 pH units), Na, K, Ca, Al, sulfate, carbonate (measurement error ± 5 %) and formate, citrate and gluconate (measurement error ± 7%) content for pure AFm phases and formate-, citrate-, gluconate-AFm phase, used to calculate the ionic activity products (IAP) at 20 ºC. The solubility products of pure phases available in literature at 25 ºC are reported in italic for comparison in the second last column.

Phases observed[a]	pH	Na (K)	Ca	Al	Sulfate	Carbonate	FOR/ CIT/ GLU	IAP [b]	log K°s[c] (this study)	log K°s[c]
					[mmol/dm³]					
Ms, monosulfate: $Ca_4Al_2(SO_4)(OH)_{12} \cdot 8H_2O \rightarrow 4Ca^{2+}+2Al(OH)_4^- +SO_4^{2-}+4OH^-+8H_2O$										
Ms	13.2	220	0.30	1.9	1.0	-	-/-/-		30.21±0.15 d	*-29.26 [251]*
Mc, monocarbonate: $Ca_4Al_2(CO_3)(OH)_{12} \cdot 5H_2O \rightarrow 4Ca^{2+}+2Al(OH)^{4-} +CO_3^{2-}+4OH^-+5H_2O$										
Mc	Mc, Cc 13.4	216	0.55	0.15		0.38e	-/-/-		- 32.00±0.15 d	*-31.47 [251]*
Hc, hemicarbonate: $Ca_4Al_2(CO_3)_{0.5}(OH)_{13} \cdot 5.5H_2O \rightarrow 4Ca^{2+}+2Al(OH)^-_4+0.5CO_3^{2-}+5OH^-+5.5H_2O$										
Hc	Hc, Mc 13.2	218	1.8	0.15	0.15	0.016f	-/-/-		- 29.26±0.17 d	*-29.13 [251]*
Formate-AFm[g]: $Ca_4Al_2(CHO_2)_2(OH)_{12} \cdot 6H_2O \rightarrow 4Ca^{2+}+2Al(OH)_4^- +2(CHO_2)^-+4OH^-+6H_2O$										
FOR-A, P	13.1	262	3.4	0.25	-	-	415/-/-	-27.6		
FOR-A, P	13.1	125	6.8	0.11	-	-	219/-/-	-28.0		
Mean								-27.8±1.2 l		
Citrate-AFm[h]: $Ca_4Al_2(C_6H_5O_7)_{2/3}(OH)_{12} \cdot 6H_2O \rightarrow 4Ca^{2+}+2Al(OH)_4^- +^2/_3(C_6H_5O_7)^{3-}+4OH^-+6H_2O$										
CIT-A, K, CA, C	13.3	213	0.69	6.1	-	-	-/1.5/-	-27.94		-
CIT-A, K, CA, C	13.1	213	5.1	0.90	-	-	-/12.7/-	-27.91	-	
CIT-A, CIT-E, C	13.4	265	152	6.9	-	-	-/20.5/-	-27.86	-	
CIT-A, P	13.7	671	0.42	4.03	-	-	-/37/-	-29.98	-	
CIT-A, CH, KC	13.8	(697)i	2.81	1.08	-	-	-/49/-	-27.80	-	
Mean								-28.3±2.8 l		
Gluconate-AFm[m]: $Ca_4Al_2(C_6O_7H_{11})_2(OH)_{12} \cdot 6H_2O \rightarrow 4Ca^{2+}+2Al(OH)_4^- +2(C_6O_7H_{11})^-+4OH^-+6H_2O$										
GLU-A, CA, K, Ca-GLU, P	13.1	182	41.9	41.8	-	-	-/-/33.1	-24.50±0.4		

[a] C: $Ca_3(C_6H_5O_7)_2 \cdot 4H_2O$; CA: tricalcium aluminate; CIT-A: citrate AFm; CIT-E: citrate-AFt; Cc: calcite; FOR-A: formate AFm; GLU-A: gluconate AFm; Ms: monosulfate; Mc: monocarboate; Hc, hemicarbonate; K: katoite, KC: potassium citrate monohydrate, P: portlandite.

[b] Ion activity product calculated in this study.

[c] log K°s reported by [251] for comparison.

[d] Mean of citrate free sample and samples containing ≤ 0.02 mM citrate.

[e] Assuming saturation with respect to calcite [251].

[f] Assuming saturation with respect to monocarbonate[251].

[g] d-spacing 8.13 Å, molar volume 280 cm³/mol (trigonal structure).

[h] d-spacing 12.27 Å, molar volume 424 cm³/mol (trigonal structure).

[i] Value in the brackets correspond to the total potassium concentration is solution.

[l] Uncertainties were calculated as three times the standard deviations of the mean value (3σ).

[m] d-spacing 10.87 Å, molar volume 376 cm³/mol (trigonal structure).

3.1.1.5.   L-AFm phases: FOR-AFt, CIT-AFt and GLU-AFt

The XRPD spectra of FOR-AFt, CIT-AFt and GLU-AFt are shown in the Figure 17. The XRPD of FOR-AFt (Figure 17a) is characterized by the same spectral peaks found for formate-AFm shown in the Figure 16 indicating that formate-AFt was not stable.

The XRPD spectrum of citrate-ettringite is characterized by two main reflections between 7º to 9º 2θ (d_{CIT-A} = 12.3 Å, d_{CIT-E} = 10.2 Å) indicating the presence of two phases. The broad reflections are associated with citrate-AFm with a basal spacing of 12.3 Å as shown in Figure 17. The reflections of citrate-AFt are much narrower with a main (100) signal at 10.2 Å, and a very small (002) reflection again at 10.7 Å in c-direction. The substitution of sulfate by citrate is expected to increase the distance

along the a-axis (x00, perpendicular to the columns) as in fact observed for citrate-AFt (Figure 17). In addition, unreacted C_3A (due to the possible retardation of dissolution by citrate) as well as of traces of calcium citrate were observed. The XRPD spectra of gluconate-AFt, shown in the Figure 17c, indicate the formation of mostly amorphous phases and precipitation of calcite. In this case, it is not possible to discuss the crystal geometry of gluconate-AFt phase, since a well-defined structure is not visible from XRPD analysis. In addition, no traces of the so-called M-phases, $(Ca_6(Al(OH)_6)_2(HCOO)_6)$, whose structure was recently studied by [253], were identified in the obtained XRPD spectrum.
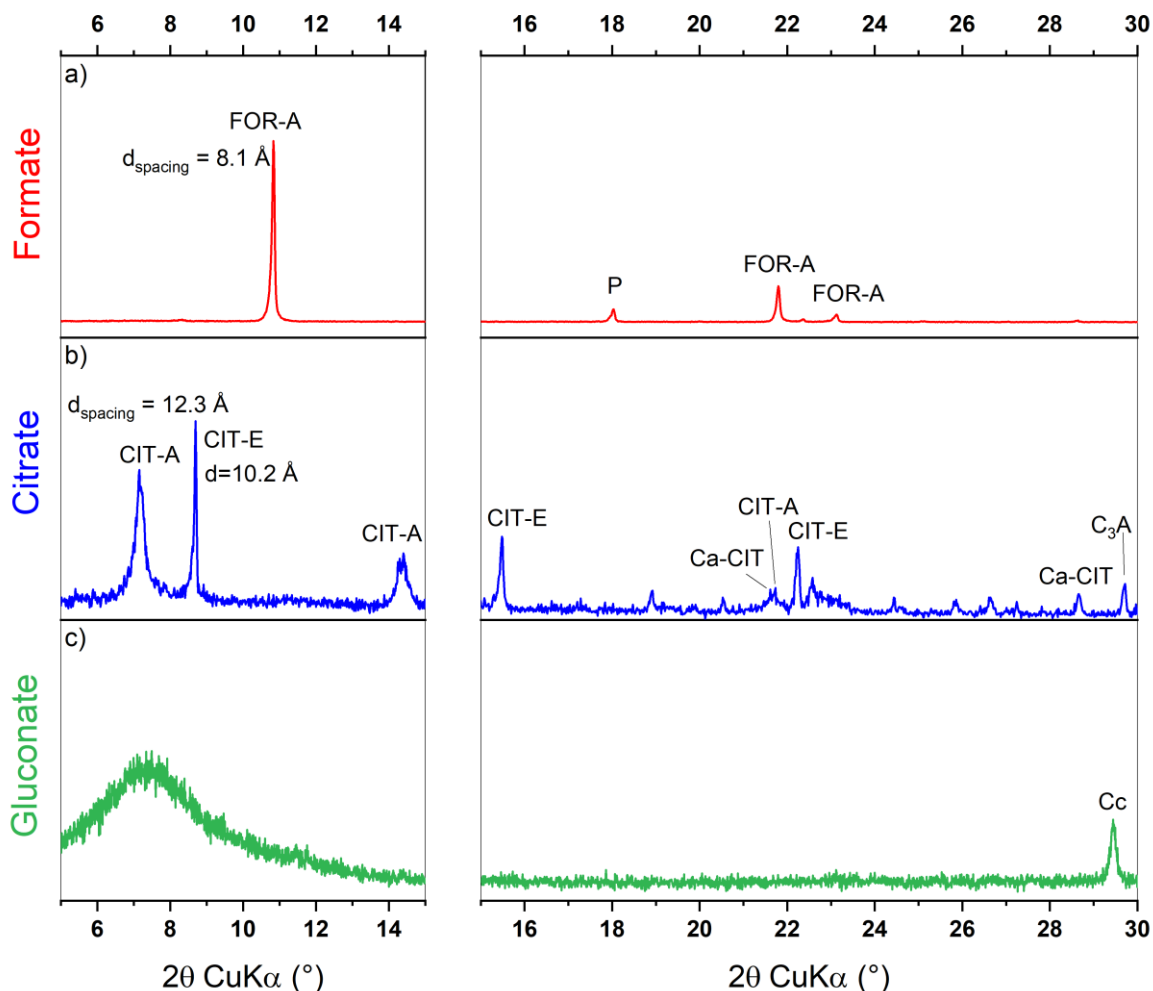
Figure 17. XRPD pattern diffraction of synthesized formate-AFt (a), citrate-AFt (b) and gluconate-AFt (c) after 2 months of equilibration time. C_3A: $Ca_3Al_2O_4$, Ca-CIT: calcium citrate $(Ca_3(C_6O_5H_7)_2 \cdot 4H_2O)$; Cc: calcite $(CaCO_3)$; CIT-E: citrate-AFt; FOR-A: formate-AFm; P: portlandite $(Ca(OH)_2)$.

The concentration of the aqueous solution in equilibrium with ettringite, formate-AFt, citrate-AFt and gluconate-AFt (see Table 8) were used to calculate the ion activity products (IAP) for sulfate-ettringite and formate-, citrate-, gluconate- AFt. The IAP of citrate-AFt is slightly higher than the solubility product of pure ettringite [252], which indicates a lower stability of citrate- AFt than that of ettringite due to lower number of anions in the dissolution equations. This is also evidenced by the higher ion concentrations and the formation of additional solids in the presence of citrate-AFt.

Table 8. Measured pH (measurement error ± 0.1 pH units), Na, K, Ca, Al, sulfate (measurement error ± 5 %) and formate, citrate and gluconate (measurement error ± 7%) content for pure ettringite and formate-, citrate- and gluconate-AFt, used to calculate the ionic activity products (IAP) at 20°C. The solubility products of pure phases available in literature at 25°C are reported for comparison.

Phases observed[a]	pH	Na (K)	Ca	Al	Sulfate	FOR/CIT/GLU	IAP[b] (this study)	log$_{10}$ K°$_S$[c]
				[mmol/dm^3]				
AFt, ettringite: $Ca_6Al_2(SO_4)_3(OH)_{12} \cdot 26H_2O \rightarrow 6Ca^{2+}+2Al(OH)_4^- +3SO_4^{2-}+4OH^- +26H_2O$								
E	13.1	205	0.09	6.87	11.61	-	-45.42±0.30[d]	-44.9 [251, 252]
Formate-AFt: $Ca_6Al_2(CHO_2)_6(OH)_{12} \cdot 26H_2O \rightarrow 6Ca^{2+}+2Al(OH)_4^- +6(CHO_2^-) +4OH^- +30H_2O$								
FOR-A, P	12.8	249	10.9	0.044	-	182/-/-	-89±25[f]	this study
Citrate-AFt[e]: $Ca_6Al_2(C_6H_5O_7)_2(OH)_{12} \cdot 26H_2O \rightarrow 6Ca^{2+}+2Al(OH)_4^- +2(C_6H_5O_7)^{3-}+4OH^- +30H_2O$								
CIT-A, CIT-E, C	13.4	265	152.3	6.9	-	-/20.5/-	-41.1±2.8[f]	this study
Gluconate-AFt: $Ca_6Al_2(C_6H_{11}O_7)_6(OH)_{12} \cdot 26H_2O \rightarrow 6Ca^{2+}+2Al(OH)_4^- +6(C_6H_{11}O_7)^-+4OH^- +30H_2O$								
GLU-E(?), Cc	12.6	173	18.0	12.8	-	-/-/107	-38.9±3.5[f]	this study

[a] C: $Ca_3(C_6H_5O_7)_2 \cdot 4H_2O$; Cc: calcite; CIT-A: citrate-AFm; CIT-E: citrate-AFt; E: ettringite, FOR-E: formate-AFt; GLU-E: gluconate-AFt, P: portlandite.

[b] Ion activity product calculated in this study.

[c] log K°$_S$ reported in literature at 25°C for comparison.

[d] Mean of citrate free sample and samples containing ≤ 0.02 mM citrate.

[e] (100) unit-cell dimension 10.16 Å, molar volume 775 cm^3/mol (hexagonal structure).

[f] Error for formate, citrate, and gluconate AFt calculated assuming an analytical error of 5% in the measured concentrations.

3.1.2. Formate uptake by C-S-H, AFm phases, ettringite and PC

3.1.2.1.   Kinetic experiments: uptake of formate

3.1.2.1.1.   C-S-H phases

The kinetics of the sorption reaction was investigated for equilibration times ranging from 1 to 14 days. Formate was added to a C-S-H suspension synthesized as described in the chapter 2 with a total concentration of 221 mM. The samples were then further equilibrated under continuous shaking until separation and characterization. The presence of formate lowered the pH values for all phases at 1 day of contacting time (Figure 18). While the pH value remained constant for C-S-H 1.2 and 1.4, the pH further decreased by ca. 0.2 pH units in the case of C-S-H 0.8 and for t > 7 days. The lower pH in the presence of formate destabilized the portlandite originally present in the C-S-H phases at C/S > 1.0 (see section 3.1.1.1). The XRPD spectra (Figure 4 in the Appendix 3.1) reported in the Appendix 3.1, confirms that the portlandite is destabilized within 1 day after the formate was added. For C/S = 1.2 the presence of a small amount of Ca-formate, $Ca(HCO_2)_2(s)$, is observed (Figure 4 in the Appendix 3.1). The aqueous concentration of formate shown in the Figure 18 is lower than the initial total concentration for all C/S ratio indicating some uptake of formate in the solid. The formate uptake is comparable at low and high C/S although the pH values are considerably lower in the presence of low C/S C-S-H. The pH decrease compared to the target pH value (pH ≈ 13.3), lowers the negative surface charge of C-S-H [254] and increases the calcium concentrations in solution, which would be expected to facilitate the uptake of anions such as formate by C-S-H phases. In general, the formate concentration presents a similar kinetic trend for all C-S-H phases within the experimental concentration error, which is likely to the unspecific uptake process due to the weak sorbent-sorbate interactions (e.g. Van der Walls bond).

Figure 18. (a) pH values (measurement error ± 0.1 pH units) and (b) formate aqueous concentrations (measurement error ± 5 %) in the presence of C-S-H phases (Ca/Si = 0.8 – 1.4) measured at different equilibration times (t = 1 – 14 days) in the presence of initial [FOR]$_{tot}$ = 221 mM and [Na]$_{tot}$ = 0.2 M as discussed in the chapter 2. Empty crossed symbols indicate the pH values in the absence of formate.

3.1.2.1.2.   AFm phases and ettringite

The kinetic of formate uptake on AFm phases and ettringite was investigated in the time interval of $1 \leq$ t(days) ≤ 14 (Figure 19). Formate was added to the pre-synthesized Ms, Mc, Hc and AFt phases to obtain a total concentration of 221 mM formate. For all kinetic experiments a constant total concentration of Na was used, in order to reproduce the alkaline conditions relevant for the Stage I of cement degradation (pH ≈ 13.3). Again, the addition of 221 mM formate strongly lowered the pH of ettringite from initially ≈ 13.1 by ca. 4 pH units and by ≈ 2 pH units for Mc. A more moderate pH decrease of about ≈ 1 pH unit was observed for Ms and Hc (both from an initial value of ≈ 13.2). In general, pH values remained constant after the first day and no further changes were observed for longer equilibration times (14 days). The pH decrease is due to the presence of high formate concentrations in solution while the sodium concentration was kept constant and equal to 0.2 M in all cases. The formate uptake slightly increased during the first days, but remained (within the measurement error) rather constant afterwards.

In parallel to the pH values and formate concentration, an increase (with a maximum detected at 7 days) of aluminium concentration was observed for all phases with the exception of Hc, while the variations in the sodium, calcium and sulphate concentrations in the case of Ms and AFt (see Table 9,13 and 15 in the Appendix 3.1) were minor. Together these data indicate that a steady state sorption was reached within 7 days and little variations occurred between 4 to 14 days. Thus, all further sorption experiments were carried out using an equilibration time of 7 days. In all cases, no additional solids formed due to the addition of citrate (see XRPD data in Figures 6-9 in the Appendix 3.1).

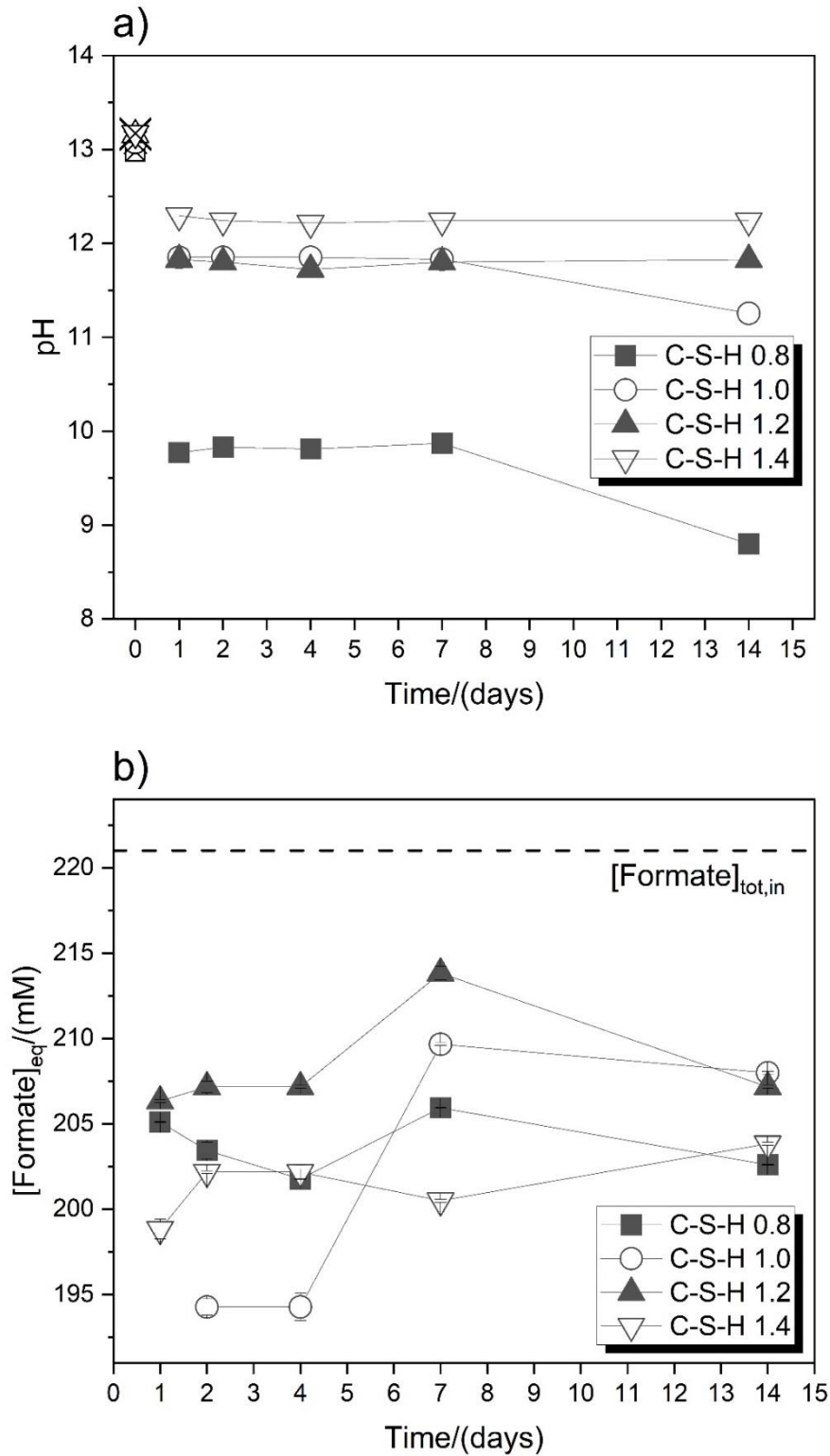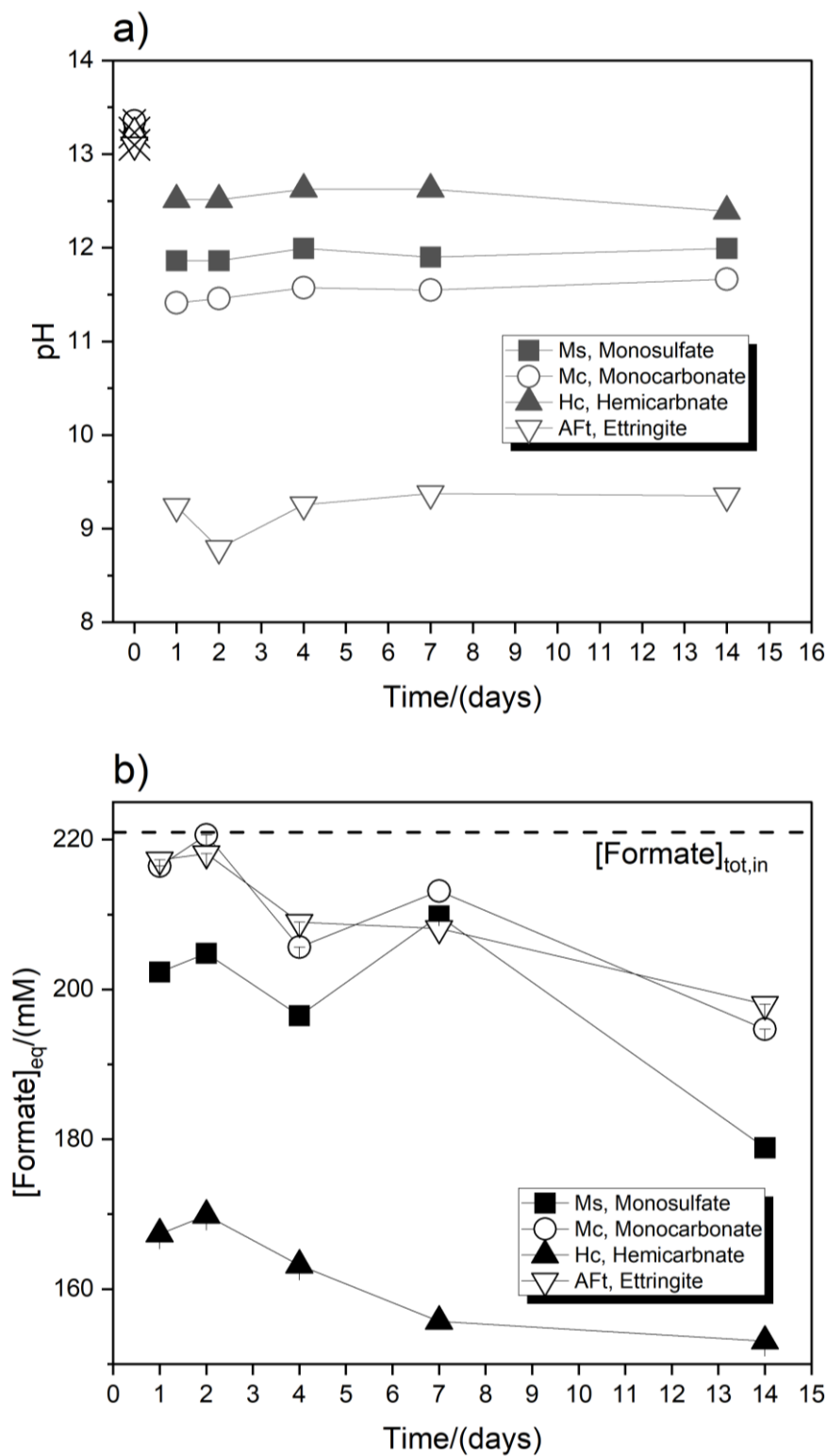*Figure 19. (a) pH values (measurement error ±0.1 pH units) and (b) formate aqueous concentration (measurement error ± 5 %) in the presence of AFm phases (Ms. Mc, and Hc) and AFt measured at different equilibration time (t = 1 – 14 days) in the presence of initial [FOR]$_{tot}$ = 221 mM and [Na]$_{tot}$ = 0.2 M. Empty crossed symbols indicate the pH values in the absence of formate.*

3.1.2.2. Sorption experiments: uptake of formate

3.1.2.2.1. C-S-H phases

Figure 20 compares the XRPD pattern of C-S-H in the presence of 221 mM of formate with C-S-H samples without formate. In the absence of formate, the interplanar distance decreases with the increase of C/S as previously reported, e.g. in [255]. In the presence of formate a broadening of the basal signal is observed, indicating a decrease in the degree of ordering and/or a decrease in the number of layers stacked in c-direction [231, 256]. A slight shift of the main basal spacing towards lower 2θ values (increase of d-spacing) of about 0.10 $2\theta^o$ units was observed for C-S-H 0.8 and C-S-H 1.4 and of 0.3 $2\theta^o$ units ($d_{(002)} = 11.9$ Å, $d_{(002), [FOR] = 0.200 M} = 12.2$ Å) for C-S-H 1.0. Such increase of d-spacing in the presence of formate may be due to the decrease in number of stacked layers (indicating by the broadened signal of the basal spacing [231, 256].

The presence of formate has also clearly an effect of the sodium and calcium uptake for low C/S ratio. Quantitative calculations of the C-S-H composition in presence of formate (Figure 10, Appendix 3.1), indicate a small decrease of the C/S for formate concentrations higher than 100 mM, due to the formation and precipitation of Ca-formate (Figure 20). The amount of portlandite originally present in C-S-H 1.2 and 1.4 is destabilized in the presence of 221 mM of formate, which led to the precipitation of calcium formate as also found in the kinetic sorption experiments (see Figure 4, Appendix 3.1). In addition, the sodium concentration increases at higher formate concentrations and lower pH values, which indicates less uptake of sodium by C-S-H. This decrease of Na uptake at high formate concentrations is related to the increase of Ca concentrations, which lowers alkali uptake on C-S-H, as Na and Ca compete for the same cation exchange sites on C-S-H [15, 257].
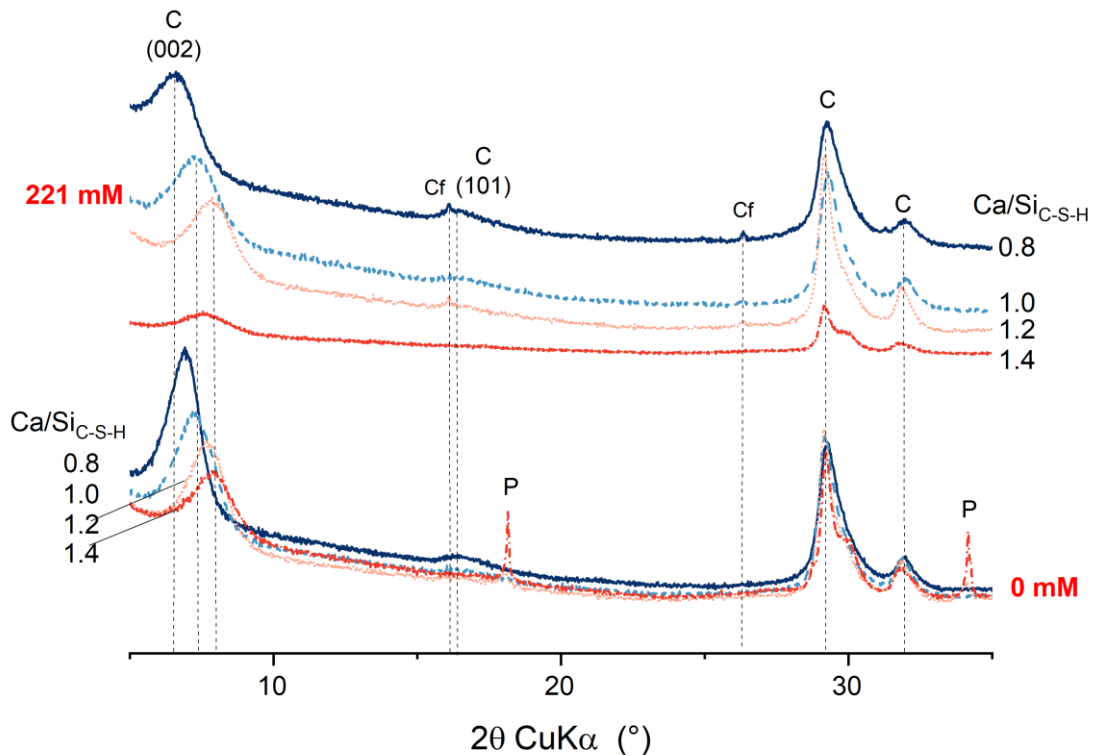
Figure 20. XRPD characterization of C-S-H phases (C/S = 0.8 – 1.4) in the presence 221 mM and in the absence of formate after 7 days of contacting time. C: C-S-H, Cf: calcium formate, Ca(HCO$_2$)$_2$, P: portlandite.

Figure 21 shows the FT-IR spectra of C-S-H phases with a C/S = 0.8-1.4 equilibrated with a 221 mM of formate concentration. The band at ≈ 950 cm^{-1} shifts towards lower wavenumbers with the increase of the C/S ratio, as also observed in the absence of formate, see Figure 9. Especially for low C/S ratio, the presence of formate results in higher wavenumbers (e.g. 962 cm^{-1} instead of 950 cm^{-1} for C/S = 0.8 in the absence of formate), which could indicate a further polymerization of C-S-H in the presence of formate. Furthermore, the intensity of the Q^1 band is weaker in the presence of formate than in its absence, again indicating less Ca in C-S-H, due to the formation of solid Ca-formate as well as due to the increased Ca-concentration in solution. In addition, the carbonate bands visible in the wavenumber region 1550 and at 1400 cm^{-1} indicate the presence of formate in C-S-H phases.
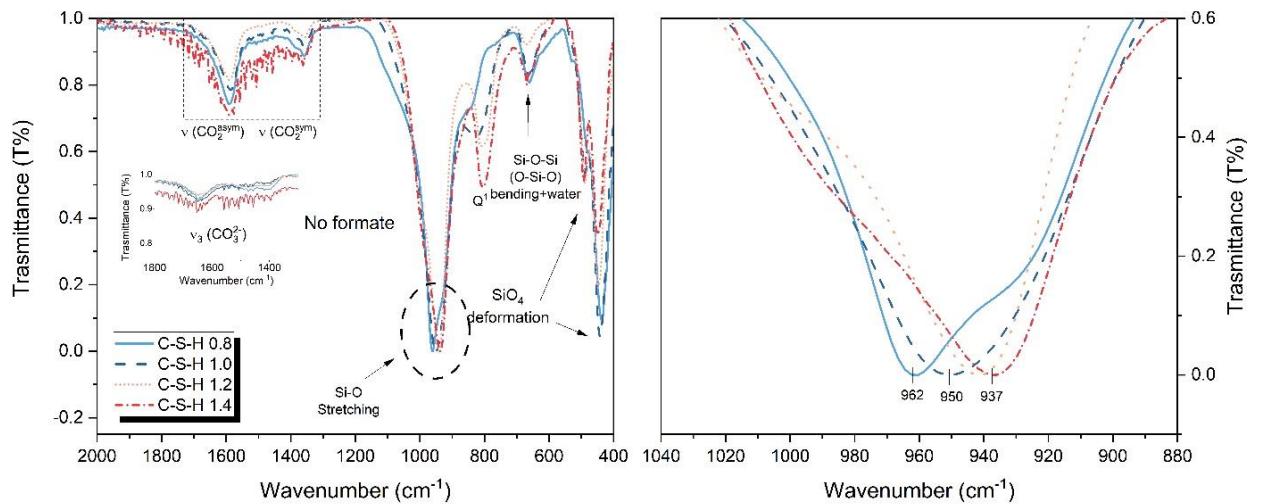
Figure 21. FT-IR characterization of C-S-H phases (Ca/Si=0.8–1.4) equilibrated with 221 mM of formate concentration for 7 days of contacting time, in the wavenumber region 2000 – 400 cm⁻¹.

Figure 22 shows the total Ca concentration in solution and the pH values as a function of the equilibrium formate concentration. The Ca concentration (Figure 22a) is roughly constant for the formate concentration range 10^{-1} mM ≤ $[FOR]_{eq,sol}$ ≤ 40 mM and increases for higher formate concentration for all C-S-H phases, where also the pH decreased considerably. For $[FOR]_{eq,sol}$ ≥ 100 mM, the calcium concentrations increase and Si concentrations decrease due to the decrease of pH value, in agreement with the trends reported in literature, where lower pH result in more Ca and less Si in solution as well as in a decalcification of C-S-H [230, 258, 259]. This is in agreement with the decreasing amount of Q^1 sites observed in the FT-IR analysis. The pH decreases with increasing addition of formate as shown in the Figure 22b. The decrease is pronounced for a formate concentration higher than 100 mM, and for low C/S the effect is higher. As observed in the kinetic experiments, the decrease of pH is due the high concentration of formate in solution. The minor pH decrease observed for C/S > 1.0 compared to C-S-H 0.8 is due to the presence of portlandite (see Figure 20) which buffers the pH to higher values for formate concentration higher than 100 mM.
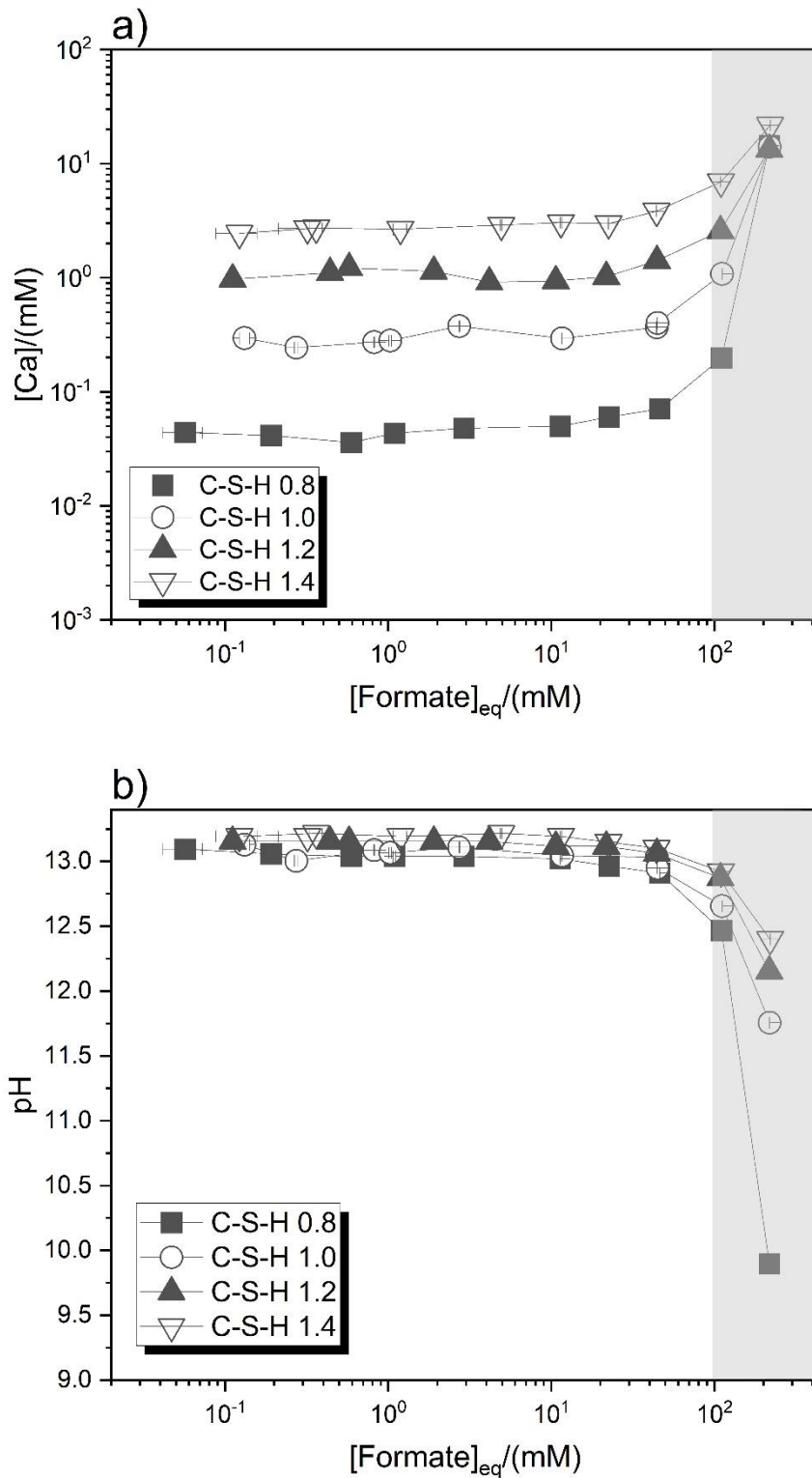
Figure 22. (a) [Ca] aqueous concentration and (b) pH values for C-S-H phases (Ca/Si=0.8 – 1.4) as function of formate concentration in solution measured after 7 days of contacting time. Shaded grey areas indicate the regions where Ca-formate formation is probable based on SI calculation and XRPD characterization.

Figure 23 shows the sorption isotherms calculated for the uptake of formate on C-S-H phases expressed as moles of formate sorbed per kg of C-S-H phases. The C-S-H weight is calculated by combined mass balance calculation and water content obtained from TGA analysis (see Table 25, Appendix 3.1).

For formate concentrations $[FOR]_{eq,sol} < \sim 10^{-3}$ M, the uptake occurs on all C-S-H phases and increases linearly with the increase of formate concentration, independent on the Ca/Si ratio of the C-S-H, in contrast to the observation for citrate and gluconate discussed in section 3.1.3.2.1 and 3.1.4.2.1. This indicates that the formation of Ca-formate complexes plays a minor role in formate sorption, in agreement with the weak aqueous Ca-formate complexes described in literature [79, 218-220]. For $[FOR]_{eq,sol} > \sim 10^{-3}$ M, the uptake of formate on C-S-H phases deviates from the linear formate uptake trend observed on PC. Such uptake decrease may hint towards to saturation of sorption sites on the surface of C-S-H phases particle.
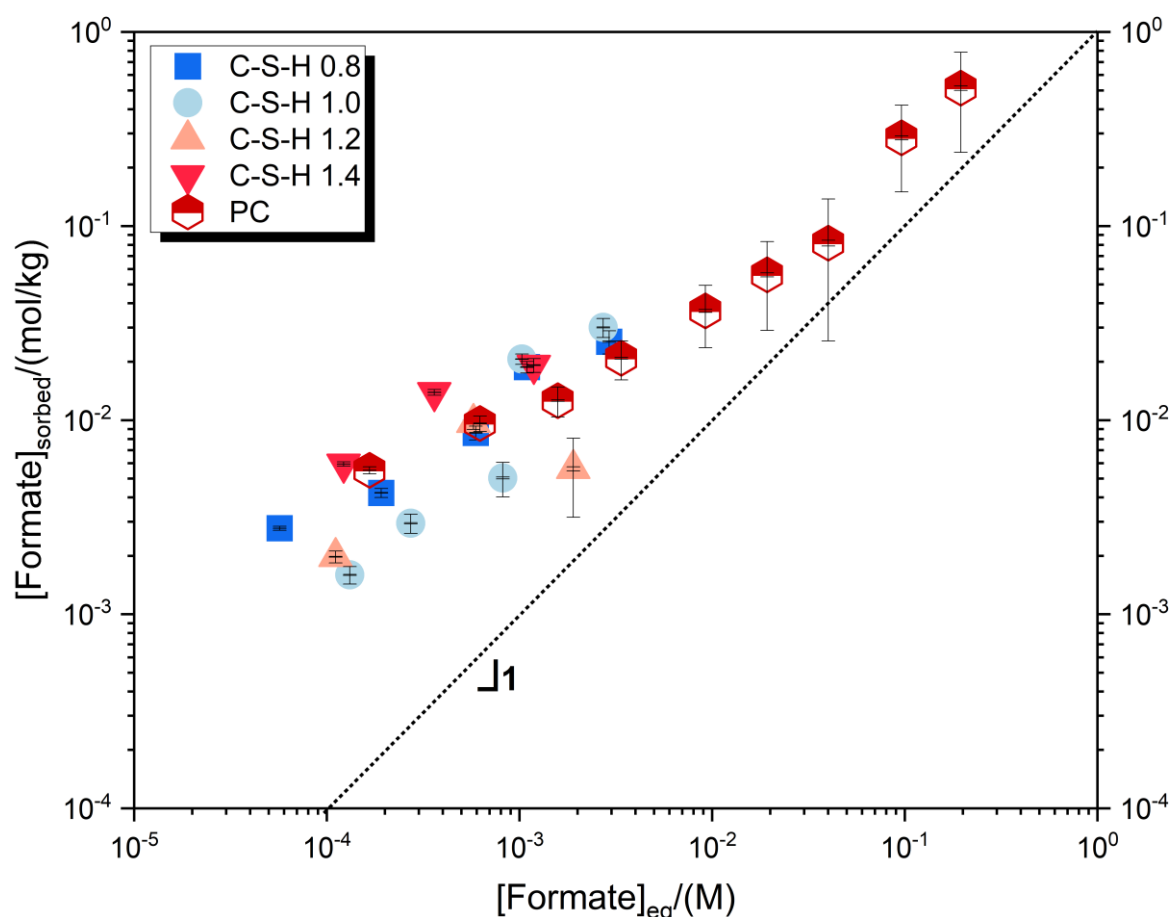
Figure 23. Sorption isotherms calculated as moles of formate sorbed per kg of solid phase, for C-S-H phases with a ratio of 0.8 ≤ C/S ≤ 1.4 and Portland cement (PC), after 7 days of contacting time the formate adding.

For an equilibrium formate solution concentration lower than 2 mM, a distribution coefficient R_d values of (25.6 ± 15.7) dm³·kg⁻¹, (12.3 ± 5.6) dm³·kg⁻¹, (12.5 ± 8.3) dm³·kg⁻¹ and (34.4 ± 16.6) dm³·kg⁻¹ for C/S of 0.8, 1.0, 1.2 and 1.4 respectively were determined, which is considerably lower than the R_d values of

190 and 102 dm^3·kg^{-1} determined by Wieland et al. [3] for low and high Ca C-S-H, respectively. The lower uptake observed in the present study is probably related to the higher pH values present in our experiments (pH > 13), which increases the negative charge on C-S-H [255] and thus decreases anion sorption, compared to the experiments of Wieland et al. (pH 10.5 to 12.5), where no additional NaOH had been added.

The uptake of formate on hydrated Portland cement paste increases linearly with the increase of formate concentration and for a formate equilibrium concentration below $\approx 10^{-3}$ M, the same linear trend is comparable with the sorbed formate concentration obtained for the C-S-H phases. Further details about the composition and quantitative analysis of PC used in this study are reported in the Appendix 3.1 (Table 100). The R_d of (8.6 ± 10.1) dm^3·kg^{-1} observed here on hydrated cement paste (pH $\approx$ 13.3), is slightly higher than the R_d values of $\approx$ 1 dm^3·kg^{-1} determined by Wieland et al. [3] for hydrated cement pastes at a pH of 12.9. The slightly lower R_d value observed for longer equilibration times by Wieland et al. might be related to the higher S/L ratio used (i.e. 333 g/dm^3) compared to the S/L ratio of 50 g/dm^3 used in this study.

3.1.2.2.2. AFm phases and ettringite

Formate affects the chemical composition and the structure of Hc. Figure 24 shows the shift of the position of the main basal spacing of Hc in presence of formate. The increase of formate concentration results in a shift of the main basal spacing towards lower 2θ° values (higher d-values). Both interlayer distances of hemicarbonate (Hc) and carbonated hemicarbonate (cHc, $C_4Ac_{0.8}H_{10.2}$ [238] increase clearly with the formate concentration (Figure 24). For formate concentrations equal or higher than 100 mM, only the reflections of cHc is present, but shifted towards lower 2θ° values, while the signal of Mc is no longer visible. The decrease of the intensity of the main basal reflection with the increased formate concentration may indicate a decrease in ordering in c-direction and/or a more variable interlayer distance. Note that the main layer signal at $\approx$ 31° 2θ related to the 110 plane did not broaden or decrease in intensity.

The XRPD characterization carried out on Ms, Mc and ettringite showed little effect of formate (see Figure 12-14 in the Appendix 3.1). Ms shows a peak broadening in the presence of formate, which could indicate the decrease of number of stacked layers in c-direction, which also would result in a small shift of the observed (003) signal to slightly higher 2θ° values [231, 256] for very high formate concentration (221 mM). This could indicate that some formate could be bound to the (outer) surface of Ms. In contrast, the basal spacing of Mc does not exhibit a clear effect in the presence of formate and no broadening is observed. These findings are in agreement with the observation previously described in the kinetic experiments section, where a broadening of the basal reflection was observed for Hc, but not for Mc, which is also in agreement with observations of Nedyalkova and co-workers [202]. The authors

observed that the anion exchange reaction occur preferentially on AFm phases with a trigonal structure such as Hc and Ms, but not on Mc, with its rigid triclinic structure and narrow basal spacing.

Despite the different structure, AFt exhibits a slight increase of the distance (100) in presence of formate. In particular, for a formate initial concentration higher than 10 mM, the signal initially at 9.1° 2θ (d = 9.7 Å) in absence of formate, shifted towards lower angles by reaching $d_{(100)}$ = 9.8 Å.
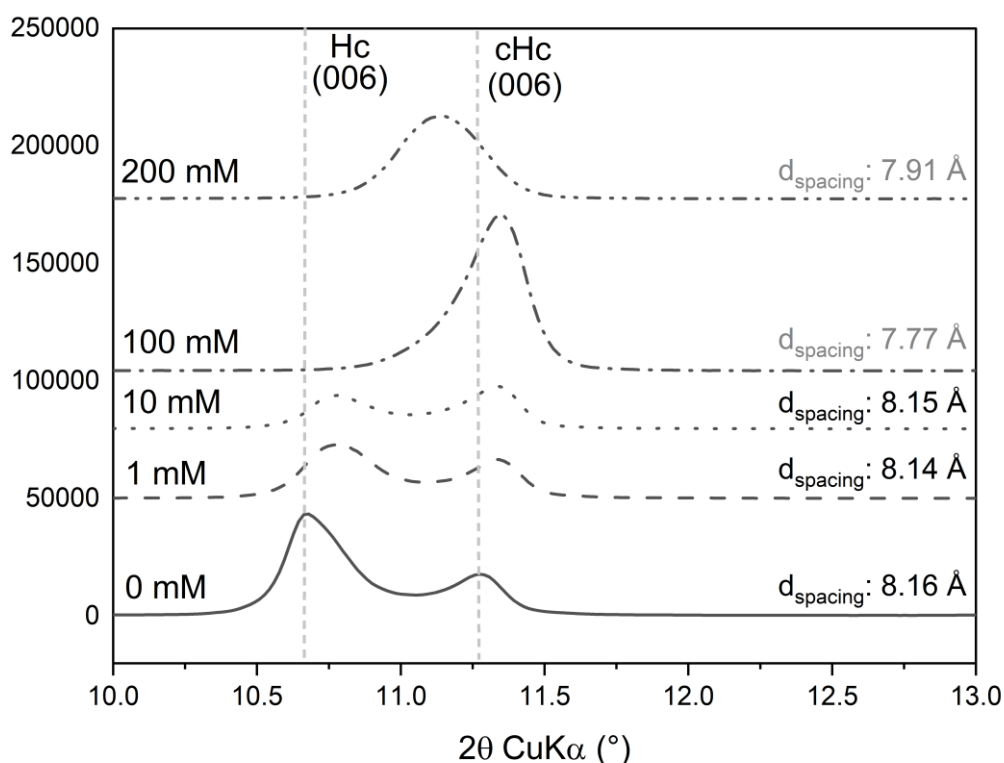
Figure 24. XRPD patterns of hemicarbonate after sorption of formate and for contacting time t = 7 days. The figure describes the shift of basal spacing of Hc (hemicarbonate) in presence of formate. cHc indicates carbonated hemicarbonate.

In general, the uptake of formate is clearly visible for Hc in the FT-IR spectra, in the wavenumber region 2000-1000 cm^{-1} as reported in Figure 25, while the uptake seems lower on Ms (Figure 26) and very low for Mc (Figure 15 in the Appendix 3.1). In the case of Hc (Figure 25), the stretching vibrations bands of the carboxylate group (C=O) increase with the increase of formate concentration, while the carbonate stretching band does not show a significant effect in presence of formate. Also, in the case of Mc, no significant effect on the intensity of the bending vibrations of CO_3^{2-} (1450 – 1400 cm^{-1}, see Figure 15 in the Appendix 3.1) and only a very minor increase of the signal associated with the carboxylate group (C=O) was observed. In the case of Ms, the intensity of the vibration band of the sulfate group decreased, and for formate concentration of 221 mM the presence of the carboxylate group of formate is clearly observed. In the case of ettringite (see Figure 16 in the Appendix 3.1), the stretching vibrations of the formate carboxylate group overlap with the bending vibrations of Ca=OH$_2$ (1660 cm^{-1}) [241], and

similarly to Ms, a small shoulder to the Ca=OH$_2$ signal appears at high formate concentration. The intensity of the sulfate stretching vibration at ≈ 1100 cm^{-1} decreases for formate concentration lower than 1 mM.
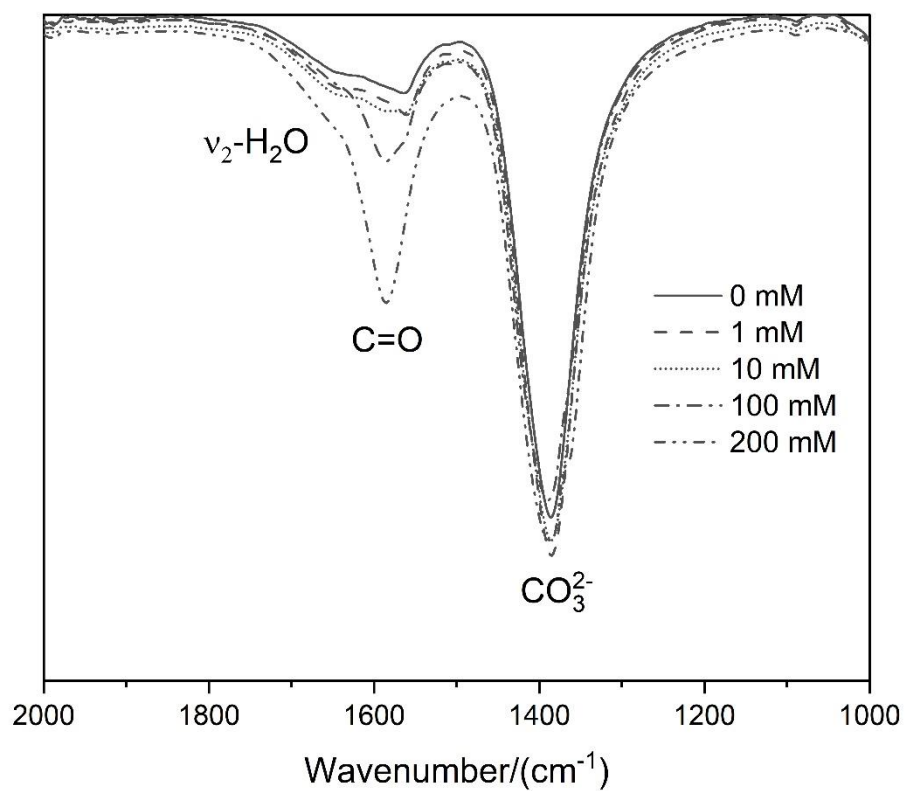
Figure 25. Effect of the initial formate concentration on the FT-IR spectra Hc, hemicarbonate at 7 days of contacting time after the formate adding.
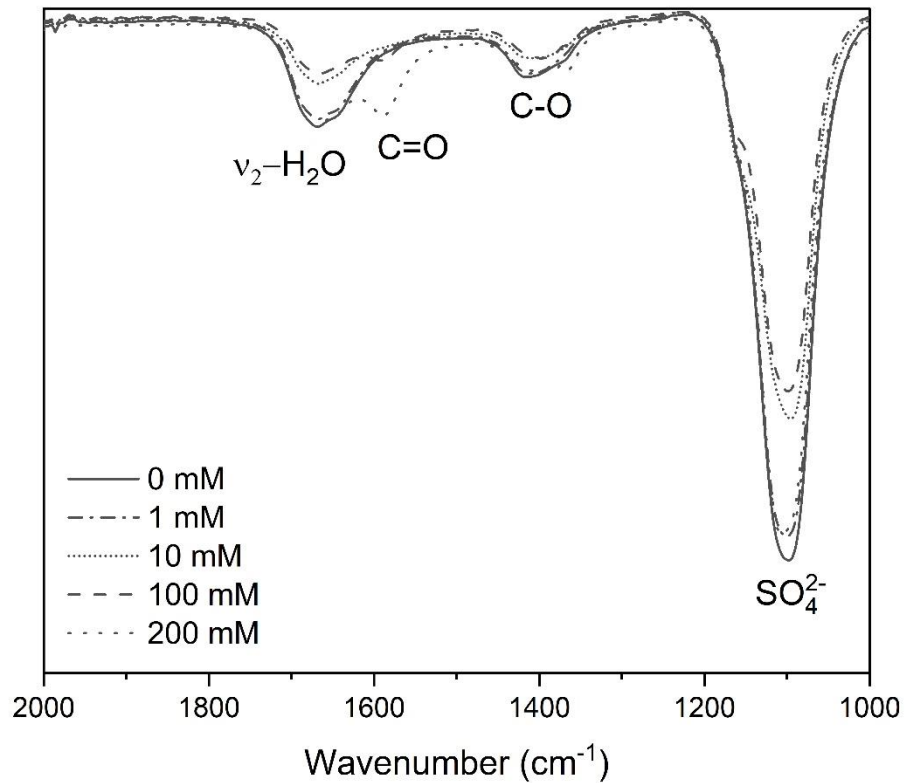
Figure 26. Effect of the initial formate concentration on the FT-IR spectra Ms, monosulfate at 7 days of contacting time after the formate adding.

Figure 27 shows the evolution of Ca and sulfate in solution and activity of protons (pH) as a function of the formate concentration. In general, at formate concentrations below 100 mM, both calcium and sulfate concentrations and pH values remain constant, indicating a very low replacement of sulfate by formate. Higher formate concentrations result in a decrease of pH, which results also in increased Ca-concentrations. For formate concentrations higher than 100 mM, also sulfate concentrations of AFt increase. The pH values are lowered slightly for Hc and Ms and by 1 pH unit for Mc and 4 pH units for AFt. Although a low Ca concentration is visible in the experiment with ettringite at low formate concentrations, the Ca concentrations increase steeply and reached higher calcium concentrations at high formate concentrations as compared to the respective experiment with AFm phases. Reversely, the sulfate concentration trend of AFt, in the case of Ms the sulfate concentration decreases by one order of magnitude at the highest formate concentrations.
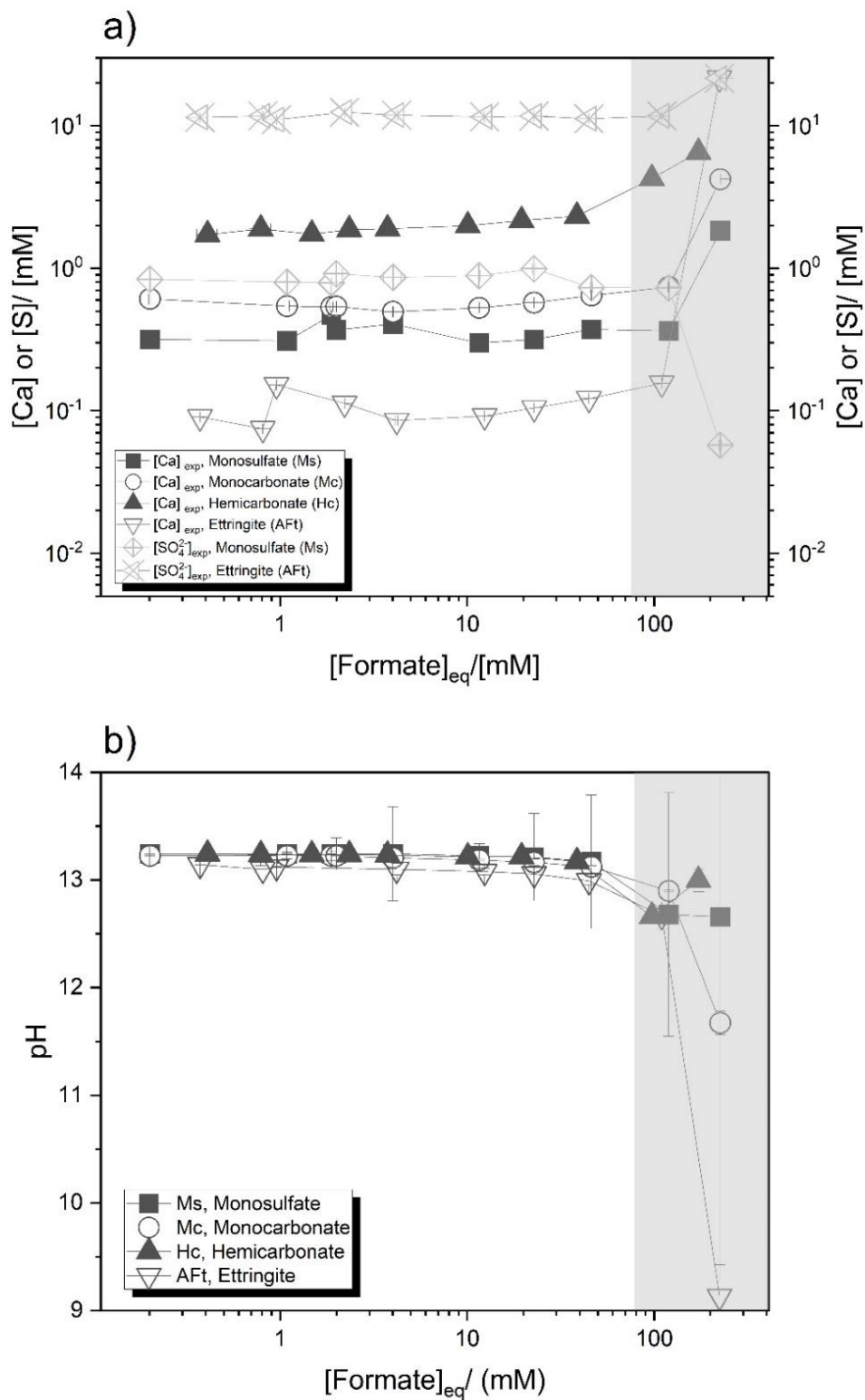
Figure 27. (a) Measured Ca aqueous concentration and (b) pH values of AFm phases (Ms. Mc, and Hc) and AFt, with [Na]$_{tot}$ = 0.2 M and a contacting time of 7 days. Shaded grey areas indicate the regions where Ca-formate formation is expected based on XRPD characterization.

The sorption isotherms for formate uptake on AFm phases and ettringite are shown in Figure 28. The overall sorption capacity, reported only for AFm phases (see horizontal lines in Figure 28), refers to the sum of surface sorption sites and interlayer sorption capacity and for all phases correspond to $\approx$ 3 mol per kg solid. For ettringite, a total sorption capacity of 1.6 mol per kg solid is calculated in this study. Assuming that the main sorption uptake mechanism occurs via electrostatic interaction between the positive charged layer and the accommodating anion, the total molar capacity per kg of solid for formate is based on the valence of formate in the anionic form (-1) and the total positive charge (+2) of the main layer $Ca_4Al_2(OH)_{12}^{2+}$ per formula unit. The uptake on the external surfaces of AFm phases has been observed to be 40 to 1000 times lower [39, 260] (see section 3.1.3), corresponding to $\approx$ 0.003 mol per kg solid.

The batch experiments, carried out at pH $\approx$ 13.3, show that formate uptake on Hc, Mc and AFt is low and comparable to each other at low formate concentrations. For $[FOR]_{eq, sol} > 10^{-2}$ M, the uptake on AFt deviates downwards from the reference sorption isotherm with a slope of 1 with the increase of formate concentration (Figure 28), while for Hc higher uptake is observed at higher concentrations following the linear isotherm line. The limited sorption of formate on ettringite and Mc seems to indicate that formate mainly sorbs on the outer surface, but is not able to replace the anions in the interlayer or the channels of ettringite. Similar to our observations, Nedyalkova et al. [13] observed that also iodide ions sorption occurred in the case of Mc on the outer surface only and reported a ratio of outer to total surface sites for AFm phases of 1:1000. Assuming the same outer to total surface sites ratio of 1:1000, as indicated by the second horizontal line in Figure 28, explains the observed upper limit of formate sorption on Mc. In the case of Ms a sorption step was observed at a higher outer to total surface sites ratio of 1:100, while for ettringite an upper limit of $\approx$ 0.01 mol per kg solid was observed. Therefore, it seems that in the case of Mc and AFt, formate sorbs mainly at the outer surface. These observations are also in agreement with the results obtained from the XRPD analysis. Only for Hc, formate sorption increases linearly with formate concentration, suggesting that both the inner and outer surface sites of Hc can be occupied by formate. The monovalent nature of interlayer anion (OH$^-$) present and structure (larger d-spacing) of Hc may justify the higher uptake capacity of formate on Hc.

For AFm phases, R_d values of $\approx$ 1.5 dm^3/kg and $\approx$ 3 dm^3/kg for Mc and ettringite, respectively, were derived for formate solution concentrations < 2 mM, while the R_d of Hc and Ms were 2.3 $\pm$ 0.1 dm^3/kg 93 $\pm$ 93 dm^3/kg respectively, over the entire range of values measured. Except for the case of Ms, these values are comparable to the values reported by Wieland et al [3]. (R_d Ms $\approx$ 2 dm^3/kg, Mc $\approx$ 0.3 dm^3/kg, ettringite $\approx$ 1 dm^3/kg and Hc $\approx$ 20 dm^3/kg at $\approx$ 3 mM formate and lower pH values of $\approx$ 12). The comparable values also seem to indicate that in the case of ettringite and AFm phases, where anions compensate the positive charge of the main layer, the pH has a minor effect on the R_d values, with the exception of Hc, where formate competes with OH$^-$ and a clearly lower uptake was observed in the present study at pH 13.2 than by Wieland et al at pH $\approx$ 12.
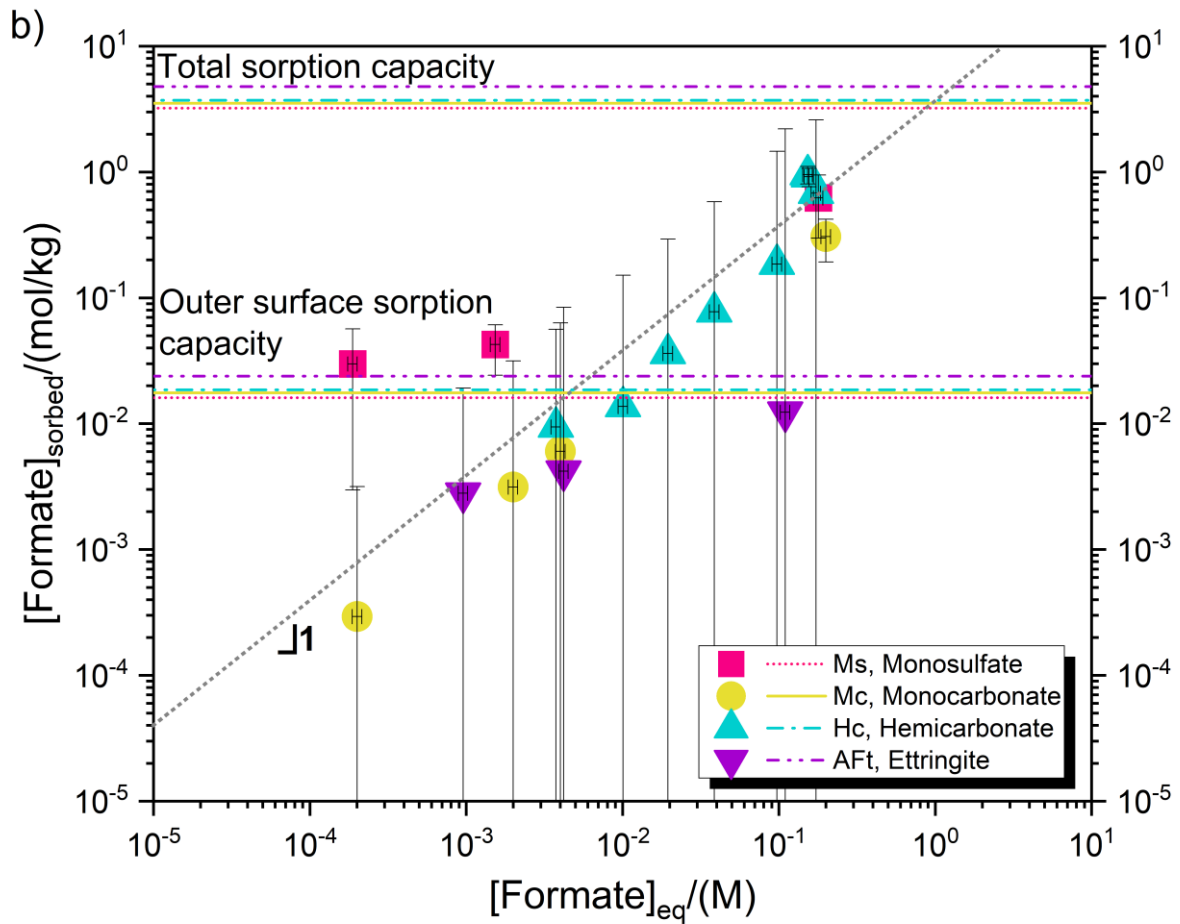
Figure 28. Experimental formate sorption isotherm for monosulfate (Ms), monocarbonate (Mc), hemicarbonate (Hc) and ettringite (AFt) after an equilibration time of 7 days. The upper and lower horizontal lines indicate the overall potential uptake and the uptake on the outer surface of Mc, Hc, and Ms respectively.

3.1.3. Citrate uptake by C-S-H, AFm phases, ettringite and PC

3.1.3.1. Kinetic experiments: uptake of citrate

3.1.3.1.1. C-S-H phases

Kinetic sorption experiments were investigated on pure C-S-H phases for equilibration times ranging from 1 to 14 days. 34.5 mM of citrate were added to the suspensions and samples were let equilibrate under continuous shaking. The pH values (Figure 29) of C-S-H 1.2 and 1.4 were constant over time, while for C/S = 0.8 and 1.0 the pH decreased by ca. 0.2 pH units. Furthermore, for C/S > 1.0, the portlandite was destabilized in the presence of $[CIT]_{tot} = 34.5$ mM, due to the formation of the aqueous complex $CaCit^-$. The XRPD characterizations (see Figure 17-Figure 20 in the Appendix 3.1) for this system showed the destabilization of portlandite 1 day after the citrate addition. The citrate concentration in solution was found to be lower than the initial citrate concentration for all C/S ratios. With the exception of C-S-H 1.4, the citrate concentration decreased over time, which is probably linked to the precipitation of Ca-citrate, $Ca_3(C_6O_5H_7)_2 \cdot 4H_2O$, as observed by XRPD analysis for longer equilibration times (Figure 20 in the Appendix 3.1) and also suggested from the calculation of saturation indices reported in the Appendix 3.1 (see Table 35, 37, 39 and Table 41).
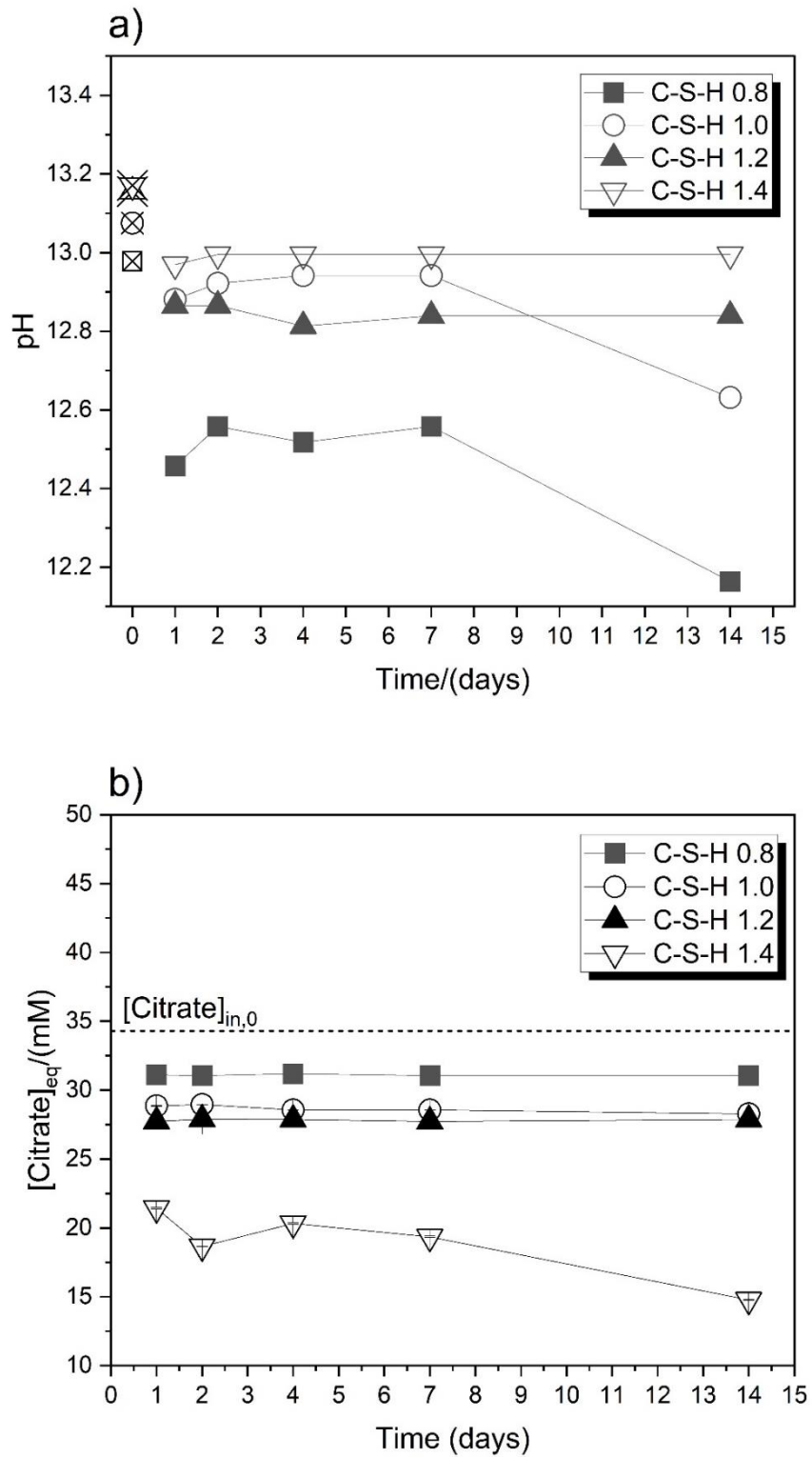
Figure 29. (a) pH values (measurement error ±0.1 pH units) and (b) citrate aqueous concentrations (measurement error ± 2 %) in the presence of C-S-H phases (Ca/Si = 0.8 – 1.4) measured at different equilibration times (t = 1 – 14 days) in the presence of initial [CIT]$_{tot}$ = 34 mM and [Na]$_{tot}$ = 0.2 M. Empty crossed symbols indicate the pH values in the absence of citrate.

3.1.3.1.2. AFm phases and ettringite

The results of time dependent sorption experiments are shown in Figure , where citrate was added to the pre-synthesized and equilibrated AFm phases and ettringite. All experiments were performed with the same total sodium concentration of 200 mM (pH ≈ 13.3). The presence of citrate lowered the pH values of AFm phases (from initially ≈ 13.3) and ettringite (from initially 13.1), to pH = 12.9 (Ms and Mc) and pH = 12.7 for ettringite (Figure a). In the case of Hc, the pH was decreased by 0.2 units (from 13.2 to 13.0) only after 1 day, due to the uptake of citrate on Hc. In general, pH values increased between 1 and 4 days of equilibration, while citrate concentrations decreased up to 4 days (Figure) significantly in the case of Hc, and moderately for Ms and AFt. In the case of Mc, small variations of both pH and citrate were observed, indicating a very weak uptake. In parallel with the changes in pH values and citrate concentrations, some variations in aluminium and calcium concentrations were observed during the first 4 days (see Table 41, Table 44, Table 46 and Table 47 in the Appendix 3.1). In general, citrate enhances the dissolution of Ca^{2+} from the solid phase, due to the formation of stable Ca-citrate complexes and/or to the precipitation of Ca-citrate salts (e.g. $Ca_3Cit_2 \cdot 4H_2O$) (Figure 32 in the Appendix 3.1). The data shown in the Figure indicate that a steady state sorption was reached within 4 days. Thus, all further sorption experiments were conducted with an equilibration time of 7 days. No additional solids formed due to the presence of citrate (see XRPD spectra, Figure 21-Figure 24 in the Appendix 3.1).
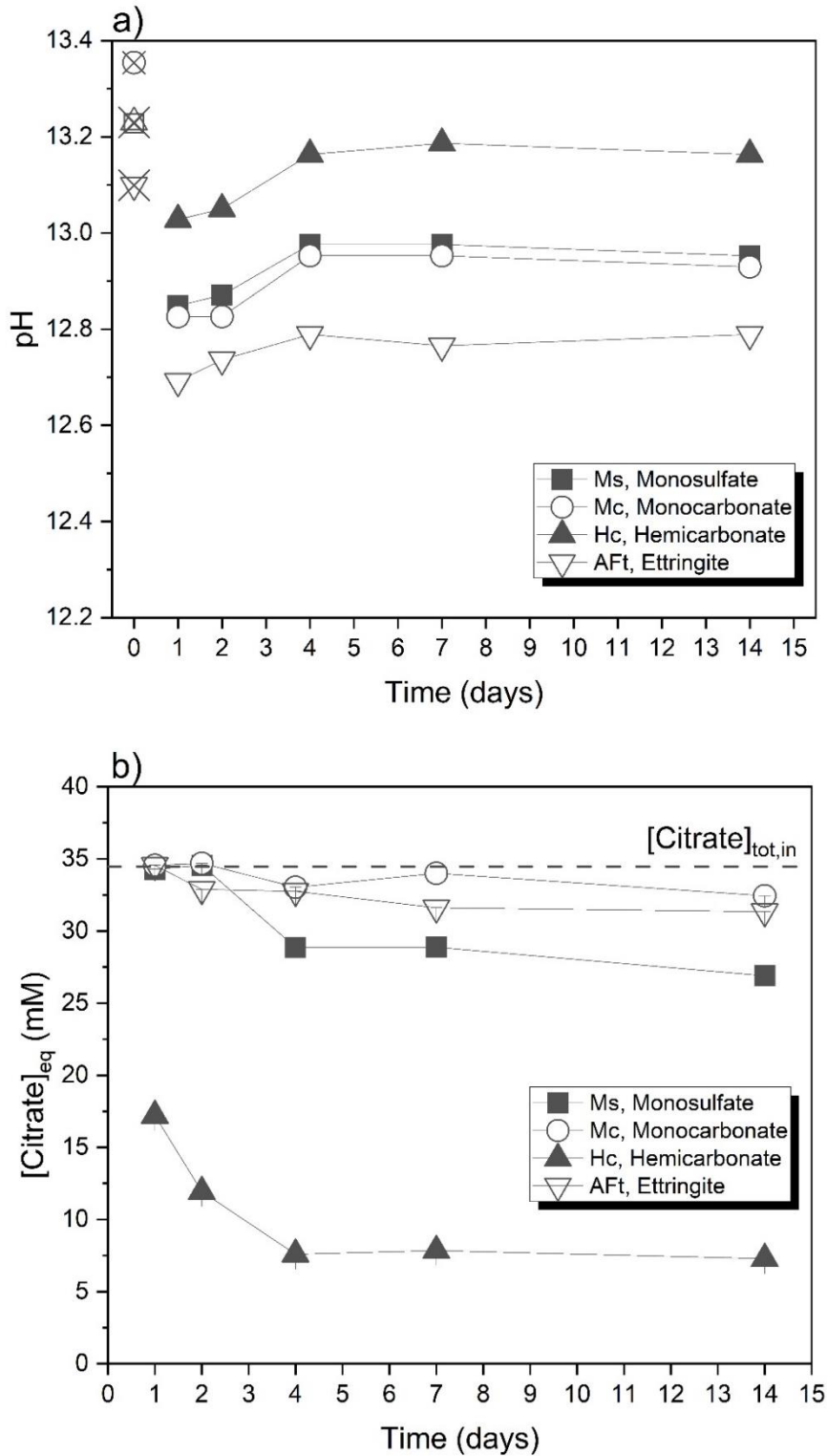
Figure 28. (a) pH values (measurement error ±0.1 pH units) and (b) gluconate aqueous concentration (measurement error ± 2 %) in the presence of AFm phases (Ms. Mc, and Hc) and AFt measured at different equilibration time (t = 1 – 14 days) in the presence of initial [CIT]$_{tot}$ = 34 mM and [Na]$_{tot}$ = 0.2 M. Empty crossed symbols indicate the pH values in the absence of citrate.

3.1.3.2.   Sorption experiments: uptake of citrate

3.1.3.2.1.   C-S-H phases

Figure shows the comparison of the XRPD spectra of C-S-H phases in presence ($[CIT]_{tot,}$ = 34 mM) and in absence of citrate. As mentioned in the section 3.1.1.1, the interplanar distance between the two main calcium layers decrease with the increase of the C/S [15, 230, 255]. Lothenbach and Nonat [15] indicate that the reduction of the interplanar distance is due to the attraction between Ca^{2+} ions in the interlayer and the negatively charged main layers. Citrate sorption has a negligible effect on the d-spacing (002) for C/S ≤ 1.0, while for C/S equal to 1.2 and 1.4 a shift of the main peak position of (002) distance towards higher $2\theta^{o}$ (decrease of interplanar distance) is visible. A similar result has been found for C-S-H with lower C/S and low pH values [230]: the decrease of the interplanar distance was due to the higher Ca-concentration present in the interlayer region, which determines the attraction of the two main layers. Since the pH conditions are different and the Ca concentration in presence of citrate is lower, it is not possible to apply the observations reported by [230] to the interplanar distance decrease observed in this study. However, a decrease of the layer distance could be related to the increase of ionic strength from ~0.2 in 0.2 M NaOH in the absence of citrate to I ~ 0.25 M in the presence of 0.034 M citrate, which lowers the thickness of the diffuse layer. A small decrease of Ca bulk concentration was observed for equilibrium citrate concentration higher than ~ 0.003 M, due to the formation and precipitation of $Ca_3Cit_2 \cdot 4H_2O$ as also suggested for saturation indices (see Table 51, Table 53, Table 55 and Table 57 in the Appendix 3.1). Furthermore, the portlandite present in the pure C-S-H phase with a C/S = 1.2 and 1.4 is destabilized by citrate, due to the formation of aqueous $CaCit^{-}$ complexes (see Figure 32 in the Appendix 3.1).
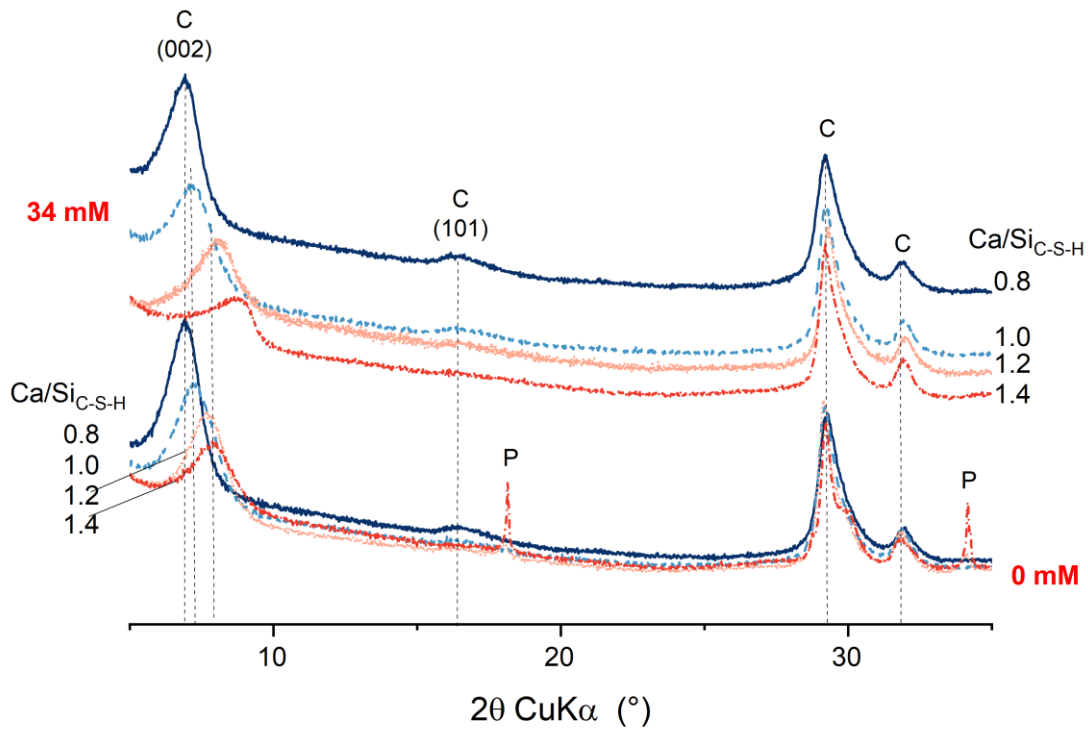
Figure 29. XRPD characterization of C-S-H phases (C/S = 0.8 – 1.4) in presence ([CIT]$_{tot}$= 34 mM) and in absence of citrate after 7 days of contacting time.

The typical stretching vibration of the Si-O bond at ≈ 950 cm^{-1} of C-S-H phases equilibrated in presence of [CIT]$_{tot}$ = 34 mM, (Figure 30) shifts systematically towards lower wavenumbers, as for the system in absence of citrate. Compared to the solid phases equilibrated in absence of organics, citrate leads to the stretching vibration towards higher wavenumbers especially for low C/S. The band at 840 – 810 cm^{-1}, labelled as Q^1 increases in intensity and the peak position shifts towards lower wavenumbers with the increase of C/S ratio. By comparing the intensity of the Q^1 band for the systems in presence and in absence of citrate, the Q^1 sites are less in presence of citrate (less Ca in C-S-H) in particular for C/S = 1.0. This observation is in agreement with the increase of Ca concentration in solution discussed in the next section. The presence of citrate for all C-S-H phases is also observable in the wavenumber range 1550-1400 cm^{-1}, where additional bands (of carboxylate group) occur.
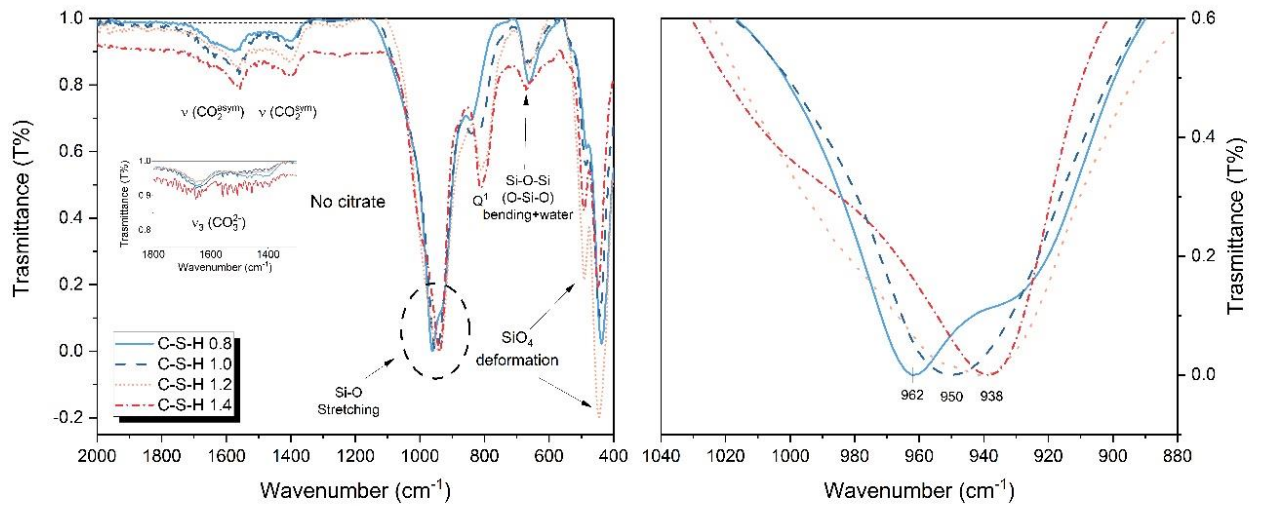
Figure 30. FT-IR characterization of C-S-H phases (Ca/Si=0.8–1.4) equilibrated with [CIT]$_{tot,}$ = 34 mM for 7 days of contacting time in the wavenumber region 2000–400 cm^{-1}.

Figure 31 shows the total Ca concentration in solution and the pH values as a function of the equilibrium citrate concentration. The Ca concentration (Figure 31a) increases linearly for all C-S-H phases with the increase of citrate concentration. A small effect on the calcium concentration is observed for citrate concentration [CIT]$_{eq, sol}$ < ≈ 0.1 mM. For [CIT]$_{eq, sol}$ ≥ 1 mM, the calcium concentrations increases due to the formation of aqueous CaCit$^-$ complexes. This observation is in agreement with the argumentation reported above regarding the effect of citrate on the C-S-H phase composition: citrate enhances the dissolution of Ca^{2+} by lowering the C/S ratio of C-S-H and consequently decreasing the fraction of Q^1 sites as observed in the FT-IR analysis. The pH values shown in the Figure 31b decrease with increasing addition of citrate, in particular for low C/S, since Na$^+$ is sorbed strongly in ion exchange sites of C-S-H phases [261].The increased uptake of Na$^+$ at low C/S C-S-H lowers the aqueous Na$^+$ concentrations and thus the pH values in the solution, while at higher C/S values, where less Na$^+$ is bound, this effect is less pronounced. In contrast to formate, where the pH values as well as Na sorption on C-S-H decreased strongly, the effect of citrate on pH values and Na sorption was less strong due to the strong sorption of citrate on C-S-H.
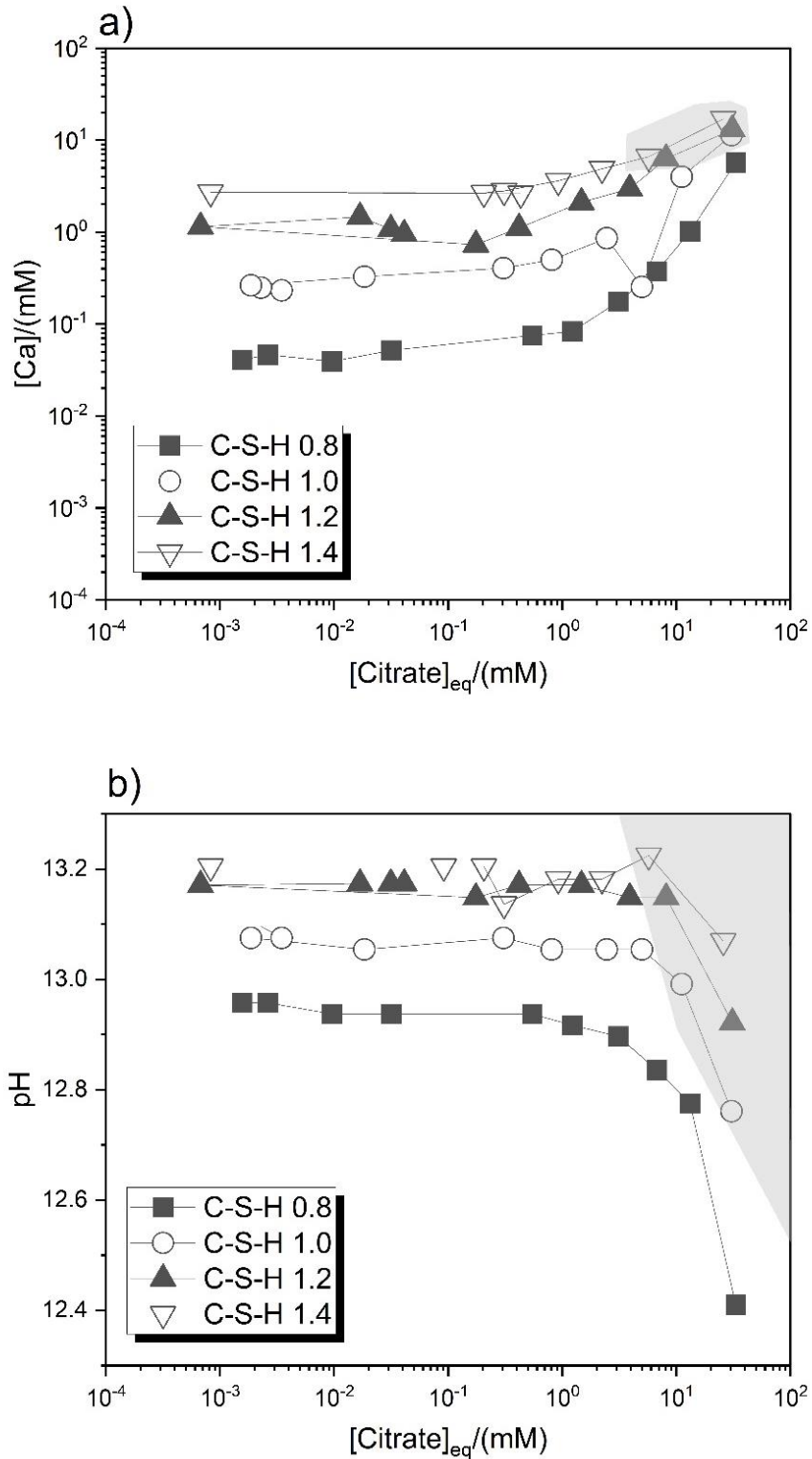
Figure 31. (a) [Ca] aqueous concentration and (b) pH values for C-S-H phases (Ca/Si=0.8 – 1.4) as function of citrate concentration in solution measured after 7 days of contacting time. Shaded grey areas indicate the regions where Ca-citrate formation is probably based on SI calculation.

The uptake of citrate on C-S-H is reported in Figure 32 as moles of citrate adsorbed per kg of C-S-H. Details about weight quantification (mass balance equations) are reported in the Table 58 in the

Appendix 3.1. Reversely to the case of formate, citrate uptake increases with increasing Ca/Si ratio and with increasing calcium concentration in solution (Figure 32).

For citrate concentrations higher than 2 mM, where the $CaCit^-$ complex dominates the Ca speciation in solution, the isotherm for citrate sorption onto C-S-H phases deviates from the "ideal" isotherm with a slope of 1. Sorption data suggest some kind of saturation and at C/S = 0.8, where little calcium is available, even a partial decrease of sorption is visible. From this observation, it is possible to deduce that the uptake of citrate is mediated by the presence of Ca^{2+} at the surface [136, 138]. In particular the uptake decrease at higher concentrations of anionic organic ligands, found also in gluconate sorption experiments [138], is caused by the depletion of Ca^{2+} at the surface being responsible for citrate sorption. Such a behavior was predicted by Turesson and coworkers [262] based on Monte-Carlo simulations for the Ca^{2+} mediated adsorption of polymers on negatively charged surfaces.
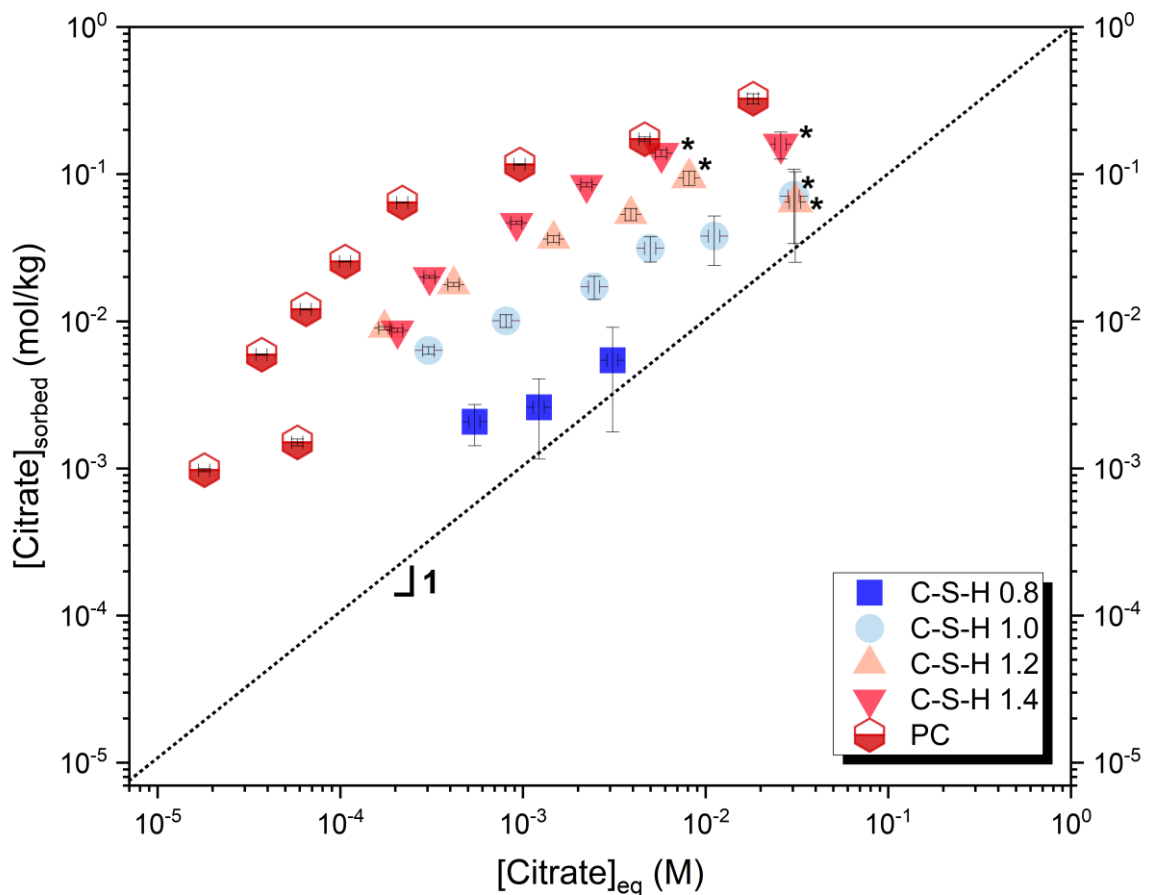
Figure 32. Sorption isotherms calculated as moles of citrate sorbed per kg of solid phase, for C-S-H phases with a ratio of $0.8 \leq C/S \leq 1.4$ and Portland cement (PC) after 7 days of contacting time the citrate adding. Symbols marked with (*) indicated the possible formation of $Ca_3Cit_2 \cdot 4H_2O$ as suggested by the calculated saturation indices.

For citrate concentrations lower than 2 mM, distribution coefficients (R_d) of (3.0 ± 1.1) $dm^3 \cdot kg^{-1}$, (16.2 ± 7.0) $dm^3 \cdot kg^{-1}$, (39.5 ± 13.7) $dm^3 \cdot kg^{-1}$ and (52.6 ± 11.5) $dm^3 \cdot kg^{-1}$ were determined for C/S of 0.8, 1.0,

1.2 and 1.4, respectively. The uptake of citrate on PC is about one order of magnitude higher than the uptake by C-S-H 1.4, with a R_d of (154 ± 16) $dm^3 \cdot kg^{-1}$. As discussed above for formate, the higher uptake on PC may be caused by the additional sorption occurring on secondary phases such as AFm and AFt present in hydrated cement (see Table 100 in the Appendix 3.1). In addition, the steep sorption isotherm observed for very low citrate concentrations on PC, may incate that the uptake of citrate could take a place via multilayer sorption mechanism.

3.1.3.2.2. AFm phases and ettringite

The presence of citrate affected the structure and composition of Hc, Ms and AFt. As observed for formate uptake experiments, the interlayer distance (006) of Hc and cHc $C_4Ac_{0.8}H_{10.2}$ [238] increases clearly with the citrate concentration (Figure 33). At the highest citrate concentration ($[CIT]_{tot} = 34$ mM), only one of the two reflections related to Hc and cHc is present. The decrease of the intensity of the main basal reflection with increasing citrate concentration may indicate a decrease in ordering and/or more variable interlayer distance. Note that the main layer signal at $\approx 31°$ 2θ related to the 110 plane did not broaden or decrease in intensity. In the case of Ms, the basal reflections of both Ms12 and Ms14 (monosulfate with 12 or 14 H_2O moles of water) show a slight shift towards lower $2\theta°$ angles with the increase of citrate concentration. Such small interlayer distance increase is a consequence of the intercalation of citrate or more likely, due to a decrease of the number of stacked layers, which shifts the XRPD signal at a constant basal spacing to lower $2\theta°$ values [231, 256]. In the case of Mc, no clear effect of citrate on the interlayer distance is observed (Figure 26 Appendix 3.1), indicating no significant uptake of citrate in the interlayer of Mc. These findings agree with the observation reported for the kinetic sorption experiments, where a similar broadening of the basal reflection was observed. As observed for the broadening of AFm phases' d-spacing in presence of formate, also for citrate the interlayer uptake via anion exchange reaction is discriminated by the structure of crystal solid phase [202]. Citrate exhibits a slight effect on the ettringite structure. The main (100) signal at $9.1°$ 2θ (d = 9.7 Å) in a direction (perpendicular to the columns) shows an increase of $0.06°$ increase with increasing citrate concentration (Figure 27, in the Appendix 3.1). In addition, for the small (002) reflection (parallel to the column) at $8.2°$ 2θ (d = 10.7 Å) no significant variations are observed.
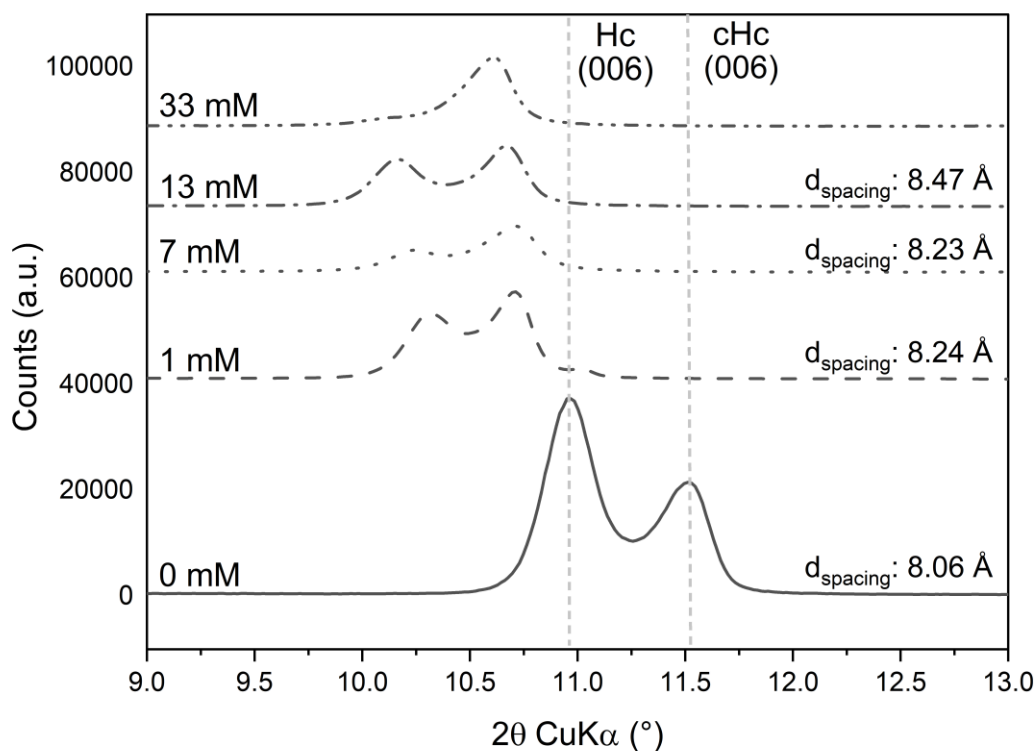
Figure 33. XRPD patterns of hemicarbonate after sorption of citrate and for contacting time t = 7 days. The figure shows the shift of basal spacing of Hc (hemicarbonate) in the presence of citrate. cHc indicates carbonated hemicarbonate.

The uptake of citrate in the AFm phases and AFt structure is also visible through the FT-IR analysis, as shown for Hc in Figure 34. In particular, the wavenumber range 2000-1000 cm^{-1} shows how the intensity of stretching vibration band of the citrate carboxylate group grows with the citrate concentration. The increase of the signal of the carboxylate group of citrate is much more intense for Hc than for Ms, indicating a more intense uptake of citrate in agreement with XRPD results. As also observed for the Ms-formate system, the intensity of the sulfate group decreases with increasing citrate concentrations (Figure 28, Appendix 3.1). For Mc, the slight decrease of the bending vibrations of CO_3^{2-} (1450 – 1400 cm^{-1}, see Figure 29 in the Appendix 3.1) with the increase of citrate concentration, indicate a lower tendency of citrate sorption via anion exchange reaction for Mc than for Ms and Hc.

In the case of ettringite the stretching vibrations of the carboxylate groups of citrate are covered by the bending vibrations of $Ca=OH_2$ (1660 cm^{-1}) [241], while the intensity of the sulfate stretching vibration at ≈ 1100 cm^{-1} shows some variations (see Figure 30 in the Appendix 3.1), but no systematic decrease with citrate concentration indicating no or only very little replacement of sulfate by citrate.
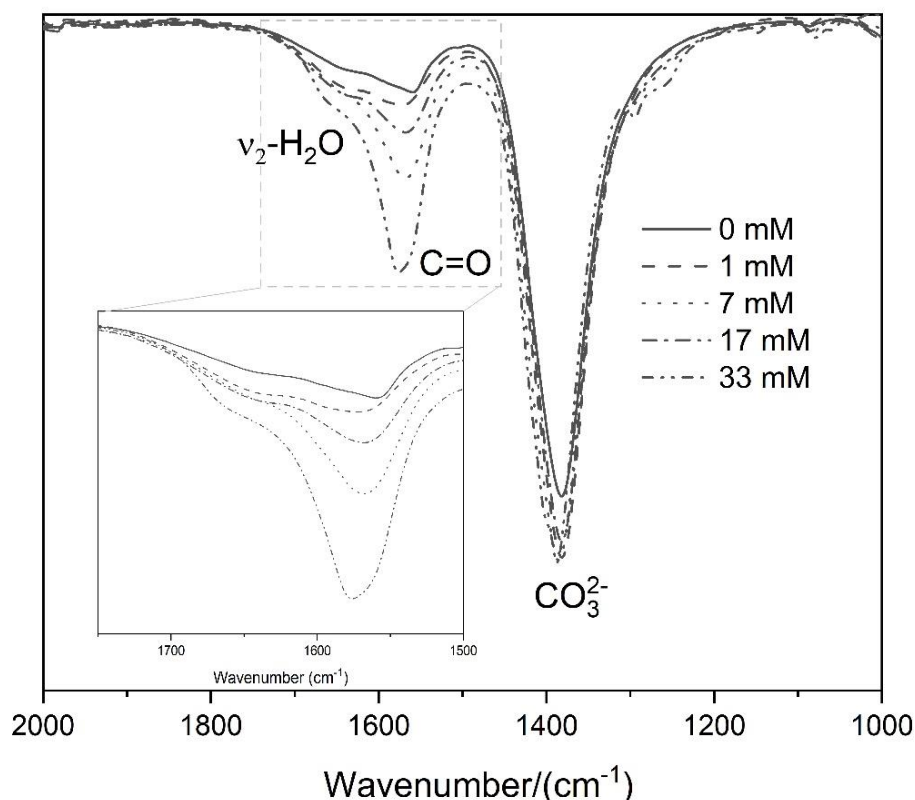
Figure 34. Effect of the initial citrate concentration on the FT-IR spectra of, Hc, hemicarbonate at 7 days of contacting time after the citrate adding.

All measured data and calculated saturation indices are provided in Table 59, Table 61, Table 63 and Table 65 in the Appendix 3.1. Figure 35 shows that the addition of citrate increases the calcium and sulfate concentrations but lowers the pH values in the presence of AFm phases and ettringite. The increase of the sulfate concentration for Ms and ettringite in the presence of citrate indicates a partial replacement of sulfate by citrate. The increase of the calcium concentration with citrate addition is mainly due to the formation of aqueous CaCit⁻ complexes, which dominate Ca speciation at citrate concentrations at > 1 mM as reportes in Figure 32 (see the Appendix 3.1). CaCit⁻ has been found as the most stable aqueous Ca complex in the presence of 2 mM citrate and above in the presence of all AFm phases and ettringite studied here. Citrate is present in solution mainly as fully deprotonated Cit³⁻ species. At high calcium concentrations and low citrate concentrations a significant fraction of CaCit⁻ is calculated to form, while the fraction of citrate complexes with Na, K or Al are negligible (< 0.1% of citrate) under all conditions considered. Although ettringite samples have the lowest Ca concentration at low citrate concentrations, the Ca concentrations increase steeply and reach comparable calcium concentrations at high citrate concentrations as observed for the AFm phases. In the case of Hc and AFt, however, the Ca concentrations drop at the highest citrate concentrations, where the solutions are oversaturated with respect to $Ca_3(Cit)_2 \cdot 4H_2O(s)$, as detailed in Table 64 (hemicarbonate) and Table 66

(ettringite) in the Appendix 3.1, pointing towards the possible precipitation of this solid phase. The saturation indices calculated from the measured aqueous concentrations show also a strong oversaturation with respect to citrate-AFm and citrate-AFt indicating a kinetic hindrance of their formation in the sorption experiments conducted.
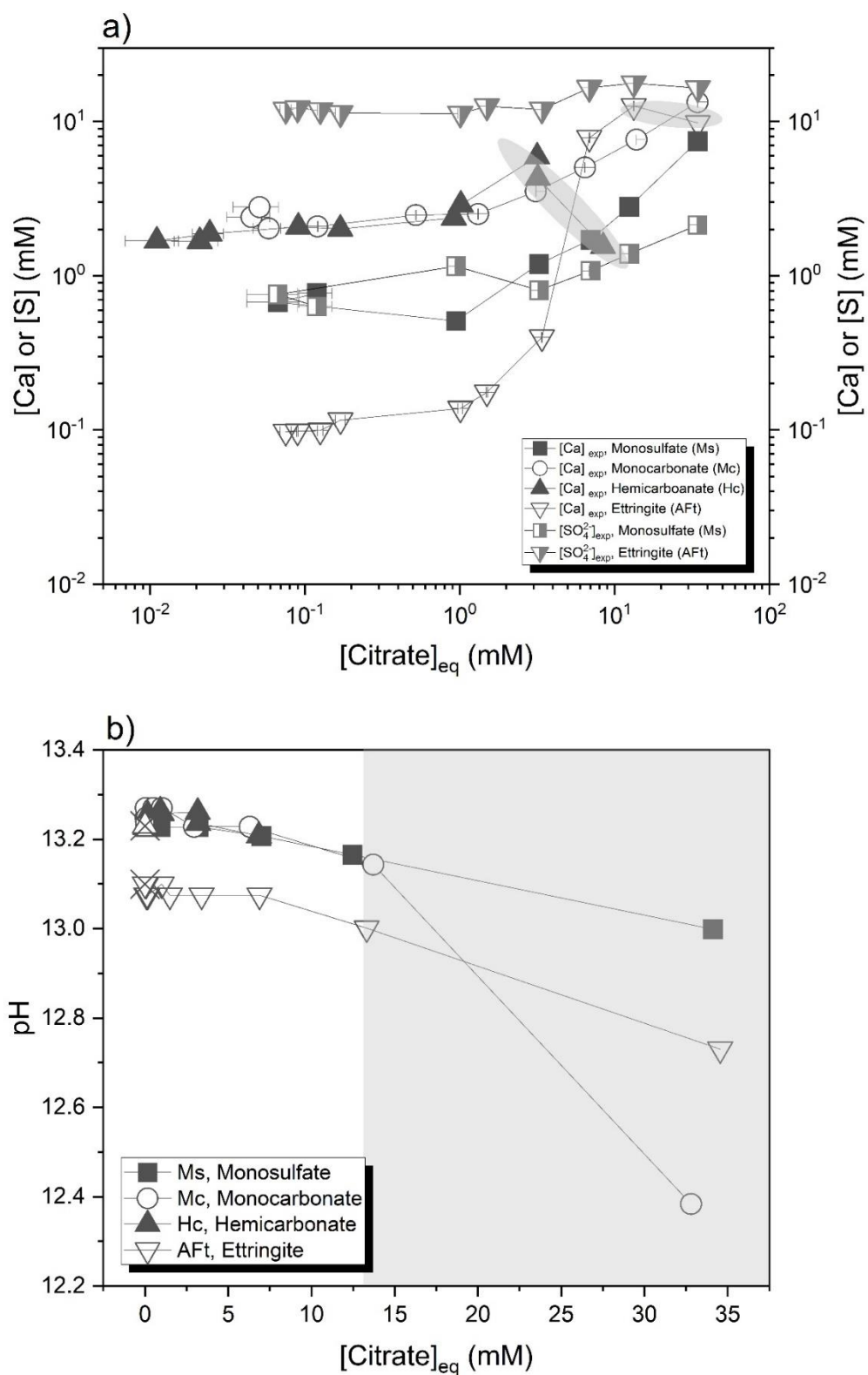
Figure 35. (a) Measured Ca aqueous concentration and (b) pH values of AFm phases (Ms. Mc, and Hc) and AFt, with [Na]$_{tot}$ = 0.2 M and a contacting time of 7 days. Shaded grey areas indicate the regions where Ca-citrate formation is expected based on SI calculation.

The sorption of citrate on AFm phases and ettringite is shown in Figure 36. Assuming that the main uptake occurs via electrostatic interaction between the positive charged layer and the accommodating anion, the total molar capacity per kg of solid for citrate is based on the valence of citrate in the anionic form (-3) and the total positive charge (+2) of the main layer $Ca_4Al_2(OH)_{12}^{2+}$ per formula unit. Figure 36 shows that citrate sorbs at low concentrations significantly on Hc and on Ms and weakly on Mc and AFt. The citrate sorption on Mc, Ms and ettringite increases with citrate concentrations up to $\approx 10^{-2}$ mol citrate per kg solid, while at higher citrate concentrations, little uptake is observed. In the case of AFt, saturation indices calculations indicate that the precipitation of Ca-citrate ($Ca_3(Cit)_2 \cdot 4H_2O(s)$) is expected for citrate concentrations higher than 6 mM (symbols marked with "*" in Figure 36). The limited sorption of citrate on Ms, ettringite and Mc observed for citrate equilibrium concentrations in a range of 10^{-3} M < $[CIT]_{eq, sol}$ < 10^{-2} M might be related to the predominant uptake of citrate by solid phase outer surface sites over the uptake on other sorption sites (e.g. interlayer sites, edge-sites). The sorption studies carried out by Ma et al. [39] and Nedyalkova et al. [13], reported a ratio of outer to total surface sites for AFm phases of 1:1000 and 1:60 respectively. The large difference of outer to total surface sites ratios determined by [13] and [39] may depend on the different experimental methods, the pH values or ionic strength used: in the case of [13] the ratio is empirically determined for the uptake of iodide on AFm phases, and in the case of [39] is calculated by means of the specific surface charachterization through BET analyses of the synthesized phases. As observed for the uptake of iodide on Mc [13], it is possible to deduce that citrate sorption occurs for Mc and AFt exclusively and in the case of Ms predominantly at at outer surface sites. In this case, the horizontal lines labelled as outer surface sorption capacity were obtained by assuming a ratio of outer surface sites to total (outer and interlayer) surface sites of 1:200 (Figure 36). This value has been accordingly chosen taking into account the plateau of the sorption isotherms observed for all phases approximately in the citrate concentration range 10^{-4} M < $[CIT]_{eq, sol}$ < 10^{-2} M. Only in the case of Hc, sorption increases with citrate concentration with a slope of 1, indicating a high affinity of citrate on Hc sorption sites, both located on outer and interlayer regions. For Ms also a strong uptake is observed at low citrate concentrations, indicating that only outer surface sites of Ms can be occupied by citrate. This observation is also in agreement with the strong decrease of the zeta potential of Ms up to ≈ 0.01 mol/kg Ms (see Figure 31 in the Appendix 3.1). For AFm phases, R_d values of ≈ 10 (Mc), ≈ 40 (Hc) and ≈ 200 dm^3/kg (Ms) were derived for citrate concentrations < 0.1 mM, while the R_d of ettringite was in the range of 1 to 18 dm^3/kg. At higher citrate concentrations, these values decreased strongly by about ≈ 2 orders of magnitude (Mc, Ms and AFt) due to limited accessibility of the available sorption sites by citrate.
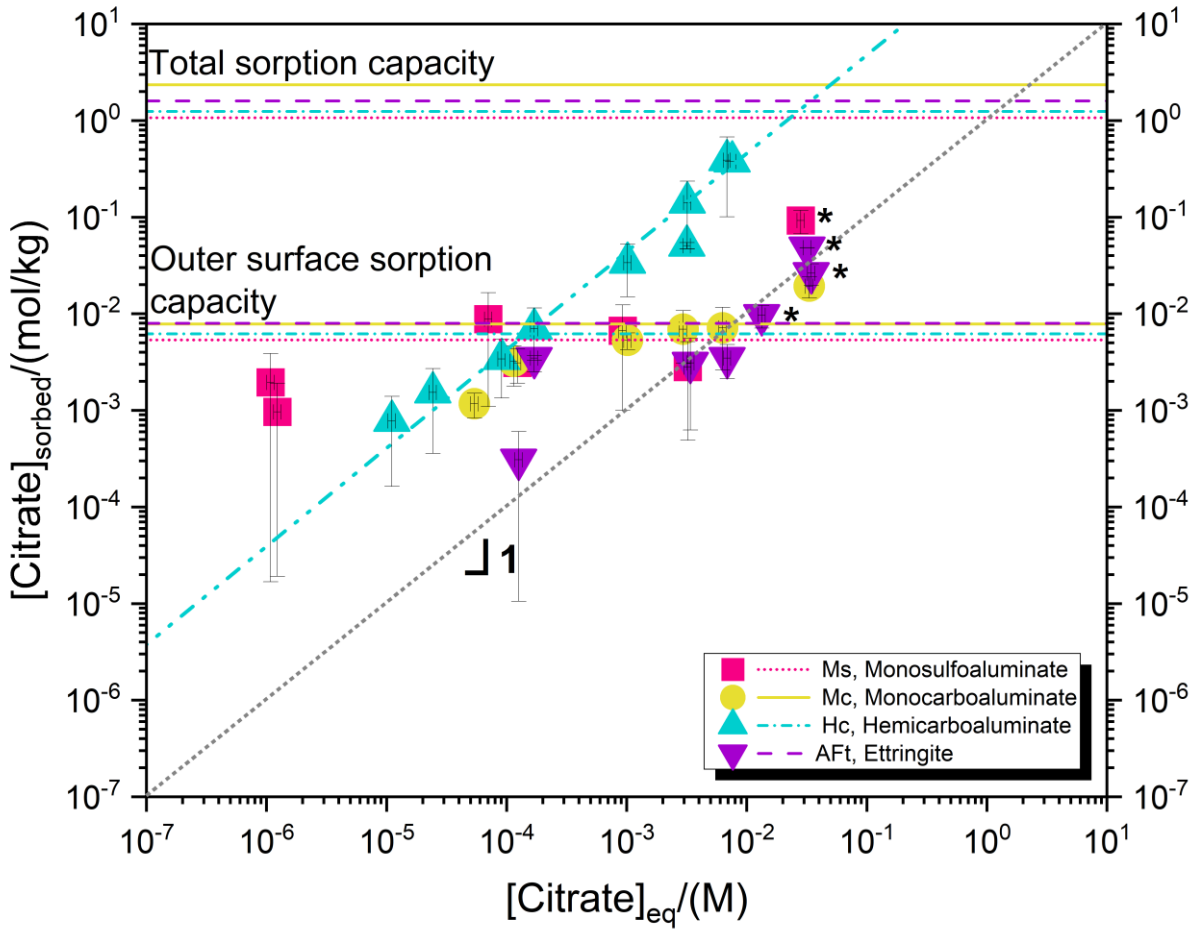
Figure 36. Experimental citrate sorption isotherm for monosulfate (Ms), monocarbonate (Mc), hemicarbonate (Hc) and ettringite (AFt) after an equilibration time of 7 days. The upper and lower horizontal lines indicate the overall potential uptake and the uptake on the outer surface of Mc, Hc, and Ms respectively. Symbols marked with (*) indicate the potential precipitation of $Ca_3Cit_2 \cdot 4H_2O$ based on the calculated saturation indices in the Appendix 3.1.

3.1.4. Gluconate uptake by C-S-H, AFm phases, ettringite and PC

3.1.4.1.   Kinetic experiments: uptake of gluconate

3.1.4.1.1.   C-S-H phases

The kinetics of gluconate sorption to C-S-H phases were investigated for times ranging from 1 to 14 days. As for the others organic ligands, a known concentration of gluconate ([GLU]$_{tot}$ = 21 mM) was added to the suspensions. The sample were further equilibrated under continuous shaking, prior to separation and analysis (see details in the chapter 2). The pH values (Figure 37a) remained constant for all C-S-H phases in the interval of time 1-7 days, but decreased slightly by 0.2 pH units for C-S-H 0.8 and 1.0 at contacting times > 7 days. As observed for formate and citrate, portlandite was destabilized in the presence of gluconate for C/S equal to 1.2 and partially for the system with a C/S = 1.4 (see Figure 35 and Figure 36, Appendix 3.1) due to the formation of CaGluOH^0, Ca$_2$(Glu)$_2$(OH)$_4^{2-}$ and Ca$_3$(Glu)$_2$(OH)$_4^0$ aqueous complexes, in agreement with the results obtained in the study of Bouzouaid et al. [138]. The XRPD spectra (see Figure 33 – Figure 36 in the Appendix 3.1) indicate that portlandite was destabilized in the presence of [GLU]$_{tot}$ = 21 mM. The aqueous gluconate concentration is shown in the Figure 37b: the gluconate concentration was found lower than the initial concentration for all C/S ratio. The decrease of gluconate concentration is probably due to the gluconate sorption onto C-S-H phases, which was found directly dependent on the Ca bulk concentration in the solid phase.
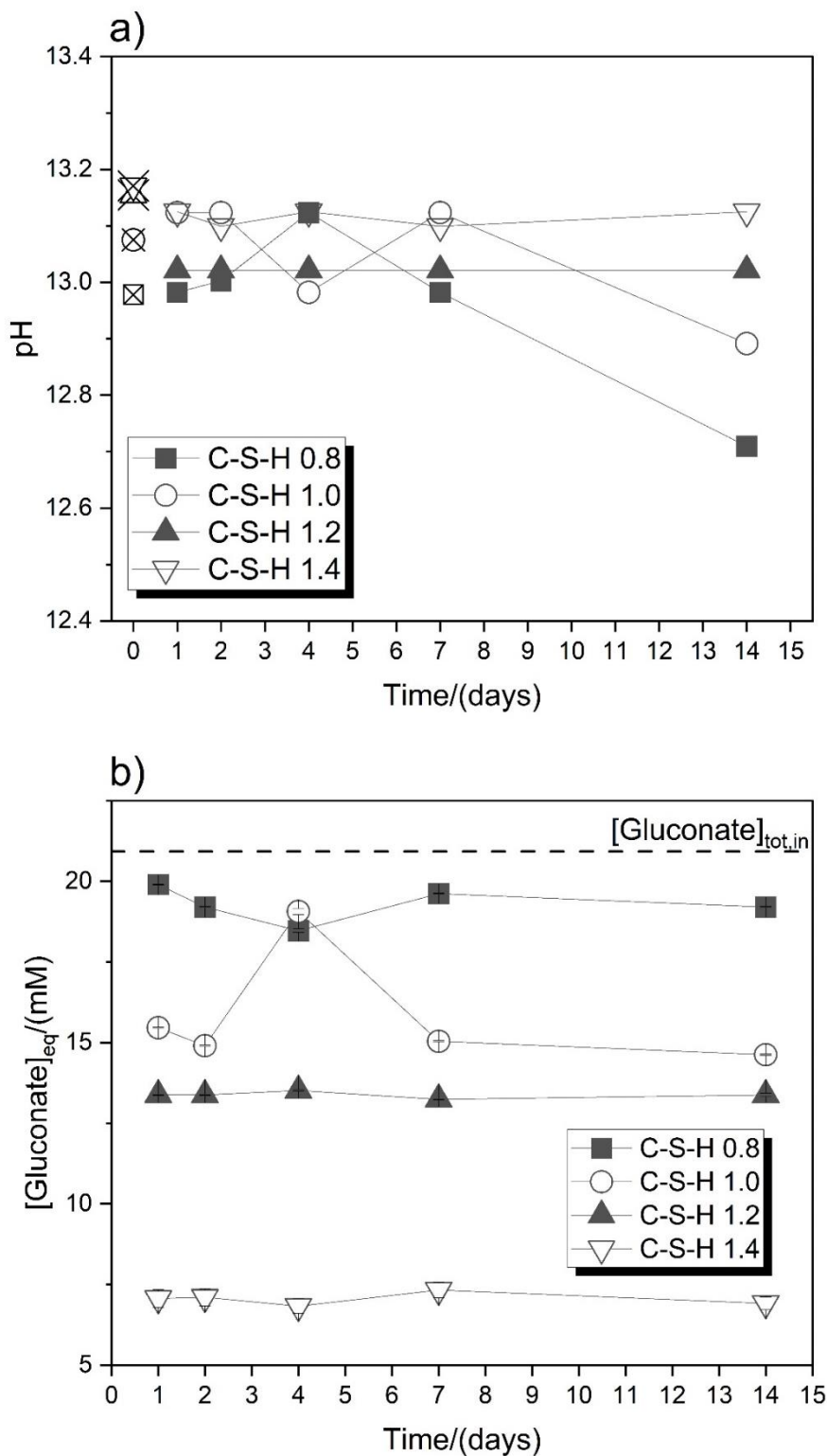
Figure 37. (a) pH values (measurement error ± 0.1 pH units) and (b) gluconate aqueous concentrations (measurement error ± 2 %) in the presence of C-S-H phases (C/S = 0.8 – 1.4) measured at different equilibration times (t = 1 – 14 days) in the presence of initial [GLU]$_{tot}$ =21 mM and [Na]$_{tot}$ = 0.2 M. Empty crossed symbols indicate the pH values in the absence of gluconate.

3.1.4.1.2.   AFm phases and ettringite

As for formate and citrate, experiments were carried out by adding a total gluconate concentration of 21 mM and, in order to have the same alkaline conditions for all samples, a total sodium concentration of 200 mM was applied. The addition of gluconate lowered the pH value of all AFm phases and ettringite by about 0.1-0.2 pH units. For equilibration times ranging from 1 day to 7 days, Figure 38a shows an increase of gluconate sorption with time for all systems concomitant with an increase of pH. In general, the observed pH varations for Ms, Mc, Hc and AFt occur within the experimental uncertanities. The gluconate solution concentrations are lowest in Hc experiments indicating a higher gluconate uptake on Hc, followed by ettringite and Ms and a more moderate uptake on Mc. The solution composition reported in the Table 75, Table 77, Table 79 and Table 81 (see in the Appendix 3.1) indicate that the presence of gluconate increases also the concentration of calcium and aluminium for Ms, Mc and AFt, while for Hc, a slight decrease of Al and Ca concentrations was observed. Overall, these data indicate that a steady state concerning gluconate sorption was reached within 7 days and little variations occurred between 4 to 14 days. In all cases, no additional solids formed due to the addition of gluconate (see XRPD data in Figure 37 - Figure 40 in the Appendix 3.1).
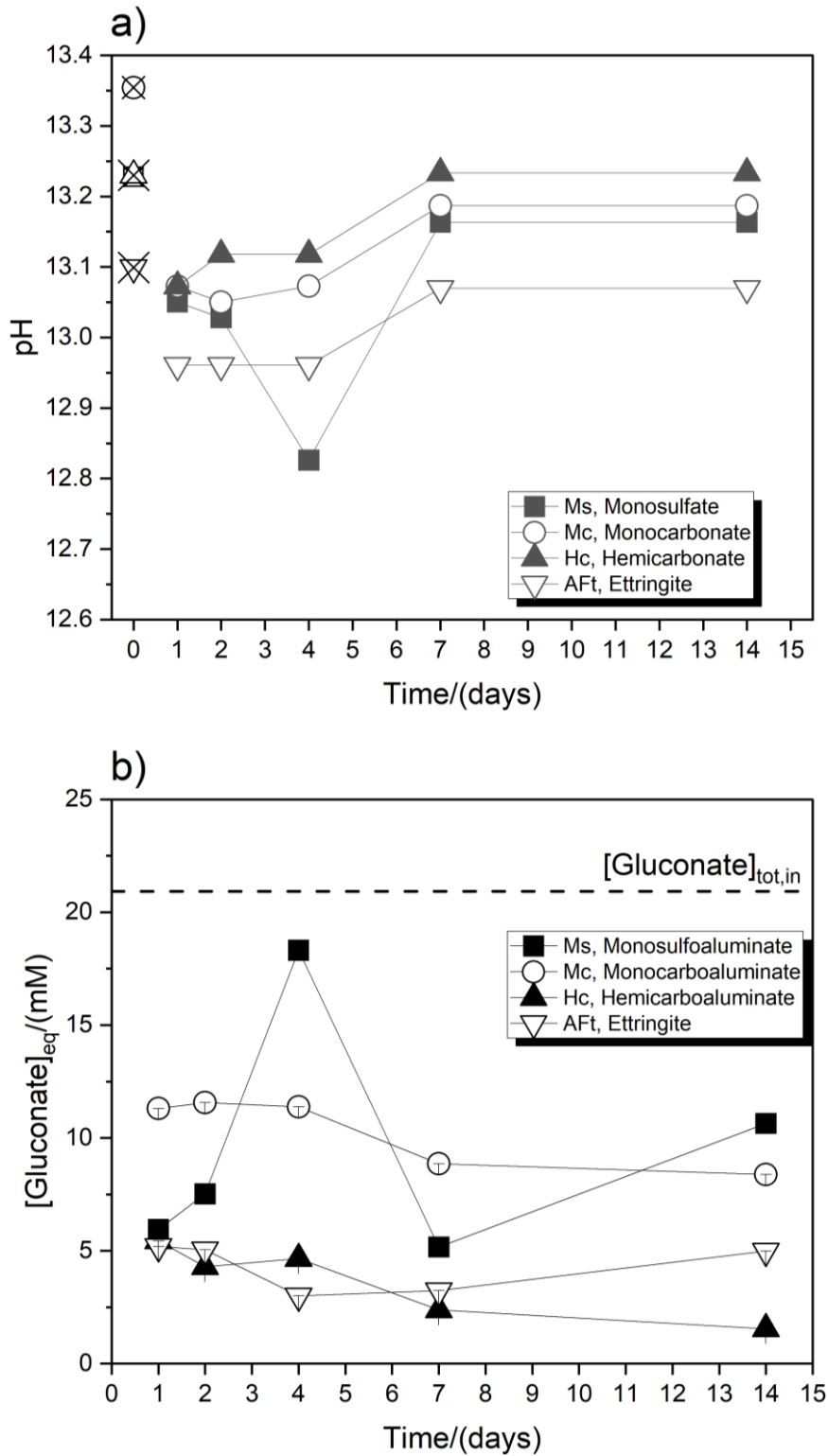
Figure 38. (a) pH values (measurement error ± 0.1 pH units) and (b) gluconate aqueous concentration (measurement error ± 2 %) in the presence of AFm phases (Ms. Mc, and Hc) and AFt measured at different equilibration time (t = 1 – 14 days) in the presence of initial [GLU]$_{tot}$ = 21 mM and [Na]$_{tot}$ = 0.2 M. Empty crossed symbols indicate the pH values in the absence of gluconate.

3.1.4.2. Sorption experiments: uptake of gluconate

3.1.4.2.1. C-S-H phases

The XRPD spectra of C-S-H phases with a C/S = 0.8 – 1.4 equilibrated in presence of 21 mM of $[GLU]_{tot}$ are shown in the Figure . The presence of gluconate has a negligible effect on the interplanar distance for C-S-H phases with $0.8 \leq C/S \leq 1.2$, while a peak broadening is observed, in particular at higher C/S, probably related to a decrease in the number of layers stacked in c-direction [231, 256]. A decrease in the number of stacked layers would also explain the apparent decrease in basal spacing from 11.1 Å (no gluconate) to 9.7 Å visible for C-S-H 1.

The determination of C/S of the bulk C-S-H phase indicates a slight decrease of Ca content at high gluconate concentrations (Figure 41, Appendix 3.1). Also, gluconate destabilized the portlandite found in the sample in absence of gluconate, mainly due the formation of calcium-gluconate(-hydroxide) aqueous complexes.
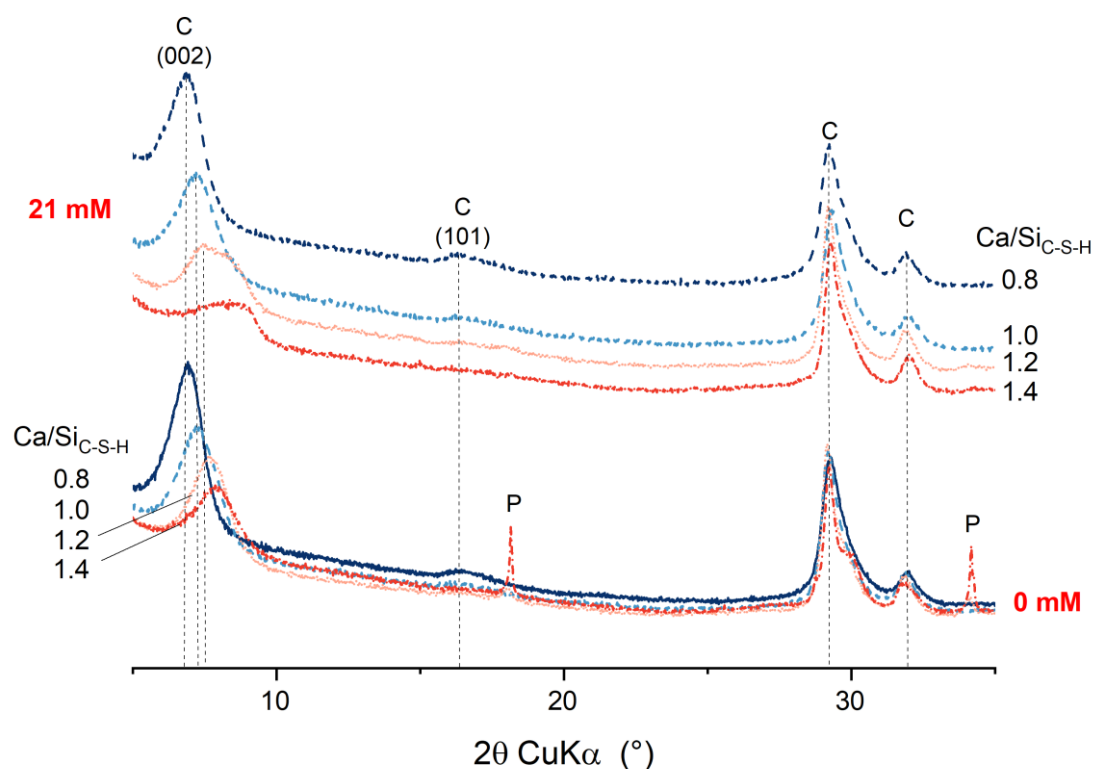
Figure 39. XRPD characterization of C-S-H phases (C/S = 0.8 – 1.4) in presence ([GLU]$_{tot}$ = 21 mM) and in absence of gluconate after 7 days of contacting time.

The FT-IR of C-S-H phases (Ca/Si = 0.8 – 1.4) equilibrated for 7 days with 21 mM of gluconate in Figure 39 shows the typical stretching band of the Si-O bond at ≈ 950 cm^{-1}, which shifts systematically towards lower wavenumbers with higher C/S as also observed in the absence of gluconate (Figure 9). The presence of gluconate led to somewhat higher wavenumbers in particular for the low C/S C-S-H samples. The Q^1 band (840 – 810 cm^{-1}) is well visible for C/S 1.2 and 1.4. The comparison with the citrate-free C-S-H samples indicates less Q^1 sites in the presence of gluconate and thus less Ca in C-S-

H, in particular for C/S = 1. This is consistent with the increased Ca concentration in the aqueous phase, as discussed in the next section. In the presence of gluconate, additional bands occurred in the wavenumber region of 1550 and at 1400 cm^{-1} indicating the presence of citrate in C-S-H for all Ca/Si ratios.
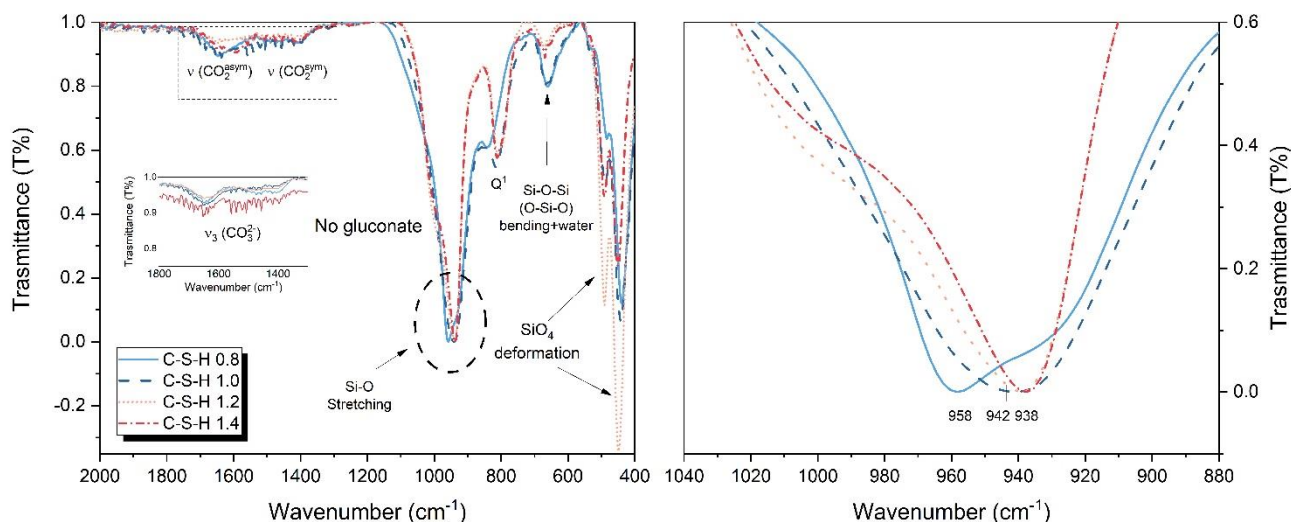
Figure 39. FT-IR characterization of C-S-H phases (C/S=0.8–1.4) equilibrated with 21 mM of gluconate concentration for 7 days of contacting time in the wavenumber region 2000–400 cm^{-1}.

Figure 40 shows the total Ca concentration in solution and the pH values as a function of the equilibrium gluconate concentration. The Ca concentration (Figure 41a) increases significantly for all C-S-H phases with the increase of gluconate concentration, in agreement with the observations reported in Bouzaid et al., 2022 [138]. Such an increase of Ca in solution is in agreement with the observed slight decalcification of C-S-H in the presence of gluconate observed in the FT-IR analysis. The pH decreases with the increase of gluconate concentration, in particular for low C/S, since Na$^+$ strongly sorbs to ion exchange sites of C-S-H phases by simultaneously releasing protons [230]. This effect is less pronounced with the increase of C/S ratio.
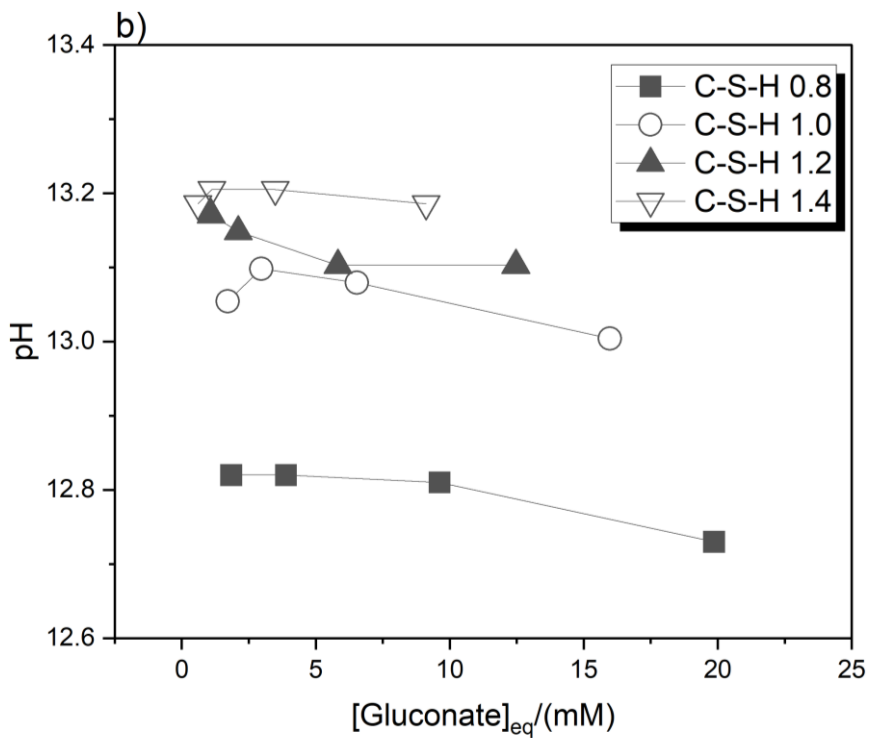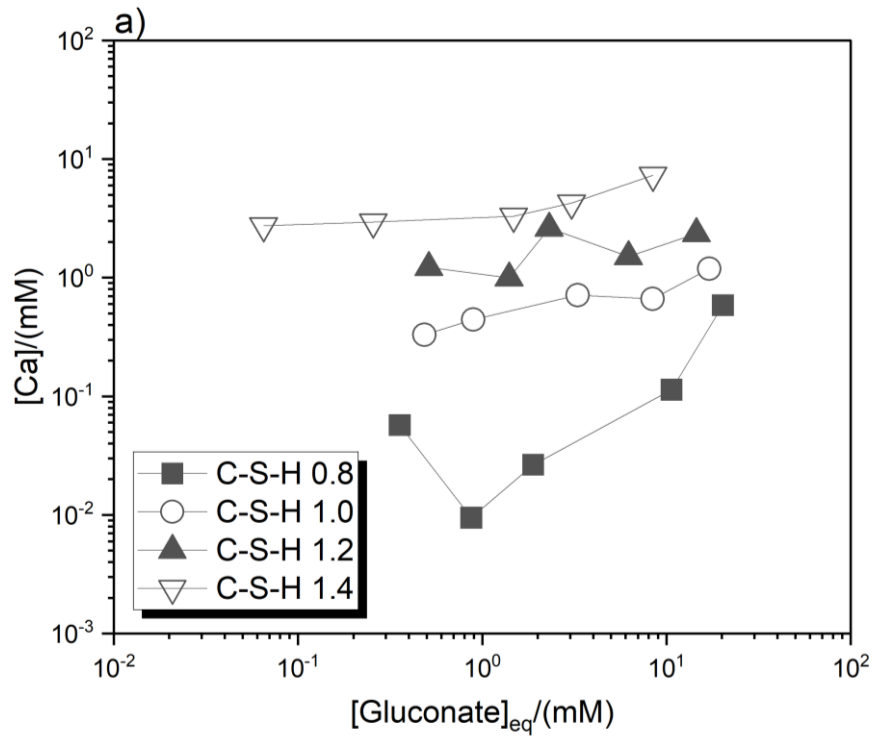
Figure 42. (a) [Ca] aqueous concentration and (b) pH values for C-S-H phases (C/S=0.8 – 1.4) as function of gluconate concentration in solution measured after 7 days of contacting time.

Figure 43 shows the sorption isotherms calculated as moles of gluconate sorbed per kg of C-S-H phases. The quantification of C-S-H weight, calculated by combining mass balance calculation and water content obtained from TGA analysis, is reported in the Table 91 (see the Appendix 3.1). The uptake of gluconate occurs on all C-S-H phases and shows a linear increase with the increase of gluconate concentration.

Gluconate seems to sorb similarly on C-S-H phases with a C/S = 0.8 - 1.0, while for C/S > 1.0, the gluconate-C-S-H phase interactions are stronger: for a fixed $[GLU]_{eq,sol}$ value, the concentration of sorbed gluconate per kg of C-S-H phase increases with the increase of C/S ratio. The uptake of gluconate is, therefore, mediated by complexation with Ca at the surface of C-S-H phases [136].
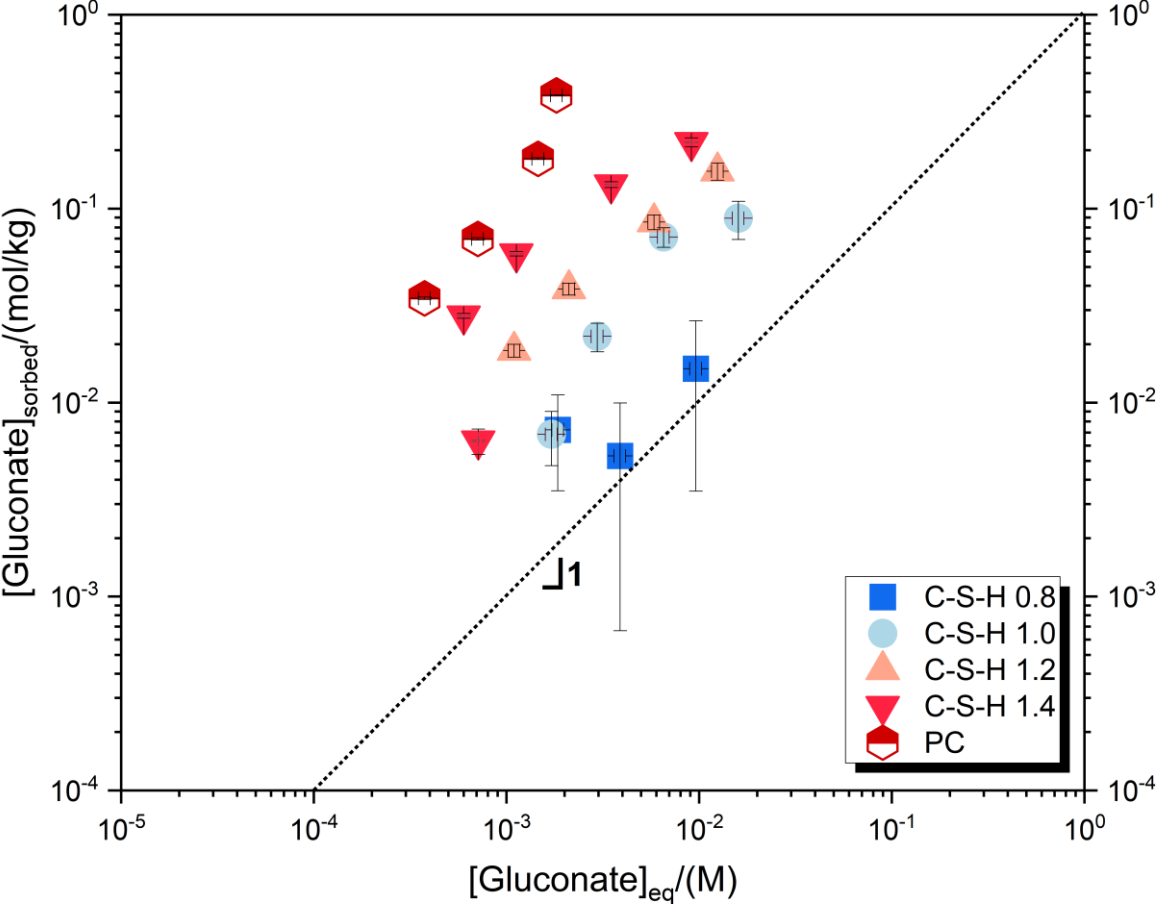
Figure 43. Sorption isotherms calculated as moles of gluconate sorbed per kg of solid phase, for C-S-H phases with a ratio of $0.8 \leq C/S \leq 1.4$ and Portland cement (PC) after 7 days of contacting time the gluconate adding.

Considering all gluconate concentrations, the gluconate uptake increases with the C/S ratio of the solid phase and R_d values of (3.9 ± 2.1) dm³·kg⁻¹, (3.9 ± 1.4) dm³·kg⁻¹, (17.6 ± 0.7) dm³·kg⁻¹ and (35.8 ± 23.5) dm³·kg⁻¹ were obtained for C/S = 0.8, 1.0, 1.2 and 1.4, respectively. The uptake of gluconate on PC occurs with a distribution ratio of (131 ± 55) dm³·kg⁻¹. This latter result indicates that gluconate sorbs

strongly on C-S-H phases, although the potential uptake on the other secondary hydrated phases present in PC cannot be excluded.

3.1.4.2.2.   AFm phases and ettringite

The uptake of gluconate affects both chemical composition and moderately the structure of AFm phases and ettringite. Figure 44 shows the shift of the position of the main basal spacing of Hc in presence of gluconate. The increase of gluconate concentration results in a slight shift of the main basal spacing towards lower $2\theta^o$ values (higher d-values). Both interlayer distances of hemicarbonate (Hc) and carbonated hemicarbonate (cHc, C4Ac0.8H10.2 [238]) increase with the gluconate concentration (Figure 44). Furthermore, the small decrease of peak intensity may indicate a decrease in ordering of the stacking structure in the presence of gluconate. The XRPD characterization carried out on the other phases (see Figure 43-Figure 45 in the Appendix 3.1), indicates only a small effect on the dimensions of the interplanar distance for AFm phase and for the distance $d_{(100)}$ of AFt. In addition, a broadening of the main signal associated with the basal spacing is observed mainly for Hc and Ms, and less for Mc, which may indicate less effect of gluconate Mc. Since the presence of gluconate enhances the concentration of calcium and sulfate (for Ms and AFt) in solution (see below), it is possible to assume that gluconate may sorb in a different sorption site, like edge-layer sites [39] or at the surface of AFm phases and ettringite particles. Also AFt exhibits a slight variation of the distance (100) in the presence of gluconate, and in addition exhibits a much stronger signal intensity in the *a* direction (perpendicular to the columns) than in the absence of organics or in the presence of formate or citrate.
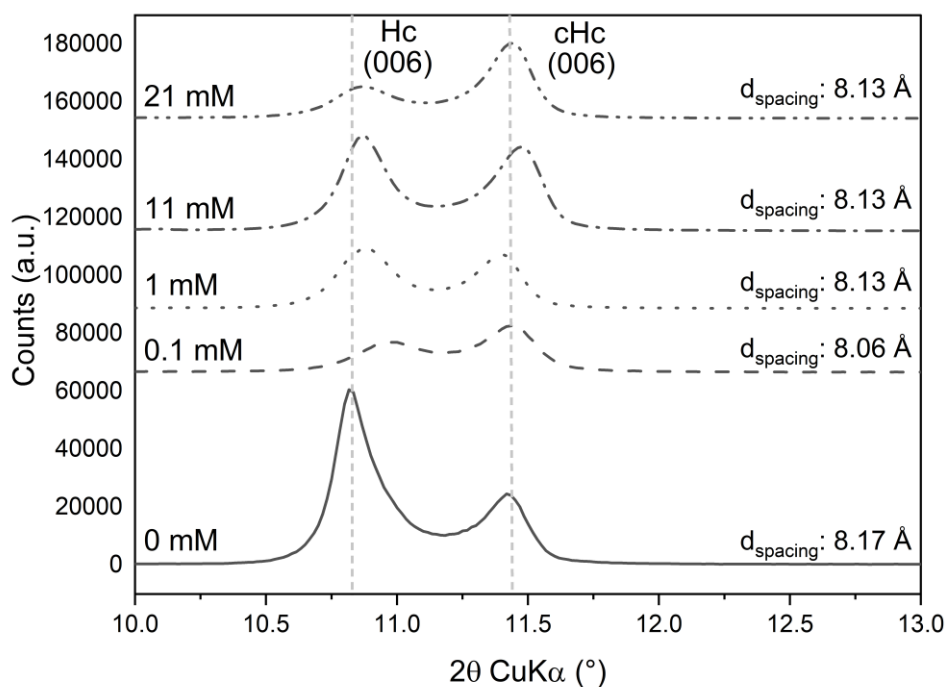
Figure 44. XRPD patterns of hemicarbonate after sorption of gluconate and for contacting time t = 7 days. The figure shows the shift of basal spacing of Hc (hemicarbonate) in the presence of gluconate. cHc indicates carbonated hemicarbonate.

In general, the uptake of gluconate is visible for all phases in the FT-IR spectra, in the wavenumber region 2000-1000 cm^{-1}, as shown in the Figure 25 for Hc. In Figure 45 it is possible to notice the increase of the stretching vibrations bands of the carboxylate group (C=O) with the increase of gluconate concentration while the carbonate stretching band changes not systematically with the gluconate concentration. For Mc the bending vibrations of CO$_3^{2-}$ (1450 – 1400 cm^{-1}, see Figure 46) in the ESM) increase for high gluconate concentration and moderately also the stretching vibrations bands of the carboxylate group. The intensity of the vibration band of the sulfate group increases with gluconate concentration, and for gluconate concentration of 21 mM, it is clear the presence of an additional vibration band related to the carboxylate group of gluconate. In the case of ettringite the stretching vibrations of carboxylate group of formate are covered by the bending vibrations of Ca=OH$_2$ (1660 cm^{-1}) [241], a small shoulder to the Ca=OH$_2$ signal appears in presence of gluconate. The intensity of the sulfate stretching vibration at ≈ 1100 cm^{-1} remains nearly constant with the increase of gluconate (see Figure 48 in the Appendix 3.1).
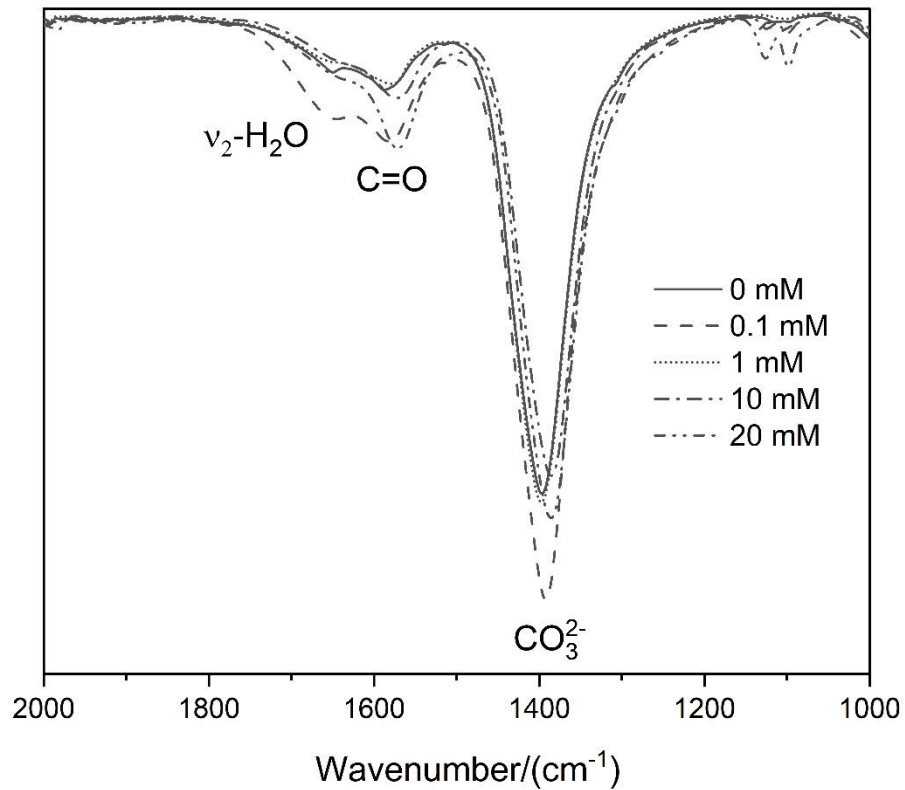
Figure 46. Effect of the initial aimed gluconate concentration on the FT-IR spectra of Hc, hemicarbonate at 7 days of contacting time after the gluconate adding.

The presence of gluconate increases the calcium and sulfate concentrations of AFm phases and ettringite, but lowers the pH in Ms and AFt suspensions by 1 pH unit and slightly lowers the pH in the Hc suspension (Figure 47).

The increase of the sulfate concentration in presence of Ms and ettringite after addition of gluconate indicates a partial replacement of sulfate by gluconate. As observed for formate and citrate, gluconate enhances the dissolution and increases the calcium concentration in solution. Such increase is mainly due to the formation of the aqueous complex $Ca_3(Glu)_2(OH)_4$, which dominates the Ca speciation at $[GLU]_{tot} > 1$ mM as shown for C-S-H 1.4 in the Figure 42 (Appendix 3.1). For high calcium concentration and low gluconate concentration a significant fraction of the complex $Ca_3(Glu)_2(OH)_4$ is predicted to form. In the case of ettringite, the Ca concentration slightly increases for gluconate concentrations 10^{-1} mM $< [GLU]_{eq, sol} < 10^1$ mM, and only for higher gluconate concentration, a steep increase of Ca concentration is observed.
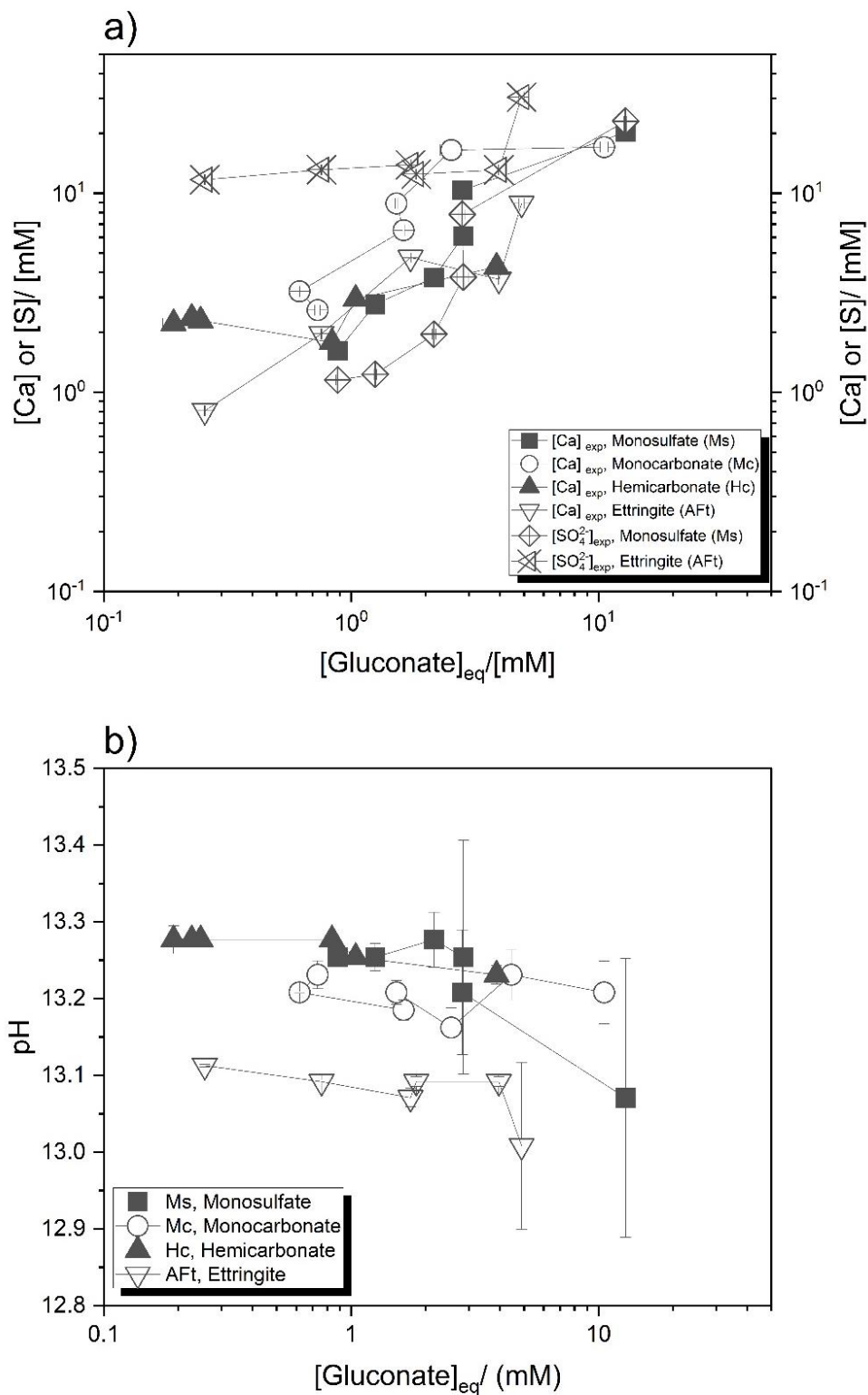
Figure 47. (a) Measured Ca aqueous concentration and (b) pH values of AFm phases (Ms. Mc, and Hc) and AFt, with [Na]$_{tot}$ = 0.2 M and a contacting time of 7 days.

The sorption of gluconate on AFm phases and ettringite is shown in Figure . The overall sorption capacity of AFm phases refers to the sum of surface sorption sites and interlayer sorption capacity. The gluconate sorption experiments show that gluconate sorbs on Ms, Hc and AFt.

In contrast to the uptake of formate or citrate, no clear sorption step was observed for gluconate, which could indicate that it adsorbs both on inter and outer surface sites in the case of Ms and Hc, in agreement with the small widening of the interlayer distance in the XRPD spectra. Also, on ettringite, gluconate sorption seems not to be limited, which might be related to the strong ordering observed in *a* direction of the XRPD signal. For the uptake of gluconate on AFm phases the R_d values of (17.7 ± 11) dm^3/kg (Ms) and (114 ± 83) dm^3/kg (Hc) were derived, while the R_d of (30.5 ± 37.3) dm^3/kg for ettringite was determined.

Following the same approach discussed in the sections 3.1.2.1.2 for formate and 3.1.3.2.2 for citrate, and based on the limited uptake observed for Mc a ratio of outer surface sites to total (outer and interlayer) surface sites equal to 1:300, as indicated by the horizontal lines labelled as outer surface sorption capacity in Figure is applied.
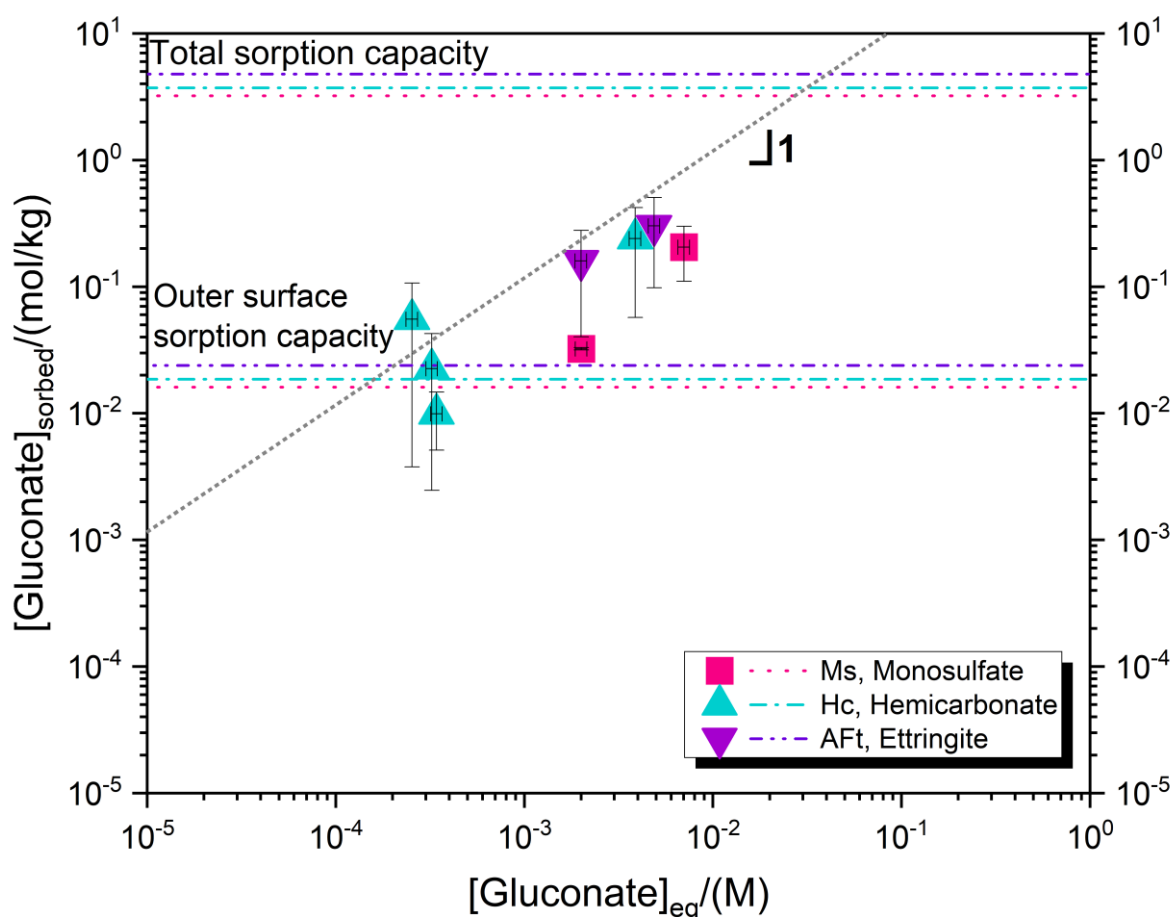
Figure 46. Experimental gluconate sorption isotherm for monosulfate (Ms), hemicarbonate (Hc) and ettringite (AFt) after an equilibration time of 7 days. The upper and lower horizontal lines indicate the overall potential uptake and the uptake on the outer surface of Ms, and Hc respectively.

3.1.5. Summary

In this chapter, the uptake of formate, citrate, and gluconate by various cement hydrates: C-S-H phases, AFm phases, ettringite and hydrated PC was investigated. Formate sorbed significantly weaker than citrate and gluconate. Formate had also little effect on the solid structure of C-S-H phases, AFm phases, and ettringite. As the major fraction of formate remained in solution, a decrease in pH was observed for ettringite, Mc, and C-S-H phases with low C/S ratio.

Citrate and gluconate sorb strongly on the C-S-H phases with high C/S ratio, hinting towards sorption mechanism driven by Ca complexation at the surface. Strong citrate and gluconate uptake was also observed on Hc and Ms, while very limited sorption was observed on Mc. Gluconate and citrate had little effect on the structure of C-S-H, Ms, Mc or ettringite. In the case of Hc an increase of the interlayer distance was observed, suggesting a possible sorption both on the outer surface of Hc as well as in its interlayer.

A slightly stronger uptake of formate, citrate, and gluconate was observed on hydrated PC than on C-S-H, underlining that also AFm phases and ettringite contribute to the binding of organics in hydrated cements.

3.2. Sorption of Pu in presence of formate, citrate and gluconate on cement phases, under reducing and hyperalkaline conditions

In the present chapter the uptake of Pu in the redox, hyperalkaline conditions in presence of formate, citrate and gluconate will be discussed. The uptake is investigated for C-S-H phases with a low (0.8) and high (1.4) C/S ratio, AFm phase and ettringite.

3.2.1.(pe + pH) measurements. Solubility and aqueous speciation

The measured pH_m and E_h (converted into pe) values of all the evaluated samples are plotted in the Pourbaix diagram of Pu shown in Figure . The Pourbaix diagram was prepared taking into account the equilibrium constants and SIT parameters as described in [169]. All pH_m and E_h values of solubility experiments in presence of formate, citrate and gluconate showed stable readings within the timeframe of this study (180 days).

Previous studies conducted under similar conditions in the presence and absence of organic ligands have reported (pe + pH) values for HQ- and Sn(II)-buffered systems [169]. The (pe + pH) values determined in this work for solubility and sorption experiments with HQ or Sn(II) in the presence of formate, citrate and gluconate agree well with previously reported data. Hence, the use of HQ as redox buffer sets moderately reducing conditions with (pe + pH) = (9 ± 1), which corresponds to the stability field of Pu(IV)$_s$ and Pu(IV)$_{aq}$. This system is accordingly considered as the reference case to assess the interaction of Pu(IV) with FOR, CIT and GLU. The use of Sn(II) sets strongly reducing conditions (pe + pH$_m$ = 1.5 ± 0.1), which can eventually promote the coexistence of both Pu(IV) and Pu(III) redox states.
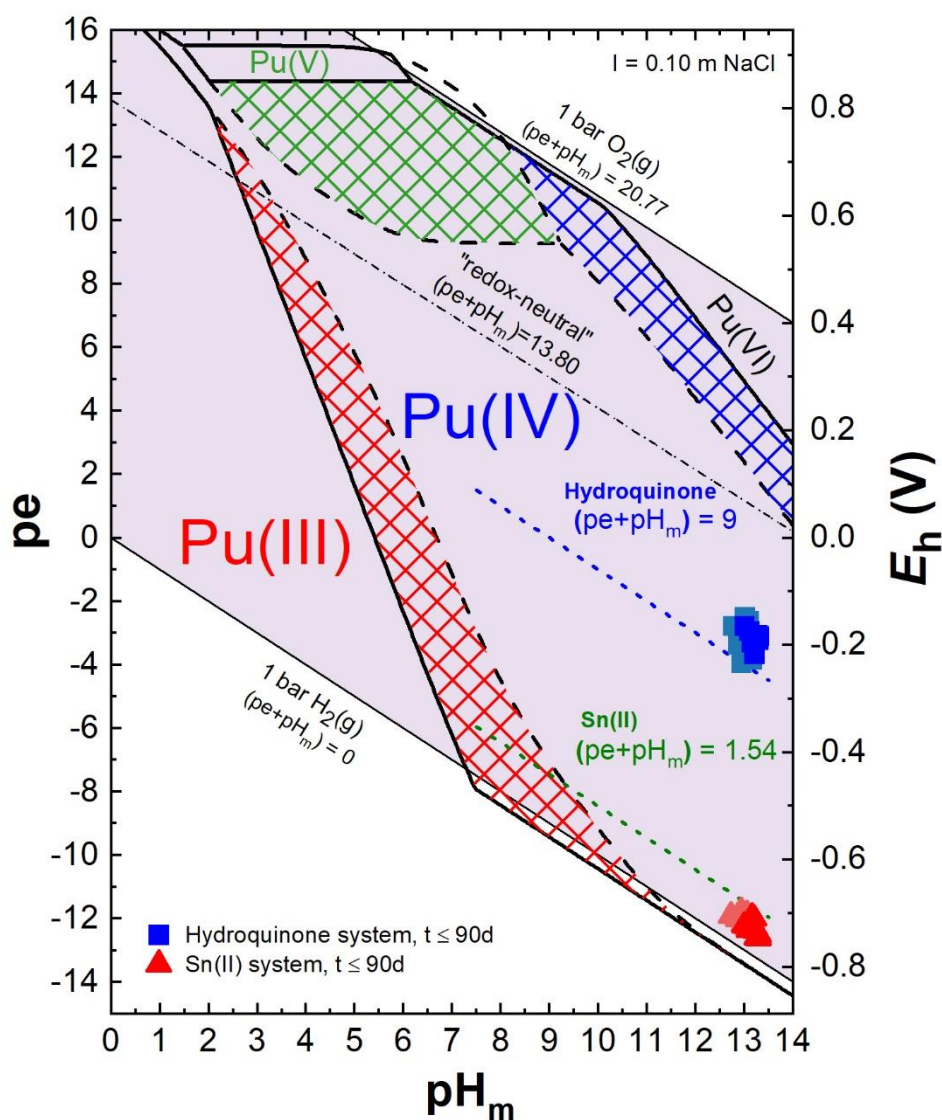
Figure 47. Pourbaix diagram of Pu calculated for m(Pu) = 10⁻⁵ m and I = 0.1 m NaCl using the thermodynamic data and (SIT) parameters as described in the text. pH_m and E_h values experimentally determined for Pu(IV) sorption experiments in the presence of formate, citrate and gluconate and redox-buffering agents: hydroquinone (■) and Sn(II) (▲). Bold lines define the regions the redox reactions between Pu(IV) and other Pu redox states: the solid line are applied to define redox states of Pu solid phases while the dashed line of Pu aqueous species. Colored regions indicate equilibrium between $Pu(IV)_s$ and $Pu(III)_{aq}$ (red), $Pu(V)_{aq}$ (green) and $Pu(VI)_{aq}$ (blue). The borderlines of the stability field of water at (pe + pH_m) = 20.77 and (pe + pH_m) = 0, the "redox-neutral" line at (pe + pH_m) = 13.8 and the lines at (pe + pH_m) = 1.54 and 9 (blue and green respectively) are shown for comparison.

Figure shows the solubility of PuO_2(ncr, hyd) as function of the organic ligand (formate, citrate and gluconate) concentration at constant $pH_m = 13.3$ measured for a contact time of $t \leq 180$ days. Solubility experiments conducted in the presence of formate and citrate show very low Pu concentrations both for HQ and Sn(II) systems, in good agreement with solubility calculations in the absence of organic ligands. These results reflect that both ligands cannot outcompete Pu(IV) hydrolysis in the hyperalkaline conditions investigated in this work. Although this observation appears evident for formate, one may expect a strong complexation of citrate with a hard Lewis acid like Pu(IV). Indeed, previous studies have shown the enhanced stability of the An(IV)-CIT complexes in acidic to moderately alkaline conditions [180, 263]. Hence, Felmy and co-workers showed that the solubility of ThO_2(am, hyd) dominated by Th(IV)-CIT complexes steadily decreased from below pH $\sim$ 8.5, reaching the same concentration as citrate-free systems at pH $\sim$ 12 (see Figure). Data shown in Figure confirm that in the hyperalkaline conditions investigated in this work, An(IV) hydrolysis is expected to dominate over An(IV)-OH-CIT complexes in the aqueous phase.

In the Pu-GLU system (see Figure c), plutonium concentration increases steadily with increasing gluconate concentration. This observation strongly supports the formation of stable Pu-GLU complexes in the aqueous phase. Some differences in solubility are identified for the HQ and Sn(II) systems, with slightly higher Pu concentrations measured in HQ-buffered samples. Differences are remarkable at low ligand concentration, whereas Pu concentrations measured at high $[GLU]_{tot}$ overlap within their corresponding uncertainties. Although these differences may reflect differences in the oxidation state of Pu, the possible complexation of gluconate with Sn(II) (or Sn(IV)) should be also considered. Note that the formation of binary Sn(II)-GLU and ternary Sn(II)-OH-GLU complexes was recently reported by Bretti and co-workers [264]. The possible formation of Sn(II)-OH-GLU complexes in the conditions of this study expectedly result in the decrease of $_{free}$ at $[Sn(II)]_{tot} > [GLU]_{tot}$.

A slope of $\sim$ 1 (log [Pu] $vs.$ log $[GLU]_{tot}$) may be assumed in the Figure c even though not fully compatible with the plotted experimental data. This assumption supports the formation of aqueous complex with a stoichiometry (Pu : GLU) $\sim$ 1 : 1 as prevailing species. In this study, solubility was investigated at constant pH, and thus no information on the (Pu : OH) ratio in the aqueous complexes could be derived. The solubility of ThO_2(am, hyd) in the presence of gluconate was previously investigated by Colàs et al. and Adam et al. [177, 191]. Based on the pH-independent behaviour of the solubility data, both studies suggested the predominance of the complex $Th(OH)_4GLU^-$ (or $Th(OH)_2GLU_{-2H}^-$) at pH < 12. An increase of the solubility of Th(IV) with a slope of $\sim$ 1 (log [Th] vs. pH_m) was observed by Adam and co-workers at pH > 12, which supports the formation of the complex $Th(OH)_5GLU^{2-}$ (or $Th(OH)_3GLU_{-2H}^{2-}$). The comprehensive thermodynamic and spectroscopic study of [186] supported by DFT calculations on Pu-ISA system suggested the formation of two Pu(IV) complexes in the HQ buffered system, $Pu(IV)(OH)_3(ISA_{-H})^-$ and $Pu(IV)(OH)_3(ISA_{-2H})^{2-}$, which involve the deprotonation ion of both α– and γ–OH groups of ISA.
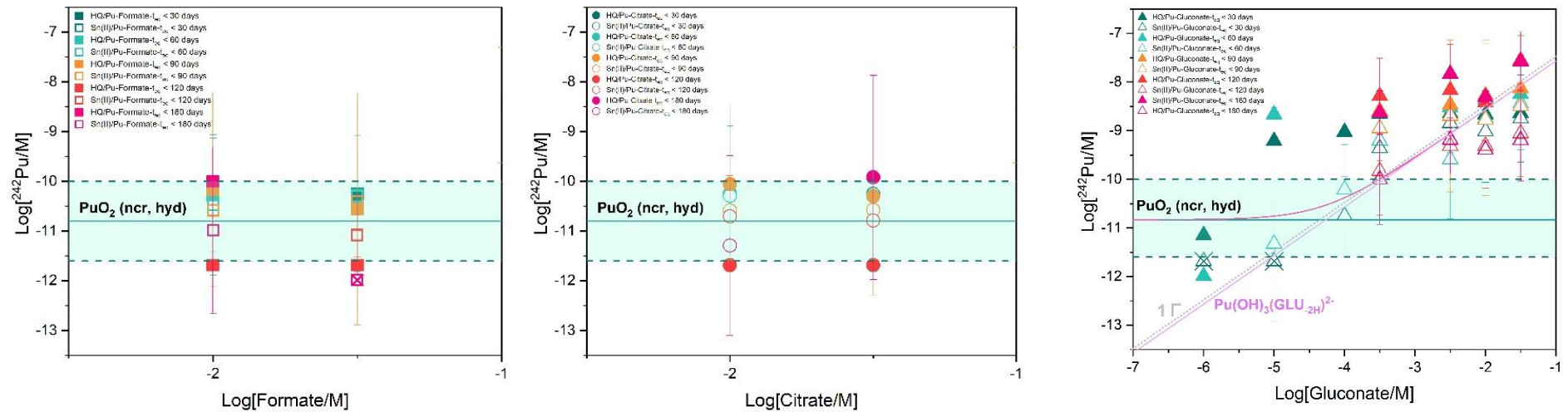
Figure 48. Experimentally measured $^{242}Pu_{tot}$ concentration in equilibrium with PuO$_2$(ncr,hyd) at pH$_m$ = 13.3 and equilibration times t_{eq} < 180 days, as function of the total ligand concentration (a) formate; (b) citrate; (c) gluconate. Solubility data obtained in the presence of HQ (full symbols) and Sn(II) (empty symbols). Solid and dashed lines represent the solubility of Pu(IV) and corresponding uncertainties calculated for the equilibrium reaction PuO$_2$(ncr, hyd) + 2H$_2$O(l) $\Leftrightarrow$ Pu(OH)$_4$(aq).
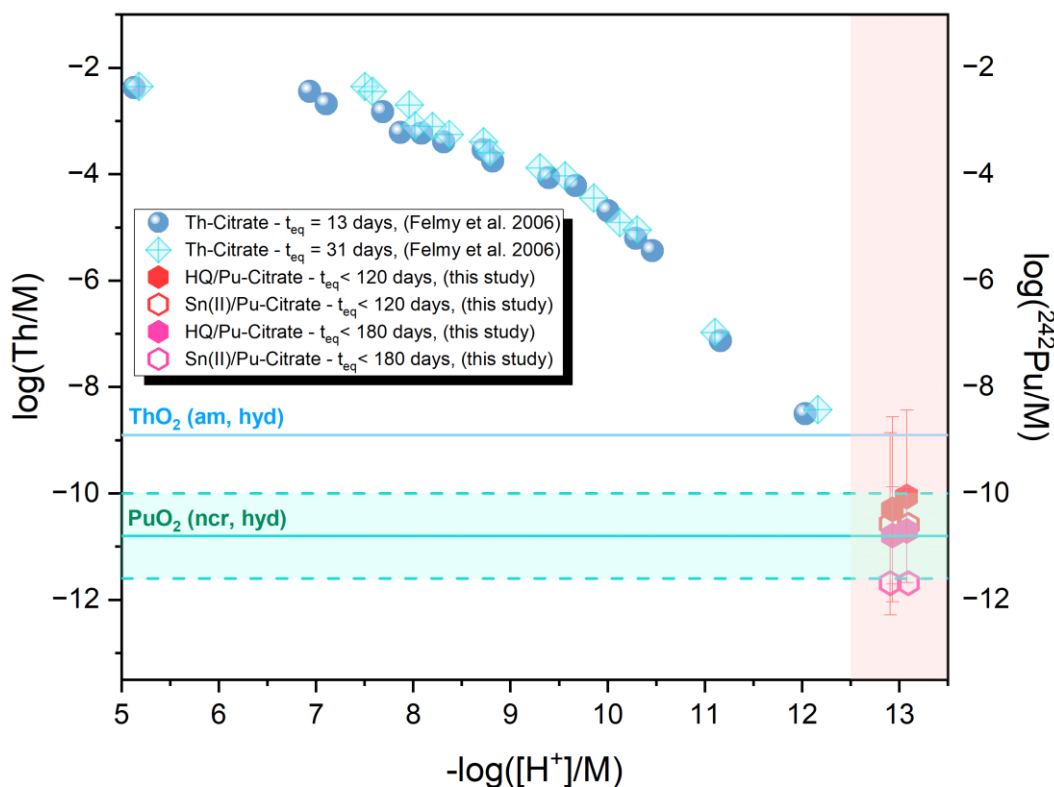
Figure 49. Solubility of ThO₂(am, hyd) in the presence of [CIT]ₜₒₜ = 0.01 M at I = 0.5 M NaNO₃ as reported in [180], and solubility of PuO₂(ncr, hyd) as determined in this work at pH ~ 13 and various citrate concentrations. Solid blue line shows the solubility of Th(IV) calculated for CIT-free systems using the NEA-TDB thermodynamic selection. Solid and dashed green lines represent the solubility of Pu(IV) and corresponding uncertainties calculated in this work.

Based on the results reported for the Th(IV)-GLU system, and considering the analogy with the Pu(IV)-ISA system, the following equilibrium reaction is proposed to control the solubility of the investigated Pu-GLU system:

$$PuO_2(ncr, hyd) + GLU^- + H_2O(l) \leftrightarrow Pu(OH)_3(GLU_{-2H})^{2-} + H^+ \qquad Eq. 1$$
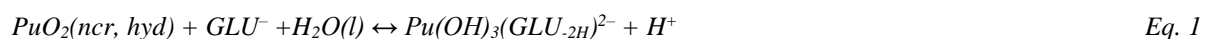
A conditional solubility constant can be calculated for this equilibrium reaction on the basis of the experimental values of [Pu] and pH_m, and assuming $[GLU]_{tot} = [GLU]_{free}$, *i.e.* $\log K'_{s,(1,3,1,-2)}$ ($I = 0.2$ M) $= -(19.1 \pm 1.2)$. Considering $\varepsilon(Pu(OH)_3(GLU_{-2H})^{2-}, Na^+) = \varepsilon(Pu(OH)_3(ISA_{-2H})^{2-}, Na^+) = -(0.10 \pm 0.10)$ kg·mol⁻¹, the conditional constant can be extrapolated to the reference state, resulting in $\log K^{\circ}_{s,(1,3,1,-2)}$ $= -(19.8 \pm 1.2)$. The combination of this value with $\log K^{\circ}_{s,0}(PuO_2(ncr, hyd)) = -(2.33 \pm 0.52)$ as reported by Tasi and co-workers [186] for the same solid phase, results in:

$$Pu^{4+} + 3H_2O(l) + GLU^- \leftrightarrow Pu(OH)_3(GLU_{-2H})^{2-} + 5H^+ \qquad Eq. 2$$

$\log \beta^{\circ}_{(1,3,1,-2)} = -(17.4 \pm 1.3)$

This value shall be considered tentative, until solubility experiments under varying pH_m are conducted to validate the proposed stoichiometry (Pu : OH) of the complex.

3.2.2. Ternary systems: C-S-H / Pu / Formate and C-S-H / Pu / Citrate

The effect of formate on the uptake of Pu by C-S-H phases in alkaline reducing conditions is shown in the Figure 48. Considering the ligand-free system as reference, no significant differences were evidenced for the systems containing $[FOR]_{tot} = 10^{-4}$ and $10^{-1.5}$ M. This observation underlines the weak interaction of formate with Pu for both HQ and Sn(II) buffered systems and therefore the small relevance of the complexing capacity of this organic ligand under the chemical conditions applied. These observations are consistent with the solubility data described in Section 3.2.1 for the system Pu-FOR. Similarly, to the system C-S-H-Pu-FOR, citrate does not affect the retention behavior of Pu on C-S-H phases under alkaline and reducing conditions. Most of the $[Pu]_{aq}$ data collected for this system are located at the detection limit and are not affected by changes in the C/S ratio of the redox buffer. As mentioned in the solubility experiments section, the negligible effect of citrate retention on Pu by C-S-H phase (Figure 51) is mainly due to the weak complexing capacity of citrate with respect to An(IV) under hyperalkaline conditions [180]. Similar results in presence of formate and citrate were observed for the system investigated with higher S/L ratio (i.e. 25 g/dm³).
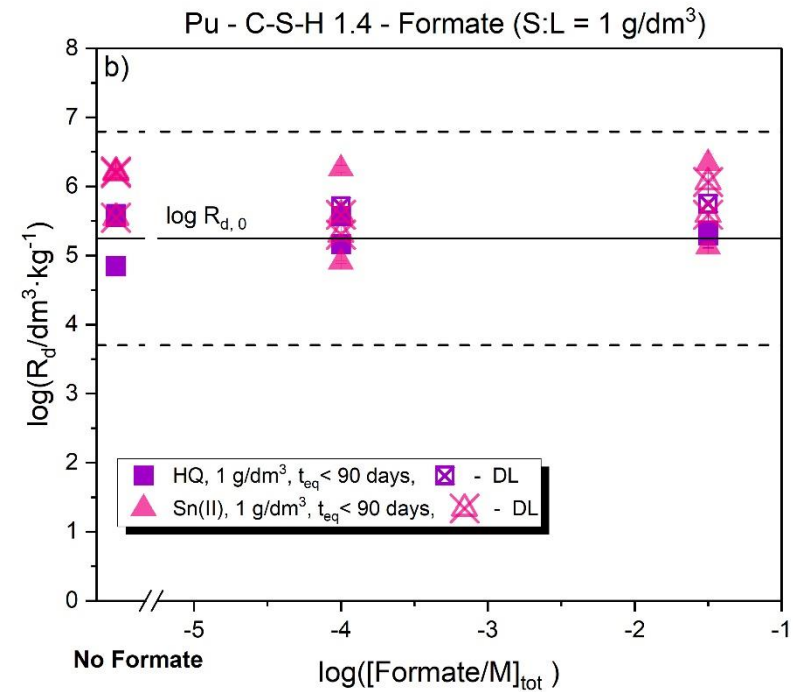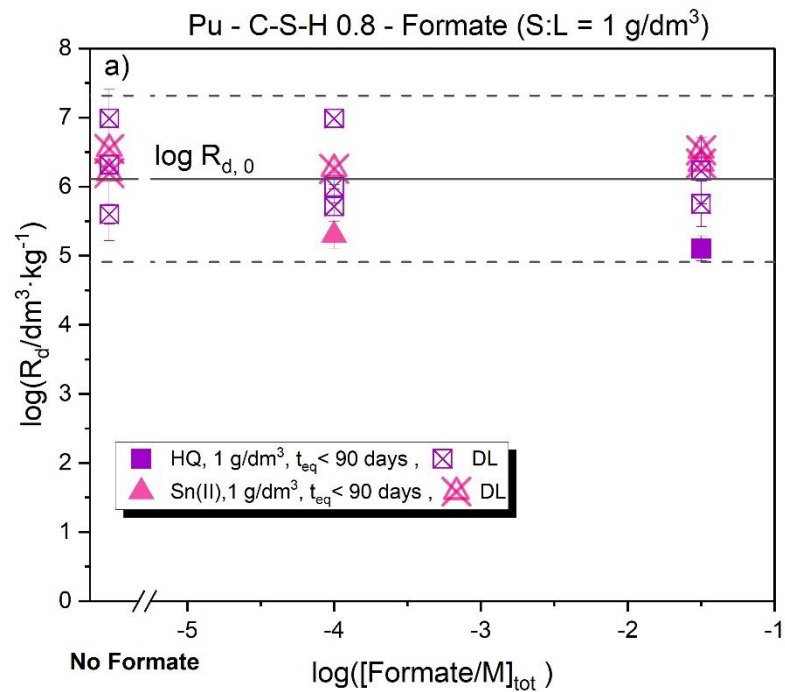
Figure 48. Distribution ratios, R_d, determined for the system (Pu-C-S-H)+FOR, for (a) C-S-H with C/S = 0.8; and (b) C-S-H with C/S = 1.4. In both cases data corresponding to pH ≈ 13.3, S/L = 1 g·dm^{-3} and 90 days of contact time. X crossed symbols refers to values at the detection limit.
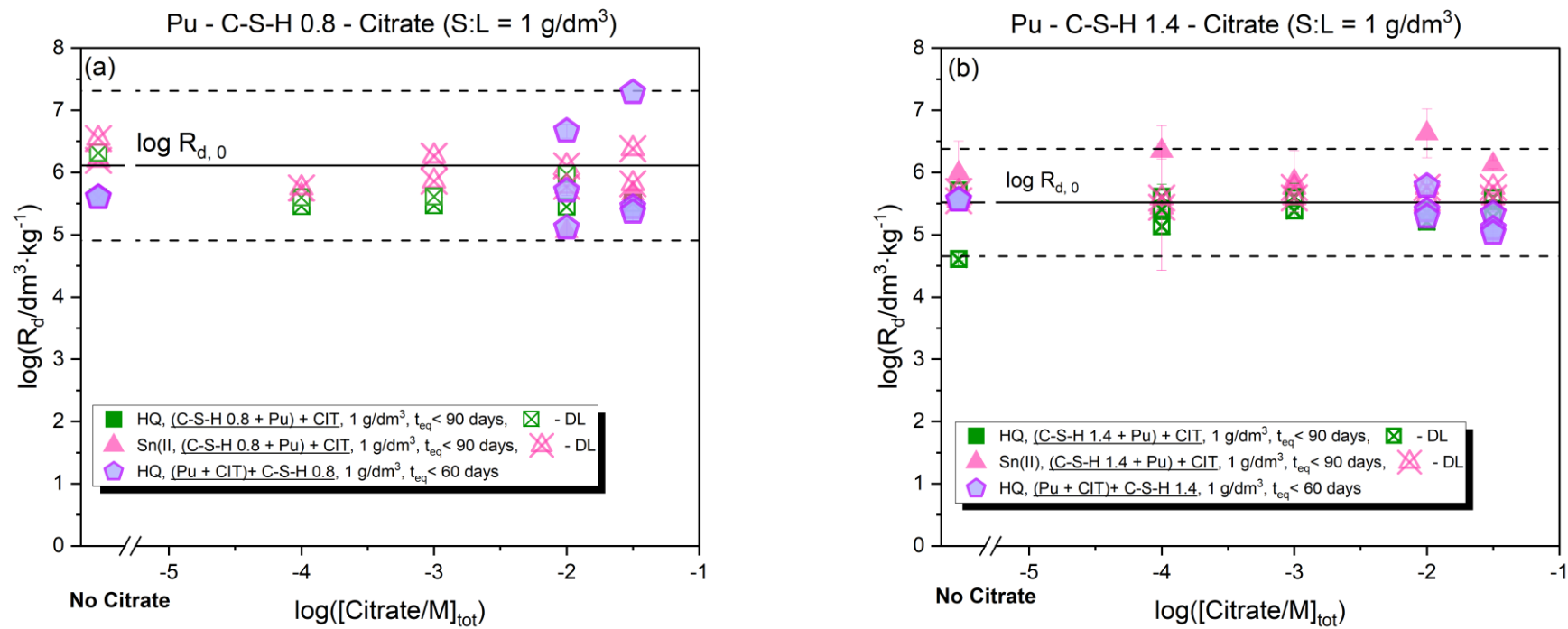
Figure 49. Distribution ratios, R_d, determined for the system (C-S-H-Pu)+CIT (t_{eq} < 90 days) and the system (Pu+CIT)+C-S-H (t_{eq} < 60 days), for (a) C-S-H with C/S = 0.8; and (b) C-S-H with C/S = 1.4. In both cases data corresponding to pH ≈ 13.3, S/L = 1 g·dm^{-3}. X crossed symbols refers to values at the detection limit.

3.2.3. Binary and ternary systems C-S-H / Pu and C-S-H / Pu / Gluconate

The effect of gluconate on the uptake of Pu by C-S-H phases is shown in the Figure 50. The average distribution ratio determined in the absence of gluconate, log $R_{d,0}$ = (6.1 ± 1.2), is in excellent agreement with the value previously reported by [4] for the uptake of Pu by HCP, *i.e.* log $R_{d,0}$ = (6.3 ± 0.6). This observation confirms the key role of C-S-H phases in the uptake of actinides by HCP, as extensively discussed in the literature [1, 168].

Figure 52 shows that gluconate strongly decreases the uptake of ^{242}Pu by C-S-H phases, both for C/S = 0.8 and 1.4. No significant differences can be observed for the two redox buffers, HQ and Sn(II), except at log[GLU]$_{tot}$ = −1.5. At this ligand concentration and notably for C-S-H phase with a C/S = 1.4, the decrease in sorption is less pronounced when Sn(II) is used as a redox buffer. This last observation may could reflect differences in the oxidation state of Pu in HQ and Sn(II) systems. Although such differences were not observed in the solubility experiments described in Section 3.2.1, it can be speculated that the different behavior of the Pu retention for the Sn(II) buffered system may hint towards the formation of stable surface complexes possibly involving the quaternary system >Ca(II)–Pu(III)–OH–GLU. Note that the formation of analogous surface complexes were proposed by Tasi and co-workers to explain their experimental observations in the system HCP–Pu–ISA [4]. The lack of reliable thermodynamic models for the Ca(II)-Pu(III/IV)-OH-GLU systems hinders a conclusive interpretation of the sorption data in the current study. Another uncertainty comes from the potential impact of Sn-GLU complex formation, which has already be discussed for the solubility studies in Section 3.2.1.

The effect of the order of addition of the individual components on the retention of plutonium in the presence of citrate and gluconate was investigated for contact times < 60 days (see
Figure 49 and Figure 50). The order of addition (Pu + L) + C-S-H does not affect Pu retention in presence of citrate, and thus similar log R_d values as those reported in
Figure 49 are obtained for both Ca/Si ration 0.8 and 1.4. This observation reflects again that citrate cannot outcompete Pu hydrolysis in the hyperalkaline conditions investigated in this work. In the case of gluconate, comparable log R_d values are quantified for the order of addition (Pu + GLU) + C-S-H, with respect to (C-S-H + Pu) + GLU as well. Note that Tasi and co-workers reported a kinetic hindrance of sorption for the sequence (Pu + ISA) + HCP [4]. These results were explained by the transient stabilization of Pu-ISA aqueous moieties / colloids in the sorption studies following the sequence (Pu + ISA) + HCP, which however decompose with time expectedly resulting in similar R_d values obtained for the sequence (HCP + Pu) + ISA. In spite of the chemical similarities between ISA and GLU, they show also clear differences in terms of sorption properties (significantly stronger uptake of GLU than ISA by cement and C-S-H) and complexation behaviour (significantly stronger RN-GLU than RN-ISA complexes), which may also explain the differences between the corresponding ternary systems.
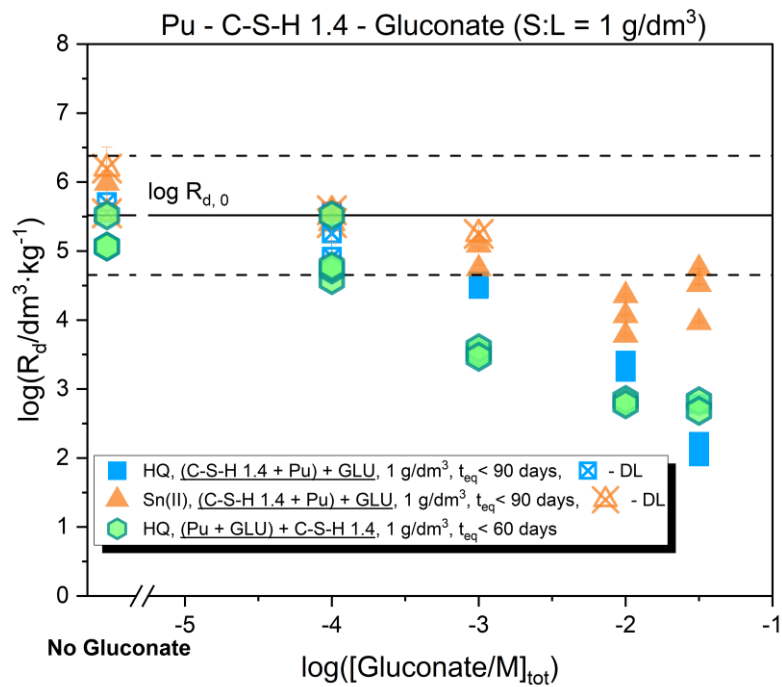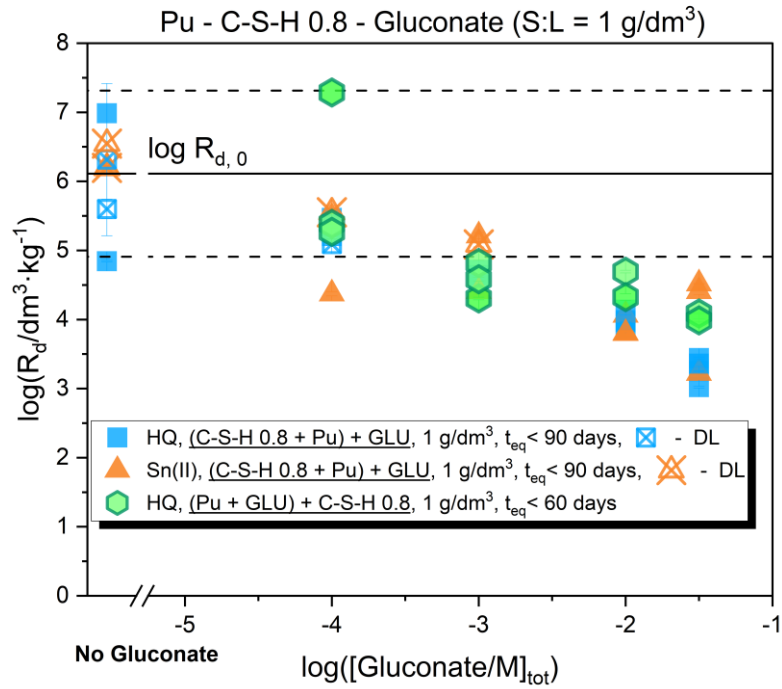
Figure 50. Distribution ratios, R_d, determined for the system (C-S-H + Pu) + GLU, for (a) C-S-H with C/S = 0.8; and (b) C-S-H with C/S = 1.4. In both cases data corresponding to pH ≈ 13.3, S/L = 1 g·dm⁻³ and 90 days of contact time (t_{eq}). X crossed symbols refers to values at the detection limit.

3.2.4. Binary and ternary systems AFm-AFt / Pu and AFm-AFt / Pu / FOR

In the absence of organic ligands, an average log $R_{d,0}$ of (5.6 ± 1.0) for AFm phases and of (5.7 ± 1.1) for AFt were measured. This highlights that the uptake of Pu is very strong not only in the case of C-S-H phases but also for AFm and AFt phases. There are virtually no previous studies in the literature investigating the uptake of An(III) or An(IV) by AFm / AFt phases. On-going work at CIEMAT (Spain) on the uptake of ^{238}Pu(IV) by ettringite resulted in log R_d values of 4.6–5.0, in line with experiments conducted in the present work with ^{242}Pu (T. Missana, personal communication). Farr and co-workers studied the uptake of Pu(IV) by brucite $Mg(OH)_2$ by means of sorption experiments and X-ray photoelectron spectroscopy (XPS) [195]. The authors observed a strong uptake within the investigated pH-range (9 – 12), and proposed that surface sorption and incorporation (into the crystal structure) are the most relevant uptake processes of Pu(IV) on brucite.

Figure 51 shows the effect of formate on the uptake of plutonium on AFm phases and ettringite. The comparison with the R_d values obtained in the absence and presence of formate indicates that the uptake of plutonium by AFm / AFt phases is not affected by formate. This observation is valid for both HQ and Sn(II) buffered-systems. Furthermore, the Ca aqueous concentration measured for longer equilibration times (see Table 4 and Table 5 in the Appendix 3.2) does not show any increasing trend at high formate concentration. These results indicate the weak complexation capacity of formate with respect to Pu and Ca in the hyperalkaline conditions investigated in this work. These observations are consistent with sorption experiments conducted for the ternary system C-S-H / Pu / FOR (see Section 3.2.2), as well as with solubility data discussed in Section 3.2.1.
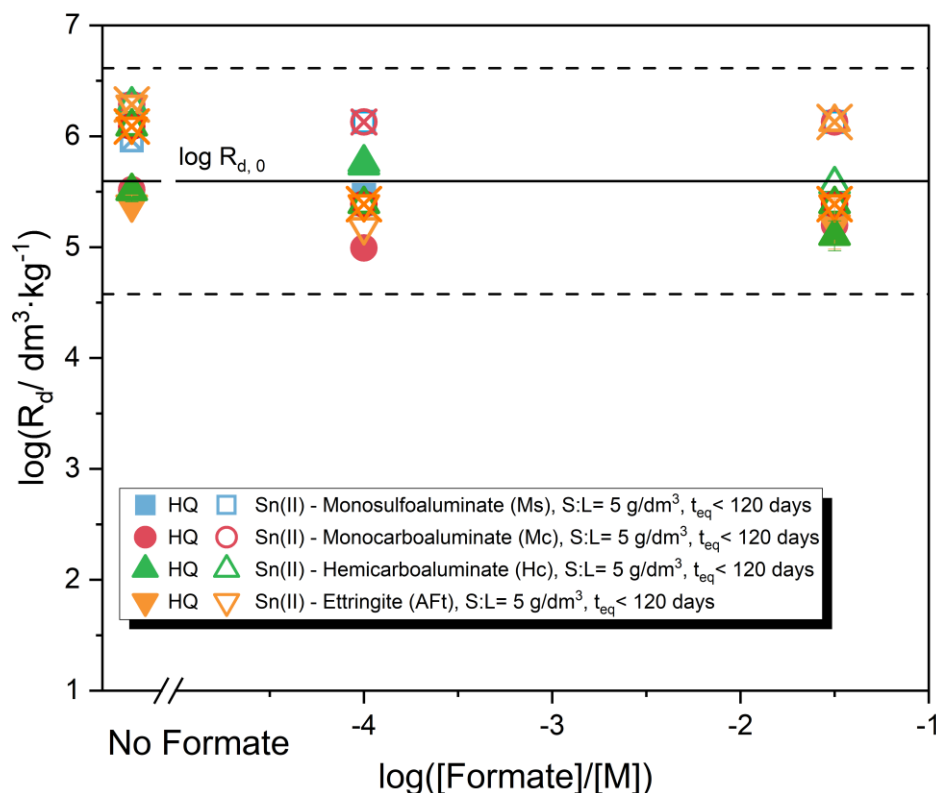
Figure 51. Distribution ratios, R_d, determined for the systems (AFm+ Pu) + FOR and (AFt+ Pu) + FOR. In both cases data corresponding to pH ≈ 13.3, S/L = 5 g·dm⁻³ and 120 days of contact time. X crossed symbols refers to values at the detection limit.

3.2.5. Ternary systems: AFm-AFt / Pu / CIT

The distribution coefficients determined for the uptake of Pu by AFm phases and ettringite in presence and absence of citrate are shown in Figure 52. The sorption of Pu remains unaffected up to log $[CIT/M]_{tot}$ < 2, but decreases at higher ligand concentrations, both for HQ and Sn(II) systems. Although the mechanism responsible for the uptake of Pu by AFm / AFt phases remains ill-defined, changes in the surface / structural properties of the latter phases may lead to a differential sorption behaviour with respect to Pu.
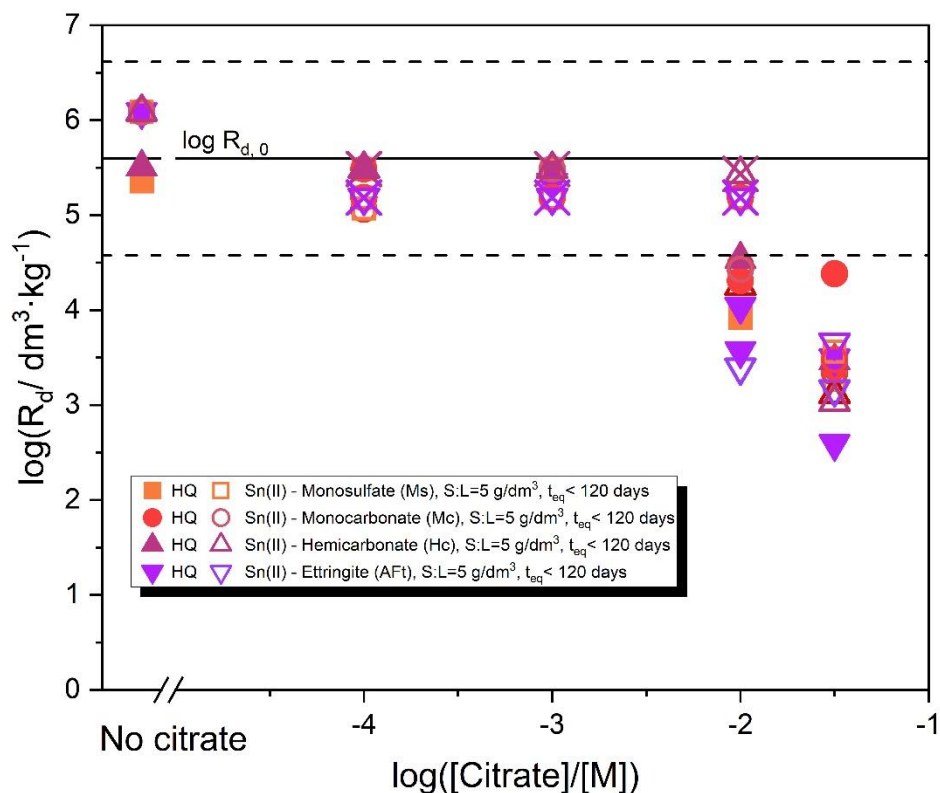
Figure 52. Distribution ratios, R_d, determined for the systems (AFm+ Pu) + CIT and (AFt+ Pu) + CIT. In both cases data corresponding to pH ≈ 13.3, S/L = 5 g·dm^{-3} and 120 days of contact time. X crossed symbols refers to values at the detection limit.

3.2.6. Ternary systems: AFm-AFt / Pu / GLU

The distribution ratios determined for the uptake of plutonium by AFm/AFt phases in absence and presence of gluconate and for the HQ- and Sn(II)- buffered systems are shown in the Figure 53 and Figure 54 respectively. For both HQ and Sn(II) systems, gluconate decreases the Pu retention by AFm / AFt phases at ligand concentrations even lower than log[GLU]$_{tot}$ ~ –4. This effect is even more remarkable than such observed for C-S-H phases. Although the values of log $R_{d,0}$ for C-S-H, AFm and AFt phases in the absence of organic ligands are similar, the trends in the distribution coefficients with increasing ligand concentration are significantly different for C-S-H and for AFm / AFt phases. As discussed for citrate, this observation highlights that in addition to the complexes possibly forming in the aqueous phase, gluconate has a significant impact on the surface / structural properties of AFm / AFt phases, and thus on their sorption properties.

116
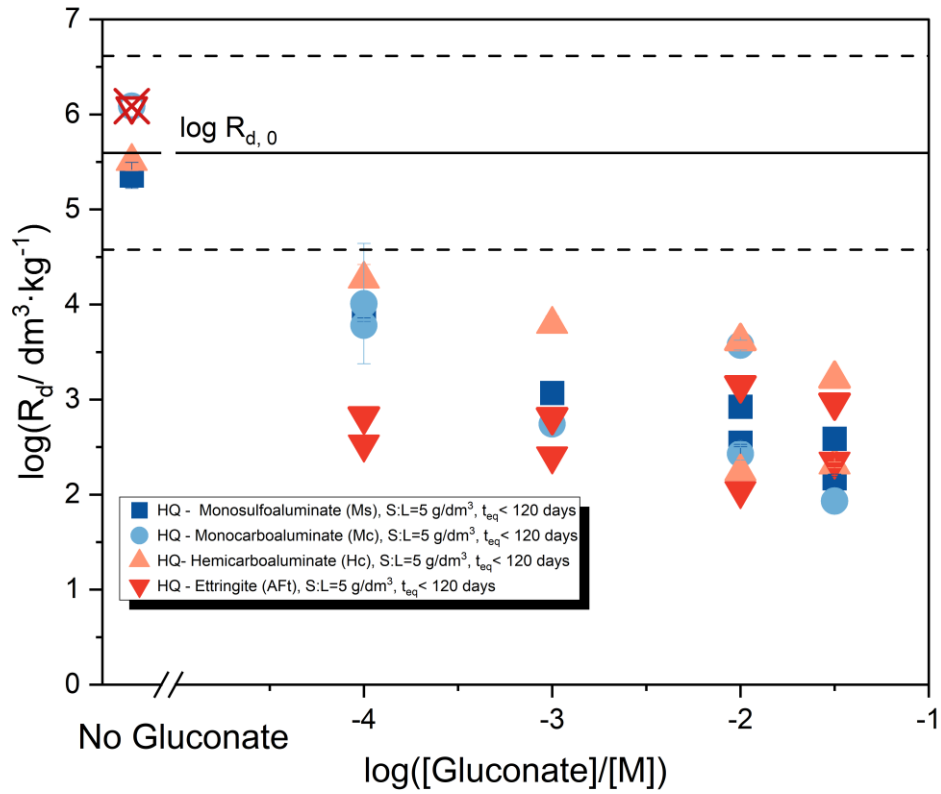
Figure 53. Distribution ratios, R_d, determined for the HQ-buffered systems (AFm+ Pu) + GLU and (AFt+ Pu) + GLU. In both cases data corresponding to pH ≈ 13.3, S/L = 5 g·dm⁻³ and 120 days of contact time. X crossed symbols refers to values at the detection limit.
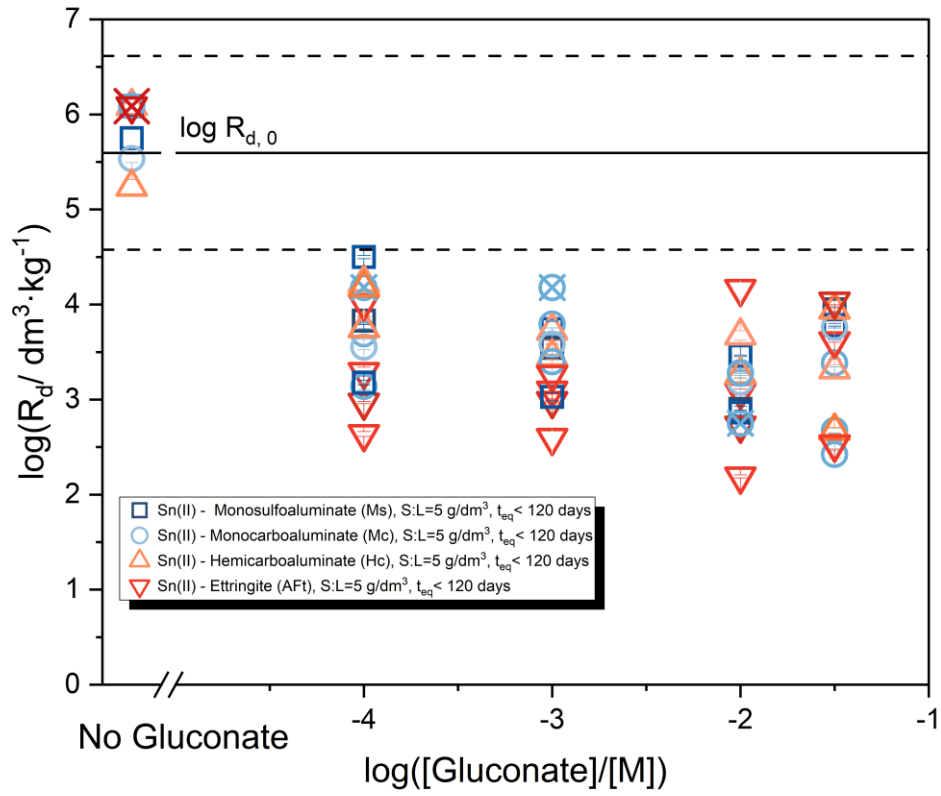
Figure 54. Distribution ratios, R_d, determined for the Sn(II)-buffered systems (AFm+ Pu) + GLU and (AFt+ Pu) + GLU. In both cases data corresponding to pH = 13.3, S/L = 5 g·dm⁻³ and 120 days of contact time. X crossed symbols refers to values at the detection limit

3.3. Uptake of Eu(III) by C-S-H phases in the absence and presence of formate, citrate and gluconate

The first part of this chapter focuses on the uptake behavior of Eu(III) by C-S-H phases in the absence and presence of formate, citrate and gluconate. As described in the chapter 2, for these systems only one order of addition was investigated: (C-S-H + RN) + L. C-S-H phases with a C/S of 0.8 and 1.4 were considered for the study of the three ligands.

The second part of this chapter is dedicated to the TRLFS (Time Resolved Laser induced Fluorescence Spectroscopy) analysis on the binary Cm(III) – GLU and ternary C-S-H – Cm(III) – GLU systems. The corresponding results complement the observations obtained from the sorption study, in particular, on the different sorption behavior observed for C-S-H phases with low and high C/S and the Ln(III) / An(III) speciation in presence of GLU.

3.3.1. Ternary systems: C-S-H / Eu(III) / FOR and C-S-H / Eu(III) / CIT

Figure 58 shows the uptake behavior of Eu(III) in the absence and presence of formate on C-S-H phases with a C/S = 0.8 and 1.4. In the absence of organic ligands, most of the measured data were found at the detection limit, resulting in very high R_d values, *i.e.* $\approx 10^{3.5}$ m^3/kg. These values are in line with previous studies investigating the uptake of Eu(III) by C-S-H phases and HCP, for which R_d values of $\approx 10^2$–10^4 m^3/kg and fast sorption kinetics were reported [1, 5, 24, 265, 266]. The formation of stable complexes of Eu(III) with the investigated organic ligands would result in a decrease of RN sorption on the solid phase. Formate has a negligible effect on Eu(III) uptake by C-S-H phases (see Figure 58), which is in line with the tendency of Eu(III) to form weak complexes with formate under hyperalkaline conditions [79]. The latter complexes can neither compete with hydrolysis nor with the strong Eu(III) sorption on C-S-H phases. A negligible effect on the uptake of Eu(III) by C-S-H phases with a C/S of 0.8 and 1.4 was also observed for citrate (Figure 59). Only for high C/S ratio (Figure 59b), a decrease of ≈ 0.5 log (R_d) units occurred for citrate concentration $[CIT]_{tot} = 10^{-2}$ M and contacting times shorter than 60 days, while for longer equilibration times no effect on Eu(III) retention was observed. Considering the high affinity of citrate to sorb on the surface of C-S-H phases ($R_d = 10$ dm^{-3}·kg^{-1} for C/S = 1.4), as discussed in the chapter 3.1, it is possible to assume that for longer equilibration times, the C-S-H-CIT interactions prevails over the Ca-Eu-CIT complexes formation. Note as well that thermodynamic calculations conducted using the ThermoChimie database indicate the predominance of Eu(III) hydrolysis species at $10 \leq pH \leq 13.5$, $[CIT]_{tot} = 10^{-1.5}$ M and $[Ca] = 10^{-3}$ M (see Figure 60). Note however, that no ternary and quaternary complexes (Ca)-An(III)-OH-CIT are currently selected in the ThermoChimie database, whose formation may affect aqueous speciation and thus sorption, especially in C-S-H systems with high C/S ratios and higher [Ca] in the aqueous phase. The formation of quaternary complexes Ca-An(III)-OH-EDTA was recently proposed by DiBlasi and co-workers based on a combined solubility and TRLFS study [178], and similar complexes might be expected for the citrate system.
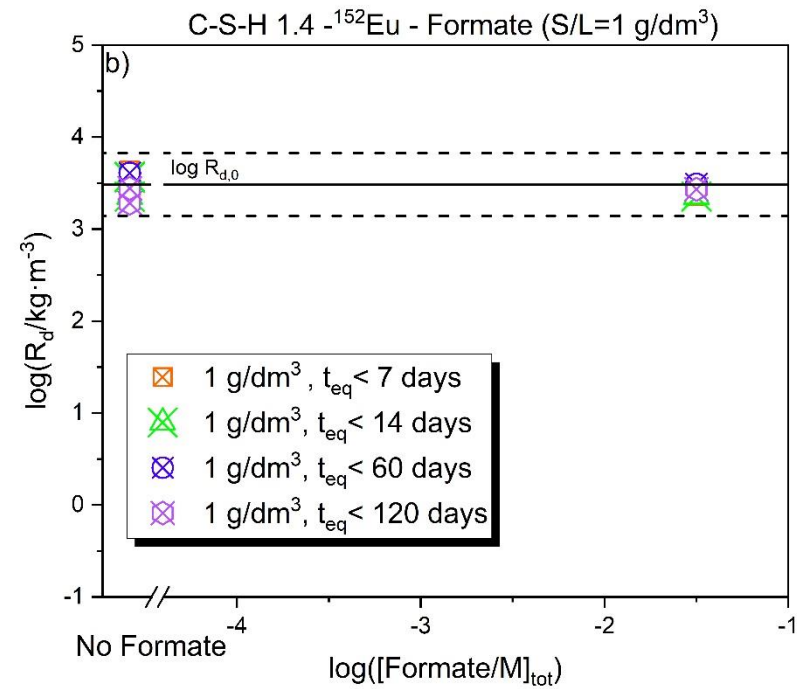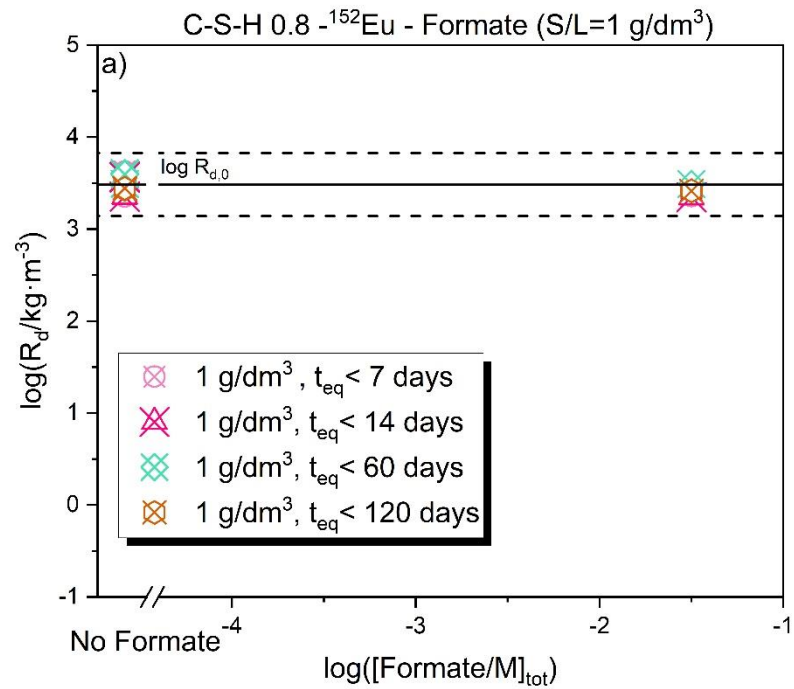
Figure 58. Distribution coefficients, R_d, for the uptake of ^{152}Eu in absence and in presence of formate ($log([FOR]_{tot}/M) = -1.5$) on C-S-H phases with a C/S of 0.8 (a) and 1.4 (b) for a contacting time $t_{eq} < 120$ days under hyperalkaline conditions (pH ≈ 13.3).
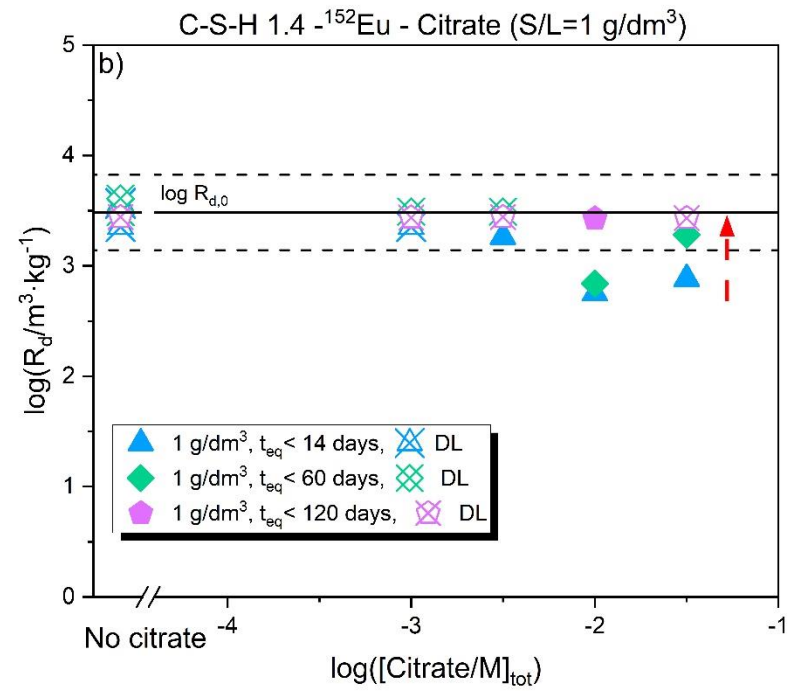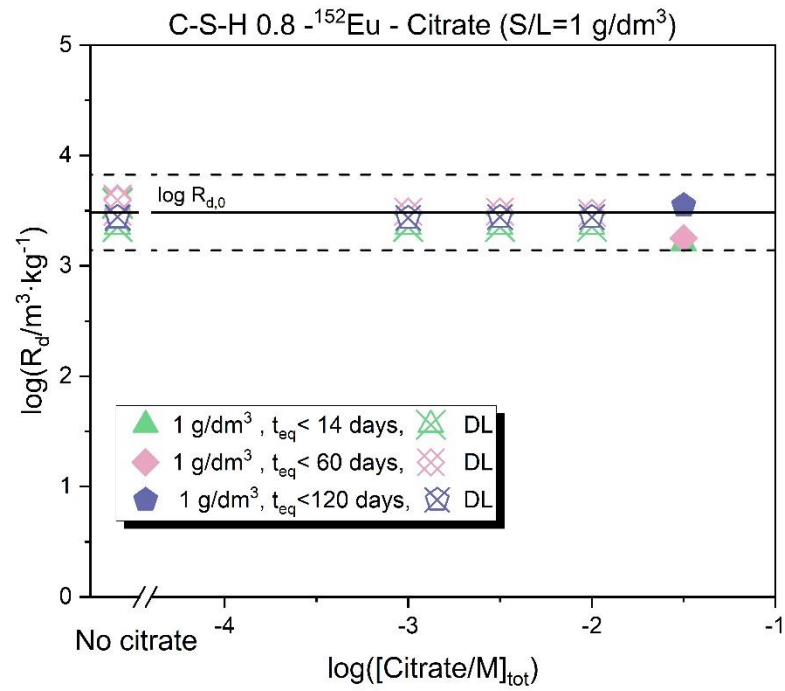
Figure 59. Distribution coefficients, R_d, for the uptake of ^{152}Eu in absence and in presence of citrate ($-3 \leq log([CIT]_{tot, in}/M) \leq -1.5$) on C-S-H phases with a C/S of 0.8 (a) and 1.4 (b) for a contacting time $t_{eq} < 120$ days under hyperalkaline conditions (pH $\approx$ 13.3).
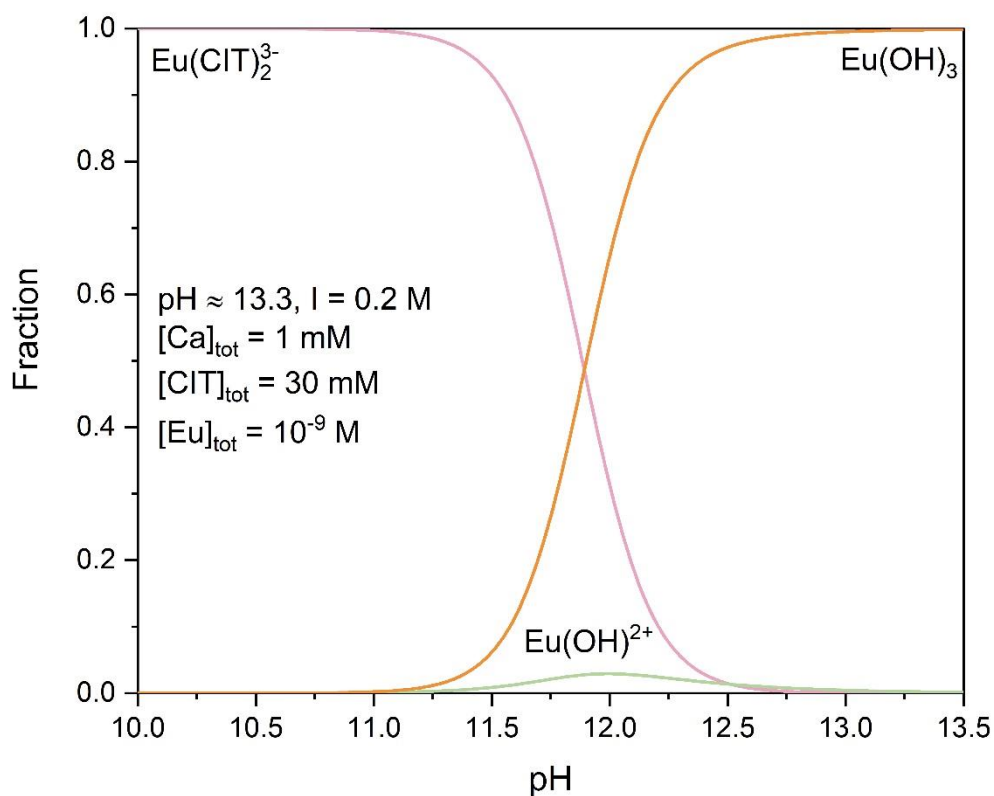
Figure 60. Species distribution diagram of Eu(III) calculated for [CIT]$_{tot}$ = 30 mM, [Ca]$_{tot}$ = 1 mM and I = 0.2 M. The ThermoChimie database is used for calculations, considering the analogy Am(III)-CIT and Eu(III)-CIT systems.

3.3.2. Ternary system: C-S-H / Eu(III) / GLU

The effect of gluconate on Eu(III) retention on C-S-H phases with a C/S of 0.8, for gluconate total concentration $-3 \leq \log([GLU]_{tot}/M) \leq -1.5$ is shown in the Figure 61. Negligible impact on the sorption is observed for total gluconate concentrations below 10^{-2} M. A slight decrease in log R_d values is quantified for log $[GLU]_{tot} = -1.5$, although long equilibration times are required to attain steady-state.
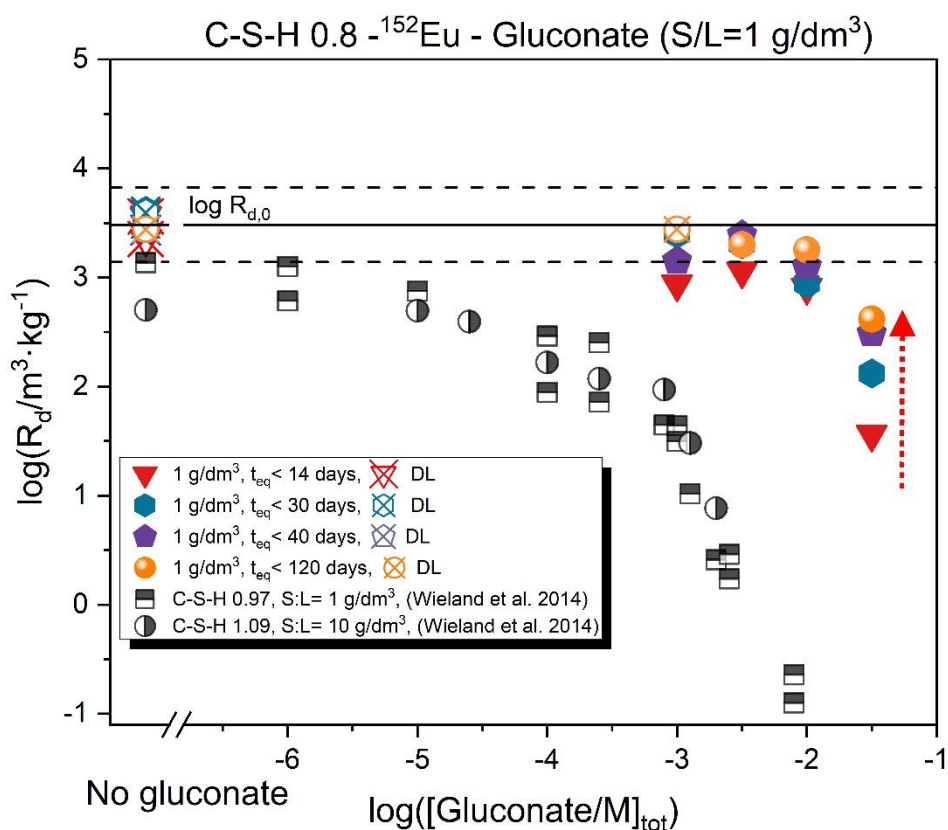
Figure 61. Distribution coefficients, R_d, for the uptake of ^{152}Eu in presence of gluconate (-3 ≤ log([GLU]$_{tot}$/M) ≤ -1.5) on C-S-H phases with a C/S of 0.8 for a contacting time t_{eq} < 120 days under hyperalkaline conditions (pH ≈ 13.3). The black solid line labelled as log R_d max indicate the maximum R_d coefficient quantifiable in the series of sorption experiments.

The effect of gluconate (-3 ≤ log([GLU]$_{tot}$/M) ≤ -1.5) on the retention of Eu(III) by C-S-H phases with a C/S of 1.4 is shown in Figure 62. In contrast to the C-S-H 0.8 system, a significant decrease of Eu(III) sorption is visible for total gluconate concentrations above 10^{-3} M. Experimental observations reported by Wieland and co-workers [1] for the uptake of Eu(III) by C-S-H 0.97 and 1.09 are in good agreement with data obtained in the present work (see Figure 62). The decrease in R_d values observed in this work for C-S-H 1.4 and in Wieland et al. [1] for C-S-H 0.97 / 1.09 is attributed to the formation of stable aqueous complexes of Eu(III) with GLU.
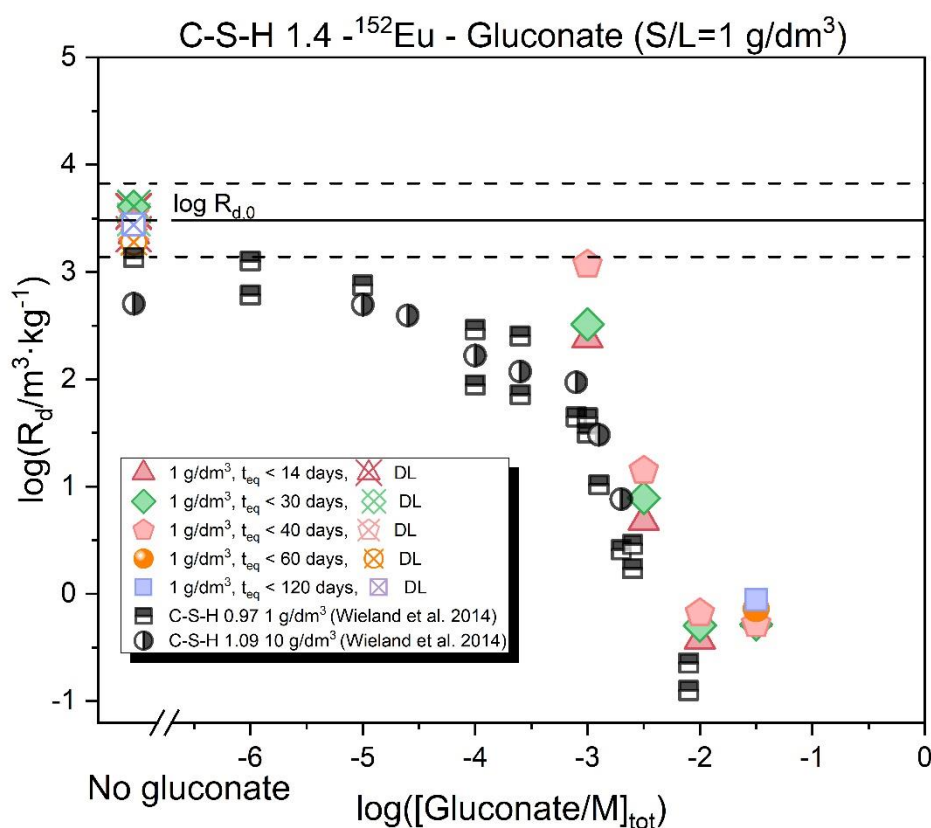
Figure 62. Distribution coefficients, R_d, for the uptake of ^{152}Eu in presence of gluconate ($-3 \leq log([GLU]_{tot}/M) \leq -1.5$) on C-S-H phases with a C/S of 1.4 for a contacting time $t_{eq} < 120$ days under hyperalkaline conditions ($pH \approx 13.3$). The black solid line labelled as log R_d max indicate the maximum R_d coefficient quantifiable in the series of sorption experiments.

The apparently discrepant behaviour of data obtained in this work for the C-S-H 0.8 system can be properly rationalized by considering the concentration of Ca in the investigated systems, and its possible role in the formation of aqueous complexes with Eu(III) and GLU. Hence, Figure 63 shows the evolution of Ca concentration in the C-S-H 0.8 and 1.4 systems investigated in this work. The figure clearly shows that the system C-S-H 0.8 investigated in this work at pH ≈ 13.3 is the one with lowest Ca concentration, which is about one order of magnitude lower than in the C-S-H 1.4 system. Note that the concentration of Ca in the experiments by Wieland et al.[1] was similar to the one obtained in the present study at C/S = 1.4, i.e. ≈ 1.6·10^{-3} M. In a recent study combining Nd(III) solubility with Cm(III) TRLFS in hyperalkaline systems containing gluconate, Rojo and co-workers confirmed the key role of Ca and the formation of quaternary complexes Ca-Ln(III)/An(III)-OH-GLU [159]. Although no thermodynamic data are available so far for these complexes, it is evident that they play a role in cementitious systems and provide a consistent explanation for the experimental observations in this work and in Wieland et al. [1].
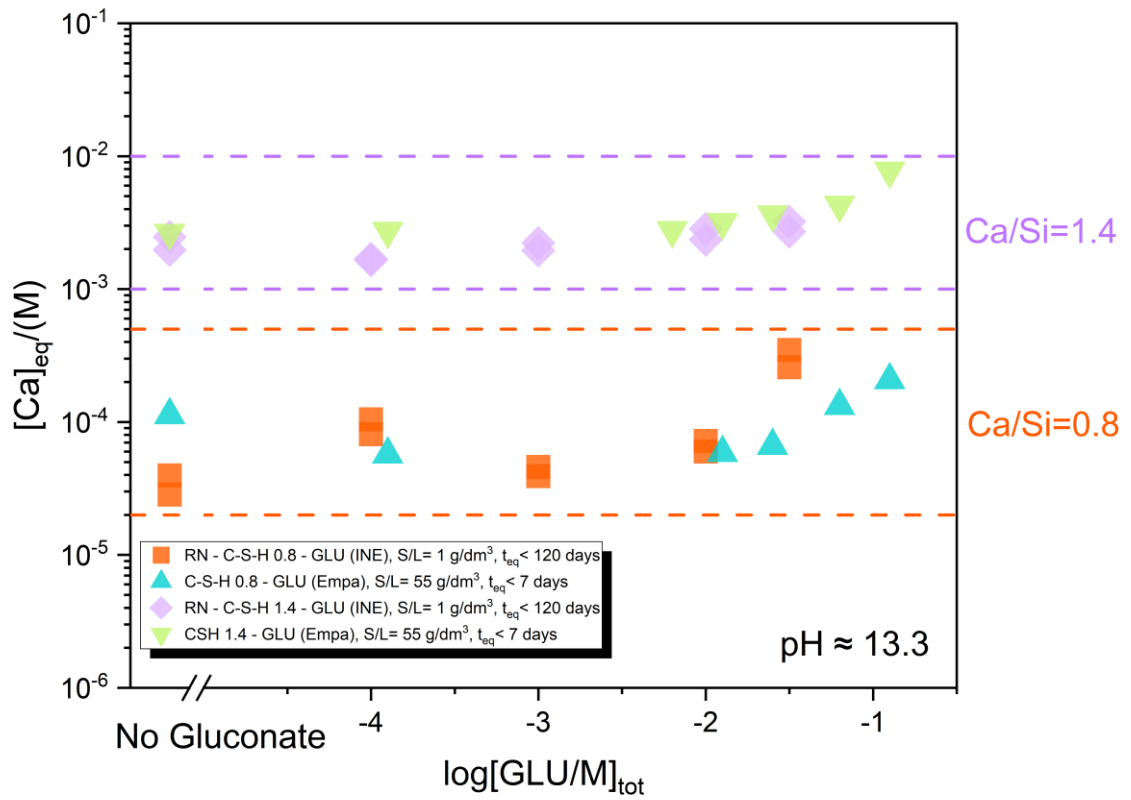
Figure 63. Comparison of Ca concentrations in the C-S-H 0.8 and 1.4 systems at pH ≈ 13.3 and increasing gluconate concentration.

3.3.3. TRLFS study on the ternary system C-S-H/ Cm /GLU

Cm(III) TRLFS analysis focuses on the identification of the aqueous (Ca)-Cm-OH-GLU complexes and on the understanding of the relevant uptake mechanism occurring on the two C-S-H phases with a different chemical composition in terms of Ca content (or C/S ratio). TRLFS spectra were collected for the aqueous samples, which replicate the same chemical conditions of the two C-S-H phases (pH ≈ 13.3, $[Ca]_{eq} \approx 10^{-5}–10^{-4}$ M (C/S = 0.8) or $[Ca]_{eq} \approx 10^{-3}–10^{-2}$ M (C/S = 1.4), $[Na]_{tot}$ = 0.2 M) investigated in the sorption experiments. In this case, the role of gluconate in the C-S-H-Cm-GLU system was investigated in the gluconate concentration interval ranging from 10^{-3} M and $10^{-1.5}$ M. The uptake mechanism over time was investigated on suspension samples, where the same chemical parameters of solution samples were applied. All samples have the same initial calcium concentration of the reference solid phases synthesized with an initial S/L ratio of 1 g/dm³. The collected normalized emission spectra of both solution and suspensions samples are summarized in the Figure 64. Figure 64a shows the TRLFS spectra of the solution sample for C-S-H with a C/S = 0.8 in presence of $-3 \leq \log[GLU]_{tot} \leq -1.5$ and pH ≈ 13.3. For the gluconate concentration below $10^{-2.5}$ M, the spectra are characterized by two main peaks, with a wavelength position of 616.5 nm and 610.5 nm (less intense peak), which can be attributed to two different (Ca)-Cm-OH-GLU species. Under similar experimental conditions, Rojo and co-workers observed a peak at λ ≈ 617 nm only in those Cm(III)-GLU systems containing Ca (with [Ca] = 1·10⁻³ M) [159] (see

Table). The appearance of a new band at λ ≈ 610.5 nm is observed for gluconate concentration $[GLU]_{tot}$ = $10^{-1.5}$ M, likely due to the formation of a new Ca-Cm-OH-GLU species containing two GLU ligands at higher GLU concentrations. Similar observation were obtained in the TRLFS emission spectra carried out by Rojo et al. [159] with a total calcium concentration of 0.01 M and pH ≈ 12, for gluconate concentration $10^{-5}M < [GLU]_{tot} < 10^{-3}M$. For the same pH and gluconate concentration, these authors reported a shift of almost ≈ 7 nm between Ca-free and Ca-containing systems [159]. These observations underpin the formation of Ca-Cm-OH-GLU complexes in those systems containing sufficiently high Ca concentrations.

Figure 64b-d show the fluorescence emission spectra of the suspensions containing Cm(III) in C-S-H phases with C/S= 0.8 in absence and in presence of gluconate ($-3 \leq \log([GLU]_{tot}) \leq -1.5$) and for different contacting times (t_{eq} 7-56 days). Two different peak maxima at ≈ 606 nm and 621 nm are visible in the spectra. The same peaks were previously reported by Tits and co-workers for C-S-H-Cm(III) systems in the absence of GLU [24]. The authors indicated that the peak at 606 nm is the result of visible transitions from thermally populated states at room temperatures and therefore, does not represent any Cm complex. The peak at λ ≈ 620-621 can be assigned to a Cm(III) complex sorbed onto or incorporated in the C-S-H structure, as previously discussed in Tits et al. [24]. No significant differences are detectable in the suspension samples after 28 days of equilibration time. At t = 56 days, a slight blue shift of ~1 nm is observed for the samples in the presence of gluconate. A more accurate interpretation

is provided below on the basis of lifetime measurements conducted for the same samples, also in connection with the observations discussed by Tits and co-workers.

TRLFS spectra collected for aqueous samples in porewater solutions corresponding to C/S = 1.4 (Figure 64e) show well-defined peaks at $\lambda \approx 610$ nm and ≈ 616 nm. These two main features agree very well with those observed for C-S-H 0.8 systems. Note however that the appearance of the band at $\lambda \approx 610$ nm occurs at $[GLU]_{tot} = 10^{-1.5}$ M for C-S-H 0.8, whereas the peak at $\lambda \approx 610$ nm is observed already at $_{tot} = 10^{-3}$ M for C-S-H 1.4. Again the Cm(III) species appearing at $\lambda \approx 616$ nm disappears at increasing GLU concentration. In connection with Eu(III) sorption data discussed in Section 3.3.2, this observation suggests the formation of a quaternary complex Ca-Cm-OH-GLU occurring at lower $[GLU]_{tot}$ in C-S-H 1.4 systems as compared to C-S-H 0.8 systems. This observation hints that the higher concentration of Ca concentration in solution (see Figure 63) expected for C-S-H phases with C/S of 1.4, promotes the earlier formation of calcium-containing quaternary complexes.

Figure 64e-h show the normalized fluorescence emission spectra of Cm(III) in C-S-H phases with C/S = 1.4 in absence and in presence of gluconate ($-3 \leq \log([GLU]_{tot}) \leq -1.5$) for different contact times (t_{eq} 7-56 days). The fluorescence spectra in absence of gluconate is characterized by peak maxima at ≈ 620 nm and the peak shape is comparable with the main peak found in the spectra collected for the C-S-H (C/S = 0.8)-Cm-GLU system shown in the Figure 64b-d, although slightly shifted towards lower wavelength number. As elaborated above, this peak can be assigned to the Cm(III) incorporated in the C-S-H structure. The slightly different peak position observed for incorporated Cm(III) in C-S-H 0.8 and 1.4 may relate on the structural differences between both solid phases. The presence of gluconate induces the formation of a new band at $\lambda \approx 610$, while the band at 620 nm observed for the gluconate-free system is strongly reduced. Such behavior is observed for all spectra collected for C-S-H 1.4 with gluconate. Moreover, no significant changes in the peak position were observed for equilibration times longer than 28 days. Taking into account the observations reported for the solution sample, the result reasonably indicate the predominance of aqueous complexes Ca-Cm(III)-OH-GLU, even in the presence of C-S-H 1.4. This observation qualitatively agrees with Eu(III) sorption data, for which a significant decrease in the uptake was only observed in the system C-S-H 1.4. However, for the lowest ligand concentration ($\log([GLU/M]_{tot}) = -3$), a strong uptake of Eu(III) by C-S-H 1.4 was observed, and thus for this particular sample most of the Cm(III) would be expected as incorporated species instead of as aqueous complex. This inconsistency is so far not understood, although it might be explained by differences in the equilibrium constants of Eu(III)-GLU and Cm(III)-GLU. In general trends, wet-chemistry and TRLFS data give a consistent picture for the interpretation of the Ln(III)/An(III) uptake by C-S-H in the presence of gluconate, also with respect to differences in C/S ratios.

127
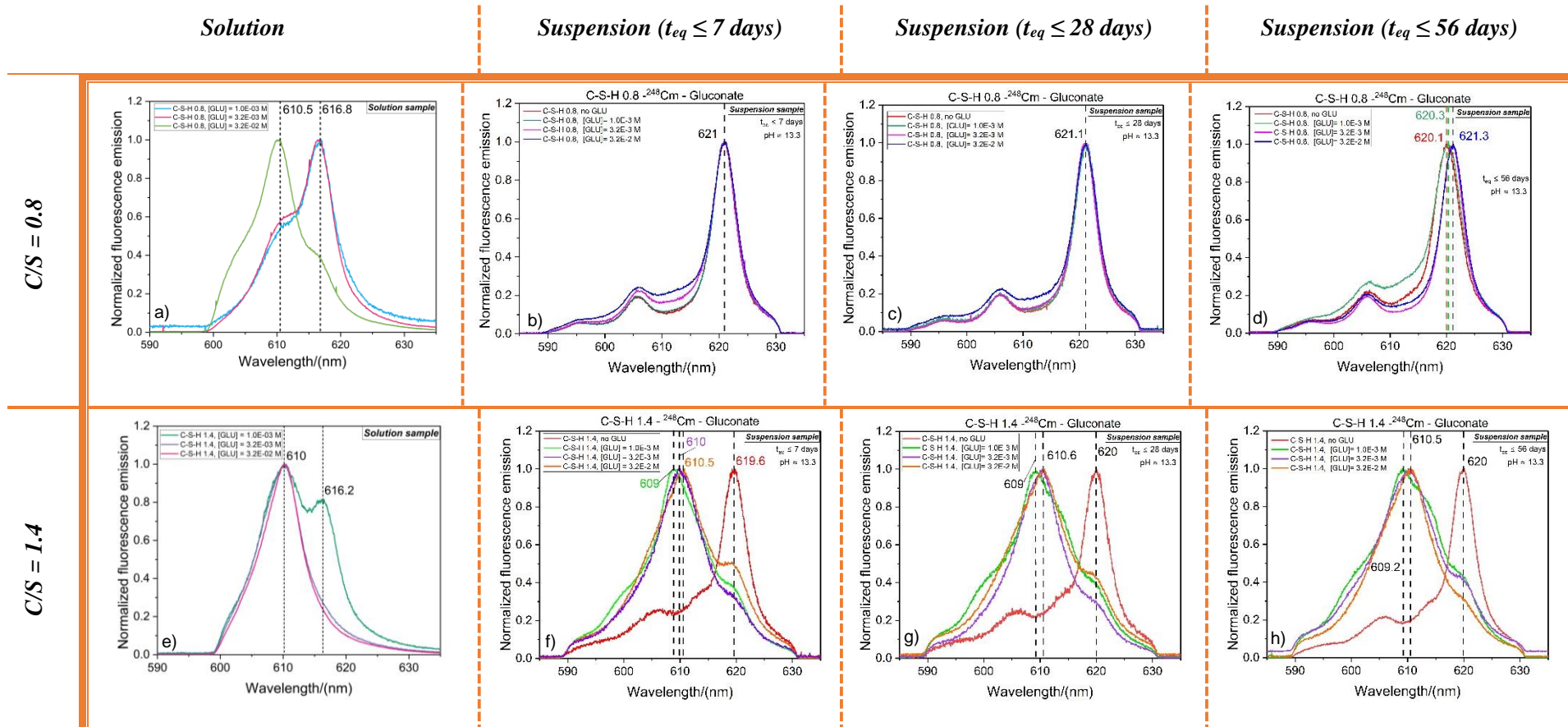
Figure 64. TRLFS normalized emission spectra of Cm(III)-C-S-H-GLU system for solution (a,e) and suspension (b, c, d, f, g, h) samples (S/L = 1 g/dm³) in presence and in absence of gluconate as a function of the contacting time. The peaks are normalized with regard to the peak height.

The fluorescence lifetime provides information on the composition of the first coordination sphere of Cm(III) on the basis of the method developed by Horrocks and Sudnick for Eu(III) [267] and applied to Cm(III) by Kimura and Choppin [154]. The fluorescence emission of each system was measured by successively increasing the delay time after the laser pulse. The results of the lifetimes and determination of number of water molecules in the first coordination sphere of Cm are reported in the Table . Note however that these methods were derived for ideal systems looking at the exchange of H_2O/D_2O. The effect of other ligands like carboxylates or alcohol groups in the measured lifetimes is not fully understood, and thus the calculated lifetimes should be taken as orientative.

For the Cm-C-S-H 0.8 system, the fluorescence signal follows a mono-exponential decay law (see Figure 68 in the Appendix 3.3) indicating the formation of one Cm-species. For equilibration times below 28 days, one species has been identified in absence of gluconate with a lifetime of (833 ± 42) µs. This species has no water molecules in the first coordination sphere, and thus corresponds to an incorporated species into C-S-H phase. For the Cm-C-S-H 0.8-GLU systems a bi-exponential decay law is observed indicating the formation of two different species. In addition to the presence of an incorporated species with no water molecules in the first coordination sphere and a lifetime of (1250 ± 62) µs, a second species with a lifetime of ≈ 400 µs and ≈ 0.5 water molecules coordinated is observed for $[GLU]_{tot} = 10^{-3}$ M.

For longer equilibration times (see Table) the sample in absence of GLU is characterized by two species with a lifetime of ≈ 800 µs and ≈ 400 µs respectively. These species are characterized by the complete or almost complete loss of water molecules in the first coordination sphere, thus indicating that they are mainly incorporated into the C-S-H structure. In the presence of gluconate, species with lifetimes of $\approx$ 1700 µs, 1250 µs, 1000 µs and ≈ 400 µs are observed. Nevertheless, all of the individuated species have a very low number of coordinating waters $(0 - 1)$, which again supports the predominance of incorporated species in the C-S-H structure (C/S = 0.8). The obtained spectroscopic result are in line with the spectra and results obtained by [24] for C-S-H (C/S =1.09) – Cm system investigates under hyperalkaline conditions. The authors observed the formations of two complexes with a lifetime of 1482 $\pm$ 200 µs (F2, peak maxima at 618.8 nm) and 289 $\pm$ 11µs (F1, peak maxima at 620.9 nm). The low number of water molecules in the first coordination sphere of the two complexes indicated that both complexes were incorporated in the C-S-H phase structure. In particular, the authors suggested that the complex F2 may substitute one of the Ca ions present in the octahedral Ca in the main layer, while F1 may substitute one Ca in the interlayer region. In addition the spectroscopic TRLFS investigation for Eu uptake on C-S-H phase with a C/S = 0.83 (pH 11.6) conducted by [265] pointed towards the presence of two sorption sites: one species with a longer lifetime (990 µs) sorbs into the framework of C-S-H phase structure, the second species instead, sorbs on the surface of C-S-H phase with a lifetime of 390 µs. In conclusion, taking into account the minor effect of gluconate on Eu(III) retention observed in batch sorption experiments (section 3.3.2) for $t_{eq} < 120$ days, it is possible to assume Eu(III) sorbs strongly on the C-S-H phases with C/S = 0.8 structure, and that complexes formed with gluconate are

not strong enough as to stabilize Eu(III) or Cm(III) in the aqueous phase. As discussed for the sorption experiments with Eu(III), Ca plays a key role in the complex formation with Cm(III) and gluconate. The relatively low concentration of Ca in equilibrium with C-S-H 0.8 at pH = 13.3 (10^{-4}–10^{-3} M, see Figure 63) prevents the significant formation of ternary / quaternary complexes Ca-Eu(III)/Cm(III)-OH-GLU. The fluorescence lifetimes and determination of number of water molecules in the first coordination sphere of Cm(III) for Cm(III)-C-S-H (C/S = 1.4)-GLU system are also reported in the Table . In most of the cases, the fluorescence signal follows a bi-exponential decay law (see Figure 70 in the Appendix 3.3) indicating the formation of at least two Cm species. In few cases, a tri-exponential decay law was applied. In absence of gluconate and $t_{eq} \leq 28$ days, three lifetime components, i.e. at least three species were observed: two species with a lifetime of 294 µs (n(H$_2$O) = 1.3) and 833 µs, and one species with a longer lifetime $\tau \approx 1700$ µs and no water molecules in the first coordination shell of Cm. The two species with longer lifetime clearly correspond to Cm(III) species incorporated into the C-S-H structure. The lifetime of the third species ($\tau = 294$ µs) is in excellent agreement with the second species reported by Tits et al. [24] ($\tau = 289$ µs). Note that based on the calculation of the coordination waters, these authors concluded that this species with shorter lifetime is also incorporated in the C-S-H structure. Similar observations were obtained at $t_{eq} = 56$ days, thus indicating that steady state conditions are reached already at $t_{eq} = 28$ days.

For a gluconate concentration log([GLU]$_{tot}$) = -3, the complex with a lifetime of ≈ 700 µs may indicate the presence of the same incorporated species found in the absence of GLU. This observation is in line with the results obtained for Eu(III) sorption at log([GLU]$_{tot}$) = -3, for which a significant retention was observed. In presence of gluconate (log([GLU]$_{tot}$) = -3 to -1.5), different species with different lifetimes ranging from of ≈ 140 µs to ≈ 650 µs were determined. Since there is so far no definitive information available about the complexes speciation that could possibly form with this chemical conditions, it is possible to speculate that these complexes may originate from the Ca-Cm(III)-OH-GLU interactions. Taking into account the observations for the Eu sorption batch experiments with the results reported from the TRLFS analysis, it is possible to deduce that the strong decrease of Eu(III)/Cm(III) retention by C-S-H 1.4 in the presence of log([GLU]$_{tot}$) $\geq$ -2.5 is clearly caused by the formation of very stable aqueous Ca-Eu(III)/Cm(III)-OH-GLU complexes. According to data in Figure 65, Eu(III) is still mainly bound to C-S-H in the presence of log([GLU]$_{tot}$) = -3, so that TRLFS appears to point to quarternary Cm(III) complexes still being associated to the solid phase. The different retention observed for the two different C-S-H phases (in terms of C/S), highlights the key role of Ca in the complex formation for the C-S-H-Ln(III)/An(III)-OH-GLU ternary/quaternary system. Similar observations were reported by Rojo and co-workers for the solubility of Nd(III) in the presence of gluconate, both in the absence and presence of Ca.

Table 9. Calculated lifetime (± 5% measurement error) and number of coordinated water molecules in the first coordination sphere of Cm(III) [154] for the Cm-C-S-H (C/S = 0.8, 1.4)-GLU system, with $[^{248}Cm]_{tot}$ = 2·10⁻⁷ M and for contacting time t_{eq} = 28 days and t_{eq} = 56 days.

Phase	Time/ days	No ligand		log([GLU]tot/M) = -3		log([GLU]tot/M) = -2.5		log([GLU]tot/M) = -1.5	
		Lifetime, τ/[µs]	$N_{(H2O)}$[a]	Lifetime, τ/[µs]	$N_{(H2O)}$[a]	Lifetime, τ/[µs]	$N_{(H2O)}$[a]	Lifetime, τ/[µs]	$N_{(H2O)}$[a]
C-S-H 0.8	28	833 ± 42 [b]	-	476 ± 24 [b]	0.48	909 ± 45 [b]	-	833 ± 42 [b]	-
C-S-H 0.8	28	-	-	1250 ± 62[b]	-	1250 ± 62[b]	-	1250 ± 62[b]	-
C-S-H 0.8	56	833 ± 42 [b]	-	454 ± 23 [b]	0.55	435 ± 22 [b]	0.61	1000 ± 50 [b]	-
C-S-H 0.8	56	417 ± 21 [b]	0.68	1250 ± 62[b]	-	1250 ± 62[b]	-	1667 ± 83 [b]	-
C-S-H 1.09	58	1482 ± 200[c]	-						
C-S-H 1.09	58	289 ± 11[c]	1.4						
C-S-H 1.4	28	294 ± 15 [b]	1.3	238 ± 12 [b]	1.9	385 ± 19 [b]	0.81	370 ± 18 [b]	0.90
C-S-H 1.4	28	833 ± 42 [b]	-	667 ± 33 [b]	0.095	588 ± 30 [b]	0.22	625± 31 [b]	0.16
C-S-H 1.4	28	1667 ± 83 [b]	-						
C-S-H 1.4	56	286 ± 14 [b]	1.4	244± 13 [b]	1.8	322 ± 16 [b]	2.1	131 ± 7 [b]	4.1
C-S-H 1.4	56	714 ± 36 [b]	0.030	500 ± 25 [b]	0.42	526 ± 26 [b]	0.36	625± 31 [b]	0.16
C-S-H 1.4	56	1428 ± 71 [b]	-						
HCP	48	66 ± 1 [d]	9						
HCP	48	1208 ± 600 [d]	-						
HCP	358	70 ± 7 [d]	8.5						
HCP	358	226 ± 26 [d]	2						
HCP	358	1375 ± 207 [d]	-						

[a]The determination of the number of water (H₂O/OH⁻) molecules is based on the empirical equation determined for H_2O/D_2O systems conducted by [154] and [213]. Therefore, the possible quenching contribution of the functional groups of the ligand (i.e. gluconate) are disregarded for the C-S-H-Cm-GLU ternary system. [b] Observed in this study, [c] [24], [d] [25].

Table 10. Summary of TRLFS peak maxima positions, species assignments, experimental conditions for Cm aqueous species, curium hydrolysis products and Ca-Cm-OH-(GLU) species.

Species	Peak maxima position, [187]	pH	$[Ca]_{tot}$, [M]	$\log([GLU]_{tot}/M)$	Reference
Cm^{3+}	593.8	≤ 8	-	-	[268, 269]
$Cm(OH)^{2+}$	598.8	8-9	-	-	[268, 269]
$Cm(OH)_2^+$	603.5	8-12	-	-	[269]
$Cm(OH)_3$	607.5	9-12	-	-	[268]
$Cm(OH)_4^{-\,a}$	609.9	10-12.5	1	-	[268]
$Cm(OH)_6^{3-\,b}$	614.7	≥ 11	2.5, 3.5	-	[268]
Ca-Cm-OH-GLU	616	12	0.1	-5	[159]
Ca-Cm-OH-GLU	608	12	3.5	-3.2	[159]
Ca-Cm-OH-GLU	611	12	3.5	-3.2	[159]
Ca-Cm(incorporated species) (from C-S-H 0.8-Cm-GLU series)	621.1^c, 620^d	≈ 13.3	$\approx 10^{-5}$	-	This study
Ca-Cm(incorporated species) (from C-S-H 0.8-Cm-GLU series)	621^c, 620^d	≈ 13.3	$\approx 10^{-5}$	-3	This study
Ca-Cm(incorporated species) (from C-S-H 0.8-Cm-GLU series)	621^c, 621.1^d	≈ 13.3	$\approx 10^{-5}$	-2.5	This study
Ca-Cm(incorporated species) (from C-S-H 0.8-Cm-GLU series)	621^c, 621^d	≈ 13.3	$\approx 10^{-4}$	-1.5	This study
Ca-Cm(incorporated species) (from C-S-H 1.4-Cm-GLU series)	620^c, 619.8^d	≈ 13.3	$\approx 10^{-3}$	-	This study
Ca-Cm-OH-GLU (from C-S-H 1.4-Cm-GLU series)	609.1^c, 613.8^d, $609^{c,d}$	≈ 13.3	$\approx 10^{-3}$	-3	This study
Ca-Cm(incorporated species) (from C-S-H 1.4-Cm-GLU series)	619.2^c, 619.9^d	≈ 13.3	$\approx 10^{-3}$	-3	This study
Ca-Cm-OH-GLU (from C-S-H 1.4-Cm-GLU series)	610.3^c, 610.2^d	≈ 13.3	$\approx 10^{-3}$	-2.5	This study
Ca-Cm(incorporated species) (from C-S-H 1.4-Cm-GLU series)	619.2^d	≈ 13.3	$\approx 10^{-3}$	-2.5	This study
Ca-Cm-OH-GLU (from C-S-H 1.4-Cm-GLU series)	610.5^c, 610.3^d	≈ 13.3	$\approx 10^{-2}$	-1.5	This study
Ca-Cm(incorporated species) (from C-S-H 1.4-Cm-GLU series)	619.7^d	≈ 13.3	$\approx 10^{-2}$	-1.5	This study

[a] Described in [158] as $Ca_2[Cm(OH)_4]^{3+}$ and [b] $Ca_3[Cm(OH)_6]^{3+}$. [c] Observed in this work for equilibration times, $t_{eq} = 28$ days. [d] Observed in this work for equilibration times, $t_{eq} = 56$ days.

Summary and conclusions

This Ph.D. study has investigated retention processes within the binary and ternary systems cement phases / organic ligands / radionuclides in cementitious systems relevant for low and intermediate level waste (L/ILW) repositories. The three organic ligands investigated (formate, citrate and gluconate) are expected in L/ILW and / or used as additives in cement formulations. Experiments tackle ^{242}Pu(III/IV) and ^{152}Eu(III), as representative and analogues of the actinide oxidation states foreseen to form in the very reducing conditions expected to develop after the closure of the repository due to the anoxic corrosion of Fe. Three main cement phases (C-S-H, AFm and ettringite) are taken into account in the sorption studies, which have been previously identified as relevant sinks for the uptake of cationic (C-S-H) and anionic (AFm, ettringite, and to less extent C-S-H) species. Within this study, the following points were addressed:

a) Sorption of formate, citrate and gluconate on cement phases and hydrated PC.
b) Retention of Pu(III/IV) in presence of formate, citrate and gluconate in cementitious systems, including solubility phenomena and (primarily) retention on cement phases.
c) Sorption of Eu(III) in the presence of formate, citrate and gluconate on C-S-H phases. This wet-chemistry study is complemented with advanced spectroscopic methods to gain insights on the retention mechanism. For this purpose, a TRLFS study of Cm(III) uptake on C-S-H phases in presence and in absence of gluconate was conducted.

The three points have been comprehensively investigated under controlled alkaline conditions (pH ≈13.3), ionic strength (I = 0.2 M) and reducing conditions (only for the point (b)). Sorption experiments of the binary system were conducted on pre-synthesized cement suspensions by varying the organic concentration. The uptake behavior of Pu(III/IV) on C-S-H phases, AFm phases and ettringite, carried out by varying the organic ligand concentration and the redox conditions, was supported by the solubility investigation of Pu(III/IV) under the same chemical and redox conditions applied in the sorption experiments (but in absence of Ca). Like wise, the sorption of Eu(III) by C-S-H phases was also investigated by varying the ligand concentration. The observations obtained by a TRLFS study on the C-S-H-Cm(III)-GLU system were used to understand and describe the uptake of Eu(III) by C-S-H phases in presence of L and as a function of the Ca concentration (i.e. C/S ratio of C-S-H). The main achievements of this study can be summarized as follows:

1. Sorption of formate, citrate and gluconate on cement phases and hydrated PC

The uptake study of formate, citrate and gluconate by AFm phases (Ms, Mc, Hc), ettringite and C-S-H phases with a C/S = 0.8-1.4 was investigated by sorption experiments and characterization of both solid and liquid phase separated after an equilibration time of 7 days. In order, to discriminate the possible formation of new organics-cement phases, also pure FOR-, CIT- GLU-AFm or AFt phases were synthesized and characterized (after an equilibration time of two months). The XRPD analysis of L-

AFm (where L is FOR, CIT, and GLU), indicated the formation of a layered structure in all cases as typical for AFm phases. In the case of FOR-AFm a d-spacing $d_{(003)} = 8.1$ Å for low $2\theta^o$ angles was observed. The presence of a signal at $\approx 31^o\, 2\theta^o$ angles points towards the formation of a trigonal structure. A similar structure was found in the case of CIT-AFm, with a d-spacing of $d_{(003)} = 12.3$ Å. The broader reflection and the presence of traces of katoite indicate a poorly ordered crystalline phase and low stability of the formed phase respectively. For GLU-AFm a d-spacing, $d_{(003)} = 10.9$ Å was observed. The presence of tricalcium aluminate ($Ca_3Al_2O_6$) indicated the traces of unreacted reagent and the detection of katoite, as for CIT-AFm, hints towards a relatively low stability of GLU-AFm phase. The lower stability of CIT-AFm and GLU-AFm was also confirmed by the comparison of the calculated ionic activity product with the solubility product of pure AFm phases. The XRPD pattern diffraction of the sample FOR-AFt, showed the formation of FOR-AFm, indicating a very low affinity of formate towards AFt phases. The X-ray diffraction of CIT-AFt showed the presence of two peaks at low $2\theta^o$ values: one sharp peak with a d-spacing of 10.2 Å (presumably belonging to the aimed CIT-AFt phase), and one broader peak with a d-spacing of 12.3 Å associated to CIT-AFm. In addition, the presence of katoite confirmed a relatively low stability of CIT-AFt, also suggested by thermodynamic calculations. In the case of GLU-AFt, the formation of an amorphous phase has been observed.

1.   Formate uptake by C-S-H, PC, AFm phases, and ettringite

The uptake of formate by C-S-H phases was visible in XRPD by a slight shift of the peak related to the interplanar distance (002) towards slightly lower $2\theta^o$ values, which could be related to a decrease of the number of layers stacked or a decrease of degree of ordering. The portlandite detected at C/S = 1.2 and 1.4 was destabilized in the presence of higher formate additions. In addition, the FT-IR analysis indicated that less Ca is bound in the solid phase in the presence of formate and an increase of the Ca concentration in solution for $[FOR]_{tot} > 100$ mM, where the addition of formate strongly lowered the pH values, while only weak aqueous Ca-formate complexes formed. The uptake of formate on C-S-H phases increases linearly with the formate concentration, while no relationship with the C/S ratio has been observed. This result suggests that Ca-formate complexes play a minor role on the overall uptake of formate. Also the uptake on Portland cement (PC) increases linearly with the formate concentration and was found with an R_d of 8.6 ± 0.3 dm^3/kg slightly higher than the uptake by C-S-H phases R_d of 3 to 7 dm^3/kg (Figure 66a).

The presence of formate has a negligible effect on the structure of Mc, Ms and AFt. Only in the case of Hc a clear shift of the XRPD signal of the main basal spacing towards lower $2\theta^o$ angles indicates an increase of the interplanar distance due to the uptake of formate. All solutions clearly show an increase of Ca concentration at formate concentrations higher than 100 mM due to the strong decrease of pH in those samples and in the case of ettringite and Ms, also an increase of SO_4^{2-} concentration, indicating the partial substitution of sulphate at the surface by formate. The sorption study indicates a comparable

uptake of formate on Mc, Hc and AFt at low formate concentration. However, the formate sorption on Ms, Mc and AFt is limited to ≈ 0.005 mol/kg solid indicating that formate sorbs only on the outer surface sites of particle. In contrast, in the case of Hc, which has a larger basal spacing, formate uptake increases linearly with the formate concentration up 1 mol/kg with an average R_d value of 2.3 dm^3/kg, indicating that formate is taken up both on the surface as well as in the interlayer sites of Hc.

2.   Citrate uptake by C-S-H, PC, AFm phases, and ettringite

The X-ray diffraction showed that uptake of citrate has a small effect of the interplanar distance (002) (distance between the two main layers) of the C-S-H phases for C/S ≤ 1.0. However, some decrease of the d-spacing (002) is observed for C/S = 1.2 and 1.4 and high citrate concentrations, which could be due to an increase of the attraction between the two main layers at higher ionic strength at higher citrate concentrations. The presence of citrate also destabilized any portlandite formed at high C/S ratios. The quantification of the C/S of the bulk phase and the evolution of the Ca concentration as function of the citrate concentration clearly indicates the formation of aqueous Ca-citrate complexes such as CaCit$^-$. In addition, in some cases, the precipitation of solid Ca$_3$Cit$_3$·4H$_2$O has been observed. Sorption experiments on C-S-H phases clearly indicate that the uptake is mediated by the Ca^{2+} ions at the surface of the C-S-H phases as the citrate uptake clearly increases with the increase of the C/S ratio. The slight decrease of uptake observed for high citrate concentration is probably due to the depletion of Ca^{2+} at the surface resulting in a reduction of citrate uptake. The uptake of citrate on PC (Figure 66b) (R_d = (154 ± 16) dm^3·kg^{-1}) was comparable or slightly higher than that found on high C/S C-S-H phases, indicating some citrate uptake also by the other hydrates present in hydrated cement. The solid phase characterization carried out on AFm phases and ettringite indicates that citrate an increase of the interplanar distance of Hc and, slightly, of Ms phases; while negligible effects were observed for Mc and ettringite. The increase of Ca concentration in solution in the presence of citrate, hints again towards the complexation of citrate with Ca ions (CaCit$^-$ dominates the aqueous speciation), and likewise the increase of sulphate concentration (for Ms and ettringite phases) indicates the potential replacement of SO$_4^{2-}$ with Cit^{3-} groups.

For low citrate concentration, the uptake of Ms and Hc is higher than one observed for Mc and AFt. As for formate, citrate sorption on Ms, Mc and AFt is limited to ≈ 0.005 mol/kg solid indicating citrate sorption on the outer surface sites only. Only in the case of Hc, the uptake of citrate on Hc increases linearly with the citrate concentration up to ≈ 0.5 mol/kg, suggesting that the uptake occurs on both outer and inner surface sites. For [CIT] < 0.1 mM, the citrate uptake on Mc, Ms, Hc and ettringite occurs with R_d coefficients ranging from 10 dm^3·kg^{-1} to 100 dm^3·kg^{-1}, while for high citrate concentration, the retention of CIT decreases of two orders of magnitude for Ms, Mc and ettringite.

3. Gluconate uptake by C-S-H, PC, AFm phases, and ettringite

The solid phase characterization on the C-S-H phases in presence of gluconate indicates that for C/S $\leq$ 1.2, gluconate has a negligible effect on the structure of C-S-H phases. Only for C/S = 1.4, a small decrease of the interplanar distance is observed, indicating increase of the attractive forces between the two main layers. Furthermore, the portlandite detected at high C/S ratio in absence of gluconate, is destabilized by the presence of gluconate and FT-IR indicates the decalcification of C-S-H in the presence of gluconate. The addition of gluconate increases the Ca concentration in solution, indicating the formation of aqueous Ca-gluconate complexes. The sorption study of gluconate on C-S-H phases, indicates that the sorption mechanism on C-S-H phase with a C/S = 0.8, 1.0 is comparable, while for higher C/S ratio, stronger gluconate uptakes were observed in agreement with other studies [136, 138]. The slight decrease of gluconate uptake detected for high gluconate concentrations is due to the possible depletion of the Ca concentration at the surface. [138]. The uptake on HCP (see Figure 66c) increases linearly with the gluconate concentration with an R_d coefficient of (11.2 ± 1.0) dm$^3\cdot$kg^{-1} which is very close to the distribution coefficient obtained for C-S-H phase with a C/S of 1.4. The X-ray diffraction analysis carried out on AFm phases and ettringite, indicates a negligible effect of gluconate on Ms, Mc and ettringite and just a small increase of the interplanar distance of Hc in presence of gluconate. The increase of the Ca and sulphate concentrations as a function of the gluconate concentration, clearly suggest the complexation (with Ca ions) and substitution of SO$_4^{2-}$ groups on the surface of AFm phases and ettringite. In addition, thermodynamic calculation indicates that Ca$_3$Glu$_2$(OH)$_4$ dominates the aqueous speciation for [GLU]$_{tot}$ > 1 mM. Gluconate uptake was observed only on Ms, Hc and ettringite in particular at low concentrations indicating that gluconate sorbs mainly on the outer surface sites of Ms, Hc and ettringite with an R_d of $\approx$ 10 dm$^3\cdot$kg^{-1}.
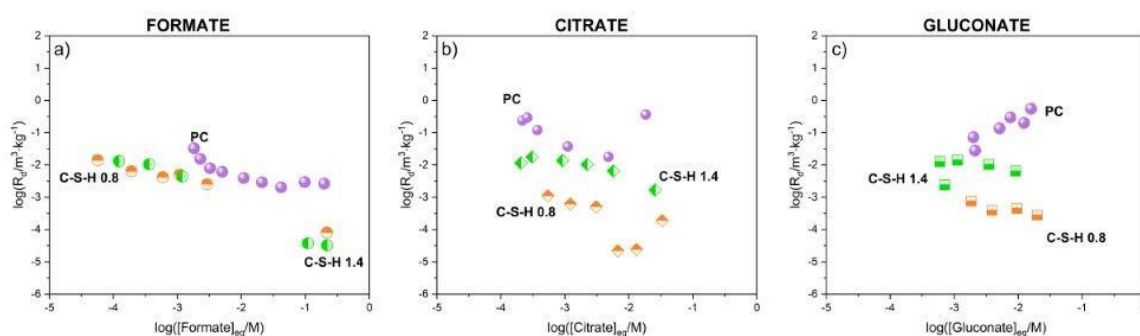
Figure 66. Distribution coefficients for the uptake of formate (a), citrate (b) and gluconate (c) on C-S-H phases with a C/S of 0.8 and 1.4, and on PC, after 7 days of contacting time (pH $\approx$ 13.3).

2. Solubility and sorption of Pu(III/IV) in presence of formate, citrate and gluconate in cementitious systems

The uptake of plutonium by cement phases (C-S-H, AFm and ettringite) was investigated under controlled hyperalkaline (pH ≈ 13.3) and reducing condition, which were set by means of two different redox buffers: HQ (with pe + pH ≈ 9) and Sn(II) (with pe + pH ≈ 1.5). These (pH + pe) values agree well with the values previously published either in presence and in absence of organic ligand. The solubility investigation of Pu in presence of organic ligands, was performed by replicating the same redox and alkaline conditions of sorption experiment (pH ≈ 13.3, $[Na]_{tot} = 0.2$ M, $[Sn(II)]_{tot} = [HQ]_{tot} = 2$ mM). In the case of solubility experiments in the presence of formate, the low and comparable Pu concentrations measured for formate-free systems hint towards the weak interaction between formate and Pu for both HQ and Sn(II) buffered systems. This is in line with solubility calculations performed with available thermodynamic data. A similar outcome was observed for citrate-Pu solubility experiments, indicating a weak complexing behavior of citrate under very alkaline conditions. Although ternary complexes An(IV)-OH-CIT have been described for Th(IV), they become outcompeted by hydrolysis in the hyperalkaline conditions investigated in this work (pH = 13.3). In the case of gluconate, the strong increase of plutonium concentration as function of the gluconate concentration clearly supports the formation of Pu-GLU complexes. At very low gluconate concentrations, differences in Pu solubility are rationalized by the decrease of -free concentration in the presence of Sn(II). At greater gluconate concentrations, where the ligand is found in excess with respect to Sn(II), the Pu concentrations determined in HQ and Sn(II) systems overlap with each other when considering the corresponding uncertainties. A linear trend with a slope of ≈ 1 can be tentatively proposed, which suggests the formation of a Pu-OH-GLU complex with a stoichiometry Pu : GLU = 1 : 1. By considering the results reported for the Th(IV)-GLU system [191], and considering the analogy with the Pu(IV)-ISA system [4], the formation of the complex $Pu(OH)_3(GLU_{-2H})^{2-}$ was proposed. Furthermore, an equilibrium constant log $\beta°_{(1,3,1,-2)} = -(17.4 \pm 1.3)$ ($Pu^{4+} + 3H_2O(l) + GLU^- \leftrightarrow Pu(OH)_3(GLU_{-2H})^{2-} + 5H^+$), was determined. This value shall be considered tentative, until solubility experiments under varying pH_m are conducted to validate the proposed stoichiometry (Pu : OH) of the complex. The remarkably different complexation behaviour of the three investigated ligands emphasizes the key role of the multiple alcohol groups in the stabilization of complexes with An(III/IV) and Ln(III) in hyperalkaline conditions. Even a strong chelating ligand like citrate cannot outcompete hydrolysis, in contrast to observations obtained for gluconate.

Sorption experiments with the Pu-C-S-H system in the absence of organic ligands show the strong retention of plutonium with log $R_{d,0}$ of 6.1 ± 1.2, in line with data available in the literature for plutonium and An(IV) in general. Formate and citrate do not show any effect on the retention of plutonium by C-S-H phases with C/S = 0.8 and 1.4 (see Figure 67a). This is in agreement with the solubility experiments, and further supports that these ligands can compete neither with hydrolysis nor with sorption on the C-S-H phases. In contrast to formate and citrate, gluconate decreases Pu uptake in C-S-H phases for both

low and high C/S ratios (Figure 67b). No differences were observed for the two redox buffers used, except at $\log[GLU/M]_{tot}$ = -1.5, which may be due to the different redox state of Pu in Sn(II) and HQ. Considering that no clear differences were observed in the solubility experiments, these results may hint towards the possible formation of stable surface complexes of the type > Pu(III)-OH-GLU.

Strong uptake of Pu in absence of any ligands was observed for AFm and AFt phases, with $\log R_d$ of (5.6 ± 1.0) and (5.7 ± 1.1), respectively. This is one of the first experimental evidences available in the literature supporting the strong uptake of plutonium by AFm and AFt, which supports its strong retention even beyond C-S-H phases. Similarly, to the C-S-H phases, formate has no effect on the uptake of Pu on AFm phases and ettringite. On the other hand, citrate does induce a decrease on Pu retention at $\log[CIT]_{tot}$ > -2, in contrast to C-S-H phases. Considering the negligible effect observed for solubility, this finding can be possibly explained by the impact of citrate on the surface and structural properties of AFm phases and ettringite. Gluconate decreases the uptake of Pu for gluconate concentrations higher than 10^{-4} M on AFm phases and ettringite for both redox buffers. The decrease of Pu retention was found more marked than the uptake trend observed for C-S-H phases. Considering the results obtained for the binary systems as well as for the solubility experiments with gluconate, these observations possibly reflect the impact of gluconate on the aqueous speciation of Pu as well as the on the structural and surface properties of AFm phases and ettringite.

3. Sorption of Eu in the presence of formate, citrate and gluconate on C-S-H phases

Europium sorbs very strongly on C-S-H phases in the absence of organic ligands ($R_{d,0} = 10^{-6.5}$ dm³·kg⁻¹) under the chemical conditions investigated in this study. This value is in line with previous studies available for the uptake of Eu(III) and Am(III) by C-S-H phases [1]. Formate has a negligible impact on Eu(III) retention on C-S-H phases due to the weak complexes forming under hyperalkaline conditions. Similarly to formate, citrate has also a negligible impact on Eu(III) uptake on C-S-H phase with a C/S of 0.8 and 1.4. The only effect on Eu(III) retention was observed for contacting times shorter than 60 days and for $[CIT]_{tot}$ > 10^{-2} M, for C-S-H(C/S=1.4)-Eu(III)-CIT system. The latter result may indicate that for longer equilibration times the incorporation of Eu(III) in the structure of the C-S-H phases is occurring, as previously described for ligand-free Eu(III) and Nd(III) systems [24, 27]. Although under the experimental conditions of this study the formation of Ca-Eu(III)-CIT complexes does not play a role on the uptake of Eu on C-S-H phases, the possible formation of quaternary complexes has been recently proposed by [178] for the Ca-An(III)-OH-EDTA system.

Gluconate has a negligible effect on Eu(III) retention on C-S-H 0.8 at $[GLU]_{tot}$ < 10^{-2} M, whereas a moderate decrease in the retention is observed for gluconate concentrations $[GLU]_{tot}$ = $10^{-1.5}$ M and for longer equilibration times. For C-S-H 1.4, a strong decrease of Eu retention was observed for $[GLU]_{tot}$ > 10^{-3} M (see Figure 67c). These observations support that more stable Eu(III)-GLU complexes are being formed in C-S-H 1.4 systems. Considering the significantly higher Ca concentrations determined

in the aqueous phase of the latter phases, this observation hints towards the formation of stable quaternary aqueous complexes involving Ca, i.e. Ca-Eu(III)-(OH)-GLU. The Cm(III) TRLFS investigation carried out on the aqueous phase of the Cm(III)-GLU-C-S-H (C/S = 0.8) system indicated the formation of at least two aqueous complexes with a peak maxima at $\approx$ 616 nm and $\approx$ 610 nm. The second peak at lower wavelength number becomes visible only for $[GLU]_{tot} = 10^{-1.5}$ M. In the case of the aqueous phase of the Cm(III)-GLU-C-S-H (C/S = 1.4) system, the same peak starts to be visible at lower gluconate concentration, and became predominant at $[GLU]_{tot} > 10^{-2.5}$ M. These results are in line with sorption experiments with Eu(III) and support the formation of ternary / quaternary complexes involving Ca. The TRLFS spectra of the Cm(III)-GLU-C-S-H (C/S = 0.8) suspension system is characterized by the formation of one main peak at $\approx$ 620 nm both in presence and in absence of gluconate (Figure 67d). The analysis of the Cm(III) emission spectra together with the determination of lifetime indicates the formation of two main Cm(III) species incorporated into the structure of the C-S-H phases. In the case of the Cm(III)-C-S-H (C/S = 1.4) suspension system in the absence of gluconate, an emission spectrum smilar to that one obtained for Cm(III)-GLU-C-S-H (C/S = 0.8) suspension, again with a main peak maxima position at $\approx$ 620 nm indicates the formation of a similar Cm(III) incorporated species. The lifetime determination supports the formation of three species, two species with a lifetime τ > 700 μs are likely incorporated into C-S-H phase structure, and one species with a lifetime $\tau \approx$ 300 μs might be sorbed on the C-S-H phase surface particle. In presence of gluconate, the same band is strongly reduced in intensity for the Cm(III)-C-S-H (C/S = 1.4) system. Furthermore, the appearance of one band at $\approx$ 610 nm for $[GLU]_{tot} \geq 10^{-3}$ M, well agrees with the emission spectra collected for the solutions system, indicating the presence of Ca-Cm(III)-OH-GLU aqueous species in the suspension system (see Figure 67d). The lifetime determination clearly supports the formation of at least two species with a lifetime of $\tau_1 < \approx$ 300 μs and $\tau_2 \approx$ 500-600 μs respectively. The identification of two species with a lower lifetime (compared for the Cm(III)-GLU-C-S-H (C/S = 0.8)) suggests that in presence of gluconate, the fraction of Ca-Cm(III)-GLU aqueous complexes dominates over the incorporated Cm(III) species. Considering these results together with the Eu(III) sorption study, it is concluded that the strong retention decrease observed for the C-S-H 1.4 can be interpreted in terms of Ca-An(III)/Ln(III)-GLU complex formation. Furthermore, since Ca plays a fundamental role in the Ca-An(III)/Ln(III)-OH-GLU aqueous complex formation, the differences underlined between the C-S-H 0.8 and C-S- H 1.4 solid phases in Eu(III) sorption experiments, can be discriminated with the respect to the C/S ratio of the solid phase, and more specifically to the Ca concentration at equilibrium, under the studied experimental conditions.
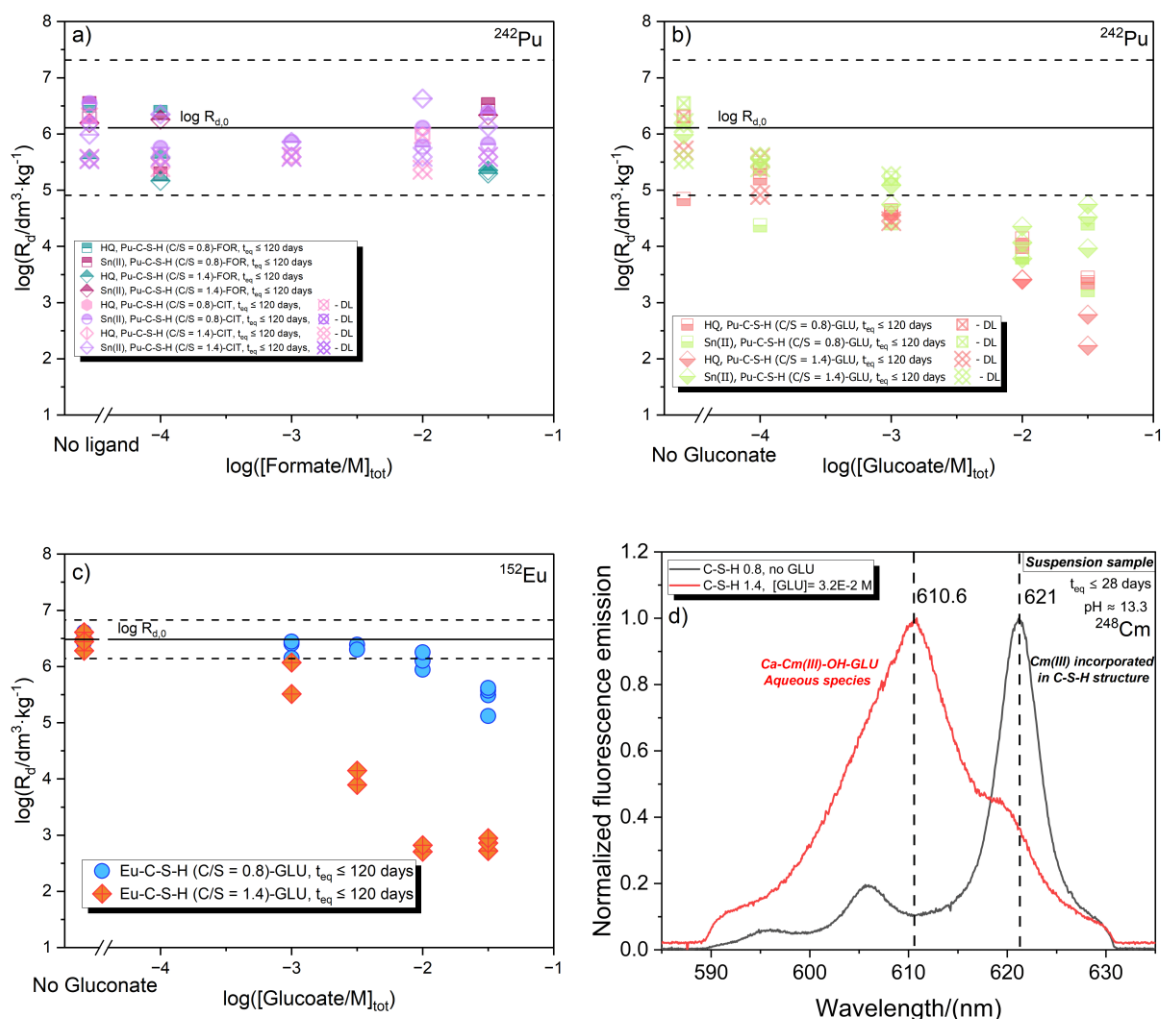
Figure 67. Distribution coefficients R_d for Pu(III/IV)-C-S-H-FOR (a), Pu(III/IV)-C-S-H-CIT (a), Pu(III/IV)-C-S-H-GLU (b) and Eu(III)-C-S-H-GLU systems under hyperalkaline and, only for plutonium sorption experiments, reducing conditions by using hydroquinone, HQ, and Sn(II)Cl₂, Sn(II), as redox buffers. Sorption data were collected for an equilibration time $t_{eq} \leq 120$ days. (d) Example of a TRLFS emission spectrum of Ca-Cm(III)-OH-GLU aqueous species (for $[GLU]_{tot} = 10^{-1.5}$ M) and of incorporated Cm(III) species in the C-S-H (C/S = 0.8) phase structure (in absence of GLU).

The conclusions summarized above provide quantitative insight on sorption phenomena and highlight the possible sorption mechanisms occurring for the Cement-L and Cement-RN-L systems. The present work clearly underlines the strong sorption of α-hydroxycarboxylic acids (e.g. citrate, gluconate) by cement phases and the impact they have on the uptake of tri- and tetravalent actinides as well as trivalent lanthanides under hyperalkaline and reducing conditions. This study provides also strong evidences on the key role of Ca in the formation of ternary / quaternary complexes with tri- and tetravalent actinides and gluconate, and thus on the retention processes. The results and conclusions of the present study define empirical basis and a mechanistic understanding to accurately evaluate the impact of formate, citrate and gluconate on the uptake of Pu(III/IV) and Eu(III) by C-S-H phases, AFm phases and ettringite and, consequently on hydrated cement.

Appendix 3.1

1. Formate uptake

1.1. Kinetic sorption experiments
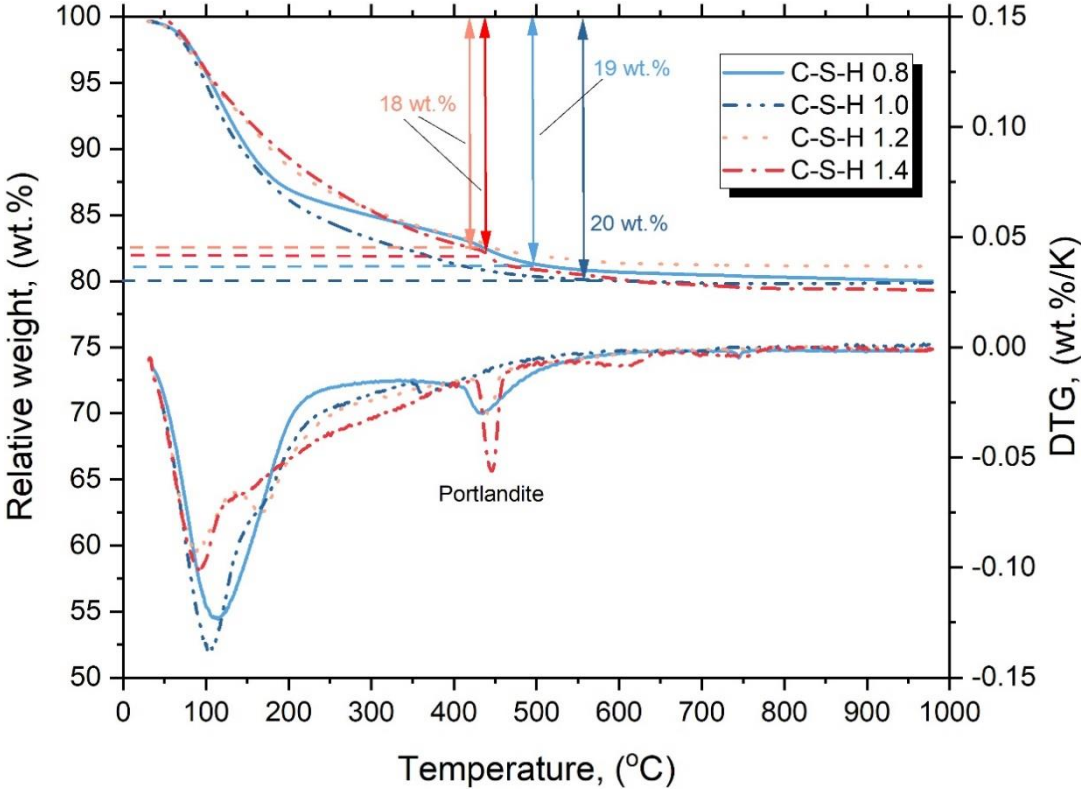
Figure 1. Thermogravimetric analysis of C-S-H phases with Ca/Si ratio of 0.8, 1.0, 1.2 and 1.4.
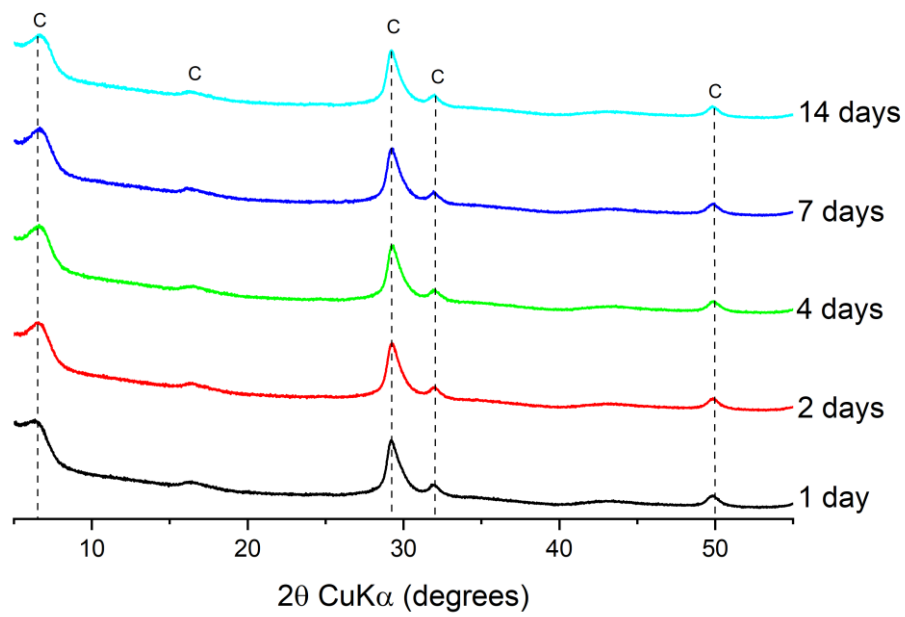
Figure 2. XRPD analysis of C-S-H 0.80 (Ca/Si) equilibrated in presence of Na-formate (0.22 M) for a contacting time of 1, 2, 4, 7 and 14 days. C: C-S-H phase.
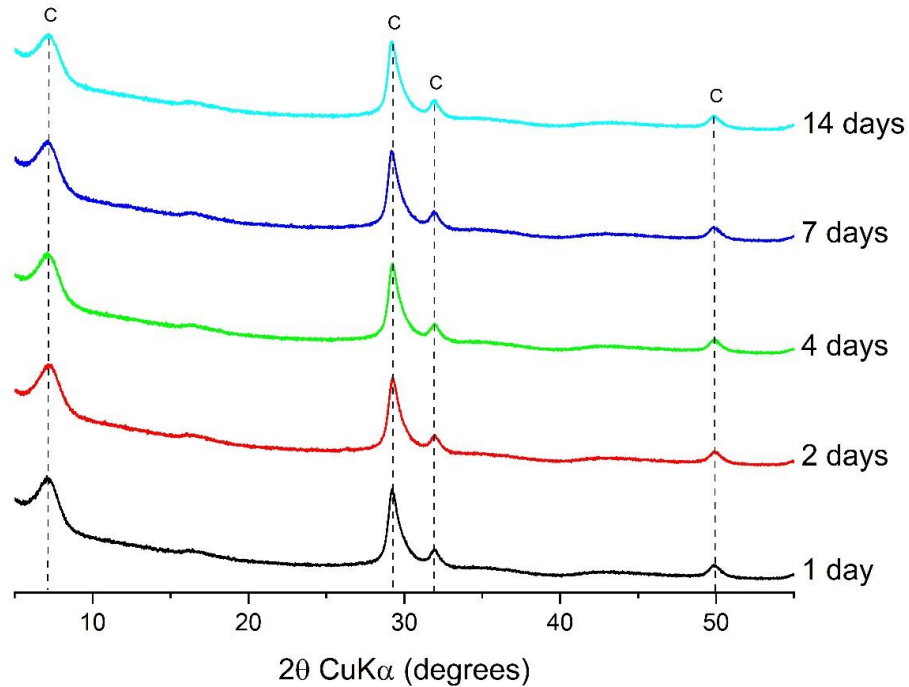
Figure 3. XRPD analysis of C-S-H 1.0 (Ca/Si) equilibrated in presence of Na-formate (0.22 M) for a contacting time of 1, 2, 4, 7 and 14 days. C: C-S-H phase.

142
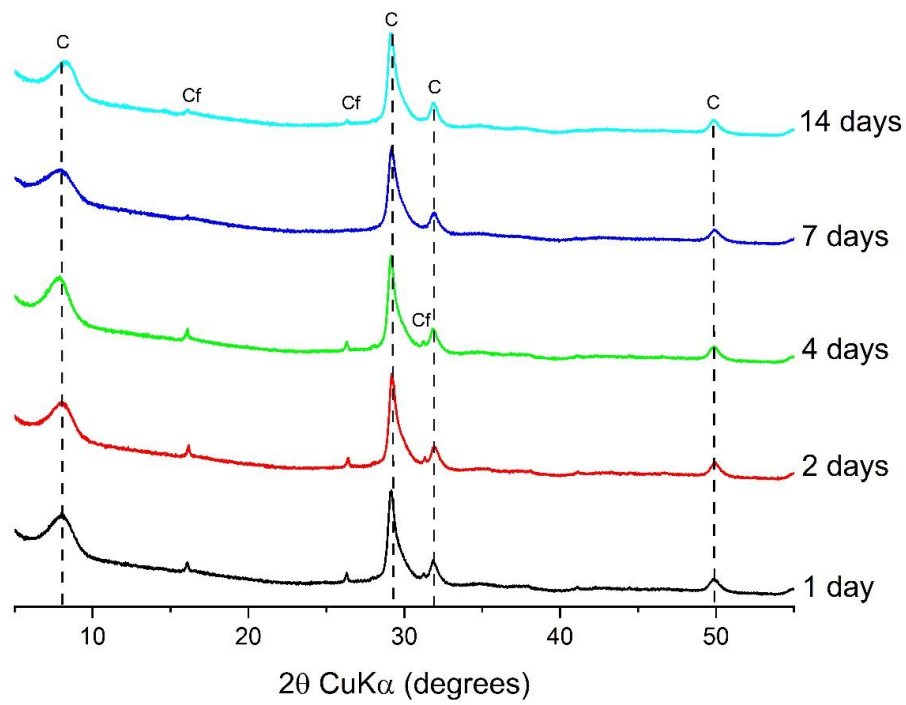
Figure 4. XRPD analysis of C-S-H 1.2 (Ca/Si) equilibrated in presence of Na-formate (0.22 M) for a contacting time of 1, 2, 4, 7 and 14 days. C: C-S-H phase; Cf: calcium formate, $Ca(HCO_2)_2$.
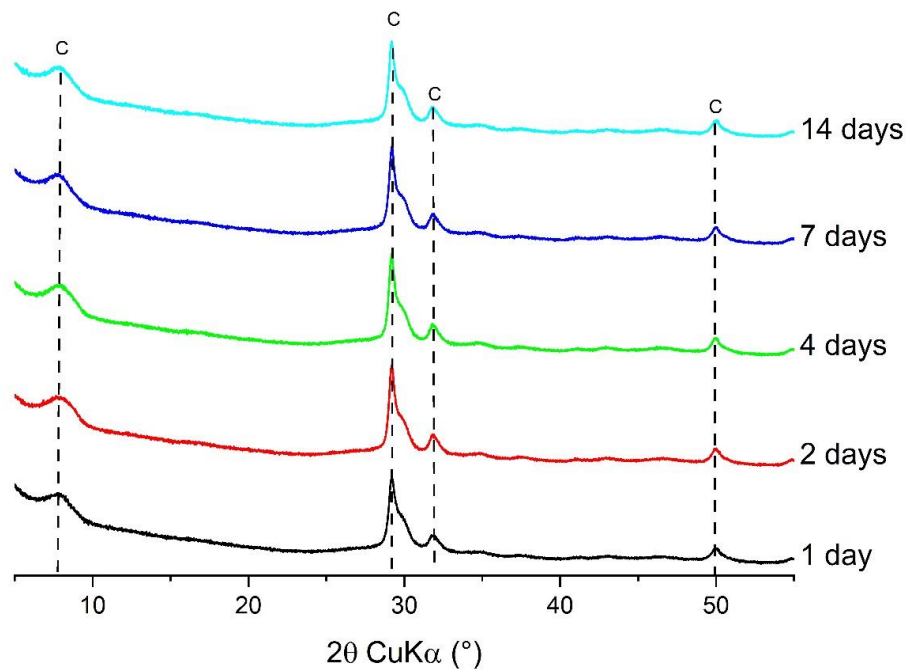
Figure 5. XRPD analysis of C-S-H 1.4 (Ca/Si) equilibrated in presence of Na-formate (0.22 M) for a contacting time of 1, 2, 4, 7 and 14 days. C: C-S-H phase.

Table 1. Solution composition of C-S-H phases with a Ca/Si = 0.8 in kinetic experiments with 221 mM of Na-formate.

Time/(days) C-S-H (Ca/Si=0.8)	[Na]	[Ca]	[Si]	[OH⁻]	Formate	Observed phase[a]
			mM			
1	197	14	33	0.059	205	C-S-H
2	197	12.0	22	0.068	203	C-S-H
4	192	13	22	0.065	202	C-S-H
7	184	13	20	0.074	206	C-S-H
14	191	13	22	0.0061	203	C-S-H

[a] Phases identification achieved by XRPD analyses. C-S-H: C-S-H phase.

Table 2. Saturation indices of C-S-H phase, lime, portlandite and silica for C-S-H phase with a Ca/Si = 0.8 in formate sorption experiments ([Na]$_{tot}$ = 0.2 M). Calculations have been carried out with GEMS software.

Time/(days)	C-S-H	Portlandite	SiO$_{2(am)}$	Ca(FOR)$_2$
	C-S-H (Ca/Si=0.8)			
1	0.67	-1.6	-3.1	-13
2	0.48	-1.7	-3.2	-13
4	0.49	-1.7	-3.1	-13
7	0.09	-3.2	-2.1	-13
14	0.44	-1.9	-3.0	-13

Table 3. Solution composition of C-S-H phases with a Ca/Si = 1.0 in kinetic experiments with 221 mM of Na-formate.

Time/(days) C-S-H (Ca/Si=1.0)	[Na]	[Ca]	[Si]	[OH⁻]	Formate	Observed phase[a]
			mM			
1	227	14	0.085	7.1	202	C-S-H
2	193	13	0.073	7.1	194	C-S-H
4	193	11	0.070	7.1	194	C-S-H
7	195	13	0.074	6.8	210	C-S-H
14	193	12	0.075	76	208	C-S-H

[a] Phases identification achieved by XRPD analyses. C-S-H: C-S-H phase.

Table 4. Saturation indices of C-S-H phase, lime, portlandite and silica for C-S-H phase with a Ca/Si = 1.0 in formate sorption experiments ([Na]$_{tot}$ =0.2 M). Calculations have been carried out with GEMS software.

Time/(days)	C-S-H	Portlandite	SiO$_{2(am)}$	Ca(FOR)$_2$
	C-S-H (Ca/Si=1.0)			
1	0.07	-0.6	-5.1	-13
2	-0.22	-1.3	-4.6	-13
4	-0.29	-1.4	-4.5	-13
7	-0.47	-2.1	-3.9	-13
14	-0.49	-2.2	-3.8	-13

Table 5. Solution composition of C-S-H phases with a Ca/Si = 1.2 in kinetic experiments with 221 mM of Na-formate.

Time/(days) C-S-H (Ca/Si=1.2)	[Na]	[Ca]	[Si]	[OH$^-$]	Formate	Observed phase[a]
	mM					
1	189	6.5	0.015	265	206	C-S-H
2	189	9.9	0.015	136	207	C-S-H
4	188	6.6	0.020	135	207	C-S-H
7	194	13	0.023	135	214	C-S-H
14	190	13	0.021	135	207	C-S-H, Ca(CHOO)$_2$

[a] Phases identification achieved by XRPD analyses. C-S-H: C-S-H phase.

Table 6. Saturation indices of C-S-H phase, lime, portlandite and silica for C-S-H phase with a Ca/Si = 1.2 in formate sorption experiments ([Na]$_{tot}$ =0.2 M). Calculations have been carried out with GEMS software.

Time/(days)	C-S-H	Portlandite	SiO$_2$(am)	Ca(FOR)$_2$
	C-S-H (Ca/Si=1.2)			
1	-4.5	-16	-2.1	-13
2	-1.5	-4.0	-3.4	-13
4	-4.5	-16	-2.0	-13
7	-1.0	-2.6	-4.0	-13
14	-0.9	-2.3	-4.3	-13

Table 7. Solution composition of C-S-H phases with a Ca/Si = 1.4 in kinetic experiments with 221 mM of Na-formate.

Time/(days) C-S-H (Ca/Si=1.4)	[Na]	[Ca]	[Si]	[OH⁻]	Formate	Observed phase[a]
	mM					
1	191	21	0.010	265	199	C-S-H
2	192	18	0.0089	136	202	C-S-H
4	193	20	0.015	135	202	C-S-H
7	192	20	0.013	135	200	C-S-H
14	191	14	0.034	135	204	C-S-H

[a] Phases identification achieved by XRPD analyses. C-S-H: C-S-H phase.

Table 8. Saturation indices of C-S-H phase, lime, portlandite and silica for C-S-H phase with a Ca/Si = 1.4 in formate sorption experiments ([Na]$_{tot}$ =0.2 M). Calculations have been carried out with GEMS software.

Time/(days)	C-S-H	Portlandite	$SiO_{2(am)}$	$Ca(FOR)_2$
	C-S-H (Ca/Si=1.4)			
1	1.3	1.0	-6.1	-13
2	1.2	1.0	-6.1	-13
4	1.4	1.0	-5.9	-13
7	1.4	1.0	-6.0	-13
14	1.6	0.82	-5.4	-13
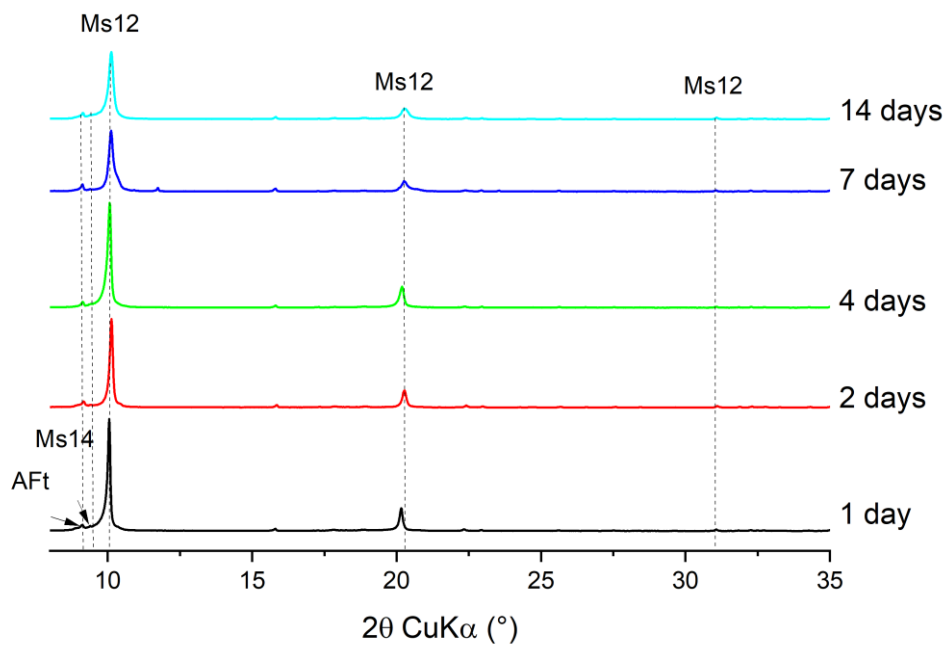
Figure 6. XRPD spectra of Ms samples in kinetic experiments with 221 mM of Na-formate. AFt: ettringite; Ms12: monosulfate-12; Ms14: monosulfate-14.
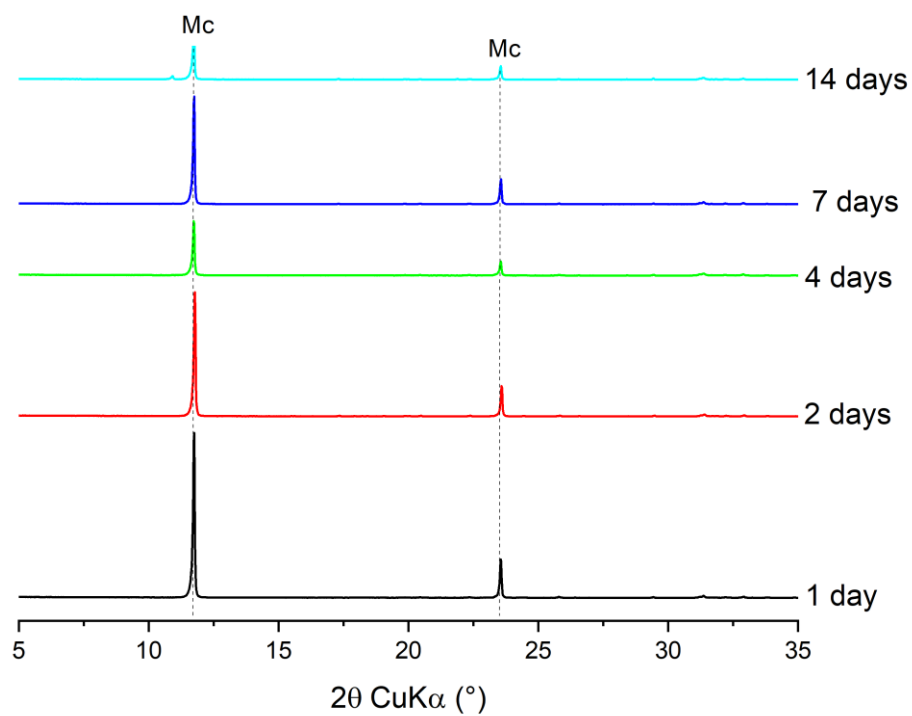
Figure 7. XRPD spectra of Mc samples in kinetic experiments with 221 mM of Na-formate. Mc: monocarbonate.
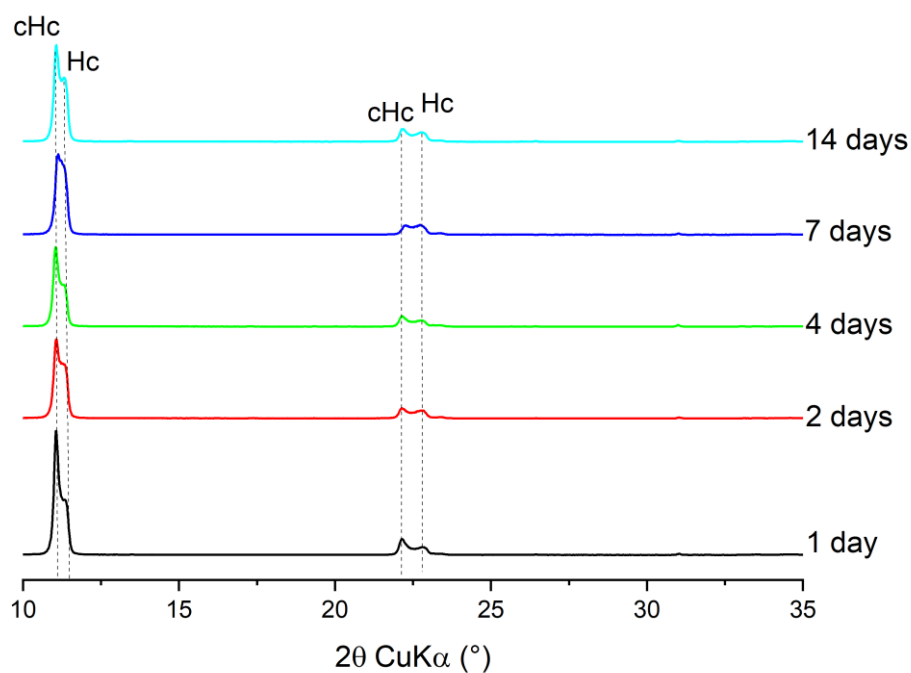
Figure 8. XRPD spectra of Hc samples in kinetic experiments with 221 of Na-formate. cHc: carbonated hemicarbonate; Hc: hemicarbonate.
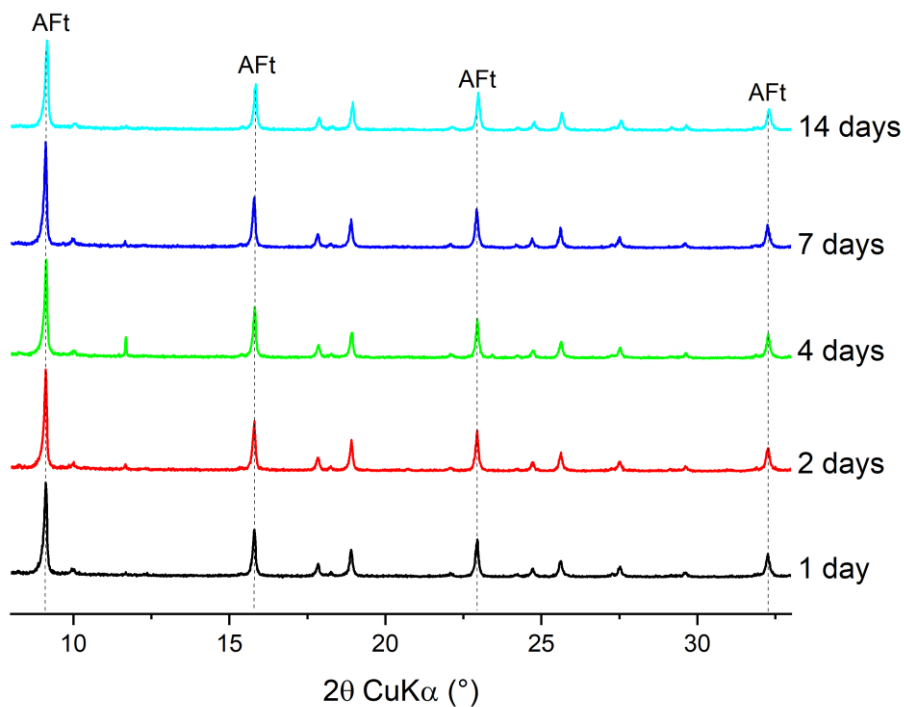
Figure 9. XRPD spectra of AFt samples in kinetic experiments with 221 of Na-formate. AFt: ettringite.

Table 9. Solution composition of Ms samples in kinetic experiments with 221 mM of Na-formate.

Time/(days) Monosulfate (Ms)	[Na]	[Ca]	[Al]	[S]	[OH⁻]	Formate	Observed phase[a]
	mM						
1	196	2.7	6.2	0.17	7.3	202	Ms12, Ms14, AFt
2	200	3.0	6.1	0.16	7.3	205	Ms12, Ms14, AFt
4	202	2.1	5.4	0.12	9.9	208	Ms12, Ms14, AFt
7	228	2.3	12	0.20	7.9	210	Ms12, Ms14, AFt
14	200	2.5	7.8	0.17	9.9	179	Ms12, Ms14, AFt

[a] Phases identification achieved by XRPD analyses. AFt: ettringite, Ms12: monosulfate-12, Ms14: monosulfate-14.

Table 10. Saturation indices of portlandite, katoite, gibbsite microcrystalline (Al(OH)₃), monosulfate (Ms), ettringite (AFt), Ca(FOR)₂, formate-AFm, for Ms system in citrate kinetic experiments ([FOR]ₜₒₜ = 0.22 M, [Na]ₜₒₜ = 0.2 M). Calculations have been carried out with GEMS software.

Time/(days)	Portlandite	katoite	Gibbsite (mic)	Ms	AFt	Ca(FOR)$_2$	Formate-AFm
1	-2.9	-4.0	0.51	-3.2	-3.3	-8.9	-2.1
2	-2.9	-3.9	0.52	-3.1	-3.3	-8.9	-2.0
4	-2.8	-3.9	0.32	-3.4	-4.1	-9.0	-2.2
7	-2.9	-3.4	0.75	-2.7	-2.9	-9.0	-1.6
14	-2.6	-3.2	0.48	-2.4	-2.5	-9.0	-1.4

Table 11. Solution composition of Mc samples in kinetic experiments with 221 mM of Na-formate.

Time/(days) Monocarbonate (Mc)	[Na]	[Ca]	[Al]	[OH-]	Formate	Observed phase[a]
	mM					
1	192	4.2	2.8	67	216	Mc, CC
2	201	4.5	2.9	67	221	Mc, CC
4	198	4.8	3.3	90	206	Mc, CC
7	201	4.7	3.3	90	213	Mc, CC
14	202	3.2	4.1	85	195	Mc, CC

[a] Phases identification achieved by XRPD analyses. Mc: monocarbonate, CC: calcite.

Table 12. Saturation indices of portlandite, katoite, monocarbonate (Mc), hemicarbonate (Hc), gibbsite microcrystalline (Al(OH)₃), Ca(FOR)₂, formate-AFm, for Mc system in citrate kinetic experiments ([FOR]$_{tot}$ = 0.22 M, [Na]$_{tot}$ = 0.2 M). Calculations have been carried out with GEMS software.

Time/(days)	Portlandite	katoite	Gibbsite (mic)	Mc	Hc	Ca(FOR)₂	Formate-AFm
1	-3.8	-6.3	0.68	0.64	-5.6	-32	0.60
2	-3.7	-6.0	0.66	0.31	-5.4	-32	0.20
4	-3.2	-5.0	0.53	0.56	-4.0	-31	0.48
7	-3.3	-5.1	0.54	0.82	-4.2	-31	0.75
14	-3.3	-5.0	0.55	0.99	-4.2	-31	0.96

Table 13. Solution composition of Hc samples in kinetic experiment with 221 mM of Na-formate.

Time/(days) Hemicarbonate (Hc)	[Na]	[Ca]	[Al]	[OH-]	Formate	Observed phase[a]
	mM					
1	196	5.2	0.24	33	167	Hc, cHc, Mc
2	201	4.5	0.34	33	170	Hc, cHc, Mc
4	199	6.1	0.16	42	163	Hc, cHc, Mc
7	199	5.9	0.28	42	156	Hc, cHc, Mc
14	201	5.4	0.29	25	153	cHc(?), Mc

[a] Phases identification achieved by XRPD analyses. cHc: carbo-hemicarbonate, Hc: hemicarbonate, Mc: monocarbonate.

Table 14. Saturation indices of portlandite, katoite, hemicarbonate (Hc), Ca(FOR)₂, formate-AFm, for Hc system in kinetic experiments ([FOR]$_{tot}$ = 0.22 M, [Na]$_{tot}$ = 0.2 M). Calculations have been carried out with GEMS software.

Time/(days)	Portlandite	katoite	Hc	Ca(FOR)₂	Formate-AFm
1	-0.90	-2.4	-0.30	-8.8	0.60
2	-0.98	-2.3	-0.23	-8.9	0.20
4	-1.1	-3.0	-1.11	-8.7	0.48
7	-0.98	-2.4	-0.30	-8.7	0.75
14	-0.96	-2.4	-0.25	-8.8	0.96

Table 15. Solution composition of AFt samples in kinetic experiments with 221 mM of Na-formate.

Time/(days) Ettringite (AFt)	[Na]	[Ca]	[Al]	[S]	[OH⁻]	Formate	Observed phase[a]
	mM						
1	197	4.3	0.54	29	91	217	AFt
2	197	4.1	0.74	28	91	218	AFt
4	197	4.2	0.12	34	91	209	AFt
7	197	3.6	3.1	30	117	208	AFt
14	195	6.0	5.6	29	117	198	AFt

[a] Phases identification achieved by XRPD analyses. AFt: ettringite.

Table 16. Saturation indices of portlandite, katoite, monosulfate (Ms), ettringite (AFt), $Ca(FOR)_2$, formate-AFm, for AFt system in citrate kinetic experiments ([FOR]$_{tot}$ = 0.22 M, [Na]$_{tot}$ = 0.2 M). Calculations have been carried out with GEMS software.

Time/(days)	Portlandite	katoite	Ms	AFt	$Ca(FOR)_2$	Formate-AFm
1	-1.5	-3.5	0.41	6.1	-8.2	-0.64
2	-1.03	-3.3	-4.1	1.6	-8.1	-5.1
4	-1.6	-2.9	-1.3	4.5	-8.1	-2.3
7	-1.6	-2.6	-1.4	4.3	-8.1	-2.4
14	-1.6	-2.7	-0.091	5.6	-8.1	-1.2

1.2. Sorption experiments
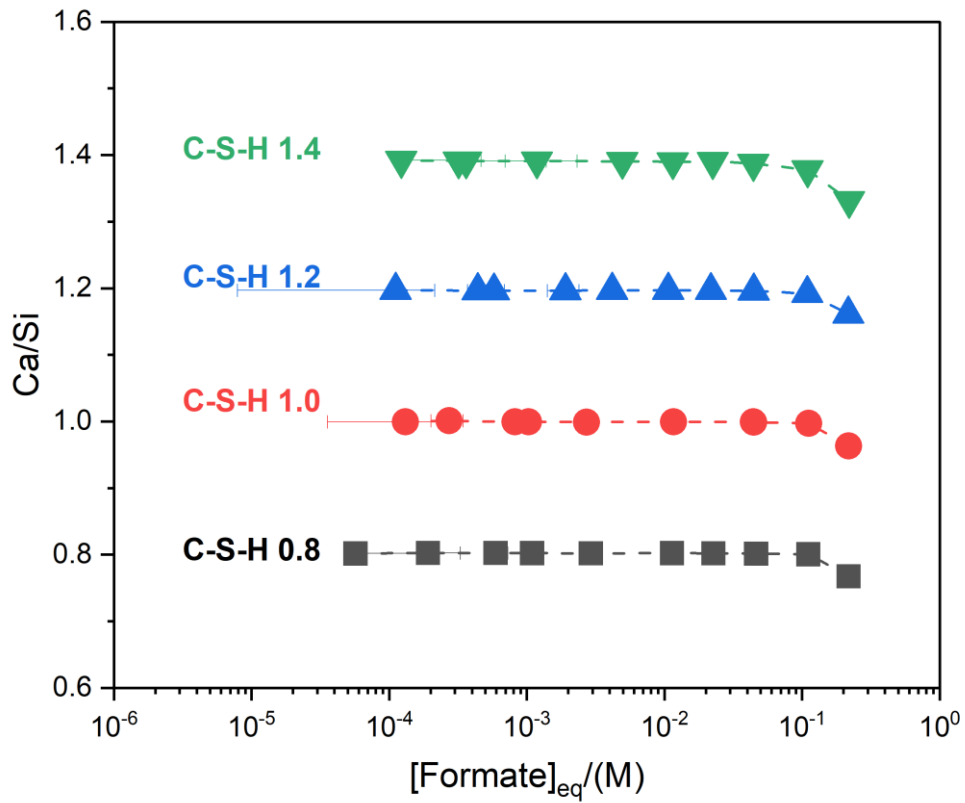
Figure 10. Calculated Ca/Si as a function of equilibrium concentration of formate for the C-S-H solid phases in presence of formate. Calculation have been carried out per 100 g of sample and taking into account the formation of portlandite by using the mass balance equation: $Ca/Si= ([Ca]_{tot,\,in}-[Ca]_{tot,\,eq}-[Ca]_{portlandite})/\,([Si]_{tot,\,in}-[Si]_{tot,\,eq})$.
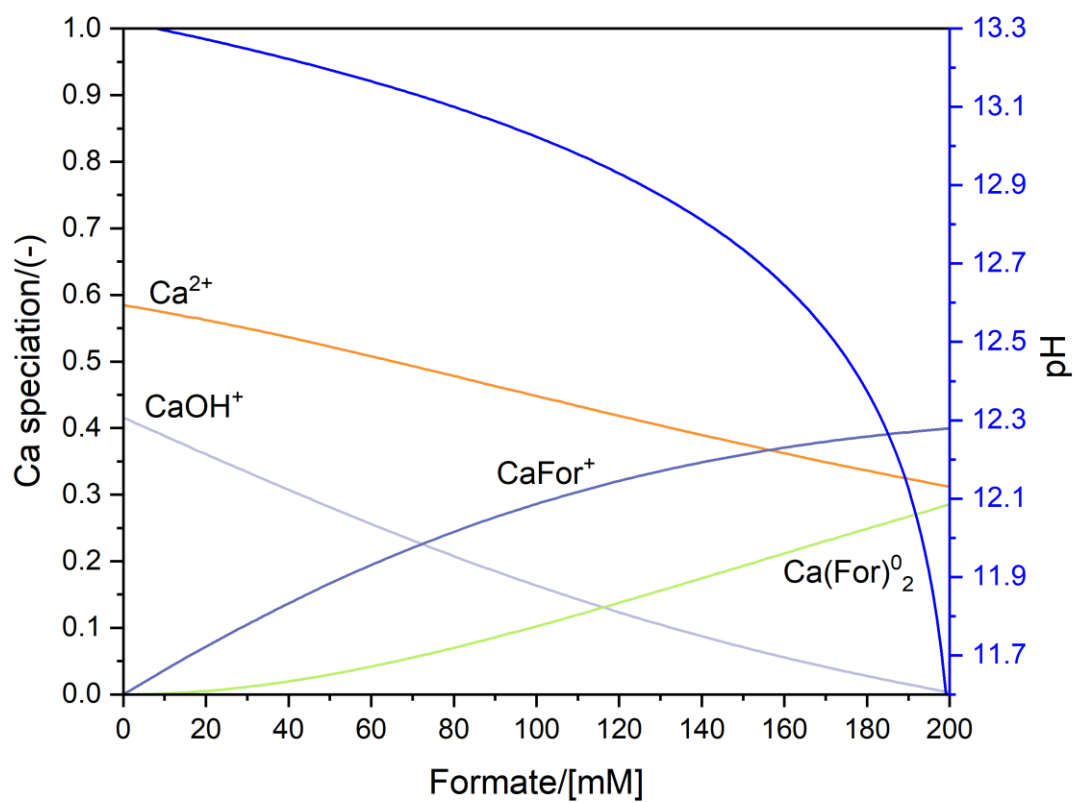
Figure 11. Calculated species distribution of Ca-complexes and pH determined with an initial calcium concentration of $[Ca]_{tot}$ = 2 mM as a function of added formate concentration.

*Table 17. Solution composition of **C-S-H phases (Ca/Si=0.8)** in formate sorption experiments.*

Measured initial formate concentration/(mM)	Measured concentrations					Observed phase[a]
	[Na]	[Ca]	[Si]	[OH⁻]	Formate	
	mM					
0	76	0.080	0.73	141	<0.020	C-S-H
0.22	74	0.044	1.10	124	<0.020	C-S-H
0.44	70	0.041	1.52	114	0.19	C-S-H
1.1	69	0.036	1.55	109	0.59	C-S-H
2.2	70	0.043	1.49	109	1.1	C-S-H
4.4	71	0.048	1.31	109	2.9	C-S-H
11	71	0.050	1.41	105	11	C-S-H
22	70	0.060	1.29	92	23	C-S-H
44	126	0.071	0.96	81	46	C-S-H
111	88	0.20	0.77	29	111	C-S-H
221	189	14	0.97	0.079	217	C-S-H

[a] Phases identification achieved by XRPD analyses. C-S-H: C-S-H phase.

*Table 18. Saturation indices of C-S-H phase, Calcite, $Ca_3Cit_2·4·H_2O$, lime, portlandite and silica for C-S-H phase with a **Ca/Si=0.8** in formate sorption experiments ([Na]$_{tot}$ = 0.20 M). Calculations have been carried out with GEMS software.*

[Formate]$_{tot}$/(mM)	C-S-H	Portlandite	SiO$_{2(am)}$	Ca(FOR)$_2$
0	-0.39	-2.2	-3.7	-17
0.22	-0.51	-2.6	-3.5	-18
0.44	-0.49	-2.8	-3.3	-18
1.1	-0.53	-2.9	-3.3	-18
2.2	-0.48	-2.8	-3.3	-18
4.4	-0.47	-2.7	-3.4	-18
11	-0.47	-2.8	-3.2	-18
22	-0.45	-2.9	-3.2	-18
44	-0.44	-2.4	-3.6	-18
111	-4.8	-19	-0.4	-16
221	-0.70	-6.6	-0.5	-13

*Table 19. Solution composition of **C-S-H phases (Ca/Si=1.0)** in formate sorption experiments.*

Measured initial formate concentration/(mM)	Measured concentrations					Observed phase[a]
	[Na]	[Ca]	[Si]	[OH⁻]	Formate	
	mM					
0	158	0.28	0.21	150	<0.020	C-S-H
0.22	159	0.30	0.19	136	0.13	C-S-H
0.44	120	0.24	0.71	101	0.27	C-S-H
1.1	155	0.27	0.23	125	0.82	C-S-H
2.2	145	0.28	0.23	115	1.0	C-S-H
4.4	162	0.38	0.16	128	2.7	C-S-H
11	156	0.29	0.21	108	12	C-S-H
22	174	0.37	0.23	108	44	C-S-H
44	163	0.40	0.18	89	45	C-S-H
111	175	1.08	0.11	45	112	C-S-H
221	204	14	0.12	6	218	C-S-H

[a] Phases identification achieved by XRPD analyses. C-S-H: C-S-H phase.
[b] Phase identification carried out by TGA characterization.

*Table 20. Saturation indices of C-S-H phase, portlandite and silica for C-S-H phase with a **Ca/Si=1.0** in formate sorption experiments ([Na]$_{tot}$ = 0.2 M). Calculations have been carried out with GEMS software.*

[Formate]$_{tot}$/(mM)	C-S-H	Portlandite	SiO$_{2(am)}$	Ca(FOR)$_2$
0	-0.19	-1.1	-4.8	-16
0.22	-0.19	-1.0	-4.9	-16
0.44	0.02	-1.5	-4.0	-16
1.1	-0.18	-1.1	-4.7	-16
2.2	-0.17	-1.1	-4.7	-16
4.4	-0.16	-0.92	-5.0	-15
11	-0.20	-1.1	-4.7	-16
22	-0.17	-1.2	-4.6	-16
44	-0.22	-1.2	-4.7	-15
111	-0.32	-1.4	-4.6	-14
221	0.51	-1.9	-2.9	-13

*Table 21. Solution composition of **C-S-H phases (Ca/Si=1.2)** in sorption experiments.*

Measured initial formate concentration/ (mM)	Measured concentrations					Observed phase[a]
	[Na]	[Ca]	[Si]	[OH⁻]	Formate	
	mM					
0	193	0.64	0.10	143	<0.020	C-S-H, CH[b]
0.22	194	1.0	0.050	143	0.11	C-S-H, CH[b]
0.44	197	1.1	0.048	143	0.44	C-S-H, CH[b]
1.1	185	1.2	0.043	143	0.58	C-S-H, CH[b]
2.2	198	1.1	0.052	143	1.9	C-S-H, CH[b]
4.4	196	0.92	0.059	143	4.2	C-S-H, CH[b]
11	193	0.94	0.055	131	11	C-S-H, CH[b]
22	193	1.0	0.060	131	22	C-S-H, CH[b]
44	199	1.4	0.076	115	44	C-S-H, CH[b]
111	201	2.6	0.049	74	109	C-S-H, CH[b]
221	217	13.3	0.031	14	217	C-S-H

[a] Phases identification achieved by XRPD analysis. C-S-H: C-S-H phase, CH: portlandite.
[b] Portlandite content per 100 g of dry sample. Phase identification carried out by TGA characterization.

*Table 22. Saturation indices of C-S-H phase, portlandite and silica for C-S-H phase with a **Ca/Si=1.2** in formate sorption experiments ([Na]$_{tot}$ = 0.2 M). Calculations have been carried out with GEMS software.*

[Formate]$_{tot}$/(mM)	C-S-H	Portlandite	SiO$_{2(am)}$	Ca(FOR)$_2$
0	-0.094	-0.57	-5.4	-15
0.22	-0.17	-0.36	-5.8	-15
0.44	-0.14	-0.30	-5.8	-15
1.1	-0.16	-0.29	-5.9	-14
2.2	-0.11	-0.29	-5.8	-15
4.4	-0.15	-0.41	-5.7	-15
11	-0.18	-0.44	-5.7	-15
22	-0.15	-0.46	-5.6	-15
44	-0.037	-0.44	-5.5	-14
111	-0.23	-0.66	-5.4	-14
221	-0.50	-1.2	-5.0	-13

*Table 23. Solution composition of **C-S-H phases (Ca/Si=1.4)** in formate sorption experiments.*

Measured initial formate concentration/ (mM)	Measured concentrations					Observed phase[a]
	[Na]	[Ca]	[Si]	[OH⁻]	Formate	
	mM					
0	211	2.9	0.085	156	<0.020	C-S-H, CH[b]
0.22	211	2.7	0.028	156	0.32	C-S-H, CH[b]
0.44	212	2.4	0.031	156	0.12	C-S-H, CH[b]
1.1	214	2.7	0.028	165	0.36	C-S-H, CH[b]
2.2	212	2.7	0.029	156	1.2	C-S-H, CH[b]
4.4	222	2.9	0.027	165	4.9	C-S-H, CH[b]
11	215	3.0	0.029	156	11	C-S-H, CH[b]
22	212	3.0	0.027	141	22	C-S-H, CH[b]
44	213	3.8	0.022	127	44	C-S-H, CH[b]
111	220	6.9	0.021	83	110	C-S-H, CH[b]
221	222	22	0.016	25	220	C-S-H, CH[b]

[a] Phases identification achieved by XRPD analyses. C-S-H: C-S-H phase, CH: portlandite.
[b] Portlandite content per 100 g of dry sample. Phase identification carried out by TGA characterization.

*Table 24. Saturation indices of C-S-H phase, portlandite and silica for C-S-H phase with a **Ca/Si=1.4** in formate sorption experiments ([Na]$_{tot}$ = 0.2 M). Calculations have been carried out with GEMS software.*

[Formate]$_{tot}$/(mM)	C-S-H	Portlandite	SiO$_{2(am)}$	Ca(FOR)$_2$
0	0.35	0.16	-5.9	-14
0.22	-0.020	0.14	-6.4	-14
0.44	-0.022	0.10	-6.3	-14
1.1	-0.011	0.15	-6.4	-14
2.2	-0.013	0.13	-6.3	-14
4.4	-0.005	0.19	-6.4	-14
11	0.030	0.20	-6.4	-14
22	0.003	0.19	-6.4	-14
44	0.017	0.30	-6.6	-14
111	0.18	0.58	-6.9	-13
221	0.49	1.1	-7.5	-13

Table 25. Mass of hydrated C-S-H phases per 2.21 g of (CaO + SiO$_2$) in 50 mL of solution calculated by combining mass balance and water content determined by TGA analysis.

[Formate]$_{tot, in}$/ (mM)	Ca/Si = 0.8	Ca/Si = 1.0	Ca/Si = 1.2	Ca/Si = 1.4
	g/g			
0	3.0	2.8	2.8	2.7
0.22	3.0	2.8	2.8	2.7
0.44	3.0	2.9	2.7	2.7
1.1	3.0	2.8	2.7	2.7
2.2	3.0	2.9	2.7	2.7
4.4	3.0	2.8	2.7	2.6
11	3.0	2.8	2.7	2.7
22	3.0	2.8	2.7	2.7
44	2.9	2.8	2.7	2.7
111	2.9	2.8	2.7	2.6
221	2.7	2.6	2.6	2.6
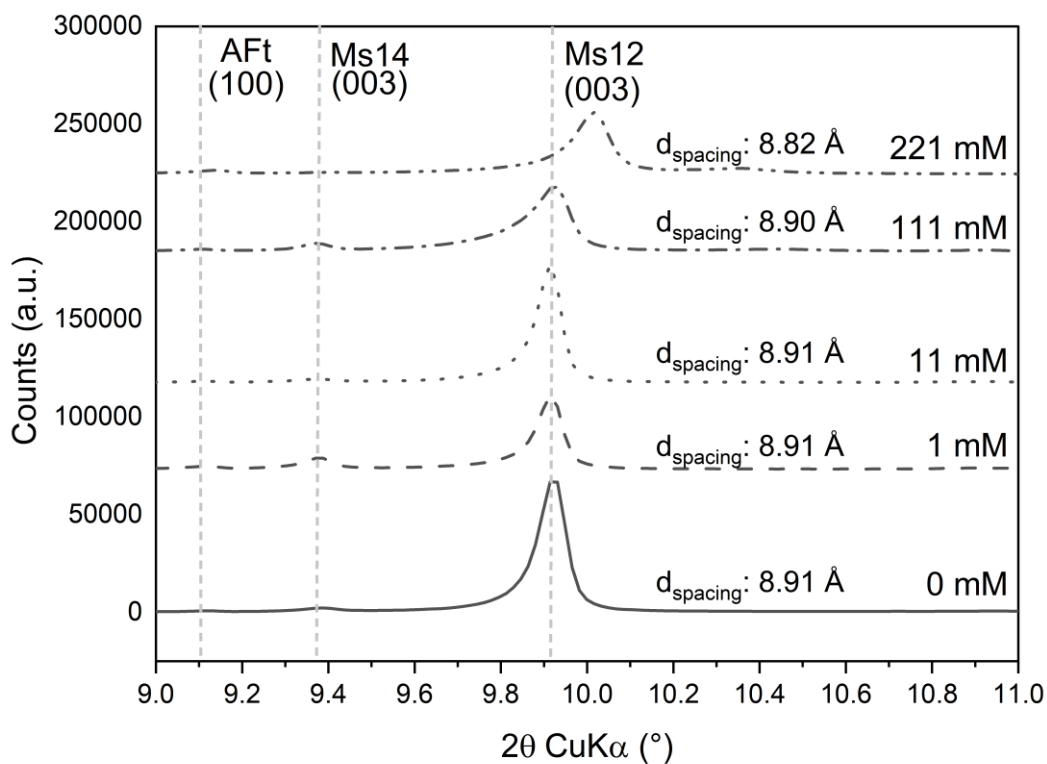
Figure 12. XRPD characterization of Ms in sorption experiments with [Formate]$_{tot}$ = 0 – 221 mM.
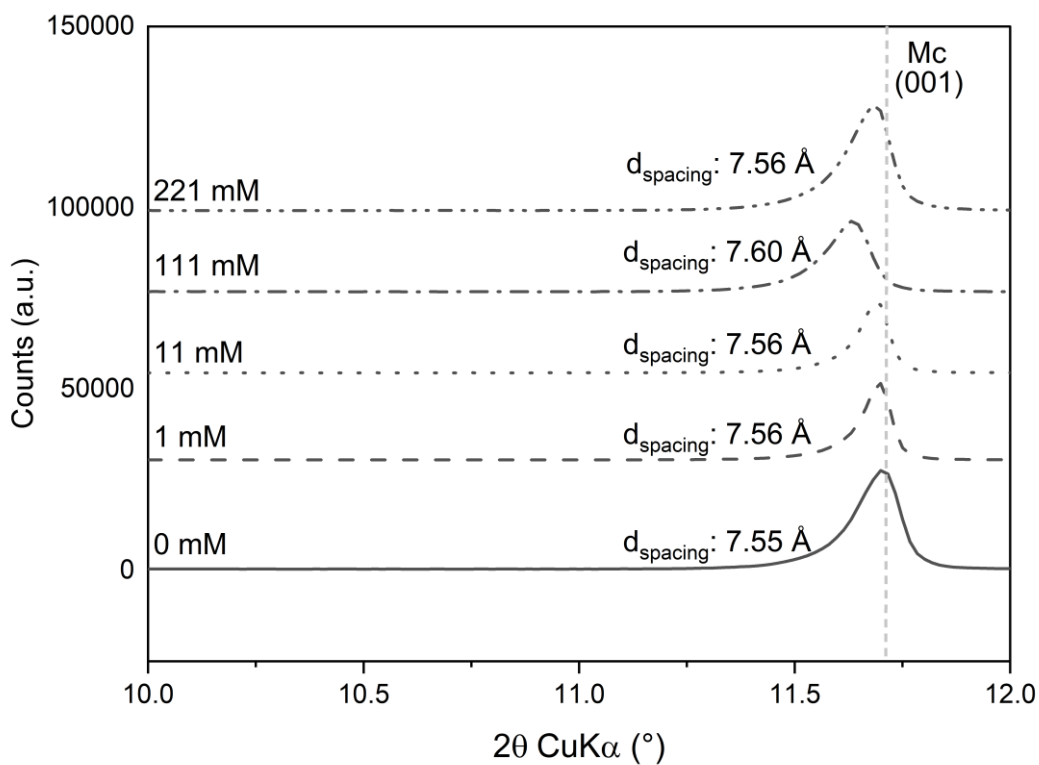
Figure 13. XRPD characterization of Mc in sorption experiments with [Formate]$_{tot}$ = 0 – 221 mM.
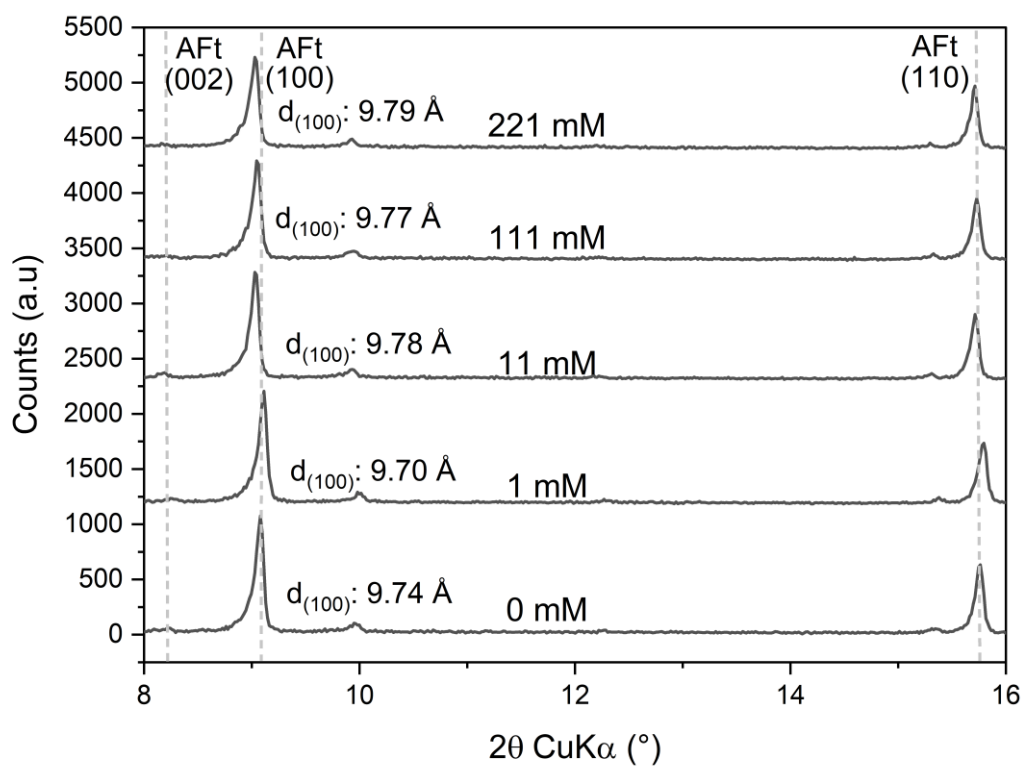
Figure 14. XRPD characterization of ettringite (AFt) in sorption experiments with [Formate]$_{tot}$ = 0 – 221 mM.
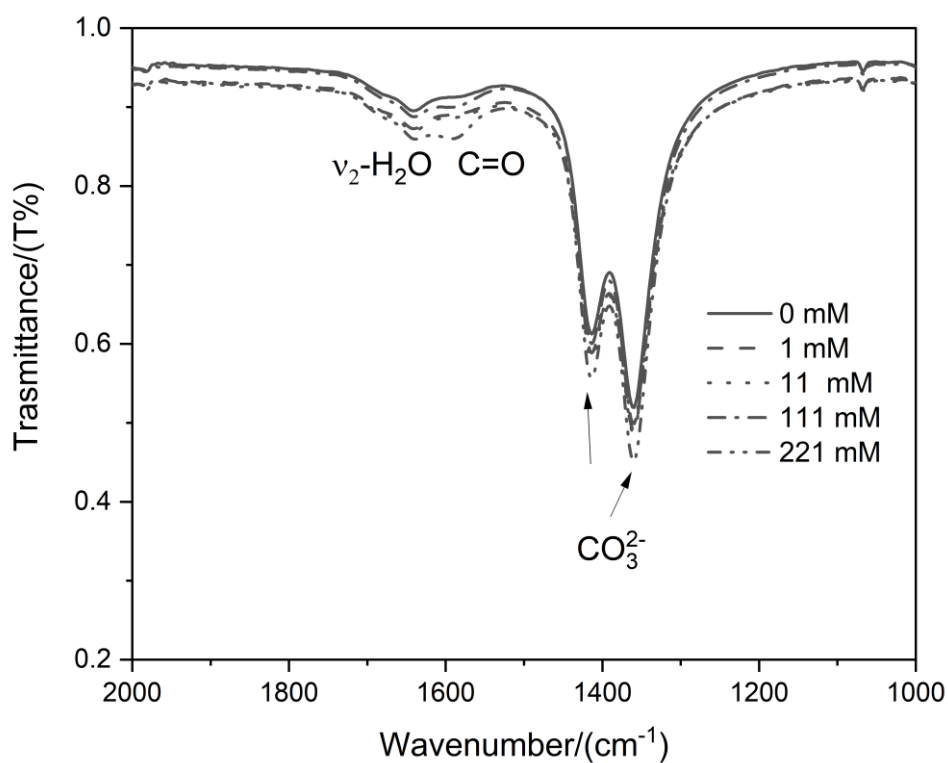
Figure 15. FT-IR characterization of Mc samples in sorption experiments (2000-1000 cm^{-1}).
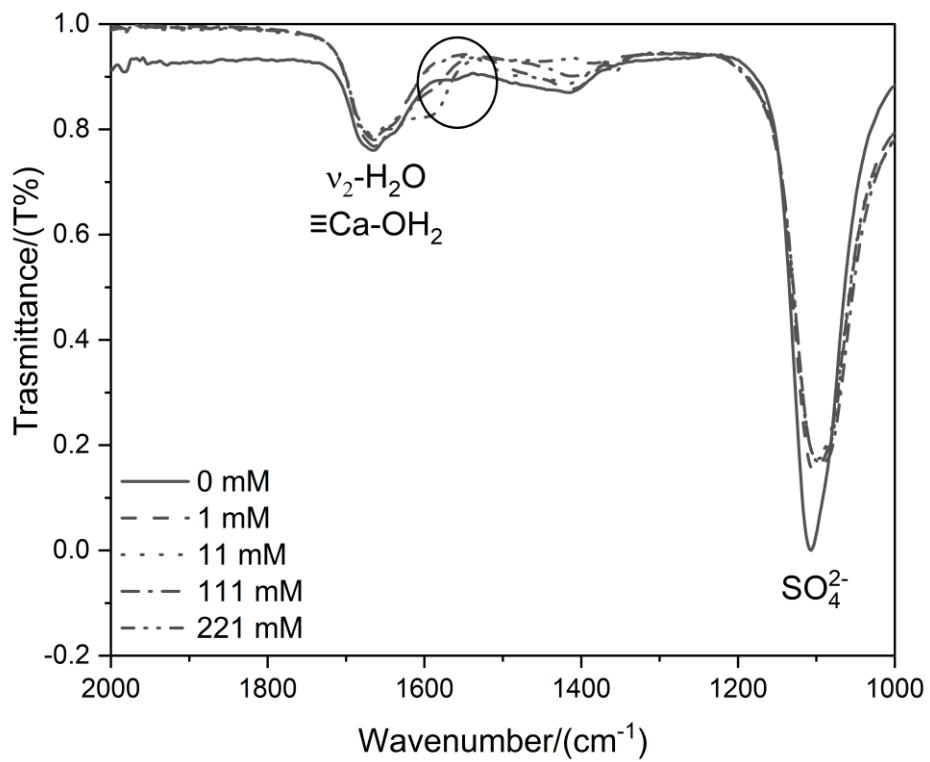
Figure 16. FT-IR characterization of AFt samples in sorption experiments (2000-1000 cm^{-1}).

*Table 26. Solution composition of **Ms** samples in formate sorption experiments.*

Measured initial formate concentration/ (mM)	Measured concentration						Observed phase[a]
	[Na]	[Ca]	[Al]	[S]	[OH⁻]	Formate	
	mM						
0	214	0.37	1.2	0.70	186	<0.020	Ms12, Ms14, AFt
0.22	216	0.32	1.4	0.84	177	<0.020	Ms12, Ms14, AFt
0.44	213	0.31	1.6	0.80	177	<0.020	Ms12, Ms14, AFt
1.1	216	0.47	1.4	0.79	169	<0.020	Ms12, Ms14, AFt
2.2	218	0.37	1.4	0.91	169	0.19	Ms12, Ms14, AFt
4.4	214	0.41	1.6	0.86	169	1.5	Ms12, Ms14, AFt
11	216	0.30	1.9	0.89	161	12	Ms12, Ms14, AFt
22	222	0.32	2.5	0.99	161	24	Ms12, Ms14, AFt
44	208	0.37	2.6	0.73	133	52	Ms12, Ms14, AFt
111	225	0.36	4.5	0.73	91	118	Ms12, Ms14, AFt
221	223	1.83	8.1	0.06	10	209	Ms12, Ms14, AFt

[a] Phases identified by XRPD analyses. AFt: ettringite, Ms12: monosulfate-12, Ms14: monosulfate-14.

*Table 27. Saturation indices of portlandite, katoite, gypsum, monosulfate (Ms), ettringite (AFt), $Ca(FOR)_2$, formate-AFm, for **Ms** system in formate sorption experiments ($[Na]_{tot} = 0.2$ M). Calculations have been carried out with GEMS software.*

[Formate]$_{tot}$/(mM)	Portlandite	katoite	Gypsum	Ms	AFt	$Ca(FOR)_2$	Formate-AFm
0	-0.85	-1.8	-3.5	-1.0	-1.2	-	-
0.22	-0.87	-1.8	-3.6	-1.0	-1.2	-24	-
0.44	-0.68	-1.3	-3.4	-1.0	-0.25	-24	-
1.1	-0.78	-1.6	-3.4	-0.41	-0.71	-24	-
2.2	-0.76	-1.4	-3.4	-0.77	-0.40	-16	-6.4
4.4	-0.94	-1.8	-3.5	-0.51	-1.2	-14	-4.3
11	-0.96	-1.6	-3.5	-1.0	-0.83	-12	-3.0
22	-1.1	-1.8	-3.5	-0.77	-1.2	-11	-2.3
44	-1.6	-2.4	-3.7	-1.0	-2.1	-11	-1.7
111	-3.0	-4.1	-4.2	-1.7	-5.5	-10	-1.7
221	-0.85	-1.8	-3.5	-4.0	-1.2	-9	-2.4

*Table 28. Solution composition of **Mc** samples in formate sorption experiments.*

Measured initial formate concentration/(mM)	Measured concentration					Observed phase[a]
	[Na]	[Ca]	[Al]	[OH⁻]	Formate	
	mM					
0	212	0.56	0.19	206	<0.020	Mc, CC
0.22	212	0.61	0.20	186	0.20	Mc, CC
0.44	216	0.54	0.48	177	1.1	Mc, CC
1.1	213	0.53	0.25	177	1.9	Mc, CC
2.2	215	0.54	0.22	168	2.0	Mc, CC
4.4	214	0.49	0.25	177	4.0	Mc, CC
11	215	0.53	0.22	168	12	Mc, CC
22	215	0.57	0.20	151	23	Mc, CC
44	215	0.64	0.20	130	46	Mc, CC
111	219	0.74	0.38	86	120	Mc, CC
221	223	4.22	2.72	6.3	226	Mc, CC

[a] Phases identification achieved by XRPD analyses. CC: calcite, Mc: monocarbonate.

*Table 29. Saturation indices of portlandite, katoite, monocarbonate (Mc), hemicarbonate (Hc), ettringite (AFt), $Ca(FOR)_2$, formate-AFm, for **Mc** system in formate sorption experiments ($[Na]_{tot} = 0.2$ M). Calculations have been carried out with GEMS software.*

[Formate]$_{tot}$/(mM)	Portlandite	katoite	Mc	Hc	Ca(FOR)$_2$	Formate-AFm
0	-0.60	-2.8	-0.38	-1.3	-	-
0.22	-0.57	-2.7	-0.27	-1.1	-16	-7.2
0.44	-0.62	-2.1	0.35	-0.55	-14	-5.1
1.1	-0.63	-2.7	-0.26	-1.2	-13	-5.3
2.2	-0.63	-2.8	-0.35	-1.2	-13	-5.3
4.4	-0.68	-2.8	-0.40	-1.3	-13	-4.8
11	-0.68	-2.9	-0.49	-1.4	-12	-3.9
22	-0.70	-3.0	-0.58	-1.5	-11	-3.4
44	-0.79	-3.1	-0.74	-1.7	-11	-3.0
111	-1.3	-3.6	-1.2	-2.4	-10	-2.6
221	-4.0	-6.7	-4.3	-6.9	-9	-4.6

*Table 30. Solution composition of **Hc** samples in formate sorption experiments.*

Measured initial formate concentration/(mM)	Measured concentration					Observed phase[a]
	[Na]	[Ca]	[Al]	[OH$^-$]	Formate	
	mM					
0	218	1.8	0.22	176	<0.020	Hc, cHc, Mc
0.22	218	1.7	0.21	174	0.41	Hc, cHc, Mc
0.44	217	1.9	0.23	172	0.79	Hc, cHc, Mc
1.1	222	1.7	0.16	172	1.5	Hc, cHc, Mc
2.2	221	1.9	0.15	172	2.3	Hc, cHc, Mc
4.4	222	1.9	0.25	170	3.7	Hc, cHc
11	224	2.0	0.17	164	10	Hc, cHc
22	218	2.2	0.19	165	20	Hc, cHc
44	218	2.3	0.09	148	39	Hc, cHc, Mc
111	221	4.3	0.06	46	97	Hc, cHc, Mc
221	222	6.5	0.15	99	173	cHc, Mc

[a] Phases identification achieved by XRPD analyses. cHc: carbo-hemicarbonate, Hc: hemicarbonate, Mc: monocarbonate.

*Table 31. Saturation indices of portlandite, katoite, hemicarbonate (Hc), Ca(FOR)$_2$, formate-AFm for **Hc** system in formate sorption experiments ([Na]$_{tot}$ =0.2 M). Calculations have been carried out with GEMS software.*

[Formate]$_{tot}$/(mM)	Portlandite	katoite	Hc	Ca(FOR)$_2$	Formate-AFm
0	-0.074	-1.1	0.69	-	-
0.22	-0.100	-1.3	0.54	-14	-0.49
0.44	-0.063	-1.1	0.75	-14	-0.80
1.1	-0.093	-1.5	0.33	-13	-0.28
2.2	-0.067	-1.4	0.37	-13	0.63
4.4	-0.066	-1.0	0.80	-13	0.67
11	-0.069	-1.3	0.50	-12	0.57
22	-0.091	-1.2	0.57	-11	1.2
44	-0.16	-2.0	-0.24	-11	0.55
111	-0.26	-2.3	-0.59	-10	1.1
221	-0.83	-2.7	-1.20	-9	0.85

*Table 32. Solution composition of **AFt** samples in formate sorption experiments.*

Measured initial formate concentration/ (mM)	Measured concentration						Observed phase[a]
	[Na]	[Ca]	[Al]	[S]	[OH⁻]	Formate	
	mM						
0	199	0.029	6.6	11	112	<0.020	AFt
0.22	197	0.090	5.8	11	106	0.37	AFt
0.44	198	0.075	7.1	12	112	0.81	AFt
1.1	199	0.15	6.0	11	119	0.96	AFt
2.2	201	0.11	7.0	12	112	2.2	AFt
4.4	198	0.085	5.9	12	112	4.2	AFt
11	198	0.092	5.8	12	112	12	AFt
22	200	0.10	5.6	12	100	23	AFt
44	201	0.12	5.8	11	89	45	AFt
111	202	0.16	5.7	12	40	110	AFt
221	201	22	0.067	22	0.0026	224	AFt

[a] Phases identified by XRPD analyses. AFt: ettringite.

*Table 33. Saturation indices of portlandite, katoite, gypsum, monosulfate (Ms), ettringite (AFt), $Ca(FOR)_2$, formate-AFm for **AFt** system in formate sorption experiments ($[Na]_{tot} = 0.2$ M). Calculations have been carried out with GEMS software.*

$[Formate]_{tot}$/(mM)	Portlandite	katoite	Gypsum	Ms	AFt	$Ca(FOR)_2$	Formate-AFm
0	-2.1	-3.9	-3.4	-3.0	-2.9	-	-
0.22	-1.6	-2.4	-2.9	-1.2	-0.07	-16	-2.0
0.44	-1.7	-2.5	-3.0	-1.3	-0.38	-15	-2.1
1.1	-1.4	-2.6	-2.7	-0.26	1.3	-14	-2.0
2.2	-1.5	-2.5	-2.8	-0.66	0.70	-14	-1.8
4.4	-1.6	-2.8	-2.9	-1.3	-0.23	-13	-1.7
11	-1.6	-2.9	-2.9	-1.3	-0.20	-12	-1.7
22	-1.7	-2.8	-2.9	-1.3	-0.06	-12	-1.1
44	-1.7	-4.2	-2.8	-1.3	-0.087	-11	-1.3
111	-2.3	-3.8	-2.8	-2.5	-1.13	-10	-0.67
221	-2.1	-2.8	-0.6	-3.0	-2.9	-8	0.093

2.   Citrate uptake

2.1.   Kinetic sorption experiments
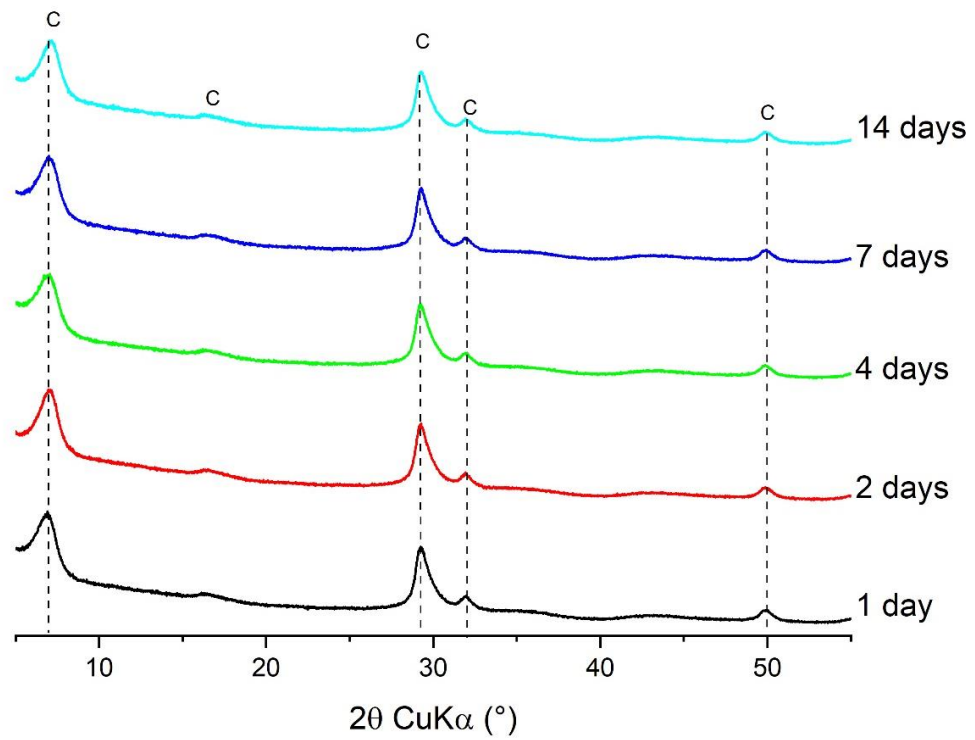
Figure 17. XRPD analysis of C-S-H 0.80 (Ca/Si) equilibrated in presence of Na$_3$-citrate (0.034 M) for a contacting time of 1, 2, 4, 7 and 14 days. C: C-S-H phase.
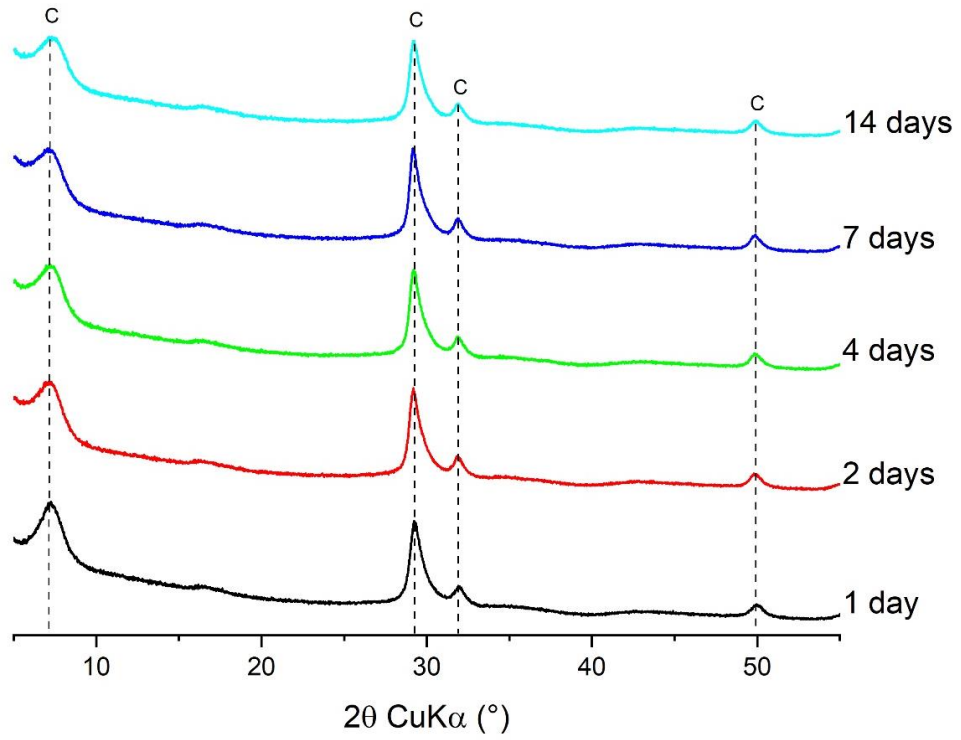
Figure 18. XRPD analysis of C-S-H 1.0 (Ca/Si) equilibrated in presence of Na₃-citrate (0.034 M) for a contacting time of 1, 2, 4, 7 and 14 days. C: C-S-H phase.
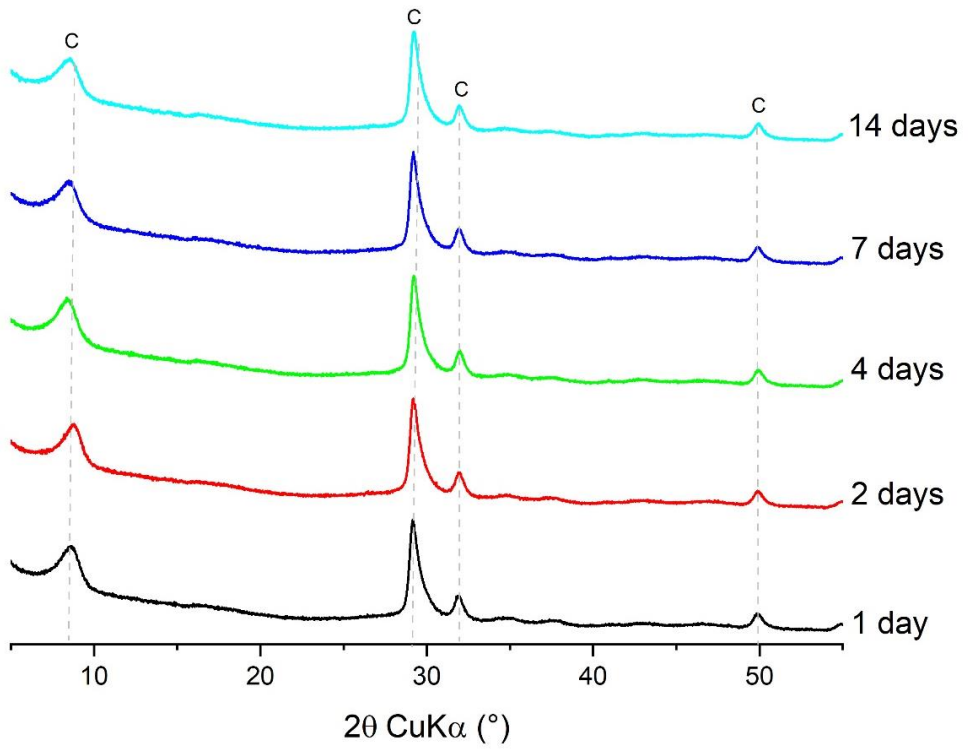
Figure 19. XRPD analysis of C-S-H 1.2 (Ca/Si) equilibrated in presence of Na₃-citrate (0.034 M) for a contacting time of 1, 2, 4, 7 and 14 days. C: C-S-H phase.

167
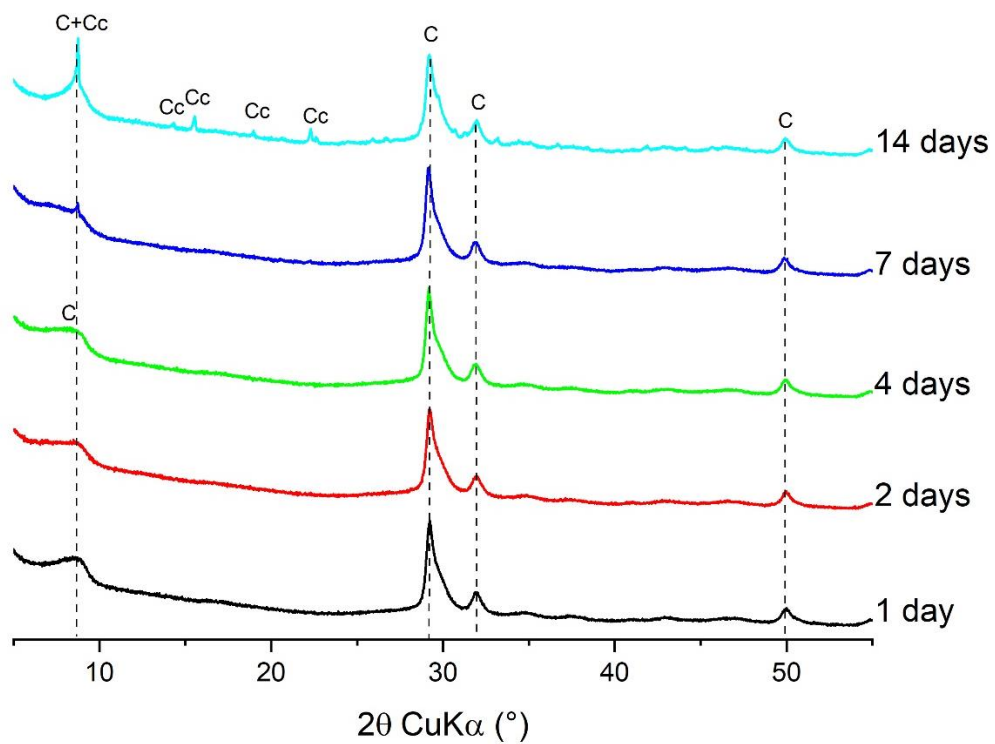
Figure 20. XRPD analysis of C-S-H 1.4 (Ca/Si) equilibrated in presence of Na$_3$-citrate (34 mM) for a contacting time of 1, 2,4, 7 and 14 days. C: C-S-H phase, Cc: Calcium citrate tetrahydrate.

Table 34. Solution composition of C-S-H phases with a Ca/Si = 0.8 in kinetic experiments with 34 mM of Na$_3$-citrate.

Time/(days) C-S-H (Ca/Si=0.8)	[Na]	[Ca]	[Si]	[OH$^-$]	Citrate	Observed phase[a]
	mM					
1	265	6.9	0.7	265	32	C-S-H
2	136	6.1	1.1	136	31	C-S-H
4	135	6.1	1.2	135	31	C-S-H
7	135	5.8	1.2	135	31	C-S-H
14	135	5.9	1.1	135	31	C-S-H

[a] Phases identification achieved by XRPD analyses. C-S-H: C-S-H phase.

Table 35. Saturation indices of C-S-H phase, Calcite, Ca$_3$Cit$_2$·4·H$_2$O, lime, portlandite and silica for C-S-H phase with a Ca/Si = 0.8 in citrate sorption experiments ([Na]$_{tot}$ = 0.2 M). Calculations have been carried out with GEMS software.

Time/(days)	C-S-H	Ca$_3$Cit$_2$·4·H$_2$O	Portlandite	SiO$_{2(am)}$
	C-S-H (Ca/Si=0.8)			
1	0.71	-0.34	-0.30	-4.7
2	0.76	-0.38	-0.75	-4.1
4	0.77	-0.40	-0.77	-4.0
7	0.74	-0.46	-0.80	-4.0
14	0.72	-0.42	-0.78	-4.1

Table 36. Solution composition of C-S-H phases with a Ca/Si = 1.0 in kinetic experiments with 34 mM of Na$_3$-citrate.

Time/(days) C-S-H (Ca/Si=1.0)	[Na]	[Ca]	[Si]	[OH$^-$]	Citrate	Observed phase[a]
	mM					
1	151	12	0.25	84	27	C-S-H
2	154	12	0.24	88	29	C-S-H
4	152	12	0.24	88	29	C-S-H
7	151	12	0.26	133	29	C-S-H
14	147	12	0.23	133	28	C-S-H

[a] Phases identification achieved by XRPD analyses. C-S-H: C-S-H phase.

Table 37. Saturation indices of C-S-H phase, Calcite, Ca$_3$Cit$_2$·4·H$_2$O, lime, portlandite and silica for C-S-H phase with a Ca/Si = 1.0 in citrate sorption experiments ([Na]$_{tot}$ = 0.2 M). Calculations have been carried out with GEMS software.

Time/(days) C-S-H (Ca/Si=1.0)	Time/(days)	C-S-H	Ca$_3$Cit$_2$·4·H$_2$O	Portlandite
	mM			
1	0.73	0.69	-7.5	-5.3
2	0.71	0.66	-7.5	-5.3
4	0.72	0.70	-7.5	-5.4
7	0.73	0.66	-7.5	-5.3
14	0.69	0.67	-7.5	-5.3

Table 38. Solution composition of C-S-H phases with a Ca/Si = 1.2 in kinetic experiments with 34 mM of Na$_3$-citrate.

Time/(days) C-S-H (Ca/Si=1.2)	[Na]	[Ca]	[Si]	[OH$^-$]	Citrate	Observed phase[a]
	mM					
1	151	12	0.084	73	28	C-S-H
2	154	14	0.071	73	28	C-S-H
4	152	13	0.15	65	28	C-S-H
7	151	14	0.086	69	28	C-S-H
14	147	14	0.10	69	28	C-S-H

[a] Phases identification achieved by XRPD analyses. C-S-H: C-S-H phase.

Table 39. Saturation indices of C-S-H phase, Calcite, Ca$_3$Cit$_2$·4·H$_2$O, lime, portlandite and silica for C-S-H phase with a Ca/Si = 1.2 in citrate sorption experiments ([Na]$_{tot}$ = 0.2 M). Calculations have been carried out with GEMS software.

Time/(days)	C-S-H	Ca$_3$Cit$_2$·4·H$_2$O	Portlandite	SiO$_{2(am)}$
	C-S-H (Ca/Si=1.2)			
1	0.43	0.70	0.25	-5.93
2	0.43	0.83	0.34	-6.08
4	0.62	0.77	0.25	-5.69
7	0.48	0.81	0.32	-5.97
14	0.53	0.81	0.30	-5.89

Table 40. Solution composition of C-S-H phases with a Ca/Si = 1.4 in kinetic experiments with 34 mM Na$_3$-citrate.

Time/(days)	[Na]	[Ca]	[Si]	[OH$^-$]	Citrate	Observed phase[a]
C-S-H (Ca/Si=1.4)	mM					
1	171	16	0.040	93	21	C-S-H, CH[b]
2	173	15	0.056	99	19	C-S-H, CH[b]
4	171	15	0.031	99	20	C-S-H, CH[b]
7	171	14	0.031	99	19	C-S-H, CH[b]
14	169	7.8	0.074	99	15	C-S-H, CH[b]

[a] Phases identification achieved by XRPD analyses. C-S-H: C-S-H phase, CH: portlandite.
[b] Phase identification carried out by TGA characterization.

Table 41. Saturation indices of C-S-H phase, Calcite, Ca$_3$Cit$_2$·4·H$_2$O, lime, portlandite and silica for C-S-H phase with a Ca/Si = 1.4 in citrate sorption experiments ([Na]$_{tot}$ = 0.2 M). Calculations have been carried out with GEMS software.

Time/(days)	C-S-H	Ca$_3$Cit$_2$·4·H$_2$O	Portlandite	SiO$_{2(am)}$
	C-S-H (Ca/Si=1.4)			
1	0.38	0.79	0.56	-6.54
2	0.51	0.68	0.59	-6.41
4	0.31	0.74	0.57	-6.65
7	0.27	0.65	0.52	-6.61
14	0.34	0.0054	0.18	-5.93
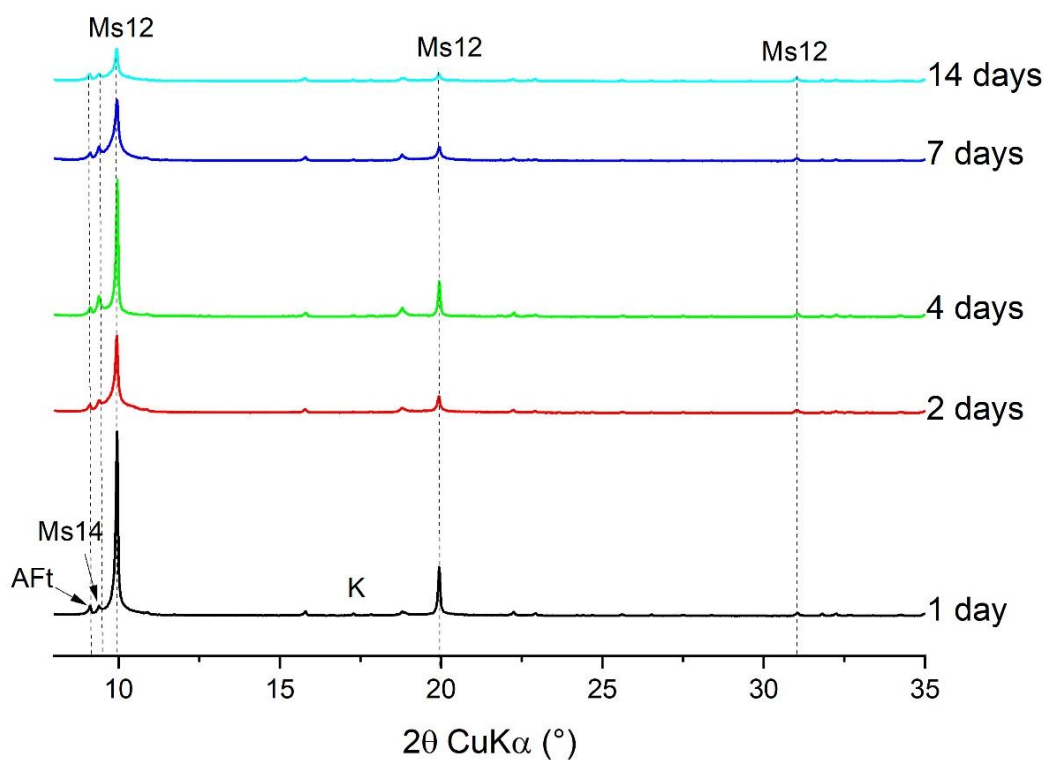
Figure 21. XRPD spectra of Ms samples in kinetic experiments with 34 mM Na$_3$-citrate. AFt: ettringite; K: katoite; Ms12: monosulfate-12; Ms14: monosulfate-14.
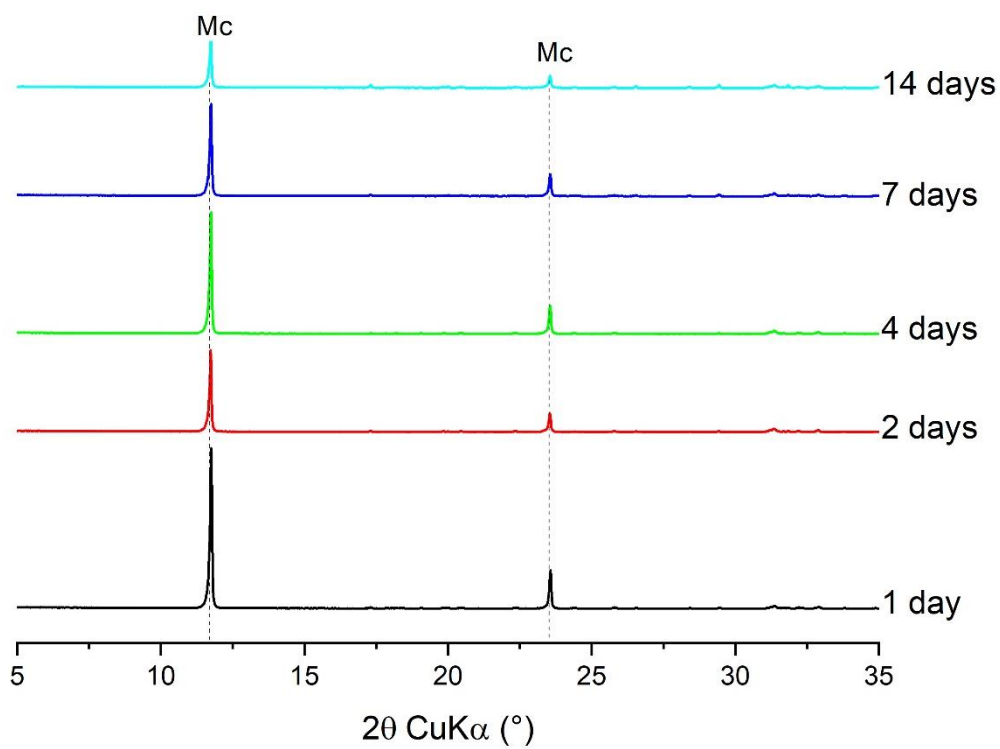
Figure 22. XRPD spectra of Mc samples in kinetic experiments with 34 mM Na$_3$-citrate. Mc: monocarbonate.

172
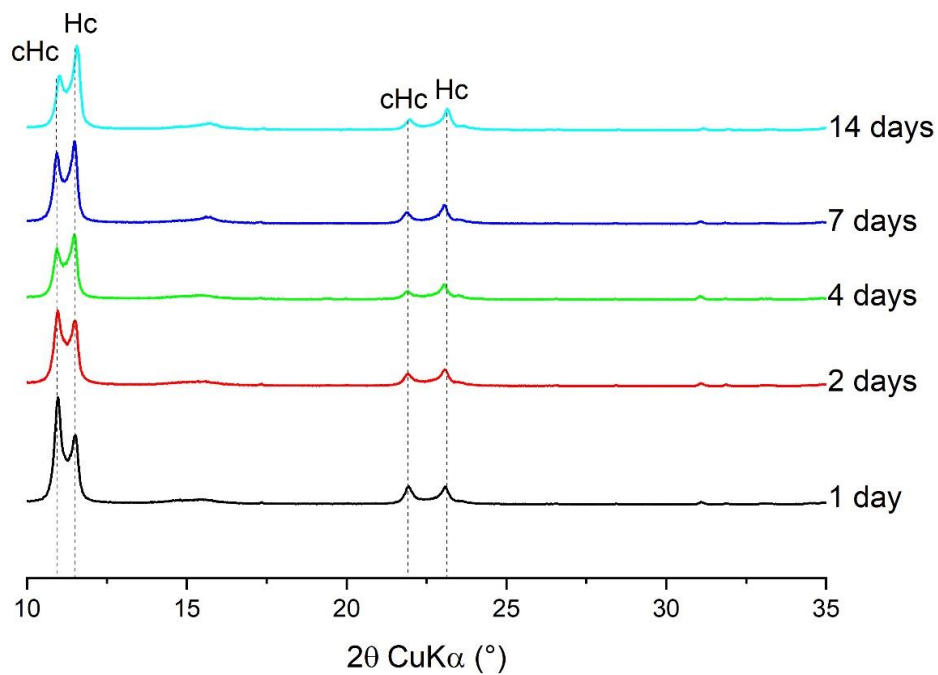
Figure 23. XRPD spectra of Hc samples in kinetic experiments with 34 mM Na₃-citrate. cHc: carbonated hemicarbonate; Hc: hemicarbonate.
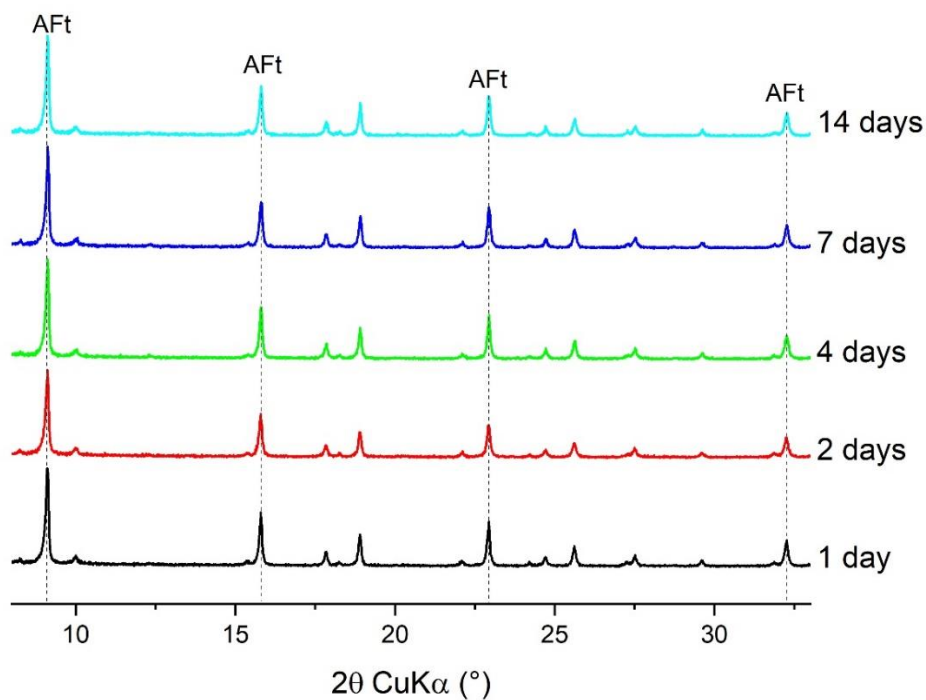
Figure 24. XRPD spectra of AFt samples in kinetic experiments with 34 mM Na₃-citrate. AFt: ettringite.

Table 42. Solution composition of Ms samples in kinetic experiments with 34 mM of Na₃-citrate.

Time/(days) Monosulfate (Ms)	[Na]	[Ca]	[Al]	[S]	[OH⁻]	Citrate	Observed phase[a]
	mM						
1	202	8.2	6.6	1.7	71	34	Ms12, Ms14, AFt
2	204	7.3	6.9	1.7	74	35	Ms12, Ms14, AFt
4	203	6.6	8.4	1.8	95	29	Ms12, Ms14, AFt
7	206	7.0	7.1	2.0	95	29	Ms12, Ms14, AFt
14	203	6.6	7.0	1.9	90	27	Ms12, Ms14, AFt

[a] Phases identification achieved by XRPD analyses. AFt: ettringite, Ms12: monosulfate-12, Ms14: monosulfate-14.

Table 43. Saturation indices of portlandite, katoite, monosulfate (Ms), ettringite (AFt), citrate-AFm, citrate-AFt and $Ca_3Cit_2 \cdot 4 \cdot H_2O$ for Ms system in citrate kinetic experiments ([CIT]$_{tot}$ = 0.034 M, [Na]$_{tot}$ = 0.2 M). Calculations have been carried out with GEMS software.

Time/(days)	Portlandite	katoite	Ms	AFt	Citrate-AFm	Citrate-AFt	$Ca_3Cit_2 \cdot 4 \cdot H_2O$
1	-1.2	-0.94	0.38	1.4	1.9	5.4	-0.15
2	-1.3	-1.1	0.15	1.0	1.7	5.1	-0.31
4	-1.2	-0.69	0.61	1.5	2.1	5.5	-0.38
7	-1.1	-0.67	0.71	1.8	2.1	5.5	-0.31
14	-1.1	-0.67	0.68	1.7	2.1	5.5	-0.37

Table 44. Solution composition of Mc samples in kinetic experiments with 34 mM of Na₃-citrate.

Time/(days) Monocarbonate (Mc)	[Na]	[Ca]	[Al]	[OH⁻]	Citrate	Observed phase[a]
	mM					
1	201	5.9	3.3	67	35	Mc, CC
2	202	5.1	3.0	67	35	Mc, CC
4	201	5.4	3.0	90	33	Mc, CC
7	206	5.4	3.2	90	34	Mc, CC
14	203	5.9	4.0	85	32	Mc, CC

[a] Phases identification achieved by XRPD analyses. Mc: monocarbonate, CC: calcite.

Table 45. Saturation indices of portlandite, katoite, monocarbonate (Mc), hemicarbonate (Hc), citrate-AFm, citrate-AFt and $Ca_3Cit_2\cdot 4\cdot H_2O$ for Mc system in citrate kinetic experiments ($[CIT]_{tot}$ = 0.034 M, $[Na]_{tot}$ = 0.2 M). Calculations have been carried out with GEMS software.

Time/(days)	Portlandite	katoite	Mc	Hc	Citrate-AFm	Citrate-AFt	$Ca_3Cit_2\cdot 4\cdot H_2O$
1	-1.4	-2.1	0.64	-0.79	0.60	3.9	-0.59
2	-1.5	-2.4	0.31	-1.17	0.20	3.3	-0.81
4	-1.4	-2.2	0.56	-0.87	0.48	3.7	-0.70
7	-1.3	-1.9	0.82	-0.55	0.75	4.0	-0.69
14	-1.3	-1.7	0.99	-0.39	0.96	4.2	-0.58

Table 46. Solution composition of Hc samples in kinetic experiment with 34 mM of Na_3-citrate.

Time/(days) Hemicarbonate (Hc)	[Na]	[Ca]	[Al]	[OH-]	Citrate	Observed phase[a]
			mM			
1	213	4.5	2.2	107	17	Hc, cHc, Mc
2	190	3.9	1.3	112	12	Hc, cHc, Mc
4	205	2.0	3.1	146	7.6	Hc, cHc, Mc
7	205	2.1	3.1	154	7.8	Hc, cHc, Mc
14	204	1.9	2.9	147	7.3	cHc(?), Mc

[a] Phases identification achieved by XRPD analyses. cHc: carbo-hemicarbonate, Hc: hemicarbonate, Mc: monocarbonate.

Table 47. Saturation indices of portlandite, katoite, hemicarbonate (Hc), citrate-AFm, citrate-AFt and $Ca_3Cit_2\cdot 4\cdot H_2O$ for Hc system in kinetic ($[CIT]_{tot}$ = 0.034 M, $[Na]_{tot}$ = 0.2 M). Calculations have been carried out with GEMS software.

Time/(days)	Portlandite	katoite	Hc	Citrate-AFm	Citrate-AFt	$Ca_3Cit_2\cdot 4\cdot H_2O$
1	-0.84	-1.2	-0.41	1.4	4.6	-0.76
2	-0.81	-1.5	-0.54	1.1	4.2	-0.83
4	-0.87	-1.1	-0.34	1.3	3.8	-1.7
7	-0.86	-1.0	-0.32	1.3	3.9	-1.6
14	-0.87	-1.1	-0.37	1.2	3.7	-1.7

Table 48. Solution composition of AFt samples in kinetic experiments with 34 mM of Na₃-citrate.

Time/(days) Ettringite (AFt)	[Na]	[Ca]	[Al]	[S]	[OH-]	Citrate	Observed phase[a]
	mM						
1	194	8.7	0.6	17	49	35	AFt
2	197	15	0.2	22	54	33	AFt
4	199	5.8	2.3	17	62	33	AFt
7	200	5.8	2.6	17	58	32	AFt
14	200	6.1	2.2	18	62	31	AFt

[a] Phases identification achieved by XRPD analyses. AFt: ettringite.

Table 49. Saturation indices of portlandite, katoite, monosulfate (Ms), ettringite (AFt), citrate-AFm, citrate-AFt and Ca₃Cit₂·4·H₂O for AFt system in citrate kinetic experiments ([CIT]$_{tot}$ = 0.034 M, [Na]$_{tot}$ = 0.2 M). Calculations have been carried out with GEMS software.

Time/(days)	Portlandite	katoite	Ms	AFt	Citrate-AFm	Citrate-AFt	Ca₃Cit₂·4·H₂O
1	-1.5	-3.5	-1.2	1.8	-0.68	2.9	-0.063
2	-1.03	-3.3	-0.51	3.40	-0.19	4.0	0.72
4	-1.6	-2.9	-0.71	1.9	-0.20	3.1	-0.61
7	-1.6	-2.6	-0.46	2.2	0.041	3.3	-0.58
14	-1.6	-2.7	-0.47	2.3	0.0046	3.3	-0.52

2.2. Sorption experiments
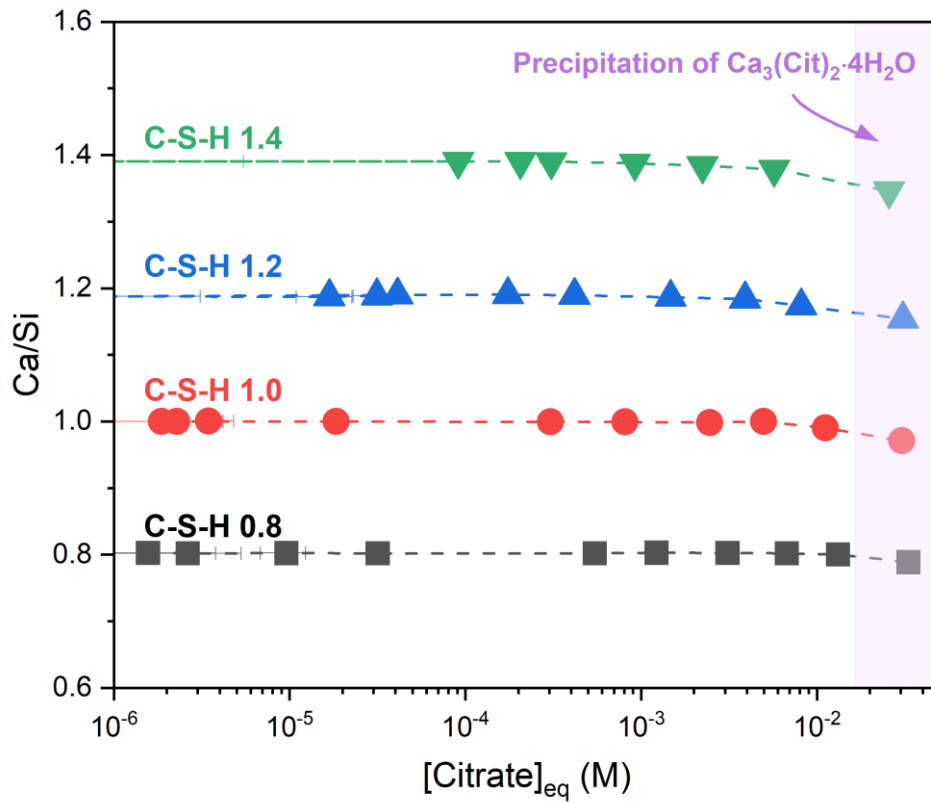
Figure 25. Calculated Ca/Si as a function of equilibrium concentration of citrate for the C-S-H solid phases in presence of citrate. Calculation have been carried out per 100 g of sample and taking into account the formation of portlandite by using the mass balance equation: Ca/Si= ([Ca]$_{tot, in}$-[Ca]$_{tot, eq}$-[Ca]$_{portlandite}$)/ ([Si]$_{tot, in}$-[Si]$_{tot, eq}$).

*Table 50. Solution composition of **C-S-H phases (Ca/Si=0.8)** in citrate sorption experiments.*

Measured initial citrate concentration/ (mM)	Measured concentrations					Observed phase[a]
	[Na]	[Ca]	[Si]	[OH⁻]	Citrate	
	mM					
0	72	0.043	1.5	95	<0.020	C-S-H
0.022	74	0.041	1.5	91	<0.020	C-S-H
0.067	72	0.046	1.3	91	<0.020	C-S-H
0.13	71	0.039	1.4	87	<0.020	C-S-H
0.33	71	0.052	1.2	87	<0.020	C-S-H
0.67	72	0.075	1.3	87	0.54	C-S-H
1.4	69	0.083	1.8	83	1.2	C-S-H
3.4	69	0.18	1.8	79	3.1	C-S-H
6.8	70	0.38	1.8	69	6.8	C-S-H
13	73	1.0	1.6	60	13	C-S-H
34	80	5.7	1.4	26	33	C-S-H

[a] Phases identification achieved by XRPD analyses. C-S-H: C-S-H phase.

*Table 51. Saturation indices of C-S-H phase, Calcite, $Ca_3Cit_2 \cdot 4 \cdot H_2O$, lime, portlandite and silica for C-S-H phase with a **Ca/Si=0.8** in citrate sorption experiments ($[Na]_{tot} = 0.2$ M). Calculations have been carried out with GEMS software.*

$[Citrate]_{tot}$/(mM)	C-S-H	$Ca_3Cit_2 \cdot 4 \cdot H_2O$	Portlandite	$SiO_{2(am)}$
0	-0.49	-	-2.7	-3.3
0.022	-0.49	-	-2.8	-3.3
0.067	-0.48	-	-2.7	-3.4
0.13	-0.52	-	-2.8	-3.3
0.33	-0.45	-	-2.6	-3.4
0.67	-0.45	-6.45	-2.7	-3.4
1.4	-0.46	-6.16	-2.9	-3.2
3.4	-0.42	-5.06	-2.8	-3.15
6.8	-0.39	-4.13	-2.9	-3.1
13	-0.33	-2.93	-2.9	-2.9
34	-3.77	-0.75	-2.7	-0.12

*Table 52. Solution composition of **C-S-H phases (Ca/Si=1.0)** in citrate sorption experiments.*

Measured initial citrate concentration/ (mM)	Measured concentrations					Observed phase[a]
	[Na]	[Ca]	[Si]	[OH⁻]	Citrate	
	mM					
0	159	0.27	0.244	119	<0.020	C-S-H
0.022	156	0.23	0.435	119	<0.020	C-S-H
0.067	160	0.25	0.25	125	<0.020	C-S-H
0.13	159	0.26	0.34	119	<0.020	C-S-H
0.33	154	0.33	0.22	113	<0.020	C-S-H
0.67	157	0.41	0.21	119	0.31	C-S-H
1.4	155	0.5	0.22	113	0.81	C-S-H
3.4	154	0.86	0.23	113	2.5	C-S-H
6.8	161	0.26	0.25	113	5	C-S-H
13	158	4.0	0.23	98	11	C-S-H
34	157	11	0.29	58	30	C-S-H

[a] Phases identification achieved by XRPD analyses. C-S-H: C-S-H phase.
[b] Phase identification carried out by TGA characterization.

*Table 53. Saturation indices of C-S-H phase, Calcite, $Ca_3Cit_2 \cdot 4 \cdot H_2O$, lime, portlandite and silica for C-S-H phase with a **Ca/Si=1.0** in citrate sorption experiments ($[Na]_{tot} = 0.2$ M). Calculations have been carried out with GEMS software.*

$[Citrate]_{tot}$/(mM)	C-S-H	$Ca_3Cit_2 \cdot 4 \cdot H_2O$	Portlandite	$SiO_{2(am)}$
0	-0.17	-	-1.1	-4.7
0.022	-0.080	-	-1.2	-4.4
0.067	-0.18	-	-1.1	-4.7
0.13	-0.091	-	-1.1	-4.6
0.33	-0.12	-	-1.0	-4.8
0.67	-0.12	-4.64	-0.99	-4.8
1.4	-0.12	-3.81	-1.0	-4.8
3.4	-0.10	-2.82	-1.0	-4.7
6.8	-0.64	-4.45	-1.8	-4.6
13	0.060	-0.91	-0.87	-4.7
34	0.11	0.22	-1.1	-4.4

*Table 54. Solution composition of **C-S-H phases (Ca/Si=1.2)** in sorption experiments.*

Measured initial citrate concentration/(mM)	Measured concentration					Observed phase[a]
	[Na]	[Ca]	[Si]	[OH$^-$]	Citrate	
	mM					
0	201	1.1	0.059	143	<0.020	C-S-H, CH[b]
0.022	198	0.95	0.054	149	<0.020	C-S-H, CH[b]
0.067	201	1.1	0.057	149	<0.020	C-S-H, CH[b]
0.13	203	1.5	0.035	149	<0.020	C-S-H, CH[b]
0.33	195	1.1	0.045	148	<0.020	C-S-H, CH[b]
0.67	184	0.73	0.092	141	0.18	C-S-H, CH[b]
1.4	195	1.1	0.052	148	0.42	C-S-H, CH[b]
3.4	201	2.1	0.053	148	1.5	C-S-H, CH[b]
6.8	198	3.0	0.057	141	3.9	C-S-H, CH[b]
13	205	6.3	0.043	141	8.1	C-S-H, CH[b]
34	189	13	0.11	84	31	C-S-H

[a] Phases identification achieved by XRPD analysis. C-S-H: C-S-H phase, CH: portlandite.
[b] Portlandite content per 100 g of dry sample. Phase identification carried out by TGA characterization.

*Table 55. Saturation indices of C-S-H phase, Calcite, $Ca_3Cit_2 \cdot 4 \cdot H_2O$, lime, portlandite and silica for C-S-H phase with a **Ca/Si=1.2** in citrate sorption experiments ([Na]$_{tot}$ = 0.2 M). Calculations have been carried out with GEMS software.*

[Citrate]$_{tot}$/(mM)	C-S-H	$Ca_3Cit_2 \cdot 4 \cdot H_2O$	Portlandite	$SiO_{2(am)}$
0	-0.071	-	-0.29	-5.8
0.022	-0.15	-	-0.37	-5.7
0.067	-0.10	-	-0.31	-5.8
0.13	-0.15	-	-0.16	-6.1
0.33	-0.15	-	-0.29	-5.9
0.67	-0.11	-4.47	-0.56	-5.4
1.4	-0.17	-3.41	-0.37	-5.8
3.4	-0.029	-1.97	-0.19	-5.8
6.8	-0.058	-1.23	-0.27	-5.8
13	-0.017	-0.23	-0.080	-6.0
34	-0.021	0.45	-0.68	-5.1

*Table 56. Solution composition of **C-S-H phases (Ca/Si=1.4)** in citrate sorption experiments.*

Measured initial citrate concentration/ (mM)	Measured concentrations					Observed phase[a]
	[Na]	[Ca]	[Si]	[OH⁻]	Citrate	
	mM					
0	210	2.5	0.027	148	<0.020	C-S-H, CH[b]
0.022	203	2.7	0.025	178	<0.020	C-S-H, CH[b]
0.067	208	2.7	0.027	160	<0.020	C-S-H, CH[b]
0.13	207	2.6	0.024	160	<0.020	C-S-H, CH[b]
0.33	206	2.7	0.026	160	<0.020	C-S-H, CH[b]
0.67	211	2.7	0.025	160	0.21	C-S-H, CH[b]
1.4	209	2.8	0.022	137	0.31	C-S-H, CH[b]
3.4	206	3.6	0.018	152	0.92	C-S-H, CH[b]
6.8	203	4.9	0.020	152	2.2	C-S-H, CH[b]
13	208	6.6	0.021	168	5.7	C-S-H, CH[b]
34	200	17	0.0036	117	26	C-S-H, CH[b]

[a] Phases identification achieved by XRPD analyses. C-S-H: C-S-H phase, CH: portlandite.
[b] Portlandite content per 100 g of dry sample. Phase identification carried out by TGA characterization.

*Table 57. Saturation indices of C-S-H phase, Calcite, $Ca_3Cit_2 \cdot 4 \cdot H_2O$, lime, portlandite and silica for C-S-H phase with a **Ca/Si=1.4** in citrate sorption experiments ($[Na]_{tot} = 0.2$ M). Calculations have been carried out with GEMS software.*

$[Citrate]_{tot}$/(mM)	C-S-H	$Ca_3Cit_2 \cdot 4 \cdot H_2O$	Portlandite	$SiO_{2(am)}$
0	-0.06	-	0.10	-6.3
0.022	-0.05	-	0.14	-6.4
0.067	-0.03	-	0.13	-6.4
0.13	-0.09	-	0.10	-6.4
0.33	-0.05	-	0.13	-6.4
0.67	-0.08	-3.23	0.11	-6.4
1.4	-0.11	-2.86	0.12	-6.4
3.4	-0.13	-1.78	0.17	-6.6
6.8	-0.08	-0.92	0.21	-6.6
13	-0.11	-0.21	0.14	-6.5
34	-0.78	0.93	-0.16	-7.0

Table 58. Mass of hydrated C-S-H phases per 2.21 g of (CaO + SiO₂) in 50 mL of solution calculated by combining mass balance and water content determined by TGA analysis.

[Citrate]$_{tot}$/(mM)	Ca/Si = 0.8	Ca/Si = 1.0	Ca/Si = 1.2	Ca/Si = 1.4
	g/g			
0	3.0	2.8	2.7	2.7
0.022	3.0	2.8	2.7	2.7
0.067	3.0	2.8	2.8	2.7
0.13	3.0	2.8	2.7	2.7
0.33	3.0	2.9	2.8	2.7
0.67	3.0	2.9	2.7	2.7
1.4	3.0	2.8	2.7	2.7
3.4	3.0	2.8	2.7	2.7
6.8	3.0	2.9	2.7	2.7
13	3.0	2.8	2.7	2.7
34	2.9	2.9	2.8	2.7
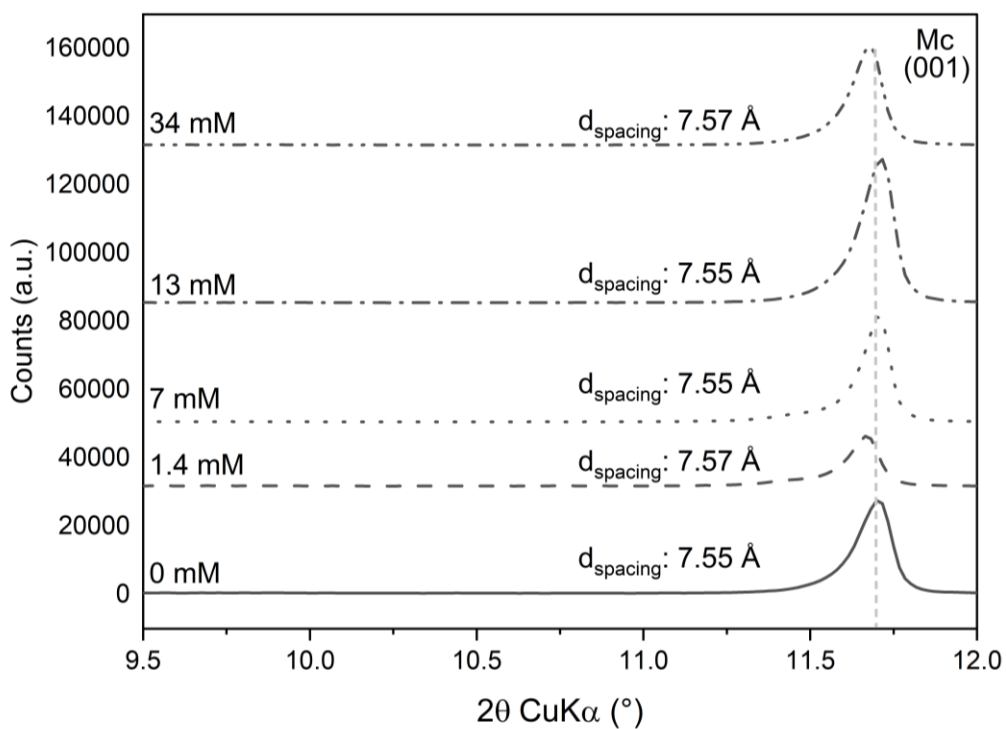
Figure 26. XRPD patterns of monocarbonate after sorption of citrate after 7 days of contacting time.
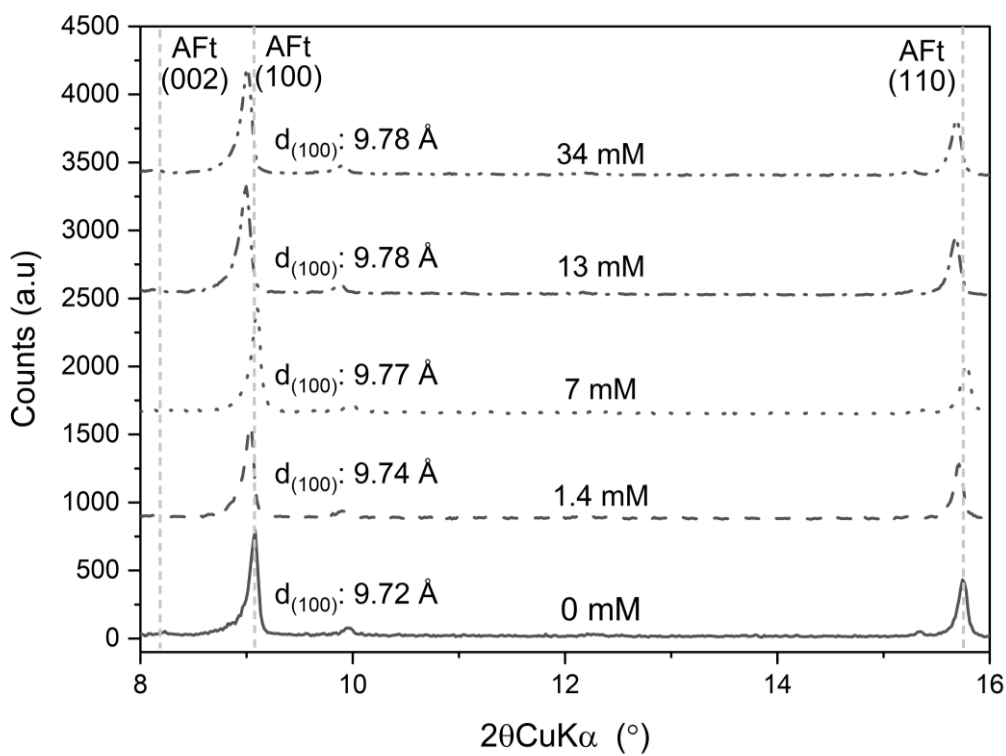
Figure 27. XRPD characterization of ettringite in sorption experiments with [Citrate]$_{tot}$ = 0 – 34 mM.
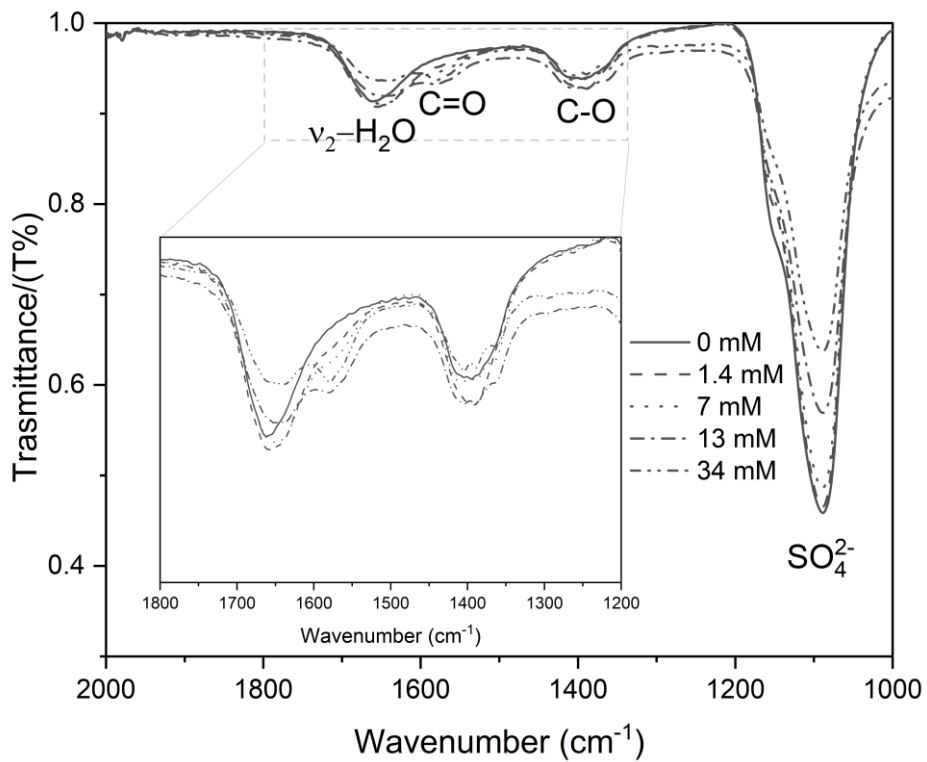
Figure 28. FT-IR characterization of Ms samples in sorption experiments (2000-1000 cm^{-1}).
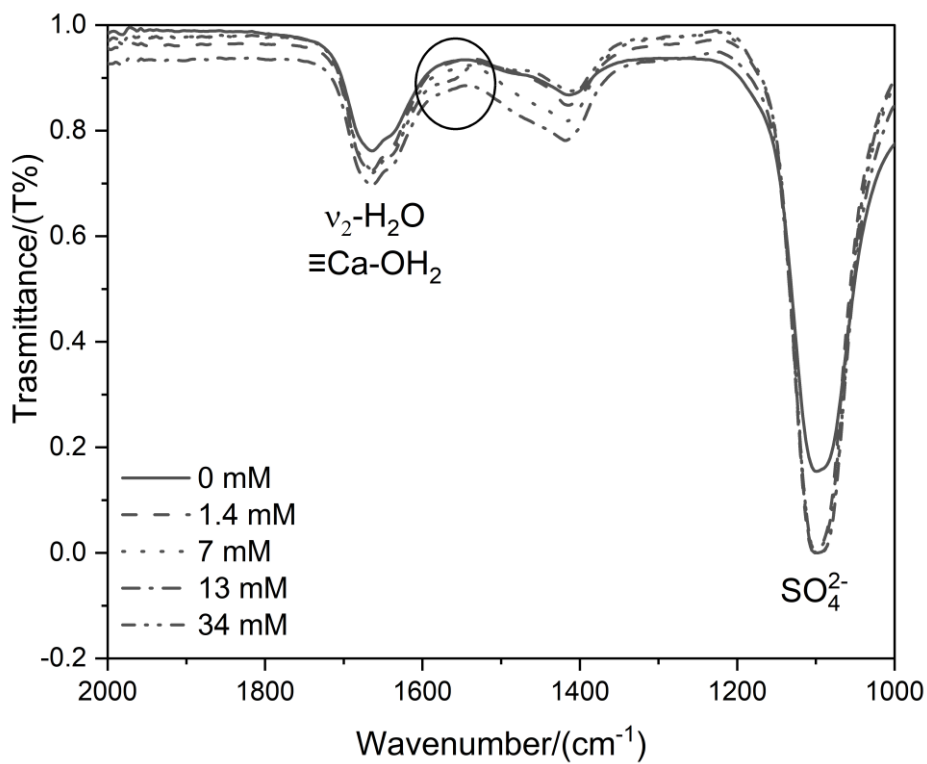
Figure 29. FT-IR characterization of monocarbonate samples in sorption experiments (2000-1000 cm^{-1}).
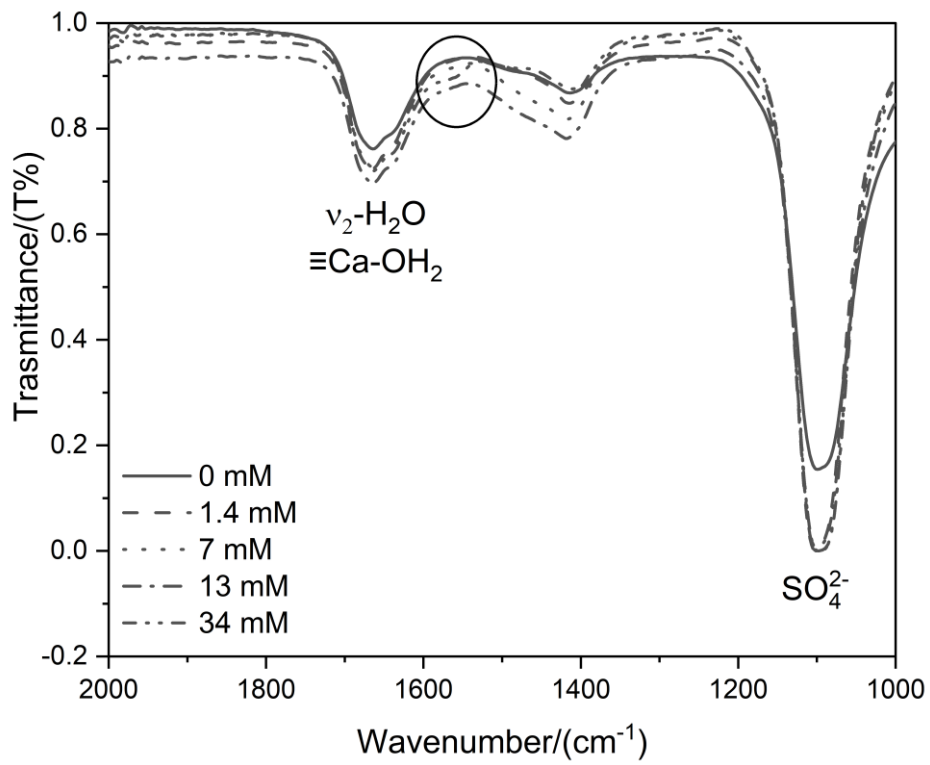
Figure 30. FT-IR characterization of ettringite samples in sorption experiments (2000-1000 cm^{-1}).
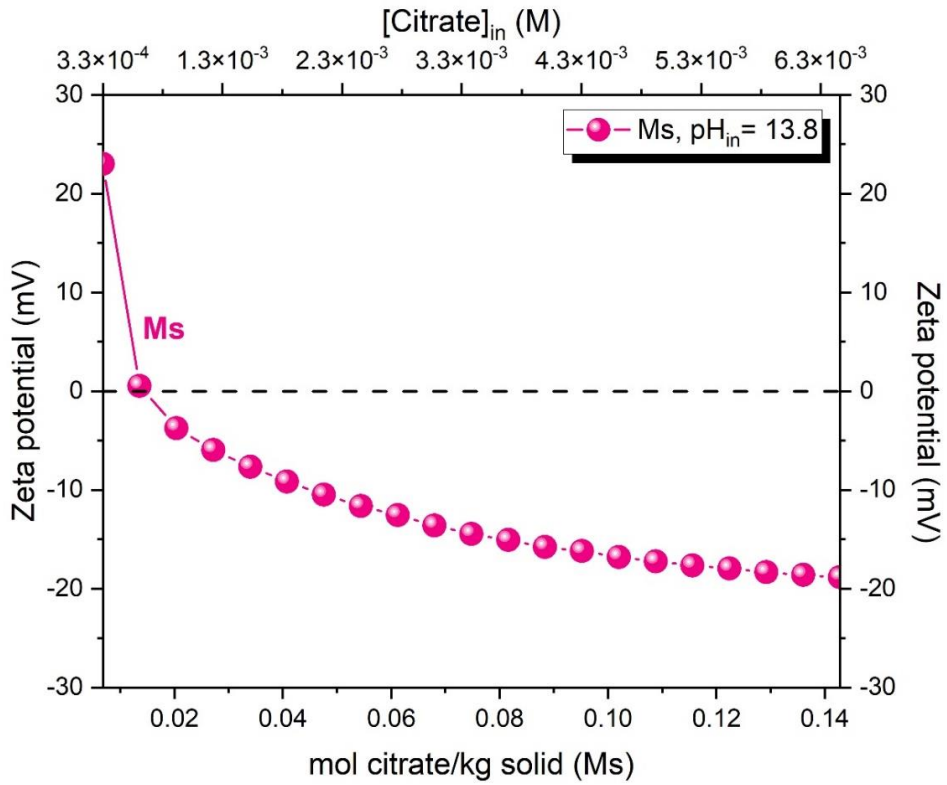
Figure 31. Zeta potential measured in the presence of citrate in Ms suspensions.
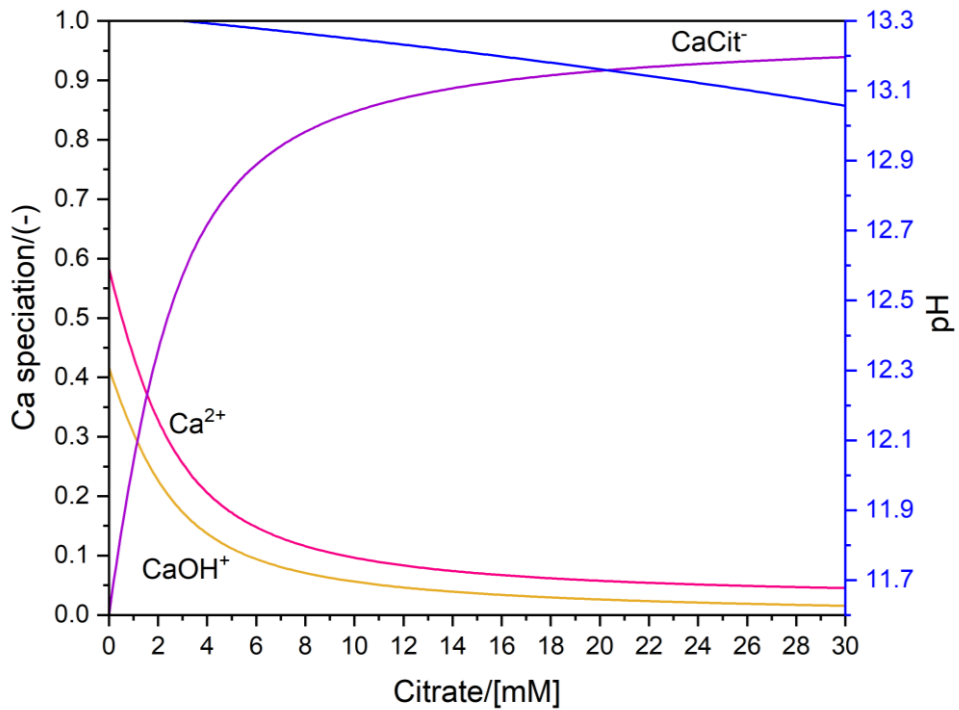
Figure 32. Calculated species distribution of Ca-complexes and pH determined with an initial calcium concentration of [Ca]$_{tot}$ = 2 mM as a function of added citrate concentration.

*Table 59. Solution composition of **Ms** samples in citrate sorption experiments.*

Measured initial citrate concentration/ (mM)	Measured concentrations						Observed phase[a]
	[Na]	[Ca]	[Al]	[S]	[OH⁻]	Citrate	
	mM						
0	220	0.30	1.9	1.0	169	<0.020	Ms12, Ms14, AFt
0.022	221	0.47	1.9	1.0	169	<0.020	Ms12, Ms14, AFt
0.067	223	0.54	1.5	0.81	169	<0.020	Ms12, Ms14, AFt
0.13	219	0.58	1.3	0.75	177	<0.020	Ms12, Ms14, AFt
0.33	217	0.77	1.2	0.63	177	0.12	Ms12, Ms14, AFt
0.67	221	0.67	1.4	0.76	169	0.067	Ms12, Ms14, AFt
1.4	225	0.51	2.7	1.2	169	0.94	Ms12, Ms14, AFt
3.4	222	1.2	1.7	0.81	169	3.3	Ms12, Ms14, AFt
6.8	222	1.7	2.2	1.1	161	7.0	Ms12, Ms14, AFt
13	223	2.8	3.1	1.4	146	13	Ms12, Ms14, AFt
34	226	7.5	6.4	2.1	99.7	34	Ms12, Ms14, AFt

[a] Phases identified by XRPD analyses. AFt: ettringite, Ms12: monosulfate-12, Ms14: monosulfate-14.

*Table 60. Saturation indices of portlandite, katoite, gypsum, monosulfate (Ms), ettringite (AFt), citrate-AFm, citrate-AFt and $Ca_3Cit_2 \cdot 4 \cdot H_2O$ for **Ms** system in citrate sorption experiments ($[Na]_{tot} = 0.2$ M). Calculations have been carried out with GEMS software.*

[Citrate]$_{tot}$/ (mM)	Portlandite	katoite	Gypsum	Ms	AFt	Citrate-AFm	Citrate-AFt	$Ca_3Cit_2 \cdot 4 \cdot H_2O$
0	-0.87	-1.7	-3.5	-0.83	-0.87	-	-	-
0.022	-0.68	-1.1	-3.0	0.23	1.2	-	-	-
0.067	-0.61	-1.1	-3.0	0.20	1.1	-	-	-
0.13	-0.59	-1.1	-3.0	0.18	1.1	-	-	-
0.33	-0.49	-0.92	-3.0	0.39	1.3	0.39	0.95	-4.6
0.67	-0.54	-0.88	-3.0	0.45	1.4	0.23	0.38	-5.3
1.4	-0.82	-1.2	-3.1	0.051	0.83	0.44	1.6	-3.7
3.4	-0.71	-1.2	-3.1	0.000016	0.74	0.88	3.0	-2.3
6.8	-0.83	-1.3	-3.0	-0.044	0.79	0.94	4.4	-1.8
13	-0.87	-1.1	-2.9	0.33	1.4	1.4	4.2	-1.3
34	-1.1	-0.77	-2.6	0.90	2.6	2.0	5.5	-0.26

*Table 61. Solution composition of **Mc** samples in citrate sorption experiments.*

Measured initial citrate concentration/(mM)	Measured concentrations					Observed phase[a]
	[Na]	[Ca]	[Al]	[OH⁻]	citrate	
	mM					
0	217	0.55	0.15	226	<0.020	Mc, CC
0.022	215	0.60	0.18	177	<0.020	Mc, CC
0.067	216	0.70	0.16	186	0.051	Mc, CC
0.13	216	0.51	0.33	186	0.058	Mc, CC
0.33	212	0.52	0.23	177	0.12	Mc, CC
0.67	217	0.62	0.22	186	0.52	Mc, CC
1.4	215	0.63	0.42	186	1.3	Mc, CC
3.4	215	0.88	0.43	169	3.1	Mc, CC
6.8	218	1.3	0.77	169	6.5	Mc, CC
13	219	1.9	1.1	139	14	Mc, CC
34	224	3.3	1.6	24	34	Mc, CC

[a] Phases identification achieved by XRPD analyses. CC: calcite, Mc: monocarbonate.

*Table 62. Saturation indices of portlandite, katoite, monocarbonate (Mc), hemicarbonate (Hc), ettringite (AFt), citrate-AFm, citrate-AFt and $Ca_3Cit_2·4·H_2O$ for **Mc** system in citrate sorption experiments ($[Na]_{tot}$ = 0.2 M). Calculations have been carried out with GEMS software.*

[Citrate]$_{tot}$/(mM)	Portlandite	katoite	Mc	Hc	Citrate-AFm	Citrate-AFt	$Ca_3Cit_2·4·H_2O$
0	-0.61	-3.1	-0.35	-1.4	-	-	-
0.022	-0.58	-2.8	-0.11	-1.1	-	-	-
0.067	-0.51	-2.7	-0.0038	-1.0	-1.7	-1.7	-5.5
0.13	-0.66	-2.5	0.20	-0.86	-1.6	-1.7	-5.7
0.33	-0.67	-2.8	-0.13	-1.2	-1.7	-1.4	-5.1
0.67	-0.66	-2.9	-0.15	-1.2	-1.3	-0.14	-3.8
1.4	-0.75	-2.6	0.12	-1.0	-0.83	0.57	-3.4
3.4	-0.85	-2.8	-0.14	-1.3	-0.86	1.0	-2.7
6.8	-0.96	-2.6	0.10	-1.1	-0.49	1.7	-2.2
13	-1.1	-2.7	0.017	-1.3	-0.45	2.0	-1.8
34	-0.98	-3.2	-0.46	-1.9	-0.75	2.0	-1.3

*Table 63. Solution composition of **Hc** samples in citrate sorption experiments.*

Measured initial citrate concentration/ (mM)	Measured concentrations					Observed phase[a]
	[Na]	[Ca]	[Al]	[OH⁻]	Citrate	
	mM					
0	218	1.8	0.15	170	<0.020	Hc, cHc, Mc
0.022	217	1.7	0.15	170	0.026	Hc, cHc, Mc
0.067	218	1.7	0.13	170	0.020	Hc, cHc, Mc
0.13	217	1.9	0.15	169	0.029	Hc, cHc, Mc
0.33	213	2.1	0.24	169	0.095	Hc, cHc, Mc
0.67	216	2.0	0.24	180	0.21	Hc, cHc
1.4	216	2.4	0.12	183	1.2	Hc, cHc
3.4	218	2.9	0.19	181	1.2	Hc, cHc
6.8	217	5.9	0.058	182	3.3	Hc, cHc, Mc
13	215	4.3	0.11	172	3.4	Hc, cHc, Mc
34	217	1.2	2.07	161	8.5	cHc(?), Mc

[a] Phases identification achieved by XRPD analyses. cHc: carbo-hemicarbonate, Hc: hemicarbonate, Mc: monocarbonate.

*Table 64. Saturation indices of portlandite, katoite, hemicarbonate (Hc), citrate-AFm, citrate-AFt and $Ca_3Cit_2 \cdot 4 \cdot H_2O$ for **Hc** system in citrate sorption experiments ($[Na]_{tot} = 0.2$ M). Calculations have been carried out with GEMS software.*

[Citrate]$_{tot}$/(mM)	Portlandite	katoite	Hc	Citrate-AFm	Citrate-AFt	$Ca_3Cit_2 \cdot 4 \cdot H_2O$
0	-0.077	-1.5	0.012	-	-	
0.022	-0.11	-1.6	-0.046	-0.49	-0.43	-5.4
0.067	-0.10	-1.7	-0.16	-0.80	-1.1	-5.9
0.13	-0.071	-1.4	-0.23	-0.28	-0.075	-5.2
0.33	-0.034	-0.92	0.22	0.63	1.7	-3.9
0.67	-0.058	-1.0	0.13	0.67	2.0	-3.5
1.4	-0.065	-1.6	-0.15	0.57	2.9	-2.0
3.4	0.023	-1.0	0.12	1.2	3.7	-1.8
6.8	0.22	-1.4	-0.21	0.55	3.7	-0.43
13	0.017	-1.4	-0.052	1.1	4.2	-0.73
34	-0.88	-1.3	-0.54	0.85	3.2	-2.0

*Table 65. Solution composition of **AFt** samples in citrate sorption experiments.*

Measured initial citrate concentration/ (mM)	Measure concentrations						Observed phase[a]
	[Na]	[Ca]	[Al]	[S]	[OH⁻]	Citrate	
	mM						
0	205	0.088	6.9	12	126	<0.020	AFt
0.022	205	0.098	7.0	12	126	0.075	AFt
0.067	203	0.098	5.8	12	119	0.090	AFt
0.13	203	0.099	5.6	12	119	0.13	AFt
0.33	201	0.116	4.9	11	119	0.17	AFt
0.67	205	0.138	4.9	11	126	1.0	AFt
1.4	202	0.175	3.9	13	119	1.5	AFt
3.4	203	0.399	2.8	12	119	3.4	AFt
6.8	205	7.9	0.005	17	119	7.0	AFt
13	204	12	0.008	18	100	13	AFt
34	208	9.8	0.73	17	54	35	AFt

[a] Phases identified by XRPD analyses. AFt: ettringite.

*Table 66. Saturation indices of portlandite, katoite, gypsum, monosulfate (Ms), ettringite (AFt), citrate-AFm, citrate-AFt and $Ca_3Cit_2 \cdot 4 \cdot H_2O$ for **AFt** system in citrate sorption experiments ($[Na]_{tot} = 0.2$ M). Calculations have been carried out with GEMS software.*

[Citrate]$_{tot}$/(mM)	Portlandite	katoite	Gypsum	Ms	AFt	Citrate-AFm	Citrate-AFt	$Ca_3Cit_2 \cdot 4 \cdot H_2O$
0	-1.6	-2.44	-2.9	-1.1	0.0025	-	-	-
0.022	-1.5	-2.4	-2.9	-0.94	0.20	-2.0	-3.2	-7.4
0.067	-1.6	-2.5	-2.9	-1.1	0.043	-2.1	-3.3	-7.2
0.13	-1.6	-2.6	-2.9	-1.2	-0.041	-2.0	-3.0	-6.9
0.33	-1.5	-2.5	-2.8	-1.0	0.24	-1.8	-2.4	-6.5
0.67	-1.6	-2.8	-3.0	-1.4	-0.42	-1.7	-1.5	-5.3
1.4	-1.6	-2.9	-2.9	-1.5	-0.30	-1.7	-1.2	-4.8
3.4	-1.4	-2.8	-2.7	-1.2	0.22	-1.1	0.055	-3.7
6.8	-0.062	-4.2	-1.2	-1.1	3.34	-1.3	2.5	0.15
13	-0.10	-3.8	-1.2	-0.66	3.93	-0.67	3.5	0.79
34	-1.2	-2.8	-1.9	-0.41	2.72	0.093	3.8	0.11

3.   Gluconate uptake

3.1.   Kinetic sorption experiments
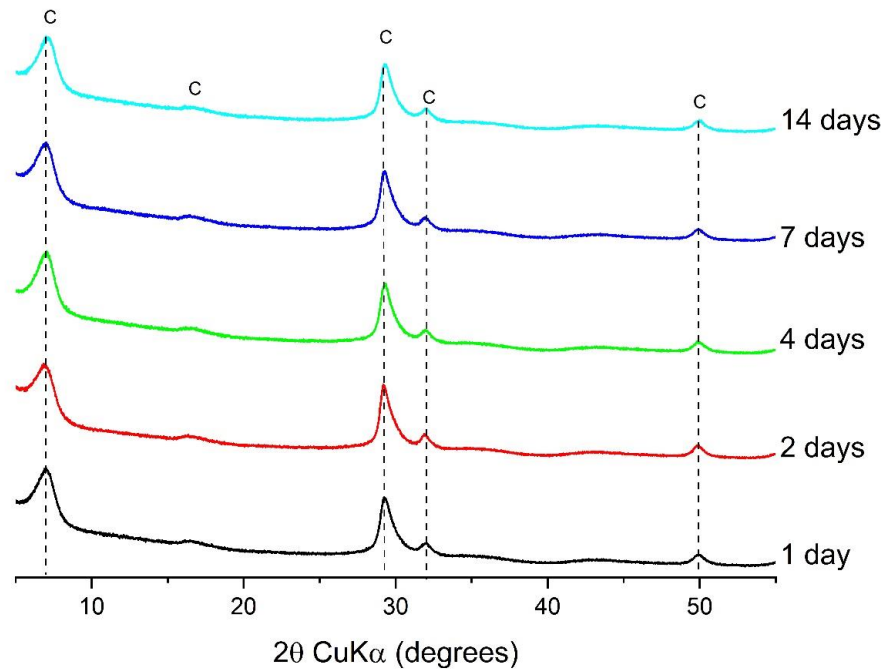
Figure 33. XRPD analysis of C-S-H 0.8 (Ca/Si) equilibrated in presence of Na-gluconate (0.021 M) for a contacting time of 1, 2, 4, 7 and 14 days. C: C-S-H phase.
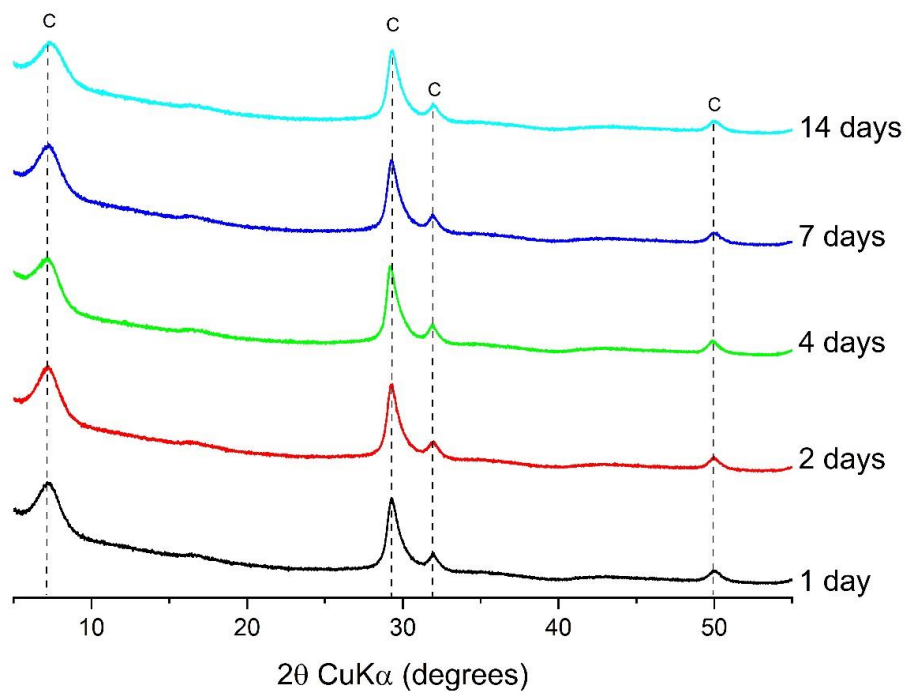
Figure 34. XRPD analysis of C-S-H 1.0 (Ca/Si) equilibrated in presence of Na-gluconate (0.021 M) for a contacting time of 1, 2, 4, 7 and 14 days. C: C-S-H phase.
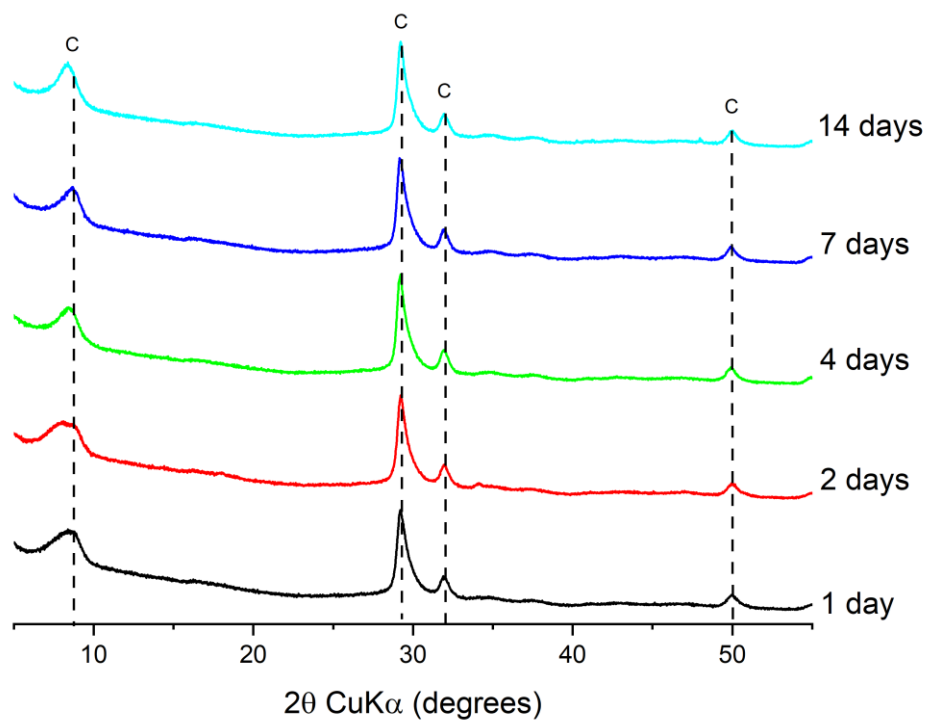
Figure 35. XRPD analysis of C-S-H 1.2 (Ca/Si) equilibrated in presence of Na-gluconate (0.021 M) for a contacting time of 1, 2, 4, 7 and 14 days. C: C-S-H phase.

192
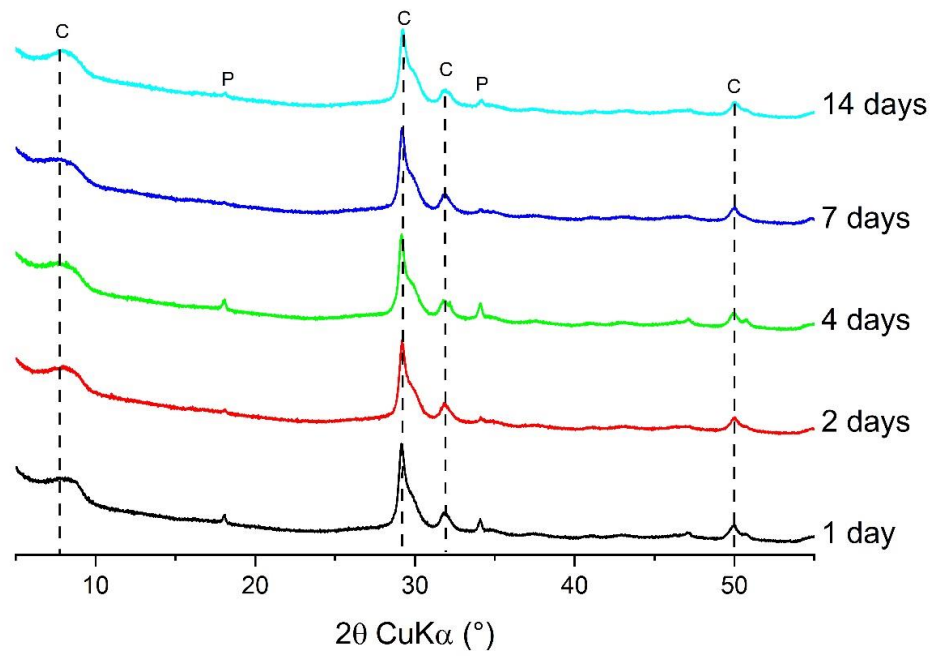
Figure 36. XRPD analysis of C-S-H 1.4 (Ca/Si) equilibrated in presence of Na-gluconate (0.021 M) for a contacting time of 1, 2, 4, 7 and 14 days. C: C-S-H phase, P: portlandite.

Table 67. Solution composition of C-S-H phases with a Ca/Si = 0.8 in kinetic experiments with 21 mM of Na-gluconate

Time/(days)	[Na]	[Ca]	[Si]	[OH⁻]	Gluconate	Observed phase[a]
C-S-H (Ca/Si=0.8)			mM			
1	126	0.36	1.1	96	20	C-S-H
2	126	0.41	0.95	101	19	C-S-H
4	153	1.63	0.26	133	15	C-S-H
7	121	0.39	1.1	96	20	C-S-H
14	123	0.50	0.97	51	19	C-S-H

[a] Phases identification achieved by XRPD analyses. C-S-H: C-S-H phase.

Table 68. Saturation indices of C-S-H phase, lime, portlandite and silica for C-S-H phase with a Ca/Si = 0.8 in gluconate sorption experiments ($[Na]_{tot}$ = 0.2 M). Calculations have been carried out with GEMS software.

Time/(days)	C-S-H	Portlandite	$SiO_{2(am)}$
		C-S-H (Ca/Si=0.8)	
1	-0.080	-1.8	-3.7
2	-0.059	-1.7	-3.8
4	0.071	-0.88	-4.7
7	-0.048	-1.8	-3.7
14	0.011	-1.7	-3.8

Table 69. Solution composition of C-S-H phases with a Ca/Si = 1.0 in kinetic experiments with 21 mM of Na-gluconate.

Time/(days)	[Na]	[Ca]	[Si]	[OH⁻]	Gluconate	Observed phase[a]
C-S-H (Ca/Si=1.0)			mM			
1	150	1.6	0.25	96	15	C-S-H
2	147	1.7	0.22	133	15	C-S-H
4	116	0.40	1.1	78	19	C-S-H
7	150	1.7	0.22	6.7	15	C-S-H
14	150	1.7	0.22	6.3	15	C-S-H

[a] Phases identification achieved by XRPD analyses. C-S-H: C-S-H phase.

Table 70.Saturation indices of C-S-H phase, lime, portlandite and silica for C-S-H phase with a Ca/Si = 1.0 in gluconate sorption experiments ([Na]$_{tot}$ = 0.2 M). Calculations have been carried out with GEMS software.

Time/(days)	C-S-H	Portlandite	SiO$_{2(am)}$
	C-S-H (Ca/Si=1.0)		
1	0.053	-0.92	-4.7
2	0.037	-0.89	-4.7
4	-0.027	-1.89	-3.7
7	0.036	-0.879	-4.8
14	0.028	-0.88	-4.8

Table 71. Solution composition of C-S-H phases with a Ca/Si = 1.2 in kinetic experiments with 21 mM of Na-gluconate.

Time/(days) C-S-H (Ca/Si=1.2)	[Na]	[Ca]	[Si]	[OH$^-$]	Gluconate	Observed phase[a]
	mM					
1	163	2.7	0.089	105	13	C-S-H
2	167	3.0	0.078	105	13	C-S-H
4	165	2.8	0.070	105	14	C-S-H
7	167	3.1	0.064	105	13	C-S-H
14	166	2.9	0.068	105	13	C-S-H

[a]Phases identification achieved by XRPD analyses. C-S-H: C-S-H phase.

Table 72.Saturation indices of C-S-H phase, lime, portlandite and silica for C-S-H phase with a Ca/Si = 1.2 in gluconate sorption experiments ([Na]$_{tot}$ = 0.2 M). Calculations have been carried out with GEMS software.

Time/(days)	C-S-H	Portlandite	SiO$_{2(am)}$
	C-S-H (Ca/Si=1.2)		
1	-0.11	-0.62	-5.3
2	-0.13	-0.58	-5.4
4	-0.18	-0.61	-5.4
7	-0.18	-0.57	-5.5
14	-0.18	-0.60	-5.4

Table 73. Solution composition of C-S-H phases with a Ca/Si = 1.4 in kinetic experiments with 21 mM of Na-gluconate.

Time/(days) C-S-H (Ca/Si=1.4)	[Na]	[Ca]	[Si]	[OH-]	Gluconate	Observed phase[a]
	mM					
1	180	4.9	0.022	133	7.1	C-S-H
2	178	5.0	0.026	126	7.1	C-S-H
4	179	5.2	0.023	133	6.8	C-S-H
7	176	4.9	0.022	126	7.3	C-S-H
14	177	5.3	0.021	133	6.9	C-S-H

[a] Phases identification achieved by XRPD analyses. C-S-H: C-S-H phase.

Table 74. Saturation indices of C-S-H phase, lime, portlandite and silica for C-S-H phase with a Ca/Si = 1.4 in gluconate sorption experiments ([Na]$_{tot}$ = 0.2 M). Calculations have been carried out with GEMS software.

Time/(days)	C-S-H	Portlandite	SiO$_{2(am)}$
	C-S-H (Ca/Si=1.4)		
1	-0.27	-0.16	-6.2
2	-0.22	-0.16	-6.1
4	-0.24	-0.14	-6.2
7	-0.28	-0.19	-6.2
14	-0.27	-0.13	-6.3
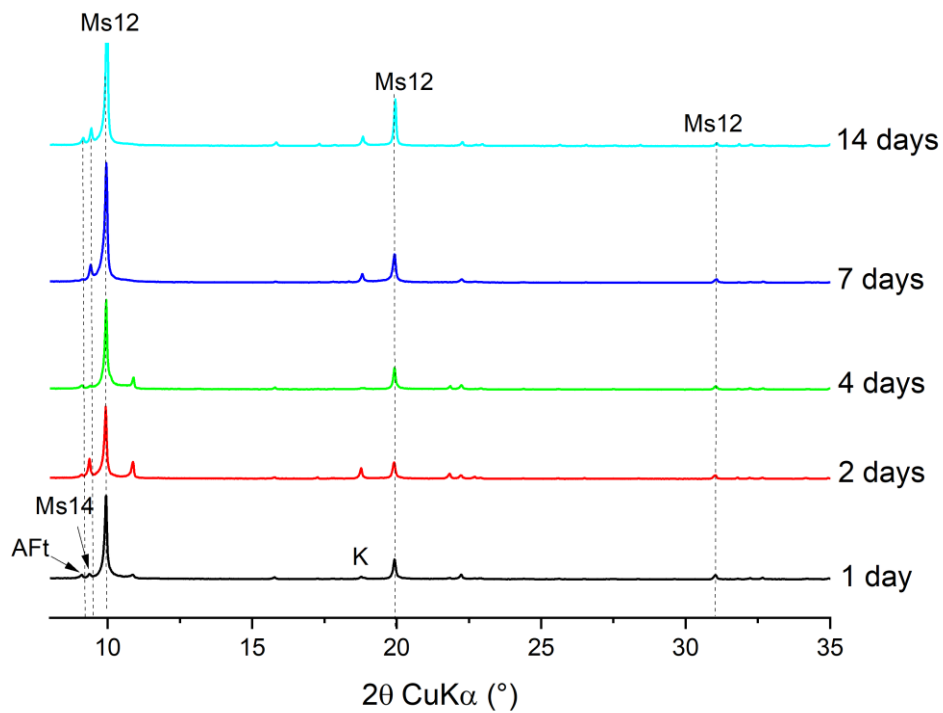
Figure 37. XRPD spectra of Ms samples in kinetic experiments with 21 mM Na-gluconate. AFt: ettringite; K: katoite; Ms12: monosulfate-12; Ms14: monosulfate-14.
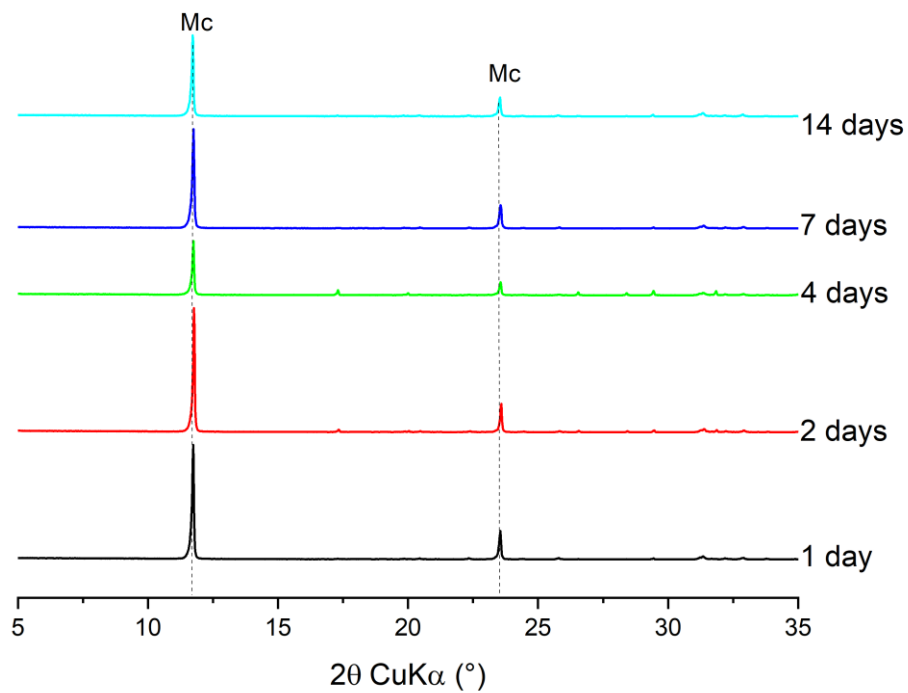
Figure 38. XRPD spectra of Mc samples in kinetic experiments with 21 mM Na-gluconate. Mc: monocarbonate.
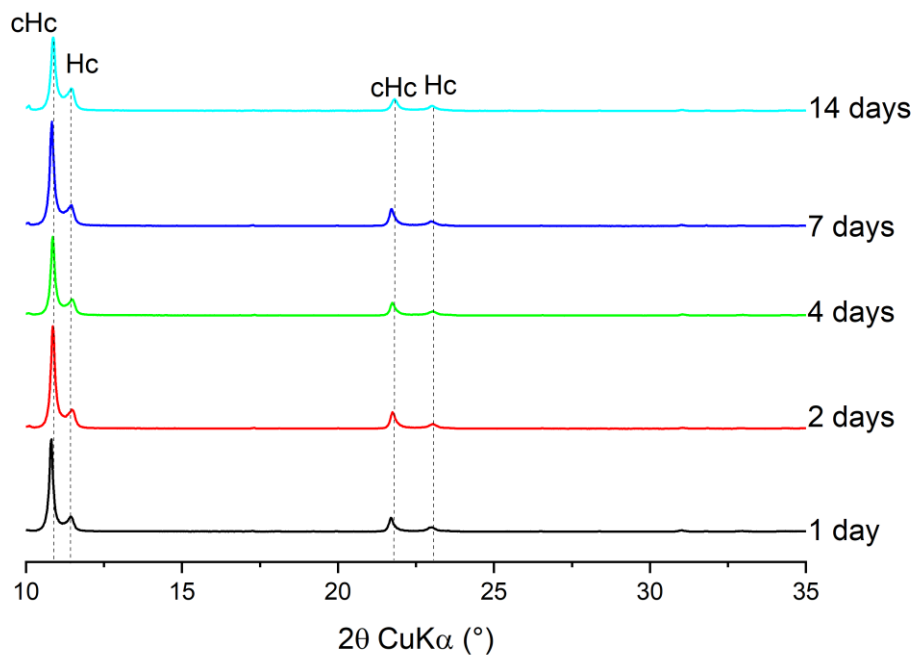
Figure 39. XRPD spectra of Hc samples in kinetic experiments with 21 of Na-gluconate. cHc: carbonated hemicarbonate; Hc: hemicarbonate.
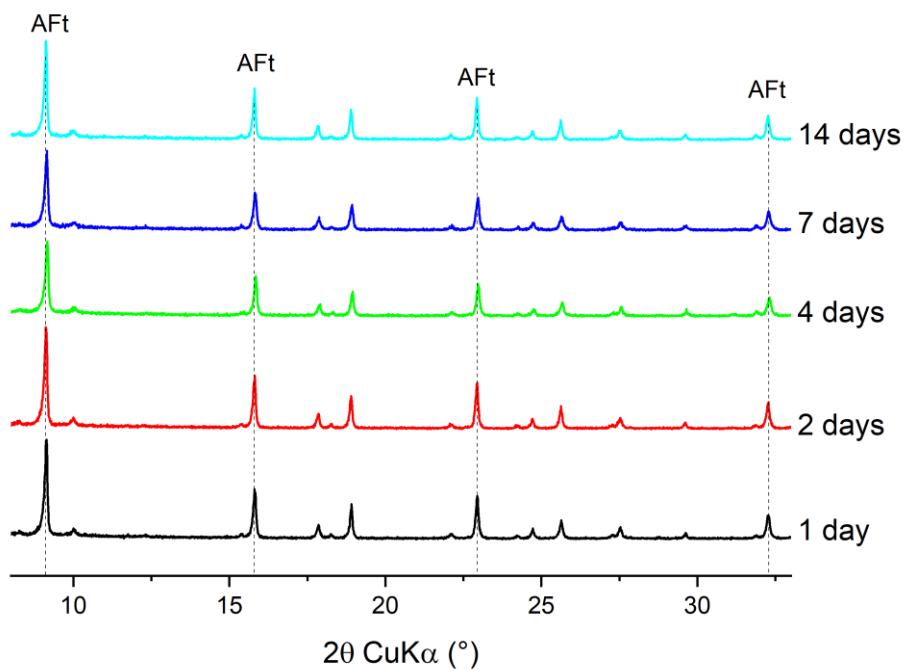
Figure 40. XRPD spectra of AFt samples in kinetic experiments with 21 of Na-guconate. AFt: ettringite.

Table 75. Solution composition of Ms samples in kinetic experiments with 21 mM of Na-gluconate.

Time/(days) Monosulfate (Ms)	[Na]	[Ca]	[Al]	[S]	[OH⁻]	Gluconate	Observed phase[a]
				mM			
1	197	3.3	3.0	11	112	6.0	Ms12, Ms14, AFt
2	193	6.8	6.3	8.4	107	5.8	Ms12, Ms14, AFt
4	140	18	16	13	67	17	Ms12, Ms14, AFt
7	196	6.5	6.0	8.7	146	5.2	Ms12, Ms14, AFt
14	200	12	11	4.6	146	11	Ms12, Ms14, AFt

[a] Phases identification achieved by XRPD analyses. AFt: ettringite, Ms12: monosulfate-12, Ms14: monosulfate-14.

Table 76. Saturation indices of portlandite, katoite, monosulfate (Ms), ettringite (AFt), gibbsite microcrystalline (Al(OH)$_3$), for Ms system in gluconate kinetic experiments ([GLU]$_{tot}$ = 0.021 M, [Na]$_{tot}$ = 0.2 M). Calculations have been carried out with GEMS software.

Time/(days)	Portlandite	katoite	Gibbsite (mic)	Ms	AFt	Ca(GLU)$_2$
1	-2.0	-4.7	-1.3	-3.6	-3.0	18
2	-2.0	-4.1	-0.91	-3.1	-2.8	18
4	-2.2	-3.7	-0.39	-2.5	-1.8	-17
7	-1.9	-4.2	-1.1	-3.4	-3.4	-18
14	-1.8	-3.2	-0.78	-3.0	-4.2	-17

Table 77.Solution composition of Mc samples in kinetic experiments with 21 mM of Na-gluconate.

Time/(days) Monocarbonate (Mc)	[Na]	[Ca]	[Al]	[OH⁻]	Gluconate	Observed phase[a]
			mM			
1	192	7.2	6.5	118	11	Mc, CC
2	193	6.7	6.1	112	12	Mc, CC
4	193	11	10	118	11	Mc, CC
7	198	8.9	8.3	154	8.9	Mc, CC
14	197	8.9	8.3	154	8.4	Mc, CC

[a] Phases identification achieved by XRPD analyses. Mc: monocarbonate, CC: calcite.

Table 78. Saturation indices of portlandite, katoite, gibbsite microcrystalline (Al(OH)₃), monocarbonate (Mc), hemicarbonate (Hc), Ca(GLU)₂, for Mc system in gluconate kinetic experiments ([GLU]$_{tot}$ = 0.021 M, [Na]$_{tot}$ = 0.2 M). Calculations have been carried out with GEMS software.

Time/(days)	Portlandite	katoite	Gibbsite (mic)	Mc	Hc	Ca(GLU)$_2$
1	-0.40	1.1	-0.71	5.6	3.8	-16
2	-0.44	0.89	-0.74	5.4	3.6	-16
4	-0.25	1.9	-0.52	6.6	4.8	-16
7	-0.21	1.8	-0.62	6.5	4.7	-16
14	-0.19	1.9	-0.63	6.6	4.8	-16

Table 79. Solution composition of Hc samples in kinetic experiment with 21 mM of Na-gluconate.

Time/(days) Hemicarbonate (Hc)	[Na]	[Ca]	[Al]	[OH⁻]	Gluconate	Observed phase[a]
	mM					
1	206	3.6	3.8	118	5.4	Hc, cHc, Mc
2	202	3.0	3.1	131	4.3	Hc, cHc, Mc
4	199	3.5	3.6	131	4.6	Hc, cHc, Mc
7	200	2.8	2.6	171	2.4	Hc, cHc, Mc
14	202	2.4	1.2	171	1.5	cHc(?), Mc

[a] Phases identification achieved by XRPD analyses. cHc: carbo-hemicarbonate, Hc: hemicarbonate, Mc: monocarbonate.

Table 80. Saturation indices of portlandite, katoite, hemicarbonate (Hc), formate-AFm, for Hc Ca(GLU)₂ system in gluconate kinetic experiments ([GLU]$_{tot}$ = 0.021 M, [Na]$_{tot}$ = 0.2 M). Calculations have been carried out with GEMS software.

Time/(days)	Portlandite	katoite	Hc	Ca(GLU)$_2$
1	-0.31	0.72	3.3	-17
2	-0.31	0.57	3.0	-17
4	-0.29	0.79	3.3	-17
7	-0.19	0.76	3.3	-17
14	-0.14	0.21	2.5	-17

Table 81. Solution composition of AFt samples in kinetic experiments with 21 mM of Na-gluconate.

Time/(days)	[Na]	[Ca]	[Al]	[S]	[OH⁻]	Gluconate	Observed phase[a]
Ettringite (AFt)	mM						
1	194	8.7	0.6	17	49	5.2	AFt
2	197	15	0.2	22	54	5.0	AFt
4	199	5.8	2.3	17	62	3.0	AFt
7	200	5.8	2.6	17	58	3.7	AFt
14	200	6.1	2.2	18	62	5.0	AFt

[a] Phases identification achieved by XRPD analyses. AFt: ettringite.

Table 82. Saturation indices of portlandite, katoite, monosulfate (Ms), ettringite (AFt), $Ca(GLU)_2$ system in gluconate kinetic experiments ($[GLU]_{tot} = 0.021$ M, $[Na]_{tot} = 0.2$ M). Calculations have been carried out with GEMS software.

Time/(days)	Portlandite	katoite	Ms	AFt	$Ca(GLU)_2$
1	-0.65	-7.8	-4.7	-0.21	-16
2	-0.72	-7.5	-4.6	-0.21	-16
4	-0.37	-9.0	-5.6	-0.36	-17
7	-2.1	-5.1	-3.7	-2.6	-18
14	-2.1	-4.7	-3.4	-2.4	-18

3.2. Sorption experiments
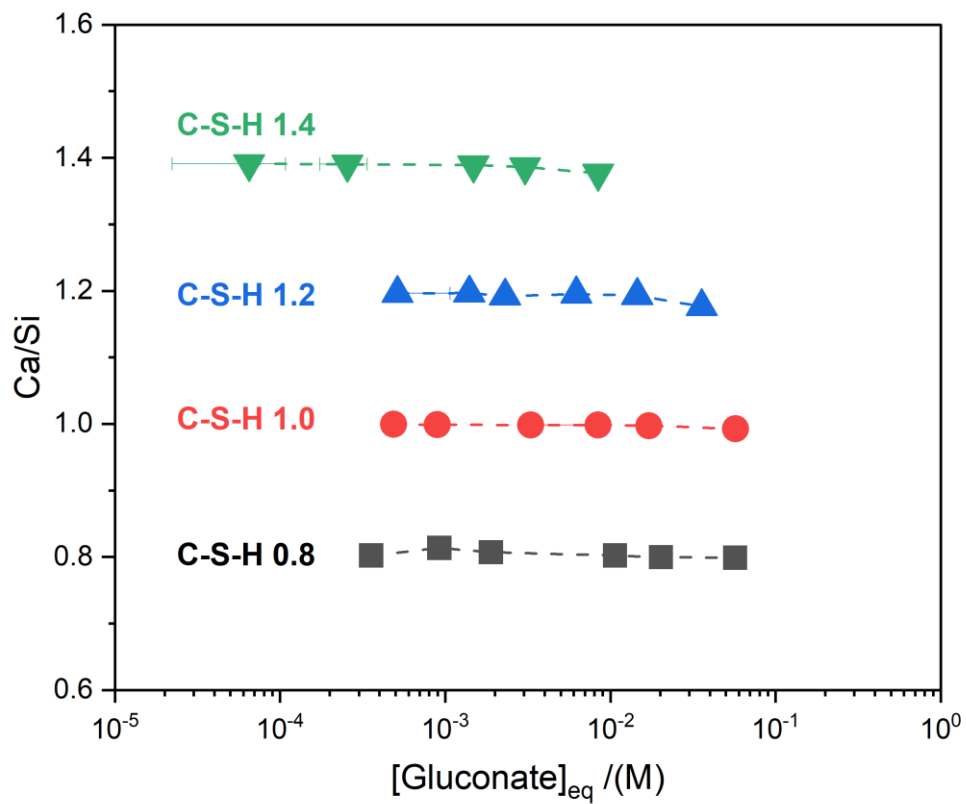
Figure 41. Calculated Ca/Si as a function of equilibrium concentration of gluconate for the C-S-H solid phases in presence of gluconate. Calculation have been carried out per 100 g of sample and taking into account the formation of portlandite by using the mass balance equation: $Ca/Si = ([Ca]_{tot,\ in} - [Ca]_{tot,\ eq} - [Ca]_{portlandite}) / ([Si]_{tot,\ in} - [Si]_{tot,\ eq})$.
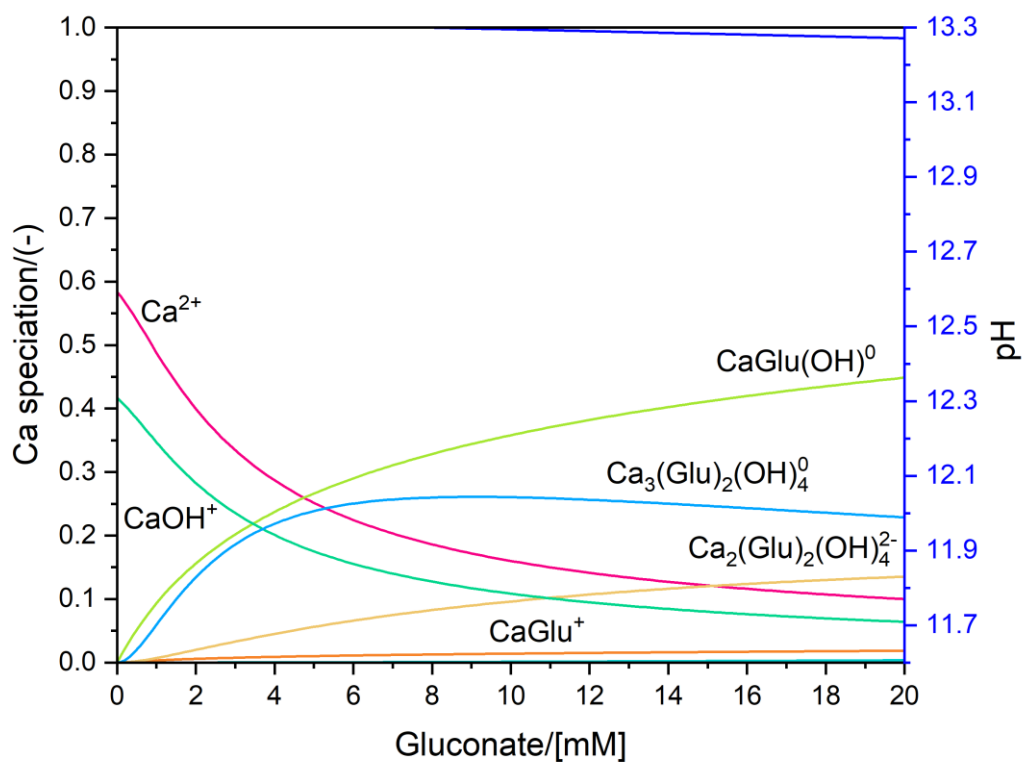
Figure 42. Calculated fraction of Ca-complexes and pH determined with an initial calcium concentration of $[Ca]_{tot}$ = 2 mM as a function of added gluconate concentration.

*Table 83. Solution composition of **C-S-H phases (Ca/Si=0.8)** in gluconate sorption experiments.*

Measured initial gluconate concentration/(mM)	Measured concentrations					Observed phase[a]
	[Na]	[Ca]	[Si]	[OH⁻]	Gluconate	
	mM					
0.00	95	0.11	0.52	127	<0.020	C-S-H
0.021	b	b	b	b	b	C-S-H
0.042	b	b	b	b	b	C-S-H
0.11	b	b	b	b	b	C-S-H
0.21	b	b	b	b	b	C-S-H
0.42	b	b	b	b	b	C-S-H
1.05	b	b	b	b	b	C-S-H
2.1	b	b	b	b	b	C-S-H
4.2	74	0.066	1.3	83	3.9	C-S-H
10.5	76	0.13	1.2	83	10	C-S-H
21	76	0.21	1.3	66	20	C-S-H

[a] Phases identification achieved by XRPD analyses. C-S-H: C-S-H phase.
[b] Concentrations not measured due to an ineffective solid-liquid phase separation by filtration.

*Table 84. Saturation indices of C-S-H phase, Ca(GLU)$_2$, portlandite and silica for C-S-H phase with a **Ca/Si=0.8** in gluconate sorption experiments ([Na]$_{tot}$ = 0.2 M). Calculations have been carried out with GEMS software.*

[Gluconate]$_{tot}$/(mM)	C-S-H	Ca(GLU)$_2$	Portlandite	SiO$_{2(am)}$
0.00	-0.32	-	-1.9	-4.0
0.021	-	-	-	-
0.042	-	-	-	-
0.11	-	-	-	-
0.21	-	-	-	-
0.42	-	-	-	-
1.05	-	-	-	-
2.1	-	-	-	-
4.2	-0.42	-18	-2.6	-3.4
10.5	-0.29	-17	-2.4	-3.4
21	-0.22	-16	-2.4	-3.3

*Table 85. Solution composition of **C-S-H phases (Ca/Si=1.0)** in gluconate sorption experiments.*

Measured initial gluconate concentration/(mM)	Measured concentrations					Observed phase[a]
	[Na]	[Ca]	[Si]	[OH$^-$]	Gluconate	
	mM					
0.00	163	0.21	0.32	132	<0.020	C-S-H
0.021	c	c	c	c	c	C-S-H
0.042	c	c	c	c	c	C-S-H
0.11	c	c	c	c	c	C-S-H
0.21	c	c	c	c	c	C-S-H
0.42	c	c	c	c	c	C-S-H
1.05	c	c	c	c	c	C-S-H
2.1	163	0.41	0.26	114	1.7	C-S-H
4.2	166	0.48	0.19	125	3.0	C-S-H
10.5	170	0.71	0.17	120	6.5	C-S-H
21	161	1.1	0.25	101	16	C-S-H

[a] Phases identification achieved by XRPD analyses. C-S-H: C-S-H phase.

[b] Phase identification carried out by TGA characterization.

[c] Concentrations not measured due to an ineffective solid-liquid phase separation by filtration.

*Table 86. Saturation indices of C-S-H phase, Ca(GLU)₂, and silica for C-S-H phase with a **Ca/Si=1.0** in gluconate sorption experiments ([Na]_tot = 0.2 M). Calculations have been carried out with GEMS software.*

$[Gluconate]_{tot}$/(mM)	C-S-H	Ca(GLU)$_2$	Portlandite	SiO$_{2(am)}$
0.00	-0.17	-	-1.2	-4.6
0.021	-	-	-	-
0.042	-	-	-	-
0.11	-	-	-	-
0.21	-	-	-	-
0.42	-	-	-	-
1.05	-	-	-	-
2.1	-0.056	-18	-0.99	-4.7
4.2	-0.13	-17	-0.95	-4.9
10.5	-0.14	-17	-0.92	-4.9
21	-0.060	-16	-1.0	-4.7

*Table 87. Solution composition of **C-S-H phases (Ca/Si=1.2)** in sorption experiments.*

Measured initial gluconate concentration/(mM)	Measured concentrations					Observed phase[a]
	[Na]	[Ca]	[Si]	[OH⁻]	Gluconate	
	mM					
0.00	212	2.3	0.030	165	<0.020	C-S-H, CH[b]
0.021	c	c	c	c	c	C-S-H, CH[b]
0.042	c	c	c	c	c	C-S-H, CH[b]
0.11	c	c	c	c	c	C-S-H, CH[b]
0.21	c	c	c	c	c	C-S-H, CH[b]
0.42	c	c	c	c	c	C-S-H, CH[b]
1.05	c	c	c	c	c	C-S-H, CH[b]
2.1	210	1.5	0.034	148	1.1	C-S-H, CH[b]
4.2	200	1.0	0.054	141	2.1	C-S-H, CH[b]
10.5	192	1.1	0.085	127	5.8	C-S-H, CH[b]
21	199	3.1	0.074	127	31	C-S-H

[a] Phases identification achieved by XRPD analysis. C-S-H: C-S-H phase, CH: portlandite.
[b] Portlandite content per 100 g of dry sample. Phase identification carried out by TGA characterization.
[c] Concentrations not measured due to an ineffective solid-liquid phase separation by filtration.

*Table 88. Saturation indices of C-S-H phase, Ca(GLU)₂, portlandite and silica for C-S-H phase with a **Ca/Si=1.2** in gluconate sorption experiments ([Na]$_{tot}$ = 0.2 M). Calculations have been carried out with GEMS software.*

[Gluconate]$_{tot}$/(mM)	C-S-H	Ca(GLU)$_2$	Portlandite	SiO$_{2(am)}$
0.00	-0.05	-	0.070	-6.3
0.021	-	-	-	-
0.042	-	-	-	-
0.11	-	-	-	-
0.21	-	-	-	-
0.42	-	-	-	-
1.05	-	-	-	-
2.1	-0.20	-18	-0.21	-6.0
4.2	-0.21	-17	-0.45	-5.7
10.5	-0.18	-16	-0.62	-5.4
21	-0.13	-16	-0.48	-5.5

*Table 89. Solution composition of **C-S-H phases (Ca/Si=1.4)** in gluconate sorption experiments.*

Measured initial gluconate concentration/(mM)	Measured concentrations					Observed phase[a]
	[Na]	[Ca]	[Si]	[OH⁻]	Gluconate	
	mM					
0.00	211	2.6	0.020	153	<0.020	C-S-H, CH[b]
0.021	c	c	c	c	c	C-S-H, CH[b]
0.042	c	c	c	c	c	C-S-H, CH[b]
0.11	c	c	c	c	c	C-S-H, CH[b]
0.21	c	c	c	c	c	C-S-H, CH[b]
0.42	c	c	c	c	c	C-S-H, CH[b]
1.05	209	2.8	0.022	153	0.71	C-S-H, CH[b]
2.1	213	3.2	0.021	153	0.60	C-S-H, CH[b]
4.2	219	3.6	0.019	160	1.1	C-S-H, CH[b]
10.5	213	4.3	0.020	160	3.5	C-S-H, CH[b]
21	211	7.7	0.034	153	9.1	C-S-H, CH[b]

[a] Phases identification achieved by XRPD analyses. C-S-H: C-S-H phase, CH: portlandite.
[b] Portlandite content per 100 g of dry sample. Phase identification carried out by TGA characterization.
[c] Concentrations not measured due to an ineffective solid-liquid phase separation by filtration.

*Table 90. Saturation indices of C-S-H phase, Ca(GLU)₂, portlandite and silica for C-S-H phase with a **Ca/Si=1.4** in gluconate sorption experiments ([Na]ₜₒₜ = 0.2 M). Calculations have been carried out with GEMS software.*

[Gluconate]$_{tot}$/(mM)	C-S-H	Ca(GLU)$_2$	Portlandite	SiO$_{2(am)}$
0.00	-0.13	-	0.13	-6.5
0.021	-	-	-	-
0.042	-	-	-	-
0.11	-	-	-	-
0.21	-	-	-	-
0.42	-	-	-	-
1.05	-0.12	-18	0.096	-6.4
2.1	-0.086	-18	0.18	-6.5
4.2	-0.11	-18	0.20	-6.6
10.5	-0.17	-17	0.065	-6.4
21	-0.068	-16	-0.028	-6.1

Table 91. Mass of hydrated C-S-H phases per 2.21 g of (CaO + SiO₂) in 50 mL of solution calculated by combining mass balance and water content determined by TGA analysis.

[Gluconate]$_{tot}$/(mM)	Ca/Si = 0.8	Ca/Si = 1.0	Ca/Si = 1.2	Ca/Si = 1.4
	g/100 g			
0.00	2.9	2.8	2.7	2.7
0.021	3.0	2.8	2.7	2.7
0.042	2.9	2.8	2.7	2.7
0.11	3.0	2.8	2.7	2.7
0.21	3.0	2.8	2.7	2.7
0.42	3.0	2.8	2.8	2.7
1.05	1.7	2.9	2.8	2.6
2.1	1.7	2.8	2.7	2.7
4.2	2.9	2.8	2.7	2.6
10.5	2.9	2.8	2.7	2.6
21	3.0	2.8	2.7	2.7
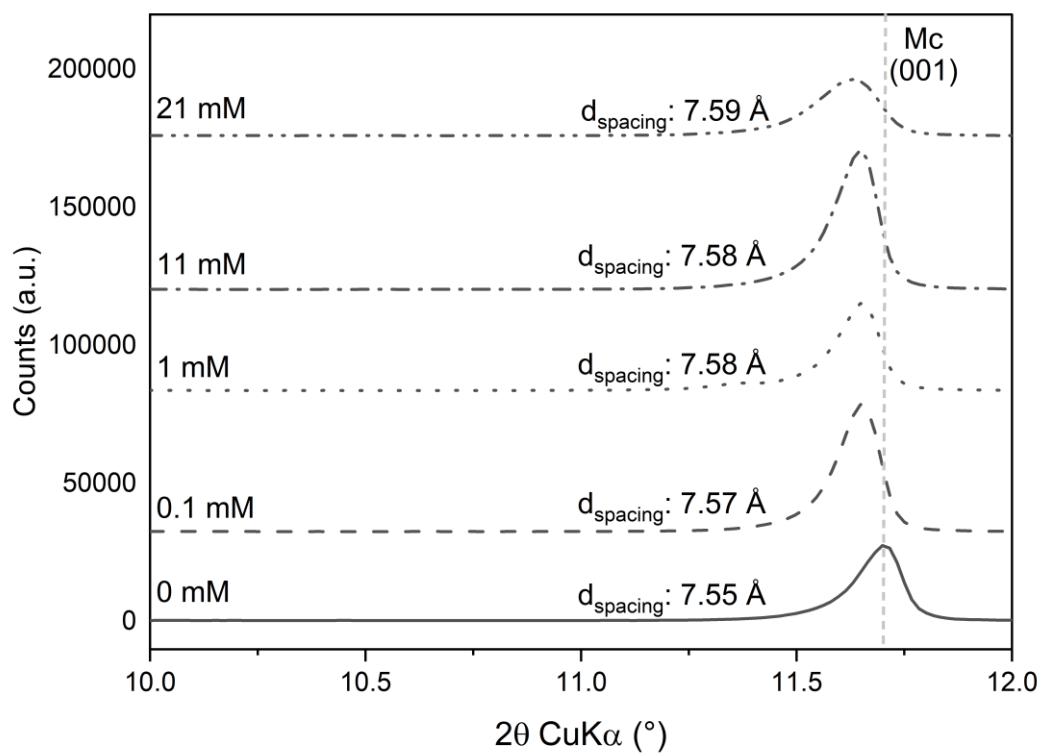
Figure 43. XRPD characterization of Ms in sorption experiments with [Gluconate]$_{tot}$ = 0 – 21 mM.
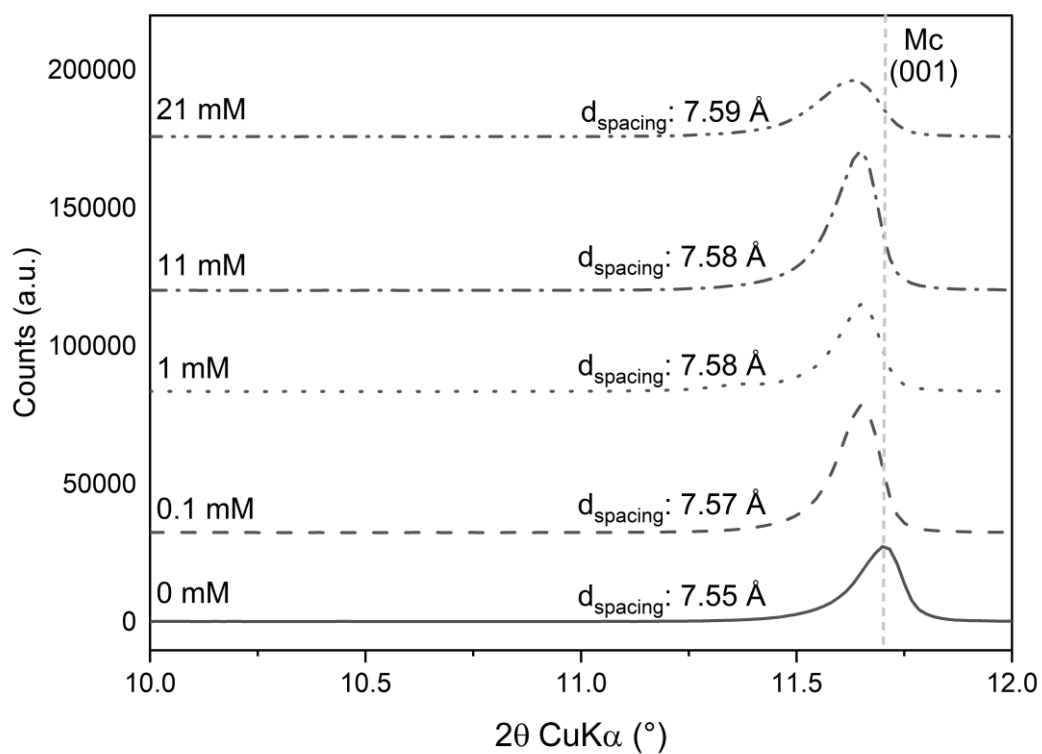
Figure 44. XRPD characterization of Mc in sorption experiments with [Gluconate]$_{tot}$ = 0 – 21 mM.
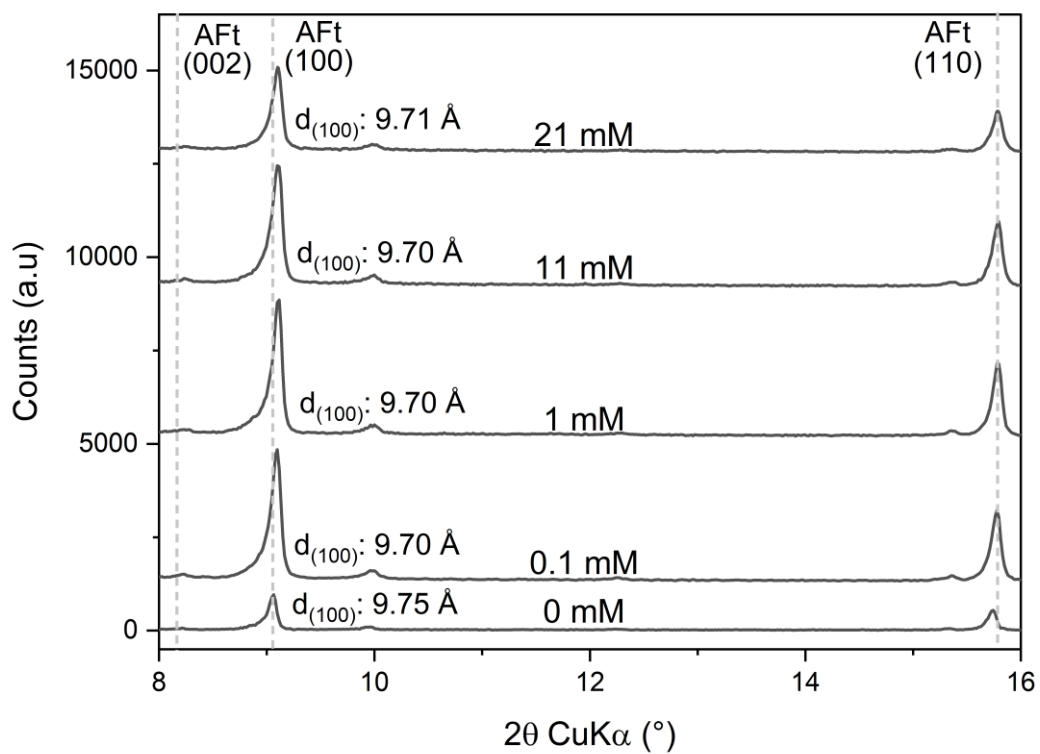
Figure 45. XRPD characterization of AFt in sorption experiments with [Gluconate]$_{tot}$ = 0 – 21 mM.
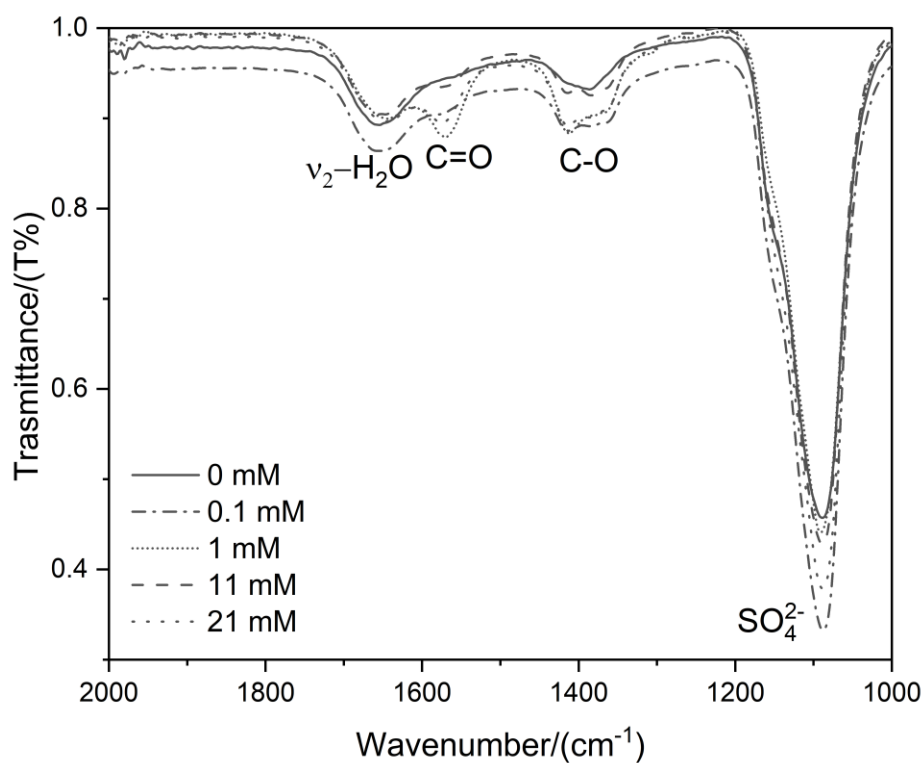
Figure 46. FT-IR characterization of Ms samples in sorption experiments (2000-1000 cm^{-1}).
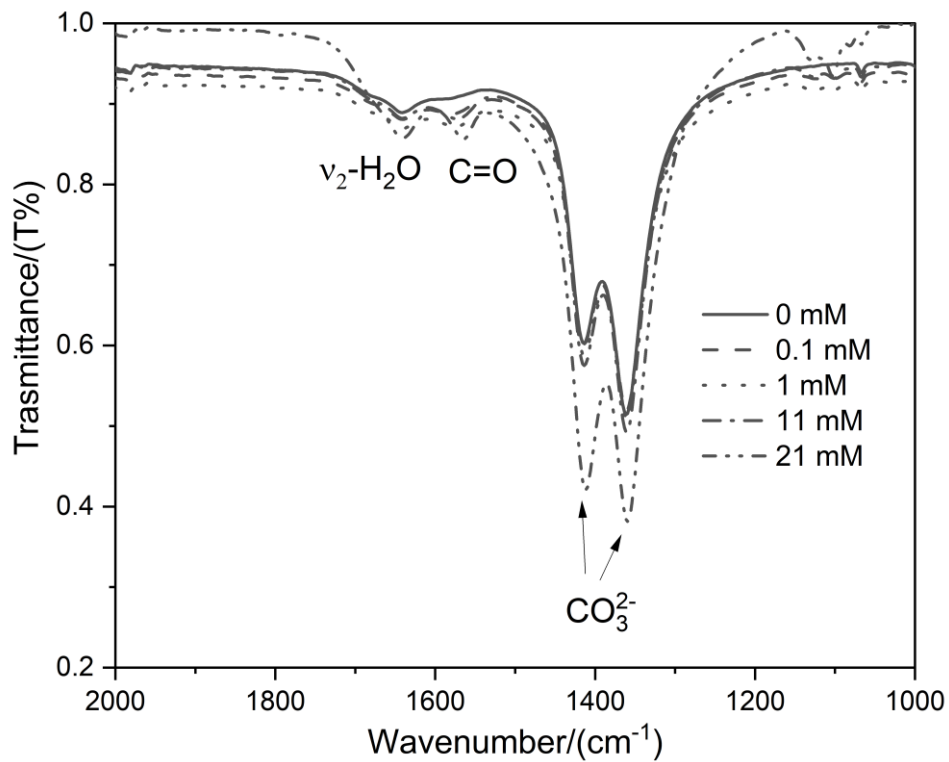
Figure 47. FT-IR characterization of Mc samples in sorption experiments (2000-1000 cm^{-1}).
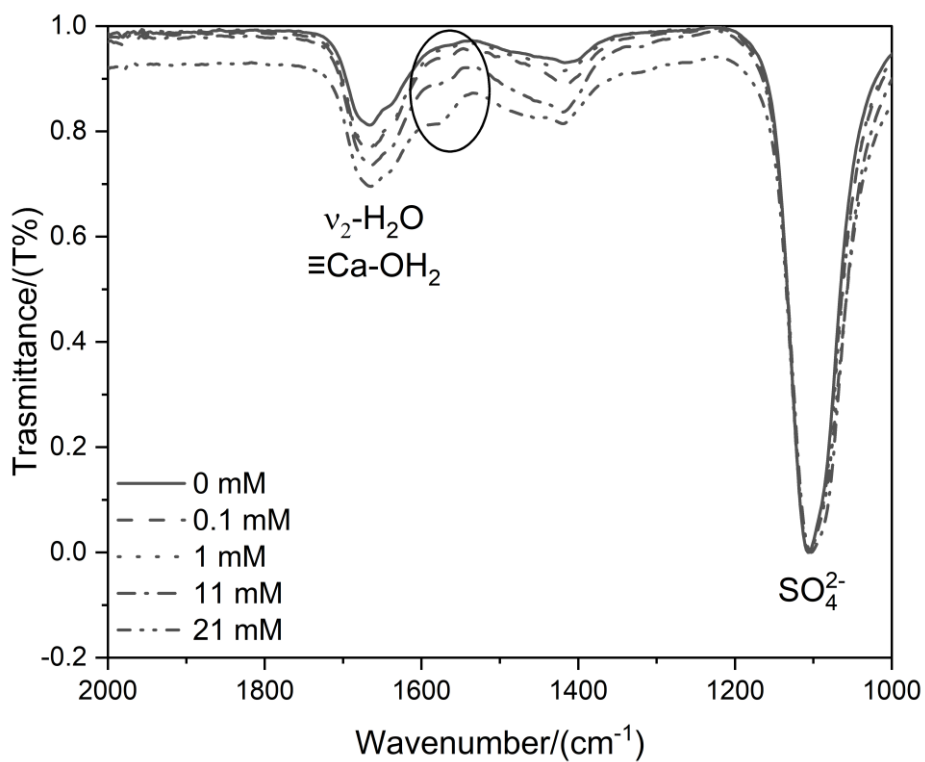
Figure 48. FT-IR characterization of AFt samples in sorption experiments (2000-1000 cm^{-1}).

*Table 92. Solution composition of **Ms** samples in gluconate sorption experiments.*

Measured initial gluconate concentration/ (mM)	Measured concentrations						Observed phase[a]
	[Na]	[Ca]	[Al]	[S]	[OH⁻]	Gluconate	
	mM						
0.00	226	0.44	1.6	1.1	179	<0.020	Ms12, Ms14, AFt
0.021	b	b	b	b	b	b	Ms12, Ms14, AFt
0.042	b	b	b	b	b	b	Ms12, Ms14, AFt
0.11	b	b	b	b	b	b	Ms12, Ms14, AFt
0.21	b	b	b	b	b	b	Ms12, Ms14, AFt
0.42	b	b	b	b	b	b	Ms12, Ms14, AFt
1.05	b	b	b	b	b	b	Ms12, Ms14, AFt
2.1	228	2.8	3.2	0.8	179	2.0	Ms12, Ms14, AFt
4.2	227	2.5	2.0	2.8	179	2.0	Ms12, Ms14, AFt
10.5	222	7.4	7.2	2.2	179	6.9	Ms12, Ms14, AFt
21	220	7.6	7.2	9.7	170	7.0	Ms12, Ms14, AFt

[a] Phases identified by XRPD analyses. AFt: ettringite, Ms12: monosulfate-12, Ms14: monosulfate-14.
[b] Concentrations not measured due to an ineffective solid-liquid phase separation by filtration.

*Table 93. Saturation indices of portlandite, katoite, gypsum, monosulfate (Ms), ettringite (AFt), Ca(GLU)$_2$ for **Ms** system in gluconate sorption experiments ([Na]$_{tot}$ = 0.2 M). Calculations have been carried out with GEMS software.*

[Gluconate]$_{tot}$/(mM)	Portlandite	katoite	Gypsum	Ms	AFt	Ca(GLU)$_2$
0.00	-1.8	-4.6	-4.3	-4.7	-0.87	-
0.021	-	-	-	-	-	-
0.042	-	-	-	-	-	-
0.11	-	-	-	-	-	-
0.21	-	-	-	-	-	-
0.42	-	-	-	-	-	-
1.05	-	-	-	-	-	-
2.1	-1.5	-2.8	-3.9	-3.3	-5.9	-17
4.2	-1.9	-4.1	-4.8	-3.4	-3.6	-17
10.5	-0.072	3.8	-3.6	-9.6	-38	-16
21	-0.032	3.9	-18	-9.7	-38	-16

*Table 94. Solution composition of **Mc** samples in gluconate sorption experiments.*

Measured initial gluconate concentration/(mM)	Measured concentrations					Observed phase[a]
	[Na]	[Ca]	[Al]	[OH$^-$]	gluconate	
	mM					
0.00	218	0.68	0.19	161	<0.020	Mc, CC
0.021	[b]	[b]	[b]	[b]	[b]	Mc, CC
0.042	[b]	[b]	[b]	[b]	[b]	Mc, CC
0.11	[b]	[b]	[b]	[b]	[b]	Mc, CC
0.21	[b]	[b]	[b]	[b]	[b]	Mc, CC
0.42	[b]	[b]	[b]	[b]	[b]	Mc, CC
1.05	214	1.5	0.90	162	[b]	Mc, CC
2.1	215	1.5	1.0	163	[b]	Mc, CC
4.2	215	2.0	1.5	146	[b]	Mc, CC
10.5	216	5.0	4.5	148	[b]	Mc, CC
21	211	8.5	8.2	150	[b]	Mc, CC

[a] Phases identification achieved by XRPD analyses. CC: calcite, Mc: monocarbonate.
[b] Concentrations not measured due to an ineffective solid-liquid phase separation by filtration.

*Table 95. Saturation indices of portlandite, katoite, monocarbonate (Mc), hemicarbonate (Hc), Ca(GLU)$_2$ for **Mc** system in gluconate sorption experiments ([Na]$_{tot}$ = 0.2 M). Calculations have been carried out with GEMS software.*

[Gluconate]$_{tot}$/(mM)	Portlandite	katoite	Mc	Hc	Ca(GLU)$_2$
0.00	-0.51	-2.6	-0.17	-1.0	-
0.021	-	-	-	-	-
0.042	-	-	-	-	-
0.11	-	-	-	-	-
0.21	-	-	-	-	-
0.42	-	-	-	-	-
1.05	-0.22	-0.35	2.1	1.4	-
2.1	-0.26	-0.33	2.2	1.4	-
4.2	-0.14	0.36	2.9	2.2	-
10.5	-0.05	1.6	4.0	3.4	-
21	-0.19	1.7	4.5	3.6	-

*Table 96. Solution composition of **Hc** samples in gluconate sorption experiments.*

Measured initial gluconate concentration/(mM)	Measured concentrations					Observed phase[a]
	[Na]	[Ca]	[Al]	[OH$^-$]	Gluconate	
	mM					
0.00	214	1.7	0.13	168	<0.020	Hc, cHc, Mc
0.021	[b]	[b]	[b]	[b]	[b]	Hc, cHc, Mc
0.042	[b]	[b]	[b]	[b]	[b]	Hc, cHc, Mc
0.11	[b]	[b]	[b]	[b]	[b]	Hc, cHc, Mc
0.21	[b]	[b]	[b]	[b]	[b]	Hc, cHc, Mc
0.42	[b]	[b]	[b]	[b]	[b]	Hc, cHc
1.05	204	2.3	0.30	165	0.34	Hc, cHc
2.1	218	2.3	0.27	183	0.32	Hc, cHc
4.2	218	2.3	0.21	164	0.25	Hc, cHc, Mc
10.5	216	1.6	0.18	166	0.74	Hc, cHc, Mc
21	214	4.3	3.7	169	3.87	cHc(?), Mc

[a] Phases identification achieved by XRPD analyses. cHc: carbo-hemicarbonate, Hc: hemicarbonate, Mc: monocarbonate.
[b] Concentrations not measured due to an ineffective solid-liquid phase separation by filtration.

*Table 97. Saturation indices of portlandite, katoite, hemicarbonate (Hc), Ca(GLU)$_2$ for **Hc** system in gluconate sorption experiments ([Na]$_{tot}$ = 0.2 M). Calculations have been carried out with GEMS software.*

[Gluconate]$_{tot}$/(mM)	Portlandite	katoite	Hc	Ca(GLU)$_2$
0.00	-0.12	-1.4	-0.62	-
0.021	-	-	-	-
0.042	-	-	-	-
0.11	-	-	-	-
0.21	-	-	-	-
0.42	-	-	-	-
1.05	-0.031	-1.2	-0.62	-19
2.1	0.013	-1.2	-0.75	-19
4.2	0.013	-1.7	0.18	-19
10.5	-0.22	-2.3	0.95	-18
21	-0.078	0.98	1.3	-17

*Table 98. Solution composition of **AFt** samples in gluconate sorption experiments.*

Measured initial gluconate concentration/(mM)	Mesasured concentrations						Observed phase[a]
	[Na]	[Ca]	[Al]	[S]	[OH$^-$]	Gluconate	
	mM						
0.00	206	0.098	7.2	12	133	<0.020	AFt
0.021	[b]	[b]	[b]	[b]	[b]	[b]	AFt
0.042	[b]	[b]	[b]	[b]	[b]	[b]	AFt
0.11	[b]	[b]	[b]	[b]	[b]	[b]	AFt
0.21	[b]	[b]	[b]	[b]	[b]	[b]	AFt
0.42	[b]	[b]	[b]	[b]	[b]	[b]	AFt
1.05	204	0.66	5.4	11	133	0.76	AFt
2.1	206	1.7	6.0	12	141	1.8	AFt
4.2	206	3.7	8.0	13	120	4.0	AFt
10.5	204	7.0	0.054	26	126	2.0	AFt
21	204	8.9	0.26	30	114	4.9	AFt

[a] Phases identified by XRPD analyses. AFt: ettringite.
[b] Concentrations not measured due to an ineffective solid-liquid phase separation by filtration.

*Table 99. Saturation indices of portlandite, katoite, gypsum, monosulfate (Ms), ettringite (AFt), Ca(GLU)$_2$ for **AFt** system in gluconate sorption experiments ([Na]$_{tot}$ = 0.2 M). Calculations have been carried out with GEMS software.*

[Gluconate]$_{tot}$/(mM)	Portlandite	katoite	Gypsum	Ms	AFt	Ca(GLU)$_2$
0.00	-2.6	-5.5	-4.0	-5.2	0.0025	-
0.021	-	-	-	-	-	-
0.042	-	-	-	-	-	-
0.11	-	-	-	-	-	-
0.21	-	-	-	-	-	-
0.42	-	-	-	-	-	-
1.05	-2.3	-5.0	-3.7	-4.4	-4.8	-19
2.1	-2.2	-4.7	-3.6	-3.9	-4.2	-19
4.2	-2.2	-4.3	-3.5	-3.6	-3.7	18
10.5	0095	-9.7	-0.86	-62	-1.08	-17
21	-0.055	-8.9	-0.88	-5.4	-0.28	-17

4. PC composition

The composition of the unhydrated cement determined by X-ray fluorescence analysis (XRF) and the phase contents by quantitative X-ray diffraction (QXRD) are reported in Table 100. Quantification was performed by Rietveld refinement using X'Pert Highscore Plus V. 4.8 following the procedure and using the structures recommended by [270]. The hydration of the paste was stopped by solvent exchange using the method by Snellings et al.[271] prior to analysis. The amorphous content in the hydrated paste was quantified using G-factor method [272, 273] with CaF_2 as external standard and includes mainly C-S-H and AFm-phases. For the hydrated paste the results were referred to 100 g of unhydrated cement using the ignited sample mass at 550 ºC as determined by thermogravimetric analysis [233].

Table 100. Chemical-mineralogical composition of unhydrated and hydrated PC (CEM I 42.5 N).

XRF[e] (mass-%)		QXRD (mass-%)		
Parameter	PC	Phase[c]	PC	hydrated PC
SiO_2	19.86	C_3S	58.3	10.0
Al_2O_3	4.86	C_2S	13.9	11.0
Fe_2O_3	2.88	C_3A cubic	2.4	0.5
Cr_2O_3	0.005	C_3A orthorh.	5.5	2.1
MnO	0.050	C_4AF	8.0	5.7
TiO_2	0.251	Lime	0.2	
P_2O_5	0.235	Portlandite[c]	1.1	15.6
CaO	63.42	Gypsum	1.8	
MgO	1.55	Bassanite	2.1	
K_2O	0.85	Anhydrite	0.3	
Na_2O	0.15	Arcanite	0.5	
SO_3	3.18	Calcite	3.5	1.3
CO_2[a]	1.61	Dolomite	0.5	0.8
L.O.I.[b]	2.54	Quartz	0.5	0.5
		Ettringite		6.5
		Amorphous/other[d]		65.4

[a] Calculated from total carbon determined by combustion analysis.
[b] Loss on ignition.
[c] TGA: 1.9 mass-% in anhydrous PC and 16.2 mass-% in hydrated PC (corrected for carbonation).
[d] Includes C-S-H, hemi- and monocarbonate and further phases.
[e] The accuracy of the measurements is in compliance with EN 196-2 and ISO 10694, respectively.

Appendix 3.2

1.1.   Ternary system: C-S-H/ Pu / L

1.1.1.   Formate
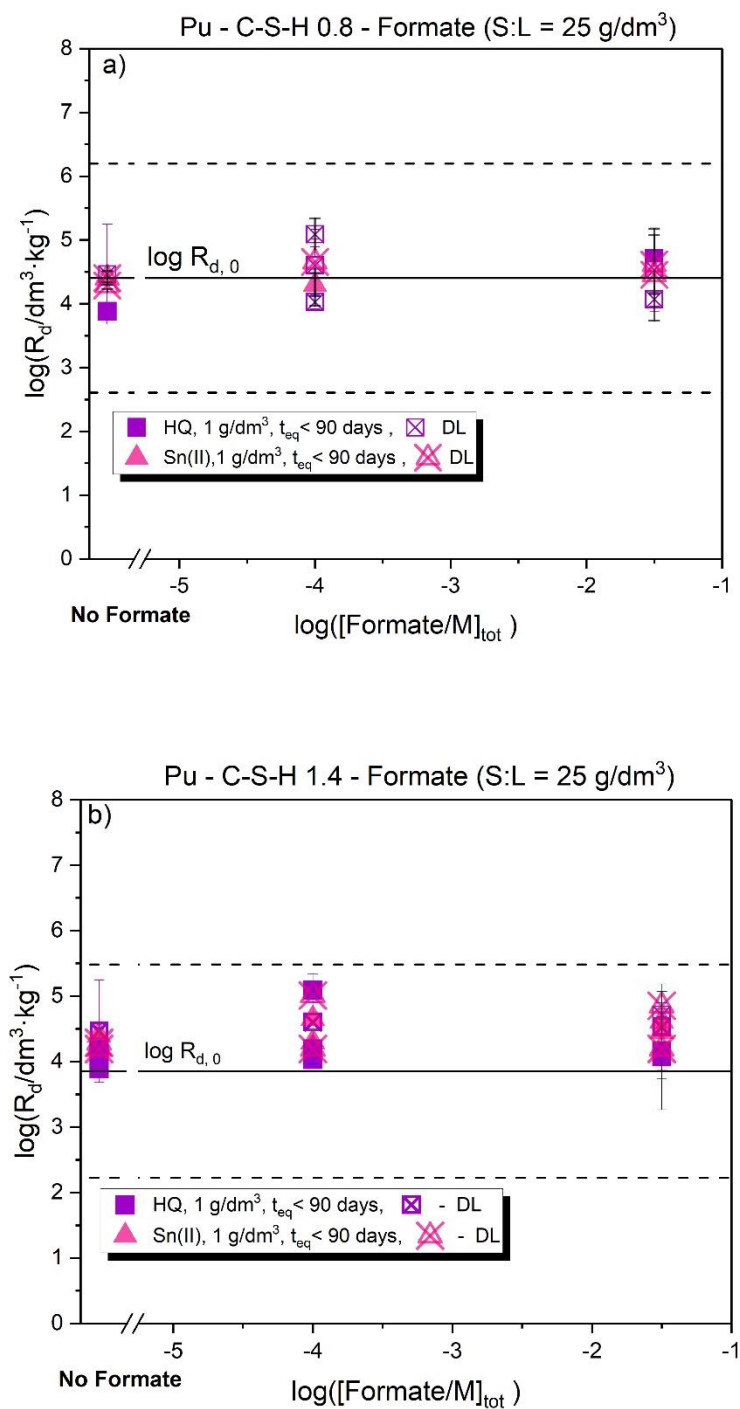
Figure 1. Distribution ratios, R_d, determined for the system (Pu-C-S-H) + FOR, for (a) C-S-H with C/S = 0.8; and (b) C-S-H with C/S = 1.4. In both cases data corresponding to pH = 13.3, S/L = 25 g·dm^{-3} and 90 days of contact time. X crossed symbols refers to values at the detection limit.

Table 1. Ca equilibrium concentration (measurement error ± 5%) measured for contacting time t_{eq} = 90 days and pH = 13.3 for the HQ buffered C-S-H (0.8-1.4)-Pu-FOR systems. C-S-H phases were synthesized with an initial S/L= 1 g·dm⁻³.

Formate concentration, log([FOR]tot/M)	C-S-H 0.8 S/L=1 g·dm⁻³	C-S-H 1.4 S/L=1 g·dm⁻³
No ligand	2.8E-05	2.0E-03
-4	4.4E-05	1.6E-03
-1.5	2.4E-04	1.6E-03

1.1.2. Citrate

Figure 2. Distribution ratios, R_d, determined for the system (Pu-C-S-H) + CIT, for (a) C-S-H with C/S = 0.8; and (b) C-S-H with C/S = 1.4. In both cases data corresponding to pH = 13.3, S/L = 25 g·dm^{-3} and 90 days of contact time. X crossed symbols refers to values at the detection limit.

Table 2. Ca equilibrium concentration (measurement error ± 5%) measured for contacting time t_{eq} = 90 days and pH = 13.3 for the HQ buffered C-S-H (0.8-1.4)-Pu-CIT systems. C-S-H phases were synthesized with an initial S/L= 1 g·dm⁻³ and 25 g·dm⁻³.

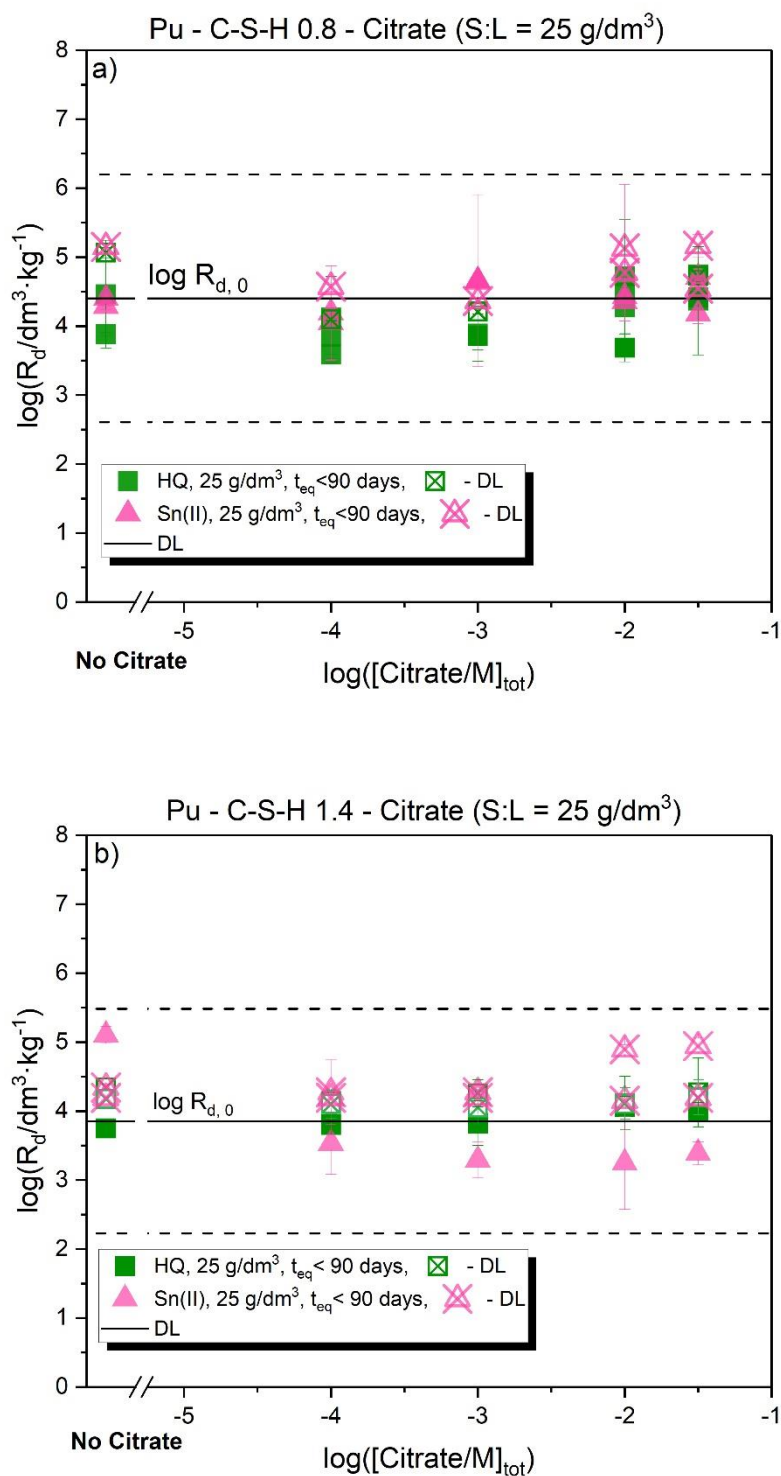| Citrate concentration, $\log([CIT]_{tot}/M)$	C-S-H 0.8 S/L=1 g·dm⁻³	C-S-H 1.4 S/L=1 g·dm⁻³	C-S-H 0.8 S/L=25 g·dm⁻³	C-S-H 1.4 S/L=25 g·dm⁻³
No ligand	2.8E-05	2.0E-03	5.1E-05	1.9E-03
-4	5.0E-05	2.0E-03	3.6E-05	1.9E-03
-3	6.1E-05	1.5E-03	6.5E-05	-
-2	4.8E-04	3.3E-03	1.0E-03	1.4E-02
-1.5	1.1E-03	4.2E-03	3.6E-03	5.1E-03
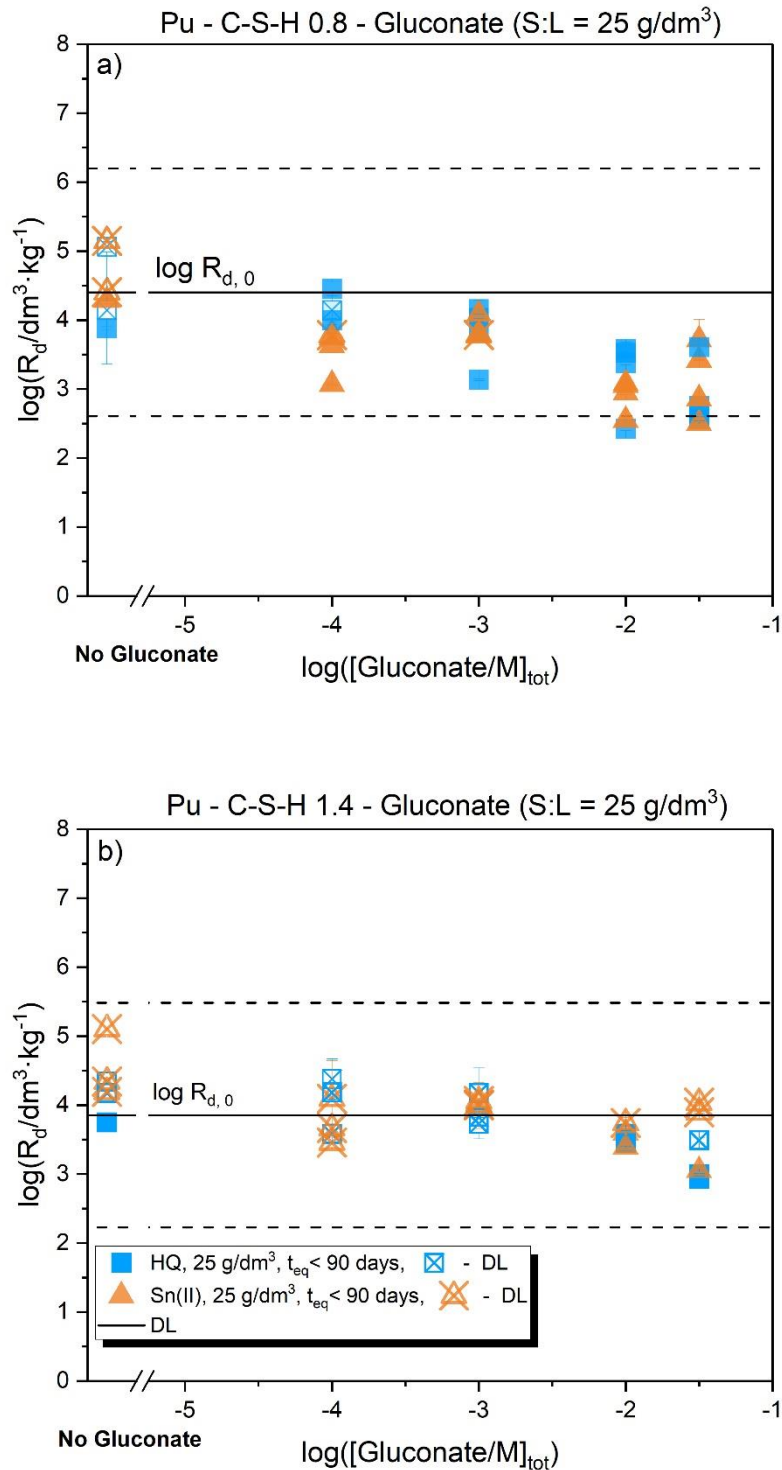
Figure 3. Distribution ratios, R_d, determined for the system (Pu-C-S-H) + GLU, for (a) C-S-H with C/S = 0.8; and (b) C-S-H with C/S = 1.4. In both cases data corresponding to pH = 13.3, S/L = 25 g·dm⁻³ and 90 days of contact time. X crossed symbols refers to values at the detection limit.

Table 3. Ca equilibrium concentration (measurement error ± 5%) measured for contacting time t_{eq} = 90 days and pH = 13.3 for the HQ buffered C-S-H (0.8-1.4)-Pu-GLU systems. C-S-H phases were synthesized with an initial S/L= 1 g·dm^{-3} and 25 g·dm^{-3}.

Gluconate concentration, log([GLU]$_{tot}$/M)	C-S-H 0.8 S/L=1 g·dm^{-3}	C-S-H 1.4 S/L=1 g·dm^{-3}	C-S-H 0.8 S/L=25 g·dm^{-3}	C-S-H 1.4 S/L=25 g·dm^{-3}
No ligand	2.8E-05	2.0E-03	5.1E-05	1.9E-03
-4	1.0E-04	1.6E-03	5.3E-05	1.8E-03
-3	4.6E-05	2.0E-03	6.4E-05	2.0E-03
-2	7.2E-05	2.3E-03	1.1E-04	3.4E-03
-1.5	2.6E-04	2.7E-03	2.4E-04	8.3E-03

1.2. Ternary system: AFm/AFt / Pu / L

1.2.1. Formate

Table 4. Ca equilibrium concentration (measurement error ± 5%) measured for contacting time t_{eq} = 120 days and pH = 13.3 for the HQ buffered AFm/AFt-Pu-FOR systems. AFm and AFt phases were synthesized with an initial S/L= 5 g·dm^{-3}.

Formate concentration, log([FOR]$_{tot}$/M)	Monosulfate (Ms)	Monocarbonate (Mc)	Hemicarbonate (Hc)	Ettringite (AFt)
No ligand	1.5E-03	2.2E-03	1.1E-03	9.0E-04
-4	1.4E-04	6.5E-05	1.8E-04	1.0E-04
-1.5	1.2E-04	6.9E-05	9.5E-05	1.0E-04

Table 5. Ca equilibrium concentration (measurement error ± 5%) measured for contacting time t_{eq} = 120 days and pH = 13.3 for the Sn(II) buffered AFm/AFt-Pu-FOR systems. AFm and AFt phases were synthesized with an initial S/L= 5 g·dm^{-3}.

Formate concentration, log([FOR]$_{tot}$/M)	Monosulfate (Ms)	Monocarbonate (Mc)	Hemicarbonate (Hc)	Ettringite (AFt)
No ligand	1.0E-03	1.1E-03	5.8E-04	6.1E-04
-4	1.1E-04	1.3E-04	6.8E-05	1.5E-04
-1.5	2.3E-04	6.8E-05	1.9E-04	1.1E-04

1.2.2.   Citrate

Table 6. Ca equilibrium concentration measured for contacting time t_{eq} = 120 days and pH = 13.3 for the HQ buffered AFm/AFt-Pu-CIT systems. AFm and AFt phases were synthesized with an initial S/L= 5 g·dm^{-3}.

Citrate concentration, log([CIT]$_{tot}$/M)	Monosulfate (Ms)	Monocarbonate (Mc)	Hemicarbonate (Hc	Ettringite (AFt)
No ligand	1.0E-03	1.1E-03	5.8E-04	6.1E-04
-4	1.3E-04	6.6E-05	1.8E-04	1.1E-04
-3	1.5E-04	7.6E-05	3.3E-04	1.3E-04
-2	3.2E-04	1.9E-04	3.7E-04	3.3E-04
-1.5	7.7E-04	4.4E-04	8.2E-04	8.3E-04

Table 7. Ca equilibrium concentration (measurement error ± 5%) measured for contacting time t_{eq} = 120 days and pH = 13.3 for the Sn(II) buffered AFm/AFt-Pu-CIT systems. AFm and AFt phases were synthesized with an initial S/L= 5 g·dm^{-3}.

Citrate concentration, log([CIT]$_{tot}$/M)	Monosulfate (Ms)	Monocarbonate (Mc)	Hemicarbonate (Hc)	Ettringite (AFt)
No ligand	1.5E-03	2.2E-03	1.1E-03	9.0E-04
-4	1.1E-04	6.8E-05	1.7E-04	1.2E-04
-3	1.5E-04	7.1E-05	2.3E-04	1.3E-04
-2	2.8E-04	2.0E-04	4.2E-04	2.9E-04
-1.5	6.7E-04	3.9E-04	1.3E-03	6.6E-04

1.2.3.   Gluconate

Table 8. Ca equilibrium concentration (measurement error ± 5%) measured for contacting time t_{eq} = 120 days and pH = 13.3 for the HQ buffered AFm/AFt-Pu-GLU systems. AFm and AFt phases were synthesized with an initial S/L= 5 g·dm⁻³.

Gluconate concentration, log([GLU]$_{tot}$/M)	Monosulfate (Ms)	Monocarbonate (Mc)	Hemicarbonate (Hc)	Ettringite (AFt)
No ligand	1.0E-03	1.1E-03	5.8E-04	6.1E-04
-4	1.3E-04	7.2E-05	1.8E-04	1.2E-04
-3	1.9E-04	1.7E-04	1.8E-04	1.5E-04
-2	5.5E-04	4.6E-04	3.9E-04	2.0E-04
-1.5	1.1E-03	1.3E-03	1.3E-03	4.7E-04

Table 9. Ca equilibrium concentration (measurement error ± 5%) measured for contacting time t_{eq} = 120 days and pH = 13.3 for the Sn(II) buffered AFm/AFt-Pu-GLU systems. AFm and AFt phases were synthesized with an initial S/L= 5 g·dm⁻³.

Gluconate concentration, log([GLU]$_{tot}$/M)	Monosulfate (Ms)	Monocarbonate (Mc)	Hemicarbonate (Hc)	Ettringite (AFt)
No ligand	1.5E-03	2.2E-03	1.1E-03	9.0E-04
-4	1.2E-04	1.1E-04	1.7E-04	1.1E-04
-3	1.3E-04	1.7E-04	1.8E-04	1.6E-04
-2	3.8E-04	4.6E-04	2.4E-04	1.1E-04
-1.5	1.0E-03	1.4E-03	1.2E-03	3.5E-04

Appendix 3.3

Figure 68. Time dependence of fluorescence emission decay of $[^{248}Cm(III)] = 10^{-7}$ M for C-S-H suspension with a C/S= 0.8, in absence (a) and in presence of gluconate (b, c, d), 10^{-3} M ≤ $[GLU]_{tot}$ ≤ $10^{-1.5}$ M and pH ≈ 13.3, after a contacting time of 28 days.

Figure 69. Time dependence of fluorescence emission decay of [^{248}Cm(III)] = 10^{-7} M for C-S-H suspension with a C/S= 0.8, in absence (a) and in presence of gluconate (b, c, d), 10^{-3} M ≤ [GLU]$_{tot}$ ≤ 10$^{-1.5}$ M and pH ≈ 13.3, after a contacting time of 56 days.

Figure 70. Time dependence of fluorescence emission decay of $[^{248}Cm(III)] = 10^{-7}$ M for C-S-H suspension with a C/S= 1.4, in absence (a) and in presence of gluconate (b, c, d), 10^{-3} M $\leq [GLU]_{tot} \leq 10^{-1.5}$ M and pH $\approx$ 13.3, after a contacting time of 28 days.
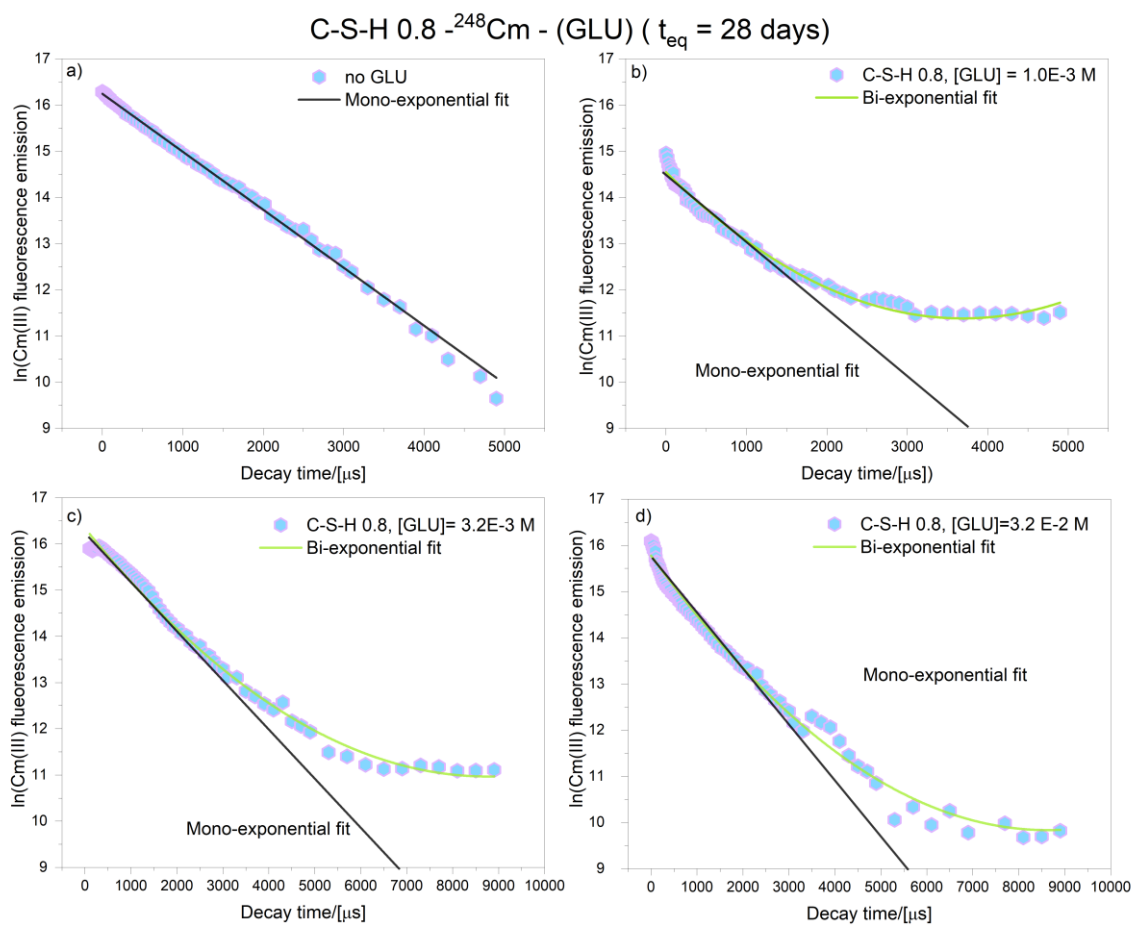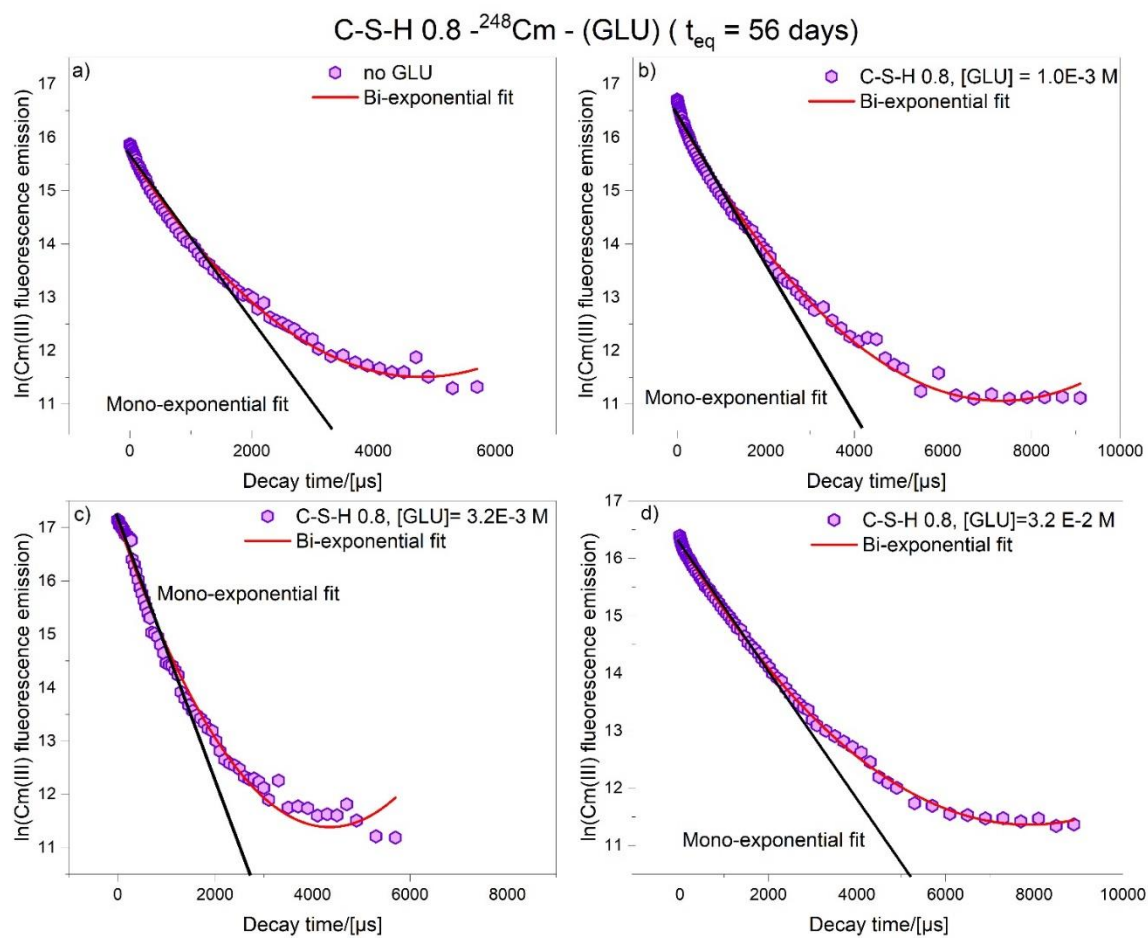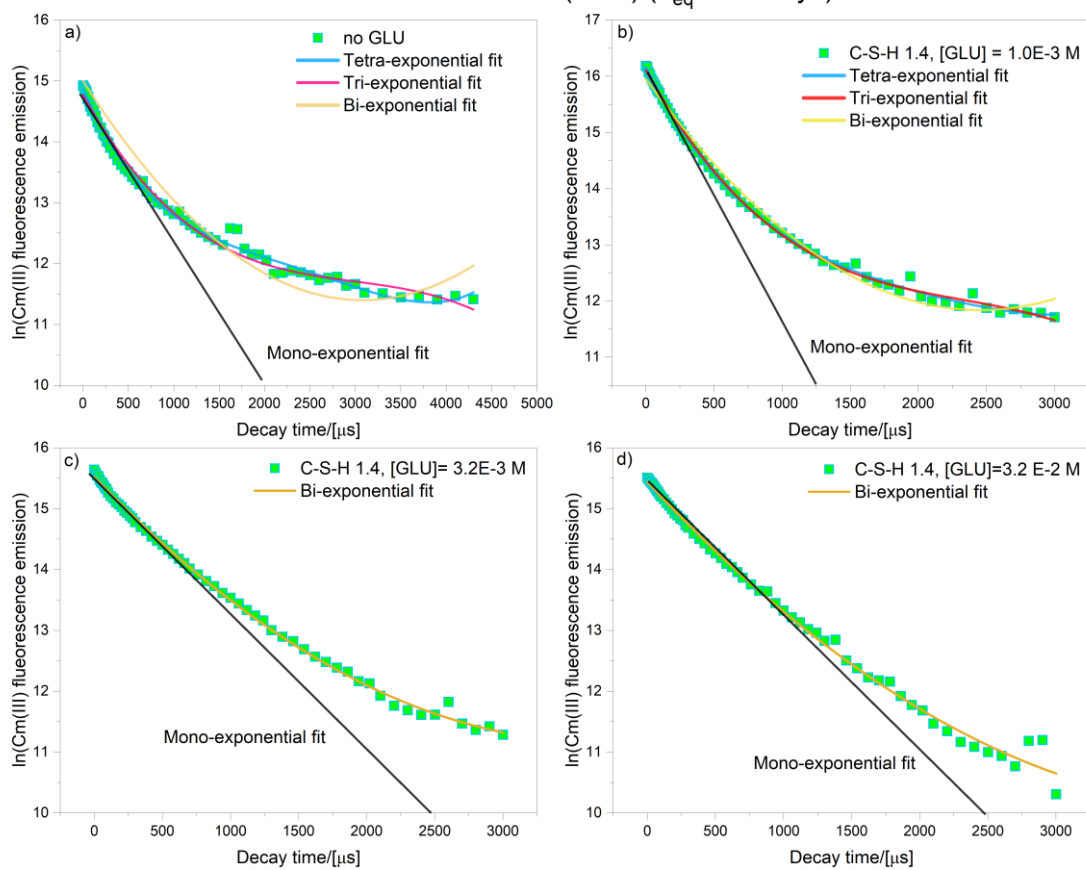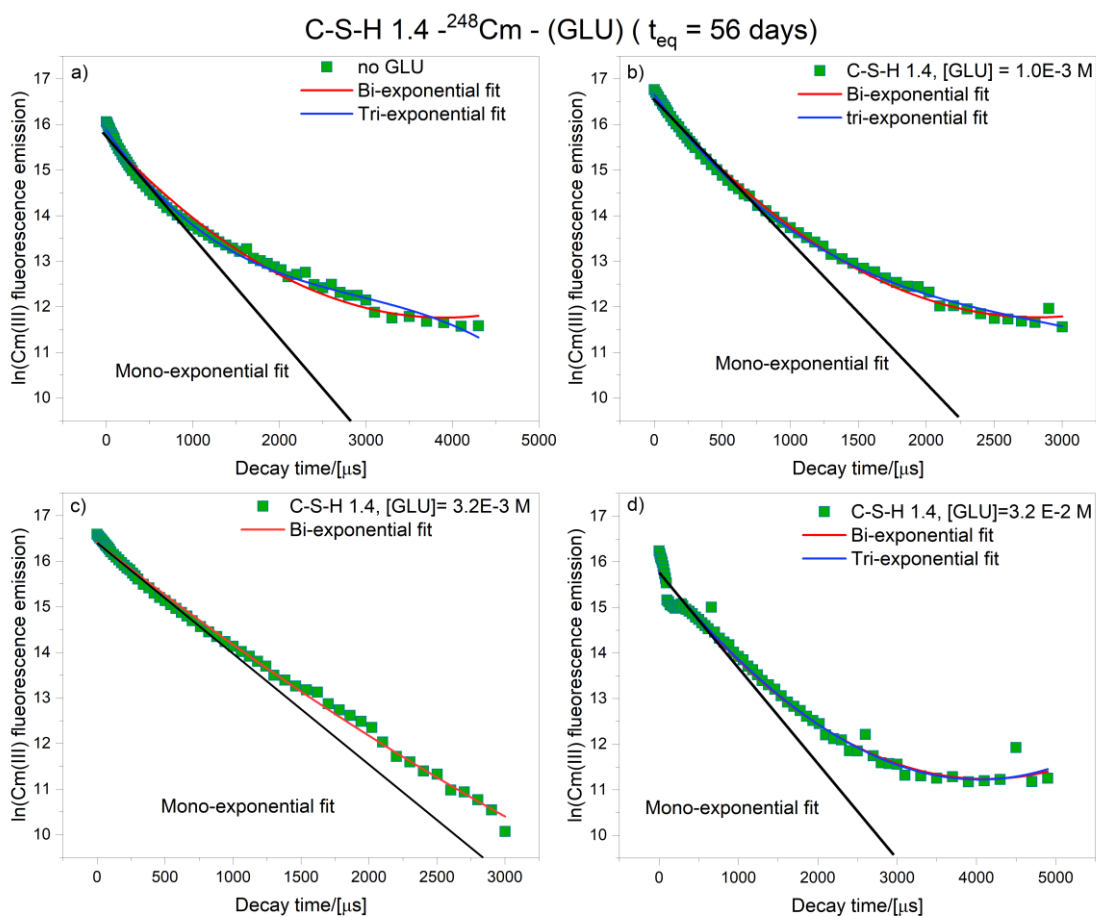
Figure 71. Time dependence of fluorescence emission decay of $[^{248}Cm(III)] = 10^{-7}$ M for C-S-H suspension with a C/S= 1.4, in absence (a) and in presence of gluconate (b, c, d), 10^{-3} M $\leq [GLU]_{tot} \leq 10^{-1.5}$ M and pH $\approx$ 13.3, after a contacting time of 56 days.

References

1.   Wieland, E., *Sorption data base for the cementitious near-field of L/ILW and ILW repositories for provisional safety analyses for SGT-E2*. 2014, Paul Scherrer Institute (PSI).

2.   NAGRA, *Waste Management Programme 2016 of the Waste Producers, Nagra Technical Report NTB 16-01E.* . 2016.

3.   Wieland, E., et al., *Sorption and diffusion studies with low molecular weight organic compounds in cementitious systems.* Applied Geochemistry, 2016. **67**: p. 101-117.

4.   Tasi, A., et al., *Plutonium retention in the isosaccharinate–cement system.* Applied Geochemistry, 2021. **126**: p. 104862.

5.   Tits, J. and E. Wieland, *Actinide Sorption by Cementitious Materials. PSI Bericht Nr. 18-02.* 2018.

6.   Wieland, E. and L.R. Van Loon, *Cementitious near-field sorption data base for performance assessment of an ILW repository in Opalinus Clay.* 2003.

7.   Jacques, D., et al., *Modelling chemical degradation of concrete during leaching with rain and soil water types.* Cement and Concrete Research, 2010. **40**(8): p. 1306-1313.

8.   IAEA, *Classification of Radioactive Waste, Safety Series No. 111-G-1.1.* 1994, Vienna.

9.   IAEA, *Classification of radioactive waste: Genaral Safety Guide GSG-1.* 2009, Vienna.

10.   Lothenbach, B. and F. Winnefeld, *Thermodynamic modelling of the hydration of Portland cement.* Cement and Concrete Research, 2006. **36**(2): p. 209-226.

11.   Glasser, F., *Application of inorganic cements to the conditioning and immobilisation of radioactive wastes*, in *Handbook of advanced radioactive waste conditioning technologies.* 2011, Elsevier. p. 67-135.

12.   Tits, J., et al., *The uptake of Eu (III) and Th (IV) by calcite under hyperalkaline conditions: The influence of gluconic and isosaccharinic acid*. 2002, Paul Scherrer Institute PSI.

13.   Nedyalkova, L., et al., *Mechanisms and thermodynamic modelling of iodide sorption on AFm phases.* Journal of Colloid and Interface Science, 2022. **608**: p. 683-691.

14.   Richardson, I.G., *The calcium silicate hydrates.* Cement and concrete research, 2008. **38**(2): p. 137-158.

15.   Lothenbach, B. and A. Nonat, *Calcium silicate hydrates: Solid and liquid phase composition.* Cement and Concrete Research, 2015. **78**: p. 57-70.

16.   Bonaccorsi, E., S. Merlino, and A.R. Kampf, *The crystal structure of tobermorite 14 Å (plombierite), a C–S–H phase.* Journal of the American Ceramic Society, 2005. **88**(3): p. 505-512.

17.   Richardson, I., *Tobermorite/jennite-and tobermorite/calcium hydroxide-based models for the structure of CSH: applicability to hardened pastes of tricalcium silicate, β-dicalcium silicate, Portland cement, and blends of Portland cement with blast-furnace slag, metakaolin, or silica fume.* Cement and concrete research, 2004. **34**(9): p. 1733-1777.

18.   Viallis-Terrisse, H., A. Nonat, and J.-C. Petit, *Zeta-potential study of calcium silicate hydrates interacting with alkaline cations.* Journal of colloid and interface science, 2001. **244**(1): p. 58-65.

19.   Labbez, C., et al., *CSH/solution interface: Experimental and Monte Carlo studies.* Cement and Concrete research, 2011. **41**(2): p. 161-168.

20.   Barbarulo, R., H. Peycelon, and S. Prene, *Experimental study and modelling of sulfate sorption on calcium silicate hydrates.* Annales de Chimie. Science des Materiaux (Paris), 2003. **28**(s1): p. S5-S10.

21.   Tits, J., et al., *Strontium binding by calcium silicate hydrates.* Journal of colloid and interface science, 2006. **300**(1): p. 78-87.

22.   Evans, D.G. and R.C. Slade, *Structural aspects of layered double hydroxides.* Layered double hydroxides, 2006: p. 1-87.

23.   Cornelis, G., et al., *Leaching mechanisms of oxyanionic metalloid and metal species in alkaline solid wastes: A review.* Applied Geochemistry, 2008. **23**(5): p. 955-976.

24.   Tits, J., et al., *Uptake of Cm (III) and Eu (III) by calcium silicate hydrates: a solution chemistry and time-resolved laser fluorescence spectroscopy study.* Environmental science & technology, 2003. **37**(16): p. 3568-3573.

25.   Stumpf, T., et al., *Uptake of trivalent actinides (curium (III)) by hardened cement paste: a time-resolved laser fluorescence spectroscopy study.* Journal of colloid and interface science, 2004. **276**(1): p. 118-124.

26.   Mandaliev, P., et al., *Macro-and microspectroscopic study of Nd (III) uptake mechanisms in hardened cement paste.* Environmental science & technology, 2009. **43**(21): p. 8462-8468.

27.   Mandaliev, P., et al., *Uptake of Eu (III) by 11 Å tobermorite and xonotlite: a TRLFS and EXAFS study.* Geochimica et Cosmochimica Acta, 2011. **75**(8): p. 2017-2029.

28.   Gaona, X., et al., *Uptake of Np (IV) by C–S–H phases and cement paste: An EXAFS study.* Environmental science & technology, 2011. **45**(20): p. 8765-8771.

29.   Tits, J., et al. *Influence of the redox state on the neptunium sorption by cementitious materials.* in *3rd Annual Workshop Proceedings of the Collaborative Project" Redox Phenomena Controlling Systems"(7th EC FP CP RECOSY): KIT Scientific Publishing, Karlsruhe.* 2011.

30.   Allmann, R., *Refinement of the hybrid layer structure $(Ca_2Al(OH)_6)^+.12SO_4. 3H_2O)$.* Neues Jahrbuch für Mineralogie, 1977. **3**.

31.   François, M., G. Renaudin, and O. Evrard, *A cementitious compound with composition 3CaO. Al2O3. CaCO3. 11H2O.* Acta Crystallographica Section C: Crystal Structure Communications, 1998. **54**(9): p. 1214-1217.

32.   Renaudin, G. and M. Francois, *The lamellar double-hydroxide (LDH) compound with composition 3CaO. Al2O3. Ca (NO3) 2.10 H2O.* Acta Crystallographica Section C: Crystal Structure Communications, 1999. **55**(6): p. 835-838.

33.   Taylor, H.F., *Cement chemistry.* Vol. 2. 1997: Thomas Telford London.

34.   Mesbah, A., et al., *Crystal Structures and Phase Transition of Cementitious Bi-Anionic AFm-(Cl−, CO32−) Compounds.* Journal of the American Ceramic Society, 2011. **94**(1): p. 261-268.

35.   Pöllman, H., *Minelarogisch-Kristallographische Untersuchugen an Hydratationsprodukten der Aluminatphase hydraulischer Bindemittel (Teil 1)*, in *Naturwissenschaftlichen Fakultät.* 1989, Friedrich-Alexander Universität: Erlagen-Nürnberg. p. 288.

36.   Baquerizo, L.G., et al., *Methods to determine hydration states of minerals and cement hydrates.* Cement and Concrete Research, 2014. **65**: p. 85-95.

37.   Baquerizo, L.G., et al., *Hydration states of AFm cement phases.* Cement and Concrete Research, 2015. **73**: p. 143-157.

38.   Zhang, M. and E.J. Reardon, *Removal of B, Cr, Mo, and Se from wastewater by incorporation into hydrocalumite and ettringite.* Environmental science & technology, 2003. **37**(13): p. 2947-2952.

39.   Ma, B., et al., *Evidence of multiple sorption modes in layered double hydroxides using Mo as structural probe.* Environmental science & technology, 2017. **51**(10): p. 5531-5540.

40.   Ma, B., et al., *Selenite uptake by Ca–Al LDH: a description of intercalated anion coordination geometries.* Environmental science & technology, 2018. **52**(3): p. 1624-1632.

41.   Aimoz, L., et al., *Structural insight into iodide uptake by AFm phases.* Environmental science & technology, 2012. **46**(7): p. 3874-3881.

42.   Momma, K. and F. Izumi, *VESTA: a three-dimensional visualization system for electronic and structural analysis.* Journal of Applied crystallography, 2008. **41**(3): p. 653-658.

43.   Perkins, R.B. and C.D. Palmer, *Solubility of ettringite (Ca6 [Al (OH) 6] 2 (SO4) 3· 26H2O) at 5–75° C.* Geochimica et Cosmochimica Acta, 1999. **63**(13-14): p. 1969-1980.

44.   Baur, I. and C.A. Johnson, *The solubility of selenate-AFt (3CaO· Al2O3· 3CaSeO4· 37.5 H2O) and selenate-AFm (3CaO· Al2O3· CaSeO4· xH2O).* Cement and concrete Research, 2003. **33**(11): p. 1741-1748.

45.   Chrysochoou, M. and D. Dermatas, *Evaluation of ettringite and hydrocalumite formation for heavy metal immobilization: Literature review and experimental study.* Journal of hazardous materials, 2006. **136**(1): p. 20-33.

46.   Möschner, G., et al., *Solid solution between Al-ettringite and Fe-ettringite (Ca6 [Al1− xFex (OH) 6] 2 (SO4) 3· 26H2O).* Cement and Concrete Research, 2009. **39**(6): p. 482-489.

47.   Dauzères, A., et al., *Impact of a 70° C temperature on an ordinary Portland cement paste/claystone interface: An in situ experiment.* Cement and Concrete Research, 2016. **83**: p. 164-178.

48.   Kosakowski, G., et al., *Geochemical evolution of the L/ILW near-field.* 2014, Paul Scherrer Institute (PSI).

49. Glaus, M., et al., *Degradation of cellulosic materials under the alkaline conditions of a cementitious repository for low and intermediate level radioactive waste: Part I: Identification of degradation products.* Analytica Chimica Acta, 1999. **398**(1): p. 111-122.

50. Glaus, M.A. and L.R. Van Loon, *Degradation of cellulose under alkaline conditions: new insights from a 12 years degradation study.* Environmental Science & Technology, 2008. **42**(8): p. 2906-2911.

51. Van Loon, L.R. and M.A. Glaus, *Experimental and theoretical studies on alkaline degradation of cellulose and its impact on the sorption of radionuclides.* 1998.

52. Christensen, B.J. and H. Farzam, *Chemical Admixtures.* Significance of Tests and Properties of Concrete and Concrete-Making Materials, 2006.

53. Wang, N., et al., *Effects of sodium citrate and citric acid on the properties of magnesium oxysulfate cement.* Construction and Building Materials, 2018. **169**: p. 697-704.

54. Suh, J.-I., et al., *The cation-dependent effects of formate salt additives on the strength and microstructure of CaO-activated fly ash binders.* Construction and Building Materials, 2019. **194**: p. 92-101.

55. Popovics, S., *Concrete materials: Properties, specifications, and testing.* 1992: William Andrew.

56. Milestone, N., *Hydration of tricalcium silicate in the presence of lignosulfonates, glucose, and sodium gluconate.* Journal of the American ceramic society, 1979. **62**(7-8): p. 321-324.

57. Banfill, P.G., *Precipitation of calcium hydroxide in the presence of organic compounds.* Journal of materials science letters, 1986. **5**(1): p. 33-34.

58. Ludwig, U. and C. Urrutia, *Zum mechanismus der Wirkung von Saccharose auf das Erstarren und Erhärten von Zementen.* ZKG international, 1989. **42**(8): p. 431-436.

59. Luke, K. and G. Luke, *Effect of sucrose on retardation of Portland cement.* Advances in cement research, 2000. **12**(1): p. 9-18.

60. Wieland, E. and W. Hummel, *Formation and stability of 14C-containing organic compounds in alkaline iron-water systems: preliminary assessment based on a literature survey and thermodynamic modelling.* Mineralogical Magazine, 2015. **79**(6): p. 1275-1286.

61. Kaneko, S., et al., *A study on the chemical forms and migration behavior of carbon-14 leached from the simulated hull waste in the underground condition.* MRS Online Proceedings Library (OPL), 2002. **757**.

62. Noshita, K., L. Johnson, and B. Schwyn. *Fundamental study of C-14 chemical form under irradiated condition.* in *Proceedings of a Nagra/RWMC Workshop on the Release and Transport of C-14 in Repository Environments.* 2008. Nagra Working Report NAB.

63. Sasoh, M., L. Johnson, and B. Schwyn. *Investigations of distribution coefficients for C-14 from activated metal.* in *Proceedings of a Nagra/RWMC Workshop on the Release and Transport of C-14 in Repository Environments.* 2008. Nagra Working Report NAB.

64. Sasoh, M., L. Johnson, and B. Schwyn. *Study on chemical behaviour of organic C-14 under alkaline conditions.* in *Proceedings of a Nagra/RWMC Workshop on the Release and Transport of C-14 in Repository Environments.* 2008. Nagra Working Report NAB.

65. Sasoh, M., *The study of the chemical forms of C-14 released from activated metals.* Nagra Arbeitsbericht, 2008: p. 08-22.

66. Hardy, L.I. and R.W. Gillham, *Formation of hydrocarbons from the reduction of aqueous CO2 by zero-valent iron.* Environmental science & technology, 1995. **30**(1): p. 57-65.

67. Campbell, T.J., et al., *Trichloroethylene and tetrachloroethylene reduction in a metallic iron–water-vapor batch system.* Environmental Toxicology and Chemistry: An International Journal, 1997. **16**(4): p. 625-630.

68. Deng, B., T.J. Campbell, and D.R. Burris, *Hydrocarbon formation in metallic iron/water systems.* Environmental Science & Technology, 1997. **31**(4): p. 1185-1190.

69. Agrawal, A., et al., *Effects of carbonate species on the kinetics of dechlorination of 1, 1, 1-trichloroethane by zero-valent iron.* Environmental Science & Technology, 2002. **36**(20): p. 4326-4333.

70. Gebler, S., *Evaluation of Calcium Formate and Sodium Formate as Accelerating Admixtures for Portland Cement Concrete.* ACI Journal Proceedings, 1983. **80**(5).

71. Myrdal, R., *Accelerating admixtures for concrete. State of the art.* 2007.

72. Vdovin, E. and V. Stroganov. *Modification of cement-bound mixtures with sodium formate additives for the construction of pavement bases at low air temperatures.* in *IOP Conference Series: Materials Science and Engineering.* 2020. IOP Publishing.

73. Wang, Y., et al., *Effect of calcium formate on the compressive strength, and hydration process of cement composite containing fly ash and slag.* Journal of Building Engineering, 2022. **50**: p. 104133.

74. Pacanovsky, J.T., et al., *Hydration control of cementitious sysstems.* 1997, Sandoz Ltd., Basel, Switzerland.

75. Ma, S., et al., *Influence of sodium gluconate on the performance and hydration of Portland cement.* Construction and Building Materials, 2015. **91**: p. 138-144.

76. Zajac, M., et al., *Effect of retarders on the early hydration of calcium-sulpho-aluminate (CSA) type cements.* Cement and Concrete Research, 2016. **84**: p. 62-75.

77. von Daake, H. and D. Stephan, *Adsorption kinetics of retarding admixtures on cement with time controlled addition.* Cement and Concrete Research, 2017. **102**: p. 119-126.

78. Möschner, G., et al., *Influence of citric acid on the hydration of Portland cement.* Cement and Concrete Research, 2009. **39**(4): p. 275-282.

79. Wieland, E., et al., *Influence of superplasticizers on the long-term properties of cement pastes and possible impact on radionuclide uptake in a cement-based repository for radioactive waste.* Applied Geochemistry, 2014. **49**: p. 126-142.

80. Parr, R.G. and R.G. Pearson, *Absolute hardness: companion parameter to absolute electronegativity.* Journal of the American chemical society, 1983. **105**(26): p. 7512-7516.

81. Pearson, R.G., *Hard and soft acids and bases—the evolution of a chemical concept.* Coordination chemistry reviews, 1990. **100**: p. 403-425.

82. Gresh, N., *Energetics of Zn2+ binding to a series of biologically relevant ligands: A molecular mechanics investigation grounded on ab initio self-consistent field supermolecular computations.* Journal of computational chemistry, 1995. **16**(7): p. 856-882.

83. Farfán, P., et al., *Dimers of formic acid: Structures, stability, and double proton transfer.* The Journal of Chemical Physics, 2017. **147**(4): p. 044312.

84. Hartmann, A., M. Khakhutov, and J.-C. Buhl, *Hydrothermal synthesis of CSH-phases (tobermorite) under influence of Ca-formate.* Materials Research Bulletin, 2014. **51**: p. 389-396.

85. Hewlet, P., *Lea's chemistry of cement and concrete.* London: Arnold, 1998.

86. Heikal, M., *Effect of calcium formate as an accelerator on the physicochemical and mechanical properties of pozzolanic cement pastes.* Cement and Concrete Research, 2004. **34**(6): p. 1051-1056.

87. Lindgård, J., et al., *Alkali–silica reactions (ASR): Literature review on parameters influencing laboratory performance testing.* Cement and Concrete research, 2012. **42**(2): p. 223-243.

88. Hummel, W., et al., *Chemical thermodynamics of compounds and complexes of U, Np, Pu, Am, Tc, Se, Ni and Zr with selected organic ligands*, ed. F.J. Mompean, M. Illemassène, and J. Perrone. Vol. 9. 2005: Elsevier Amsterdam.

89. Strizhakova, N., K. Karlysheva, and I. Sheka, *Citrate complexes of zirconium.* UKRAINSKII KHIMICHESKII ZHURNAL, 1978. **44**(3): p. 227-231.

90. Baker, E.N., et al., *Chelation of nickel (II) by citrate. The crystal structure of a nickel–citrate complex, K2 [Ni (C6H5O7)(H2O) 2]·4H2O.* Inorganica Chimica Acta, 1983. **78**: p. 281-285.

91. Matzapetakis, M., et al., *Synthesis, spectroscopic and structural characterization of the first mononuclear, water soluble iron− citrate complex,(NH4) 5Fe (C6H4O7) 2 ⊙ 2H2O.* Journal of the American Chemical Society, 1998. **120**(50): p. 13266-13267.

92. Kaduk, J.A., *Crystal structures of tricalcium citrates.* Powder Diffraction, 2018. **33**(2): p. 98-107.

93. Skorik, N. and V. Kumok, *Solubility products of some metal citrates.* Zhurn Neorg Khim, 1969. **14**: p. 98-101.

94. Apelblat, A., *Enthalpies of solution of citrates and hydrogen citrates of lithium, sodium, and potassium.* The Journal of Chemical Thermodynamics, 1994. **26**(1): p. 49-51.

95. De Robertis, A., A. Gianguzza, and S. Sammartano, *Solubility of some calcium-carboxylic ligand complexes in aqueous solution.* Talanta, 1995. **42**(11): p. 1651-1662.

96.   Ciavatta, L., G. De Tommaso, and M. Iuliano, *The solubility of calcium citrate hydrate in sodium perchlorate solutions.* Analytical letters, 2001. **34**(6): p. 1053-1062.

97.   Schwarz, W., *Novel cement matrices by accelerated hydration of the ferrite phase in Portland cement via chemical activation: kinetics and cementitious properties.* Advanced Cement Based Materials, 1995. **2**(5): p. 189-200.

98.   Burris, L.E. and K.E. Kurtis, *Influence of set retarding admixtures on calcium sulfoaluminate cement hydration and property development.* Cement and Concrete Research, 2018. **104**: p. 105-113.

99.   Rottstegge, J., M. Wilhelm, and H.W. Spiess, *Solid state NMR investigations on the role of organic admixtures on the hydration of cement pastes.* Cement and Concrete Composites, 2006. **28**(5): p. 417-426.

100.   Singh, N., A. Singh, and S.P. Singh, *Effect of citric acid on the hydration of Portland cement.* Cement and Concrete Research, 1986. **16**(6): p. 911-920.

101.   Kastiukas, G., et al., *Effects of lactic and citric acid on early-age engineering properties of Portland/calcium aluminate blended cements.* Construction and Building Materials, 2015. **101**: p. 389-395.

102.   Xu, L., et al., *Effects of citric acid on the rheology, hydration and strength development of alkali aluminosilicate cement.* Advances in Cement Research, 2018. **30**(2): p. 75-82.

103.   Nguyen, H., et al., *Ettringite-based binder from ladle slag and gypsum–The effect of citric acid on fresh and hardened state properties.* Cement and Concrete Research, 2019. **123**: p. 105800.

104.   Singh, N.B., A.K. Singh, and S.P. Singh, *Hydration Study of the System Ca3Al2O6–CaSO4· 2H2O–Ca (OH) 2–H2O with and without Citric Acid.* Journal of the American Ceramic Society, 1990. **73**(10): p. 3063-3068.

105.   Castro-Cabado, M., A. Casado, and J. San Román, *Effect of CaO in the thermal crosslinking of maltodextrin and citric acid: A cooperative action of condensation and ionic interactions.* Journal of Applied Polymer Science, 2016. **133**(46).

106.   Jolicoeur, C. and M.-A. Simard, *Chemical admixture-cement interactions: Phenomenology and physico-chemical concepts.* Cement and Concrete Composites, 1998. **20**(2): p. 87-101.

107.   Ramachandran, S., et al., *Gluconic acid: properties, applications and microbial production.* Food Technology & Biotechnology, 2006. **44**(2).

108.   Dewick, P.M., *Medicinal natural products: a biosynthetic approach.* 2002: John Wiley & Sons.

109.   Pecsok, R.L. and R.S. Juvet Jr, *The gluconate complexes. I. Copper gluconate complexes in strongly basic media1.* Journal of the American Chemical Society, 1955. **77**(1): p. 202-206.

110.   Pecsok, R.L. and R.S. Juvet Jr, *The Gluconate Complexes. III. The Lead Gluconate System1.* Journal of the American Chemical Society, 1956. **78**(16): p. 3967-3972.

111.   Pecsok, R.L. and J. Sandera, *The gluconate complexes. II. The ferric-gluconate system.* Journal of the American Chemical Society, 1955. **77**(6): p. 1489-1494.

112.   Pecsok, R.L. and J. Sandera, *The Gluconate Complexes. IV. The Cadmium-Gluconate System.* Journal of the American Chemical Society, 1957. **79**(15): p. 4069-4072.

113.   Coccioli, F. and M. Vicedomini, *On the protonation of gluconate ions and the complex formation with lead (II) in acid solution.* Journal of Inorganic and Nuclear Chemistry, 1978. **40**(12): p. 2103-2105.

114.   Escandar, G.M. and L.F. Sala, *Complexes of Cu (II) with D-aldonic and D-alduronic acids in aqueous solution.* Canadian Journal of Chemistry, 1992. **70**(7): p. 2053-2057.

115.   Escandar, G.M., L.F. Sala, and M.G. Sierra, *Complexes of cobalt (II) and nickel (II) with D-aldonic and D-alduronic acids in aqueous solution.* Polyhedron, 1994. **13**(1): p. 143-150.

116.   Zhang, Z., et al., *Lactonization and protonation of gluconic acid: a thermodynamic and kinetic study by potentiometry, NMR and ESI-MS.* Journal of Solution Chemistry, 2007. **36**(10): p. 1187-1200.

117.   Zhang, Z., et al., *Complexation of uranium (VI) by gluconate in acidic solutions: a thermodynamic study with structural analysis.* Inorganic chemistry, 2009. **48**(8): p. 3814-3824.

118.   Gargalovic, P.S., et al., *Identification of inflammatory gene modules based on variations of human endothelial cell responses to oxidized lipids.* Proceedings of the National Academy of Sciences, 2006. **103**(34): p. 12741-12746.

119. Kutus, B., et al., *Recent advances in the aqueous chemistry of the calcium (II)-gluconate system–Equilibria, structure and composition of the complexes forming in neutral and in alkaline solutions.* Coordination Chemistry Reviews, 2020. **417**: p. 213337.

120. Pallagi, A., et al., *Multinuclear complex formation between Ca (II) and gluconate ions in hyperalkaline solutions.* Environmental science & technology, 2014. **48**(12): p. 6604-6611.

121. Pallagi, A., et al., *Complexation of Al (iii) with gluconate in alkaline to hyperalkaline solutions: Formation, stability and structure.* Dalton Transactions, 2013. **42**(37): p. 13470-13476.

122. Mitchell, R.E. and F.R. Duke, *Kinetics and equlibrium consents of the gluconic acid-gluconolactone system.* Annals of the New York Academy of Sciences, 1970. **172**(7): p. 131-138.

123. Kutus, B., et al., *The acidity and self-catalyzed lactonization of l-gulonic acid: Thermodynamic, kinetic and computational study.* Carbohydrate research, 2018. **467**: p. 14-22.

124. Pallagi, A., et al., *Multinuclear complex formation in aqueous solutions of Ca (II) and heptagluconate ions.* Dalton Transactions, 2013. **42**(23): p. 8460-8467.

125. Kutus, B., et al., *Configuration-dependent complex formation between Ca (II) and sugar carboxylate ligands in alkaline medium: Comparison of L-gulonate with D-gluconate and D-heptaguconate.* Carbohydrate research, 2018. **460**: p. 34-40.

126. Pallagi, A., et al., *Multinuclear NMR and molecular modelling investigations on the structure and equilibria of complexes that form in aqueous solutions of Ca2+ and gluconate.* Carbohydrate research, 2010. **345**(13): p. 1856-1864.

127. Escandar, G.M., et al., *Interaction of divalent metal ions withd-gluconic acid in the solid phase and aqueous solution.* Polyhedron, 1996. **15**(13): p. 2251-2261.

128. Gajda, T., et al., *Coordination chemistry of polyhydroxy acids: role of the hydroxy groups.* Inorganica chimica acta, 1998. **275**: p. 130-140.

129. Taga, T., Y. Kuroda, and M. Ohashi, *Structures of lanthanoid complexes of glyceric acid, gluconic acid, and lactobionic acid from the lanthanoid-induced 1H NMR shifts: pH dependence of the lanthanoid-substrate equilibria.* Bulletin of the Chemical Society of Japan, 1978. **51**(8): p. 2278-2282.

130. Tajmir-Riahi, H., *coordination chemistry of vitamin c. part I. Interaction of L-Ascorbic Acid with Alkaline Earth Metal Ions in the Crystalline Solid and Aqueous Solution.* Journal of inorganic biochemistry, 1990. **40**(2): p. 181-188.

131. Kutus, B., et al., *Formation of mono-and binuclear neodymium (III)–gluconate complexes in aqueous solutions in the pH range of 2–8.* Dalton Transactions, 2017. **46**(18): p. 6049-6058.

132. Nedyalkova, L., et al., *Sorption Experiments with HTO, 36-Cl, 125-I and 14-C Labeled Formate on Aged Cement Matrices Retrieved from Long-term In-situ Rock Laboratory Experiments.* Journal of Advanced Concrete Technology, 2021. **19**(7): p. 811-829.

133. Pointeau, I., N. Coreau, and P.E. Reiller, *Uptake of anionic radionuclides onto degraded cement pastes and competing effect of organic ligands.* Radiochimica Acta, 2008. **96**(6): p. 367-374.

134. Glaus, M.A., A. Laube, and L.R. Van Loon, *Solid–liquid distribution of selected concrete admixtures in hardened cement pastes.* Waste Management, 2006. **26**(7): p. 741-751.

135. Van Loon, L., et al., *Sorption of isosaccharinic acid, a cellulose degradation product, on cement.* Environmental science & technology, 1997. **31**(4): p. 1243-1245.

136. Androniuk, I., et al., *Adsorption of gluconate and uranyl on CSH phases: Combination of wet chemistry experiments and molecular dynamics simulations for the binary systems.* Physics and Chemistry of the Earth, Parts A/B/C, 2017. **99**: p. 194-203.

137. Nalet, C. and A. Nonat, *Ionic complexation and adsorption of small organic molecules on calcium silicate hydrate: Relation with their retarding effect on the hydration of C3S.* Cement and Concrete Research, 2016. **89**: p. 97-108.

138. Bouzouaid, L., et al., *Gluconate and hexitols effects on CSH solubility.* Cement and Concrete Research, 2022. **160**: p. 106894.

139. Choppin, G.R. and E.N. Rizkalla, *Solution chemistry of actinides and lanthanides.* Handbook on the physics and chemistry of rare earths, 1994. **18**: p. 559-590.

140. Altmaier, M., X. Gaona, and T. Fanghänel, *Recent advances in aqueous actinide chemistry and thermodynamics.* Chemical reviews, 2013. **113**(2): p. 901-943.

141. Pearson, R.G., *Hard and soft acids and bases.* Journal of the American Chemical society, 1963. **85**(22): p. 3533-3539.

142. Freeman, A. and D. Koelling, *The Actinides, ed. AJ Freeman and JB Darby*. 1974, Academic Press, New York.

143. Freeman, A., *f-Electrons in solids: Electronic structure and properties of actinides and rare-earths.* Physica B+ C, 1980. **102**(1-3): p. 3-11.

144. Johansson, B., et al., *Presence and character of the 5f electrons in the actinide metals.* Physica B+ C, 1980. **102**(1-3): p. 12-21.

145. Sullivan, J., et al., *Pulse radiolysis studies on the hydroxyl radical-induced oxidation of thiolatometal complexes.* Inorganic Chemistry, 1976. **15**(11): p. 2864-2868.

146. Propst, R. and M. Hyder, *Electrochemistry of berkelium in acidic aqueous solution.* Journal of Inorganic and Nuclear Chemistry, 1970. **32**(7): p. 2205-2216.

147. Nugent, L., et al., *Electron-transfer and f→ d absorption bands of some lanthanide and actinide complexes and the standard (III–IV) oxidation potentials for each member of the lanthanide and actinide series.* Journal of Inorganic and Nuclear Chemistry, 1971. **33**(8): p. 2503-2530.

148. Neck, V., M. Altmaier, and T. Fanghänel, *Solubility of plutonium hydroxides/hydrous oxides under reducing conditions and in the presence of oxygen.* Comptes Rendus Chimie, 2007. **10**(10-11): p. 959-977.

149. Wieland, E., et al., *Interaction of Eu (III) and Th (IV) with sulfate-resisting Portland cement.* MRS Online Proceedings Library (OPL), 1997. **506**: p. 573.

150. Mandaliev, P., et al., *Mechanisms of Nd (III) uptake by 11 Å tobermorite and xonotlite.* Applied geochemistry, 2010. **25**(6): p. 763-777.

151. Tits, J., et al., *The uptake of Eu (III) and Th (IV) by cement-type minerals in the alkaline disturbed zone of a nuclear waste repository.* Proc 6th Int Cong Appl Mineralogy, Göttingen, Germany, 2000. **2**: p. 691-694.

152. Mandaliev, P., et al., *EXAFS study of Nd (III) uptake by amorphous calcium silicate hydrates (C–S–H).* Journal of Colloid and Interface Science, 2010. **342**(1): p. 1-7.

153. Shannon, R.D., *Revised effective ionic radii and systematic studies of interatomic distances in halides and chalcogenides.* Acta crystallographica section A: crystal physics, diffraction, theoretical and general crystallography, 1976. **32**(5): p. 751-767.

154. Kimura, T. and G.R. Choppin, *Luminescence study on determination of the hydration number of Cm (III).* Journal of Alloys and Compounds, 1994. **213**: p. 313-317.

155. Kim, J., *Chemical behavior of transuranic elements in natural aquatic systems.* Handbook on the Physics and Chemistry of the Actinides, 1986. **4**: p. 413-455.

156. Berner, U., *Project Opalinus Clay--Radionuclide concentration limits in the near-field of a repository for spent fuel and vitrified high-level waste*. 2002, Paul Scherrer Institute PSI.

157. Guillaumont, R., et al., *Update on the chemical thermodynamics of uranium, neptunium, plutonium, americium and technetium, chemical thermodynamics.* Nucl. Energy Agency, Elsevier Sci. Publ, 2003. **918**.

158. Neck, V., et al., *Thermodynamics of trivalent actinides and neodymium in NaCl, MgCl2, and CaCl2 solutions: Solubility, hydrolysis, and ternary Ca-M (III)-OH complexes.* Pure and Applied Chemistry, 2009. **81**(9): p. 1555-1568.

159. Rojo, H., et al., *Complexation of Nd (III)/Cm (III) with gluconate in alkaline NaCl and CaCl2 solutions: Solubility, TRLFS and DFT studies.* Applied Geochemistry, 2021. **126**: p. 104864.

160. Herm, M., et al., *Solubility and spectroscopic study of AnIII/LnIII in dilute to concentrated Na–Mg–Ca–Cl–NO3 solutions.* Pure and Applied Chemistry, 2015. **87**(5): p. 487-502.

161. Baston, G., M. Cowper, and T. Marshall, *Sorption properties of aged cements.* Mineralogical Magazine, 2012. **76**(8): p. 3411-3423.

162. Wieland, E. and L. Van Loon, *Near-field sorption database for performance assessment of a ILW repository in Opalinus clay and crystalline host rock.* PSI Report and Nagra Technical Report NTB, 2002.

163. Höglund, S., et al., *Sorption of some fission products and actinides in concrete systems.* MRS Online Proceedings Library (OPL), 1985. **50**.

164. Allard, B., L. Eliasson, and K. Andersson, *Sorption of Cs, I, and actinides in concrete systems.* 1984, Swedish Nuclear Fuel and Waste Management Co.

165. Aggarwal, S., M. Angus, and J. Ketchen, *Sorption of radionuclides onto specific mineral phases present in repository cements.* Report AEA Technology NSS, 2000. **312**(1).

166. Pointeau, I., et al., *Am (III), Zr (IV), Pu (IV), Nb (V), U (VI) et Tc (IV) par les matériaux cimentaires dégradés.* CEA report, 2004: p. 03-037.

167. Baston, G., et al., *Sorption of plutonium and americium on repository, backfill and geological materials relevant to the JNFL low-level radioactive waste repository at Rokkasho-Mura.* MRS Online Proceedings Library (OPL), 1994. **353**.

168. Ochs, M., D. Mallants, and L. Wang, *Radionuclide and metal sorption on cement and concrete.* Vol. 2. 2016: Springer.

169. Tasi, A., et al., *Redox behavior and solubility of plutonium under alkaline, reducing conditions.* Radiochimica Acta, 2018. **106**(4): p. 259-279.

170. Grenthe, I., et al., *Second update on the chemical thermodynamics of uranium, neptunium, plutonium, americium and technetium. Chemical thermodynamics volume 14.* 2020, Organisation for Economic Co-Operation and Development.

171. Altmaier, M., Fellhauer, D., Gaona, X., Yancintas, E. , *Assessment of Np(IV) and U(IV) as Improved Analogs for Pu(IV) in High Ionic. Strength Brine Systems.* 2017, Karlsruhe Institute of Technology, KIT.

172. Altmaier, M., V. Neck, and T. Fanghänel, *Solubility of Zr (IV), Th (IV) and Pu (IV) hydrous oxides in CaCl2 solutions and the formation of ternary Ca-M (IV)-OH complexes.* Radiochimica Acta, 2008. **96**(9-11): p. 541-550.

173. Rai, D., et al., *Thermodynamic model for ThO2 (am) solubility in alkaline silica solutions.* Journal of solution chemistry, 2008. **37**(12): p. 1725-1746.

174. Rand, M., *Chemical thermodynamics of thorium.* 2008.

175. Choppin, G.R., *Structure and thermodynamics of lanthanide and actinide complexes in solution.* Pure and Applied Chemistry, 1971. **27**(1-2): p. 23-42.

176. Choppin, G., P. Thakur, and J. Mathur, *Complexation thermodynamics and structural aspects of actinide–aminopolycarboxylates.* Coordination chemistry reviews, 2006. **250**(7-8): p. 936-947.

177. Colàs, E., et al., *The effect of gluconate and EDTA on thorium solubility under simulated cement porewater conditions.* Journal of Solution Chemistry, 2013. **42**(8): p. 1680-1690.

178. DiBlasi, N.A., et al., *Impact of Ca (II) on the aqueous speciation, redox behavior, and environmental mobility of Pu (IV) in the presence of EDTA.* Science of The Total Environment, 2021. **783**: p. 146993.

179. Thakur, P., et al., *Thermodynamics and the structural aspects of the ternary complexes of Am (III), Cm (III) and Eu (III) with Ox and EDTA+ Ox.* Dalton transactions, 2006(40): p. 4829-4837.

180. Felmy, A.R., et al., *The aqueous complexation of thorium with citrate under neutral to basic conditions.* Radiochimica Acta, 2006. **94**(4): p. 205-212.

181. Colàs Anguita, E., *Complexation of Th (IV) and U (VI) by polyhydroxy and polyamino carboxylic acids.* 2014, Universitat Politècnica de Catalunya (UPC).

182. Greenfield, B., et al., *The effects of the products from the anaerobic degradation of cellulose on the solubility and sorption of radioelements in the near field.* Nirex report NSS, 1997. **376**.

183. Rai, D., L. Rao, and D.A. Moore, *The influence of isosaccharinic acid on the solubility of Np (IV) hydrous oxide.* Radiochimica Acta, 1998. **83**(1): p. 9-14.

184. Rai, D., et al., *Comprehensive thermodynamic model applicable to highly acidic to basic conditions for isosaccharinate reactions with Ca (II) and Np (IV).* Journal of Solution Chemistry, 2003. **32**(8): p. 665-689.

185. Warwick, P., et al., *Stability constants of uranium (IV)-α-isosaccharinic acid and gluconic acid complexes.* Radiochimica Acta, 2004. **92**(12): p. 897-902.

186. Tasi, A., et al., *Thermodynamic description of the plutonium–α–d–isosaccharinic acid system ii: Formation of quaternary Ca (II)–Pu (IV)–OH–ISA complexes.* Applied Geochemistry, 2018. **98**: p. 351-366.

187. Boggs, M.A., et al., *Complexation of Tc (IV) with acetate at varying ionic strengths.* 2010.

188. Fröhlich, D.R., A. Skerencak-Frech, and P.J. Panak, *Complex formation of Cm (III) with formate studied by time-resolved laser fluorescence spectroscopy.* Applied Geochemistry, 2015. **61**: p. 312-317.

189. Fröhlich, D.R., A. Skerencak-Frech, and P.J. Panak, *A spectroscopic study on the formation of Cm (III) acetate complexes at elevated temperatures.* Dalton Transactions, 2014. **43**(10): p. 3958-3965.

190. Francis, A.J., C.J. Dodge, and J. Gillow, *Biotransformation of plutonium complexed with citric acid.* Radiochimica Acta, 2006. **94**(9-11): p. 731-737.

191. Adam, N., et al., *Impact of selected cement additives and model compounds on the solubility of Nd (III), Th (IV) and U (VI): screening experiments in alkaline NaCl, MgCl2 and CaCl2 solutions at elevated ionic strength.* Radiochimica Acta, 2021. **109**(6): p. 431-443.

192. Gaona, X., et al., *Review of the complexation of tetravalent actinides by ISA and gluconate under alkaline to hyperalkaline conditions.* Journal of Contaminant Hydrology, 2008. **102**(3-4): p. 217-227.

193. Vercammen, K., M.A. Glaus, and L.R. Van Loon, *Complexation of calcium by R-isosaccharinic acid under alkaline conditions.* Acta Chem. Scand, 1999. **53**: p. 241-246.

194. Tanaka, K., Y. Suzuki, and T. Ohnuki, *Sorption and oxidation of tetravalent plutonium on Mn oxide in the presence of citric acid.* Chemistry letters, 2009. **38**(11): p. 1032-1033.

195. Farr, J.D., R.K. Schulze, and B.D. Honeyman, *Aqueous Pu (IV) sorption on brucite.* Radiochimica Acta, 2000. **88**(9-11): p. 675-680.

196. Tits, J., E. Wieland, and M. Bradbury, *The effect of isosaccharinic acid and gluconic acid on the retention of Eu (III), Am (III) and Th (IV) by calcite.* Applied Geochemistry, 2005. **20**(11): p. 2082-2096.

197. Holgersson, S., et al., *Effects of gluco-isosaccharinate on Cs, Ni, Pm and Th sorption onto, and diffusion into cement.* Radiochimica Acta, 1998. **82**(s1): p. 393-398.

198. Wieland, E., et al., *The effect of α-isosaccharinic acid on the stability of and Th (IV) uptake by hardened cement paste.* Radiochimica Acta, 2002. **90**(9-11): p. 683-688.

199. Tits, J., et al., *The uptake of Cs, Sr, Ni, Eu and Th by CSH phases under high pH cement pore water conditions.* PSI Interim Report TM-44-98-01, Paul Scherrer Institut, Villigen, Switzerland, 1998.

200. Rojo, H., et al., *Thermodynamics of Np (IV) complexes with gluconic acid under alkaline conditions: sorption studies.* Radiochimica Acta, 2013. **101**(3): p. 133-138.

201. Schepperle, J., *Untersuchungen zur Löslichkeit und Komplexierung von vierwertigem Plutonium und Neptunium in verdünnten und konzentrierten Salzlösungen (on-going).* Institute for Nuclear Waste Disposal (INE), 2017.

202. Nedyalkova, L., et al., *Effect of redox conditions on the structure and solubility of sulfur-and selenium-AFm phases.* Cement and Concrete Research, 2019. **123**: p. 105803.

203. Çevirim-Papaioannou, N., et al., *Uptake of niobium by cement systems relevant for nuclear waste disposal: Impact of ISA and chloride.* Cement and Concrete Research, 2022. **153**: p. 106690.

204. Tasi, A., et al., *Thermodynamic description of the plutonium–α-D-isosaccharinic acid system I: Solubility, complexation and redox behavior.* Applied Geochemistry, 2018. **98**: p. 247-264.

205. Traynor, B., et al., *Methodology for pH measurement in high alkali cementitious systems.* Cement and Concrete Research, 2020. **135**: p. 106122.

206. Zingg, A., et al., *Adsorption of polyelectrolytes and its influence on the rheology, zeta potential, and microstructure of various cement and hydrate phases.* Journal of Colloid and Interface Science, 2008. **323**(2): p. 301-312.

207. Kosmulski, M., *The pH dependent surface charging and points of zero charge. VI. Update.* Journal of Colloid and Interface Science, 2014. **426**: p. 209-212.

208. Hufner, S., *Optical Spectra of Transparent Rare.* Earth Compounds (Academic Press. Inc, London, 1978), 1978.

209. Carnall, W. and H.M. Crosswhite, *Optical spectra and electronic structure of actinide ions in compounds and in solution*, in *The Chemistry of the Actinide Elements*. 1986, Springer. p. 1235-1277.

210. Beitz, J.V., *Laser-induced fluorescence studies of Cm3+ complexes in solution.* Radiochimica Acta, 1991. **52**(1): p. 35-40.

211. Cotton, S., *Lanthanide and actinide chemistry*. 2013: John Wiley & Sons.

212. Edelstein, N.M., et al., *Optical properties of Cm (III) in crystals and solutions and their application to Cm (III) speciation.* Coordination Chemistry Reviews, 2006. **250**(7-8): p. 948-973.

213. Horrocks Jr, W.D. and D.R. Sudnick, *Lanthanide ion probes of structure in biology. Laser-induced luminescence decay constants provide a direct measure of the number of metal-coordinated water molecules.* Journal of the American Chemical Society, 1979. **101**(2): p. 334-340.

214. Kimura, T., et al., *Determination of the hydration number of Cm (III) in various aqueous solutions.* Radiochimica Acta, 1996. **72**(2): p. 61-64.

215. Wagner, T., et al., *GEM-Selektor geochemical modeling package: TSolMod library and data interface for multicomponent phase models.* The Canadian Mineralogist, 2012. **50**(5): p. 1173-1195.

216. Lothenbach, B., et al., *Cemdata18: A chemical thermodynamic database for hydrated Portland cements and alkali-activated materials.* Cement and Concrete Research, 2019. **115**: p. 472-506.

217. Kulik, D.A., *Improving the structural consistency of C-S-H solid solution thermodynamic models.* Cement and Concrete Research, 2011. **41**(5): p. 477-495.

218. Shock, E.L., *Organic acids in hydrothermal solutions; standard molal thermodynamic properties of carboxylic acids and estimates of dissociation constants at high temperatures and pressures.* American Journal of Science, 1995. **295**(5): p. 496-580.

219. Shock, E.L. and C.M. Koretsky, *Metal-organic complexes in geochemical processes: Estimation of standard partial molal thermodynamic properties of aqueous complexes between metal cations and monovalent organic acid ligands at high pressures and temperatures.* Geochimica et Cosmochimica Acta, 1995. **59**(8): p. 1497-1532.

220. Shock, E.L., et al., *Inorganic species in geologic fluids: correlations among standard molal thermodynamic properties of aqueous ions and hydroxide complexes.* Geochimica et Cosmochimica Acta, 1997. **61**(5): p. 907-950.

221. Lumsden, J.S., *XXXIV.—Solubilities of the calcium salts of the acids of the acetic series.* Journal of the Chemical Society, Transactions, 1902. **81**: p. 350-362.

222. De Stefano, C., et al., *Speciation of low molecular weight carboxylic ligands in natural fluids: protonation constants and association with major components of seawater of oxydiacetic and citric acids.* Analytica chimica acta, 1999. **398**(1): p. 103-110.

223. Akram, N. and X. Bourbon, *Analyse critique de donnees thermodynamiques: Povoir complexant de l'EDTA, du NTA, du citrate et de l'oxalate vis a vis de cations metalliques.* ANDRA report C RP O. GES, 1996. **92**.

224. Blanc, P., et al., *ThermoChimie database developments in the framework of cement/clay interactions.* Applied Geochemistry, 2015. **55**: p. 95-107.

225. Sari, H., *Determination of stability constants of citrate complexes with divalent metal ions (M2+ = Mg, Ca, Ni, Cu and Zn) in aqueous solutions solutions.* Energy Education Science and Technology, 2001. **6** p. 85-103.

226. Gácsi, A., et al., *The structure of calcium citrate complex forming in hyperalkaline aqueous solution.* Journal of molecular structure, 2016. **1118**: p. 110-116.

227. Bouzouaid, L., et al., *Portlandite solubility and Ca2+ activity in presence of gluconate and hexitols.* Cement and Concrete Research, 2021. **149**: p. 106563.

228. Helgeson, H.C., D.H. Kirkham, and G.C. Flowers, *Theoretical prediction of the thermodynamic behavior of aqueous electrolytes by high pressures and temperatures; IV, Calculation of activity coefficients, osmotic coefficients, and apparent molal and standard and relative partial molal properties to 600 degrees C and 5kb.* American journal of science, 1981. **281**(10): p. 1249-1516.

229. Kulik, D.A., et al., *GEM-Selektor geochemical modeling package: revised algorithm and GEMS3K numerical kernel for coupled simulation codes.* Computational Geosciences, 2013. **17**: p. 1-24.

230. Yan, Y., et al., *Effect of alkali hydroxide on calcium silicate hydrate (CSH).* Cement and Concrete Research, 2022. **151**: p. 106636.

231. Grangeon, S., et al., *X-ray diffraction: a powerful tool to probe and understand the structure of nanocrystalline calcium silicate hydrates.* Acta Crystallographica Section B: Structural Science, Crystal Engineering and Materials, 2013. **69**(5): p. 465-473.

232.   Masoumi, S., et al., *Effective interactions between calcium-silicate-hydrate nanolayers.* The Journal of Physical Chemistry C, 2019. **123**(8): p. 4755-4766.

233.   Lothenbach, B., P. Durdzinski, and K. De Weerdt, *Thermogravimetric analysis.* A practical guide to microstructural analysis of cementitious materials, 2016. **1**: p. 177-211.

234.   Churakov, S.V., et al., *Intrinsic acidity of surface sites in calcium silicate hydrates and its implication to their electrokinetic properties.* The journal of physical chemistry C, 2014. **118**(22): p. 11752-11762.

235.   Yu, P., et al., *Structure of calcium silicate hydrate (C-S-H): Near-, Mid-, and Far-infrared spectroscopy.* Journal of the American Ceramic Society, 1999. **82**(3): p. 742-748.

236.   Kuzel, H.-J. and H. Pöllmann, *Hydration of C3A in the presence of Ca (OH) 2, CaSO4· 2H2O and CaCO3.* Cement and Concrete Research, 1991. **21**(5): p. 885-895.

237.   Pöllmann, H., T. Witzke, and H. Kohler, *Kuzelite,[(SO4)∑ 6H2O], a new mineral from Maroldsweisach/Bavaria, Germany.* Neues Jahrbuch f¸ r Mineralogie-Monatshefte, 1997: p. 423-432.

238.   Runčevski, T., et al., *Crystal structures of calcium hemicarboaluminate and carbonated calcium hemicarboaluminate from synchrotron powder diffraction data.* Acta Crystallographica Section B: Structural Science, 2012. **68**(5): p. 493-500.

239.   Nakamoto, K., *Infrared and Raman spectra of inorganic and coordination compounds, part B: applications in coordination, organometallic, and bioinorganic chemistry*. 2009: John Wiley & Sons.

240.   Götz-Neunhoeffer, F. and J. Neubauer, *Refined ettringite (Ca6Al2 (SO4) 3 (OH) 12· 26H2O) structure for quantitative X-ray diffraction analysis.* Powder diffraction, 2006. **21**(1): p. 4-11.

241.   Myneni, S.C., et al., *Vibrational spectroscopy of functional group chemistry and arsenate coordination in ettringite.* Geochimica et Cosmochimica Acta, 1998. **62**(21-22): p. 3499-3514.

242.   Scholtzová, E., et al., *Structural and spectroscopic characterization of ettringite mineral– combined DFT and experimental study.* Journal of Molecular Structure, 2015. **1100**: p. 215-224.

243.   Meyn, M., K. Beneke, and G. Lagaly, *Anion-exchange reactions of layered double hydroxides.* Inorganic Chemistry, 1990. **29**(26): p. 5201-5207.

244.   Von Hoessle, F., J. Plank, and F. Leroux, *Intercalation of sulfonated melamine formaldehyde polycondensates into a hydrocalumite LDH structure.* Journal of Physics and Chemistry of Solids, 2015. **80**: p. 112-117.

245.   Okoronkwo, M.U., et al., *Stability of Calcium–Alumino Layered-Double-Hydroxide Nanocomposites in Aqueous Electrolytes.* Industrial & Engineering Chemistry Research, 2018. **57**(40): p. 13417-13426.

246.   Wang, Q., et al., *Superplasticizer to layered calcium aluminate hydrate interface characterized using model organic molecules.* Cement and Concrete Research, 2018. **110**: p. 52-69.

247.   Tronto, J., et al., *In vitro release of citrate anions intercalated in magnesium aluminium layered double hydroxides.* Journal of Physics and Chemistry of Solids, 2004. **65**(2-3): p. 475-480.

248.   Zhang, J., et al., *Synthesis of layered double hydroxide anionic clays intercalated by carboxylate anions.* Materials Chemistry and Physics, 2004. **85**(1): p. 207-214.

249.   Geffroy, C., et al., *Surface complexation of calcite by carboxylates in water.* Journal of Colloid and Interface science, 1999. **211**(1): p. 45-53.

250.   Giraudeau, C., et al., *Surface and Intercalation Chemistry of Polycarboxylate Copolymers in Cementitious Systems.* Journal of the American Ceramic Society, 2009. **92**(11): p. 2471-2488.

251.   Matschei, T., B. Lothenbach, and F.P. Glasser, *Thermodynamic properties of Portland cement hydrates in the system CaO–Al2O3–SiO2–CaSO4–CaCO3–H2O.* Cement and Concrete Research, 2007. **37**(10): p. 1379-1410.

252.   Lothenbach, B., et al., *Thermodynamic modelling of the effect of temperature on the hydration and porosity of Portland cement.* Cement and Concrete Research, 2008. **38**(1): p. 1-18.

253.   Dalconi, M.C., et al., *The crystal structure of a new calcium aluminate phase containing formate.* Cement and Concrete Research, 2021. **146**: p. 106490.

254.   Barzgar, S., et al., *The effect of sodium hydroxide on Al uptake by calcium silicate hydrates (CSH).* Journal of colloid and interface science, 2020. **572**: p. 246-256.

255.   L'Hôpital, E., et al., *Incorporation of aluminium in calcium-silicate-hydrates.* Cement and Concrete Research, 2015. **75**: p. 91-103.

256. Mesecke, K., L.N. Warr, and W. Malorny, *Structure modeling and quantitative X-ray diffraction of C-(A)-SH.* Journal of applied crystallography, 2022. **55**(1).

257. Bernard, E., Y. Yan, and B. Lothenbach, *Effective cation exchange capacity of calcium silicate hydrates (CSH).* Cement and Concrete Research, 2021. **143**: p. 106393.

258. L'Hôpital, E., et al., *Influence of calcium to silica ratio on aluminium uptake in calcium silicate hydrate.* Cement and Concrete Research, 2016. **85**: p. 111-121.

259. Liu, X., et al., *Effects of pH on the nano/micro structure of calcium silicate hydrate (CSH) under sulfate attack.* Cement and Concrete Research, 2021. **140**: p. 106306.

260. Nedyalkova, L., et al., *Uptake of iodide by calcium aluminate phases (AFm phases).* Applied Geochemistry, 2020. **116**: p. 104559.

261. Yan, Y., et al., *Al uptake in calcium silicate hydrate and the effect of alkali hydroxide.* Cement and Concrete Research, 2022. **162**: p. 106957.

262. Turesson, M., C. Labbez, and A. Nonat, *Calcium Mediated Polyelectrolyte Adsorption on Like-Charged Surfaces.* Langmuir, 2011. **27**(22): p. 13572-13581.

263. Felipe-Sotelo, M., et al., *Effect of anthropogenic organic complexants on the solubility of Ni, Th, U (IV) and U (VI).* Journal of Hazardous Materials, 2015. **300**: p. 553-560.

264. Bretti, C., et al., *Acid–Base and Thermodynamic Properties of d-Gluconic Acid and Its Interaction with Sn2+ and Zn2+.* Journal of Chemical & Engineering Data, 2016. **61**(6): p. 2040-2051.

265. Pointeau, I., et al., *Sorption mechanisms of Eu3+ on CSH phases of hydrated cements.* Journal of Colloid and Interface Science, 2001. **236**(2): p. 252-259.

266. Szabo, P.G., et al., *Uptake of Ni(II), Eu(III) and Pu(III/IV) by Hardened Cement Paste in the Presence of Proxy Ligands for the Degradation of Polyacrylonitrile.* Frontiers in Nuclear Engineering, 2023. **2**.

267. Horrocks Jr, W.D. and D.R. Sudnick, *Lanthanide ion luminescence probes of the structure of biological macromolecules.* Accounts of Chemical Research, 1981. **14**(12): p. 384-392.

268. Rabung, T., et al., *A TRLFS study of Cm (III) hydroxide complexes in alkaline CaCl2 solutions.* Radiochimica Acta, 2008. **96**(9-11): p. 551-560.

269. Fanghänel, T., et al., *Thermodynamics of radioactive trace elements in concentrated electrolyte solutions: hydrolysis of Cm3+ in NaCl-solutions.* Radiochimica Acta, 1994. **66**(s1): p. 81-88.

270. Snellings, R., *X-ray powder diffraction applied to cement.* A practical guide to microstructural analysis of cementitious materials, 2016. **2**: p. 104-176.

271. Snellings, R., et al., *Report of TC 238-SCM: hydration stoppage methods for phase assemblage studies of blended cements—results of a round robin test.* Materials and structures, 2018. **51**(4): p. 1-12.

272. O'Connor, B.H. and M.D. Raven, *Application of the Rietveld refinement procedure in assaying powdered mixtures.* Powder Diffraction, 1988. **3**(1): p. 2-6.

273. Jansen, D., et al., *A remastered external standard method applied to the quantification of early OPC hydration.* Cement and Concrete Research, 2011. **41**(6): p. 602-608.